Continuum structure of few-body systems

Kontinuumsstruktur von Wenig-Teilchen Systemen
Zur Erlangung des Grades eines Doktors der Naturwissenschaften (Dr. rer. nat.)
Genehmigte Dissertation von Sebastian Dietz aus Hanau
Tag der Einreichung: 10. November 2022, Tag der Prüfung: 19. Dezember 2022

1. Gutachten: Prof. Dr. Hans-Werner Hammer
2. Gutachten: Prof. Achim Schwenk, Ph.D.
Darmstadt, Technische Universität Darmstadt

TECHNISCHE
UNIVERSITÄT
DARMSTADT

Physics Department
Institut für Kernphysik
Theoriezentrum
AG Hammer

Continuum structure of few-body systems
Kontinuumsstruktur von Wenig-Teilchen Systemen

Accepted doctoral thesis by Sebastian Dietz

Date of submission: 10. November 2022
Date of thesis defense: 19. Dezember 2022

Darmstadt, Technische Universität Darmstadt

Erklärungen laut Promotionsordnung

§ 8 Abs. 1 lit. c PromO

Ich versichere hiermit, dass die elektronische Version meiner Dissertation mit der schriftlichen Version übereinstimmt.

§ 8 Abs. 1 lit. d PromO

Ich versichere hiermit, dass zu einem vorherigen Zeitpunkt noch keine Promotion versucht wurde. In diesem Fall sind nähere Angaben über Zeitpunkt, Hochschule, Dissertationsthema und Ergebnis dieses Versuchs mitzuteilen.

§ 9 Abs. 1 PromO

Ich versichere hiermit, dass die vorliegende Dissertation selbstständig und nur unter Verwendung der angegebenen Quellen verfasst wurde.

§ 9 Abs. 2 PromO

Die Arbeit hat bisher noch nicht zu Prüfungszwecken gedient.

Darmstadt, 10. November 2022

_____

S. Dietz

Zusammenfassung

Der Fokus dieser Arbeit liegt auf der Untersuchung von Zuständen auf den unphysikalischen Blättern der komplexen Energieebene für Wenig-Teilchen Systeme unter Verwendung von Potentialen hergeleitet aus der führenden Ordnung der pionenlosen effektiven Feldtheorie (EFT($\not{\pi}$)). Ziel ist es eine Aussage über die Kontinuumsstruktur des Drei-Neutronen System zu treffen. Hierzu werden verschiedene Methoden angewendet. Diese ermöglichen die Berechnung von Observablen sowohl auf dem physikalischen als auch den unphysikalischen Blättern. Komplementiert wird diese Gruppe von Methoden durch Rechnungen im endlichen Volumen.

Anhand von verschiedenen Zwei-Teilchen Testsystemen werden Methoden zur Berechnung der Streuphasen bzw. Zeitverzögerungen, der analytischen Fortsetzung in der Kopplungskonstanten (ACCC) und die analytische Fortsetzung der Lippmann-Schwinger Gleichung auf das unphysikalische Blatt anhand der Schwierigkeit und Möglichkeiten ihrer Anwendung und der Qualität ihrer Ergebnisse miteinander verglichen.

Im Folgenden werden verschiedene Drei-Teilchen Systeme betrachtet. Die Methode der analytischen Fortsetzung wird auf ein System aus drei spinlosen Bosonen angewendet. Dieses bietet die Möglichkeit sowohl Resonanzen als auch virtuelle Zustände auf beiden an das physikalische Blatt anschließenden unphysikalischen Blättern zu untersuchen. Weiterhin werden spinbehaftete Drei-Teilchen Systeme betrachtet. Für die Neutron-Deuteron Streuung wird die Streuphasen Anomalie untersucht. Nachfolgend wird das Drei-Neutronen System betrachtet. Hierzu werden zuerst die Streuphasen auf dem physikalischen Blatt durch Extrapolation von einem gebundenen zu dem physikalischen Dineutron extrahiert. Im Folgenden wird die Polstruktur des Drei-Neutronen System auf dem unphysikalischen Blatt durch analytische Fortsetzung untersucht. In beiden Fällen zeigt sich kein Anzeichen einer Resonanz oder eines virtuellen Zustandes. Dieses Ergebnis wird unterstützt durch die Berechnung der Punktproduktionsamplitude und ihres Vergleichs mit den Vorhersagen der nicht-relativistischen konformen Feldtheorie. Die Punktproduktionsamplitude wird weiterhin für ein Vier-Neutronen System sowie für das System der drei spinlosen Bosonen hergeleitet. Das System der drei Bosonen dient hierbei als Benchmark für die Existenz einer Resonanz.

Abschließend werden unter Verwendung des Lüscher Formalismus die Spektren der Dineutron-Neutron sowie Dineutron-Dineutron Streuung für unphysikalisch gebundene Dineutronen in endlichem Volumen berechnet. In beiden Fällen zeigt sich, dass selbst für eine unphysikalisch erhöhte Wechselwirkungsstärke weder Drei- noch Vier-Neutronen Resonanzen auftreten.

Zusammengefasst zeigt diese Arbeit unter Anwendung verschiedener Methoden, dass das Drei-Neutronen System weder Resonanzen noch virtuelle Zustände besitzt. Weiterhin wird die Nicht-Existenz von Resonanzen im Vier-Neutronen System anhand zweier Methoden motiviert.

Abstract

The focus of this work is on the study of states on the unphysical sheets of the complex energy plane for few-particle systems using potentials derived from leading order pionless effective field theory (EFT($\not{\pi}$)). The aim is to obtain a statement about the continuum structure of the three-neutron system. For this purpose, various methods are applied. These allow the computation of observables on both, the physical and unphysical sheets. This group of methods is complemented by calculations in finite volume.

On the basis of different two-particle test systems, methods for the calculation of the phase shifts and time delays, the analytical continuation in the coupling constant (ACCC) and the analytical continuation of the Lippmann-Schwinger equation to the unphysical sheet are compared with each other by the difficulty and possibilities of their application and the quality of their results.

In the following, different three-particle system are considered. First, the method of analytical continuation is applied to a system of three spinless bosons. This offers the possibility to investigate resonances as well as virtual states on both unphysical sheets connected to the physical one. Furthermore, three-particle systems containing spin are considered. First, the phase shift anomaly of the neutron-deuteron system is investigated. Subsequently the three-neutron system is considered. For this purpose, first the phase shifts on the physical sheet are extracted by extrapolation from a bound to the physical dineutron. In the following, the pole structure of the three-neutron system on the unphysical sheet is investigated by analytical continuation. In both cases, no sign of a resonance or a virtual state is found. This result is supported by the calculation of the point production amplitude and its comparison with the predictions of the nonrelativistic conformal field theory. The point production amplitude is further derived for a four-neutron system as well as for the system of the three spinless bosons. The system of the three bosons serves here as a benchmark for the existence of a resonance.

Finally, using the Lüscher formalism, the spectra of the dineutron-neutron as well as the dineutron-dineutron scattering for unphysically bound dineutrons in finite volume are calculated. In both cases, it is shown that even for an unphysically increased interaction strength neither three- nor four-neutron resonances occur.

In summary, this work shows using different methods, that the three-neutron system neither presents resonances nor virtual states. Furthermore, the non-existence of resonances in the four-neutron system is motivated by two methods.

Contents

1 Introduction

The field of nuclear physics goes back to the discovery of the nucleus by Rutherford and collaborators at the beginning of the 20th century [1–5], where the name "nucleus" was first introduced [6]. In 1919, Rutherford discovered the first nucleon, the proton [7]. It took a further decade up to the discovery of the neutron by Chadwick in 1932 [8].

In the following years the field rapidly evolved. In 1935 Yukawa predicted an interaction binding nucleons together into the nucleus by the exchange of a meson [9]. This meson was discovered experimentally in 1947 [10] and is nowadays known as the pion. In the same year, the first so-called strange particles were observed in cosmic rays [11]. An important step to the modern field of nuclear physics was made by the postulation of up, down and strange quarks by Gell-Mann in 1964 [12]. This journey finally results in the proposal of quantum chromodynamics (QCD).

At low energies, QCD is non-perturbative due to the so-called confinement. In general, this means that all interactions have to be treated explicitly. A prominent example for these type of calculations is lattice QCD [13, 14], which describes nuclei and their properties fully from fundamental forces on a discrete grid in space-time. However, lattice QCD is numerically highly expensive and therefore restricted, at the moment, to smaller systems only. An alternative approach in the recent decades has been the application of model potentials, e.g., the Argonne potentials [15, 16]. However, these phenomenological potentials have the disadvantage of a missing error quantification. An approach to overcome these problems is the application of effective field theories (EFT), which were pioneered in the field of nuclear physics by Weinberg [17, 18]. They present a controlled and model-independent description of nuclei, based on an expansion in the ratio of short- and long-distance scales. The accuracy can be systematically improved by including higher orders in the calculation.

Within this work, pionless EFT (EFT($\not{\pi}$)) [19–22] at leading order is applied. It is perfectly suited for the treatment of few-body systems with large scattering length up to momenta at the order of the pion mass. A prominent example for these type of system is the neutron with a neutron-neutron scattering length due to the strong interaction of $a_0 = -18.9(4)\,\mathrm{fm}$ [23].
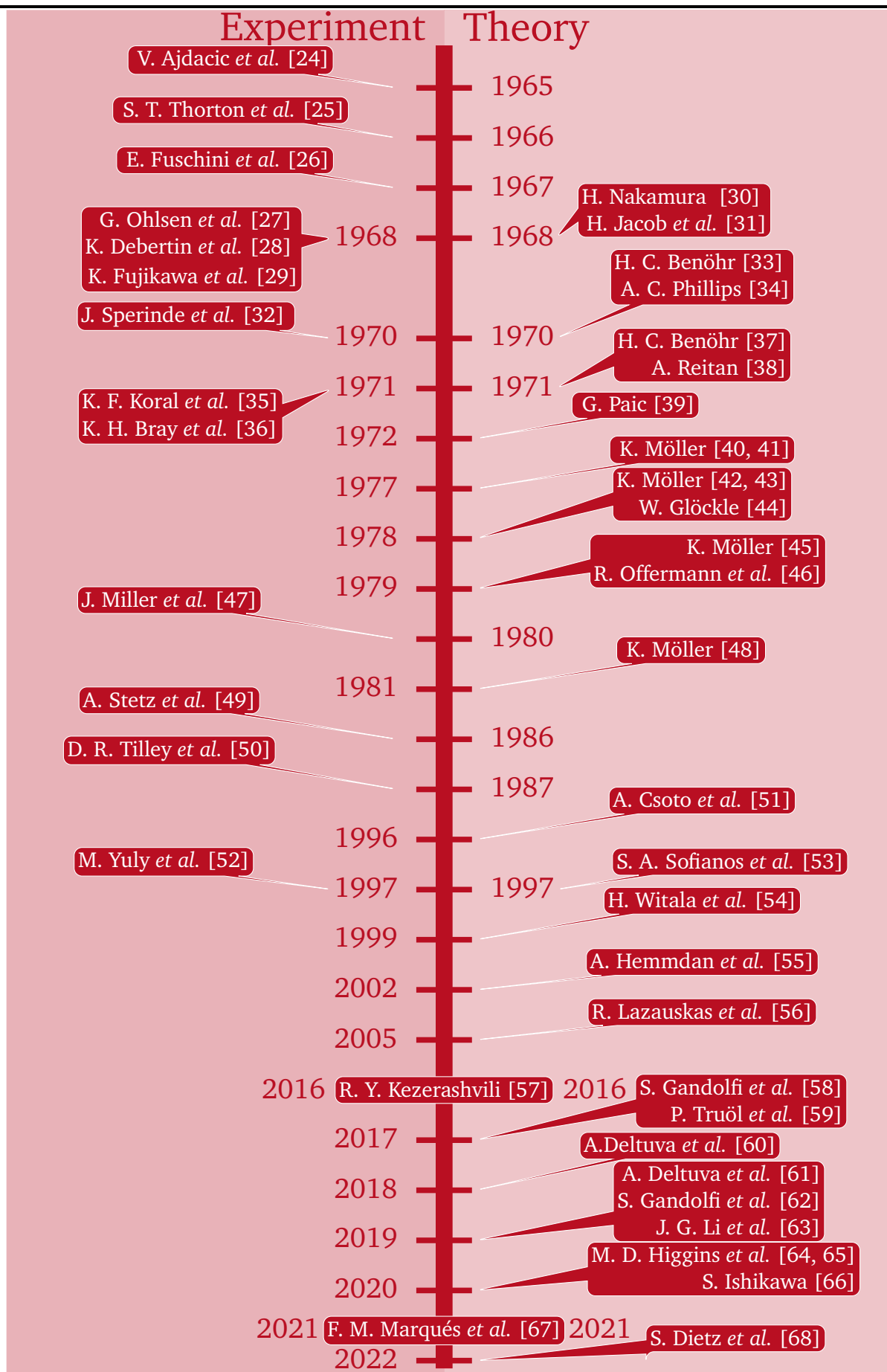
Figure 1.1.: A time line presenting an overview of the publications on three-neutron systems.

In general, there are many more unknown neutron-rich than unknown proton-rich nuclei. These high numbers of neutron-rich nuclei results in a large experimental and theoretical interest. The theoretical description of these systems requires a precise knowledge of the neutron-neutron interaction. Pure neutron systems present a perfect playground to investigate this interaction. The simplest possible configuration of these states are few-neutron systems. They are in the focus of physical research for more than half a century. But still there is no final conclusion for three and four neutron systems. In particular, a special interest is on their continuum structure, i.e., the existence of resonances and virtual states. Figure 1.1 shows a timeline presenting an overview of theoretical and experimental publications dealing with the three-neutron system. As one can see, there are many more theoretical than experimental publications. The reason for this is that there are no systems with three neutrons weakly bound to a core. Therefore, an experimental realization of a three-neutron system becomes very difficult. This, on the other hand, is possible for example for a four-neutron system [69]. A more detailed historical overview can be found in Refs. [57, 67].

Regarding the three-neutron system, especially the theoretical publications present ambiguous results. Let us mention some of these publications, applying methods used in this work, in more detail. A big part of this work is dedicated to the derivation and application of the formalism of analytical continuation. In the 1970s, this formalism was applied to the three-neutron system for the first time by Glöckle [44] and Möller [40–43, 45], independently. They used a neutron-neutron interaction in the $^1S_0$ channel derived from the Yamaguchi model, finding no evidence for a three-neutron resonance. A coordinate space version of the analytical continuation is the so-called complex scaling method (CSM). It was applied to the three-neutron system in the 1990s indicating the existence of a resonance with an unphysically large width [51, 54]. These results were supported by Ref. [55], extending Glöckle's earlier work [44] to more partial-wave channels for the neutron-neutron interaction. In contrast, a further theoretical work applying not only the CSM but also the analytical continuation in the coupling constant (ACCC) excluded a possible three-neutron resonance [56]. At this time almost every method on the market had been applied together with the up to this time available realistic nucleon-nucleon interaction potentials. A new interest on the three-neutron system was raised in the year 2016 by an experimental evidence for a possible four-neutron resonance by Kisamori *et al.* [70]. This result was supported by a recent experiment by Duer *et al.* [69]. A further recent experiment by Faestermann *et al.* even suggested that the tetraneutron could be bound [71]. Following the publication by Kisamori *et al.*, a theoretical work applying a formalism related to the ACCC suggested that a possible three-neutron resonance could exist at energies lower than the tetraneutron resonance. This result was supported by a calculation using the *ab-initio* no-core Gamow shell model [63]. However, these results lead to a controversial discussion [59, 61, 62] as well as further publications applying other methods [60, 66], which found no evidence for a three-neutron resonance. A further theoretical work performed in the recent years applied the hyperspherical formalism to calculate the so-called Wigner-Smith time delay [64, 65], a quantity we will also investigate within this work. They could show that the Pauli repulsion is too large, such that no resonance is formed, but a peak in the time delay appears.

All in all, this historical overview shows that the question on the structure of the three-neutron system is still not finally solved. Especially within the recent years, a new interest on these systems arised. This work approaches this problem combining the benefits of an effective field theory with different methods to search for states on the unphysical sheets, i.e., resonances and virtual states. These methods can be grouped into two classes: approaches that perform calculations on the physical sheet and methods that allow to access the unphysical sheets directly. A type of formalism that can not directly be connected to one of these classes are calculations in finite volume [72–76]. A resonance in finite volume shows up as a so-called avoided level crossing. This type of formalism has already been applied to the three-neutron system, presenting no indication of a resonance [68]. The four-neutron system within the finite volume

formalism is currently under investigation. Similar to the three-neutron system, it will not only be investigated for the physical neutron-neutron scattering length, but also for a bound dineutron. This results in the contribution of the dineutron-dineutron scattering to the spectrum. To identify these levels, the dineutron-dineutron spectrum including topological corrections is calculated applying the Lüscher formalism [77–79] within this work.

Coming back to the two classes of methods, the calculations on the physical sheet are much more straightforward. Typically, one applies standard techniques, e.g., the calculation of phase shifts and time delays. For some of these methods, it is necessary to unphysically modify the system by altering the interaction strength or adding a further potential. An example applied within this work is the ACCC [80–84], which analytically extrapolates the pole trajectory from the physical to the unphysical sheet. While the calculations for this first class of methods are rather simple, the extrapolation to the unphysical sheets can be delicate or even questionable. In opposite, the second class of methods has the complicating feature, that before performing the calculations a lot of work deriving the formalism is needed. However, as soon as this is done, the application is again rather straightforward and relies on similar techniques as the first class of methods. Further, the results derived on the unphysical sheets directly are much more robust and reliable. Within this work, the general procedure of performing this analytical continuation for two- and three-body systems on the basis of the momentum-space Lippmann-Schwinger [85] and Faddev equations [86], respectively, is presented. It relies on the transformation of the cut-structure of the complex energy plane. We will restrict the application to two special implementations proposed by Glöckle [44], performing an implicit transformation, and Afnan [87–91], rotating the cut analogous to the CSM.

Few-neutron systems are not only very important in the understanding of the nuclear interaction, but also an example for a so-called "unnucleus" [92]. An unnucleus is a field in a nonrelativistic conformal field theory [93] characterized solely by two parameters, its mass m and the scaling dimension Δ. Considering a nuclear reaction, where a few-neutron final state is created, this final state can be interpreted as an unnucleus in a certain energy range. This energy range is bounded from below by the scale set through the large scattering length $a_0 = -18.9(4)$ fm and from the top by the small effective range $r_0 \approx 2.8$ fm. By calculating the point production amplitude R, a quantity similar to the cross section, one can on the one hand compare the predictions by nonrelativistic conformal field theory and for free particles with the spectrum. On the other hand, the point production amplitude is a quantity related to the first class of methods. So, it can be used to search for the existence of resonances and virtual states close to threshold.

The two complementary classes of methods applied within this work allow to overcome the disjoint disadvantages of both classes. Together with the leading order pionless EFT interaction, which is perfectly suited to describe the low-energy properties of neutron matter very well (see, e.g., Ref. [94]), it allows to make a clear statement on the pole structure of the three-neutron system. All higher-order corrections, including attractive P-wave channels, are perturbative and we do not expend them to alter the low-energy resonance structure of the system.

This work is structured in the following way. Chapter 2 represents an introduction into the concepts of scattering theory for few-body systems applied in the following Chapters. The concept of a resonance is presented and the sheet structure of the complex energy plane is discussed. In Chapter 3, the idea of a EFTs is introduced. On the example of pionless EFT, it is applied to two- and three-body systems. The Lagrangians are used to derive the scattering equations for systems of three bosons, a neutron and a deuteron, and the three-neutron system. Further, the pionless EFT is applied to derive an effective interaction potential. This potential is used together with the Faddeev equations, which are introduced in the following Chapter, Chapter 4, for a general single-channel problem including two- and three-body interactions. Chapter 5 derives the methods of the second class, introduced previously, to perform

an analytical continuation for two- and three-body systems as well as technical and numerical details of the analytical continuation. Further, the derivation of the ACCC is presented. These methods are applied in Chapter 6 together with further methods of the first class to investigate the pole trajectories for two two-body toy potentials and to extract resonance and virtual state energies. In anticipation of the application to the three-body systems, the results of the different methods are compared and their benefits and shortcomings are discussed.

In the following, different three-body systems are investigated. In Chapter 7, a system of three spinless bosons presenting the Efimov effect is considered. The Faddeev equations derived from the Lagrange and the Faddeev formalism are presented and compared to identify the structures relevant for the analytical continuation. Further, the renormalization of the three-body force is discussed. Furthermore, another representation of the Faddeev equation introduced by Bringas *et al.* [95] is presented. Together with the previously introduced Faddeev equation, it is used to calculate the Efimov trajectory for negative scattering lengths, located on the physical and unphysical sheet, applying the analytical continuation. This calculation serves as a benchmark for the following investigation of the three-neutron system. Furthermore, the Faddeev equation derived within this work, is used with the analytical continuation to calculate the Efimov trajectory on the physical and unphysical sheets for positive scattering length. So, together with the previous results, the full spectrum of the three-boson system on the physical and both unphysical sheets is presented.

Chapter 8 investigates the neutron-deuteron system in the quartet and doublet channel. The phase shift anomaly in the doublet channel is studied and its effect on the cross section is examined. A system of three neutrons on the physical sheet is investigated in Chapter 9. The phase shifts for a bound dineutron system with the third neutron in a relative S-, P- and D-wave are calculated. It is shown that they follow universal predictions, which are determined and compared to previous calculations. Further, the phase shifts are extrapolated to the physical, virtual dineutron system using different models. The resulting phase shifts are compared to an existing calculation using a hyperspherical formalism [64, 65]. Based on the phase shift technique, which is part of the first class of methods, it is shown that the three-neutron system presents no sign of a resonance.

In the following Chapter, Chapter 10, the three-neutron system is analytically continued to the unphysical sheets. This method is part of the second class of formalism previously discussed. First, it is shown that the three-neutron system in pionless EFT does not present any bound state. So, the calculation for a bound dineutron is benchmarked to a calculation using the Yamaguchi model. Decreasing the scattering length to the physical value it is shown, using the analytical continuation, that the three-neutron system neither presents a resonance nor a virtual state.

In Chapter 11, the point production of a three-boson, a three-neutron and the four-neutron system is considered. The point production amplitude for these systems is derived. It is a quantity related to the cross section. So, this formalism is part of the first class of methods introduced. The effect of the resonance in the three-boson system onto the amplitude is investigated. Further, the three-neutron amplitude is calculated and compared to predictions for free particles and to nonrelativistic conformal field theory. It is shown that the amplitude follows these predictions, not showing a resonance structure. Finally, the equations for the four-neutron point production amplitude are derived. On the basis of the predictions by nonrelativistic conformal field theory it is discussed that it is unlikely that the four-neutron system presents a resonance.

Chapter 12 presents calculations using the third class of formalism considered, the finite volume approach. Applying the Lüscher formalism the dineutron-neutron and dineutron-dineutron energy spectra including topological corrections for an unphysically bound dineutron system are calculated. The spectra are compared to the three- and four-neutron spectra derived by the solution of the Hamiltonian in finite volume to identify the corresponding energy levels.

Finally, a summary and outlook are given in Chapter 13.

2 Scattering theory for few-body systems

In the following Chapter, an introduction to the basic concepts of scattering theory, needed to understand the results presented in this work, is given. The structure follows the work by Taylor [96]. First, a focus is on the two-body system. Following the general picture of the scattering process, the S- and T-matrix as well as various representations of the Lippmann-Schwinger equation are presented. The phase shift and the Jost function are introduced and connected to bound states and resonances. Further, the sheet structure of the complex energy plane for two- and higher-body systems is investigated.

Here and throughout the entire thesis natural units, $\hbar = c = 1$, are used. Further, an uniform color coding describing the sheet structure is used. The physical sheet and poles thereon correspond to an orange color and/or a shading of the form ⬜ , while the unphysical sheets and corresponding poles correspond to a blue color and a shading like ⬜ . The definition of the physical and unphysical sheets will be given in the following Sections.

2.1. General idea

We are interested in the scattering of a particle on a target. This process can in general be divided into three parts; the free incoming particle, the scattering process itself, and the free outgoing particle. Figure 2.1 shows a sketch of the system close to the scattering region. The process is characterized by three wave functions, $\psi_{\text{in/out}}$ describing the free ingoing (outgoing) particle and ψ representing the scattering process. The interaction of the particle and the target is determined by the Hamiltonian $H = H_0 + V$, where H_0 is the kinetic part and V represents the interaction potential. Note that in general there does not have to be an outgoing particle, e.g. a bound state is formed.

Experimentally only the in- and outgoing particles can be observed, while the scattering process itself is not observable. So, in describing the scattering process we should concentrate on the incoming and outgoing wave functions. These can be connected to the scattering wave function by introducing the Møller operators $\Omega_{\pm}$,

$$
\begin{aligned}
|\psi\rangle &= \lim_{t \to -\infty} U(t)^{\dagger} U^{(0)}(t) |\psi_{\text{in}}\rangle & := \Omega_{+} |\psi_{\text{in}}\rangle \, , \\
&= \lim_{t \to +\infty} U(t)^{\dagger} U^{(0)}(t) |\psi_{\text{out}}\rangle & := \Omega_{-} |\psi_{\text{out}}\rangle \, .
\end{aligned}
\tag{2.1}
$$

$U(t) = \exp\left(-iHt\right)$ represents the time evolution operator for the full Hamiltonian, while $U^{(0)}(t)$ is the time evolution operator for the kinetic part of the Hamiltonian H_0 only. The time is chosen such that the scattering process takes place at $t = 0$, i.e. $|\psi\rangle \equiv |\psi(t = 0)\rangle$. In the following, it is assumed that an
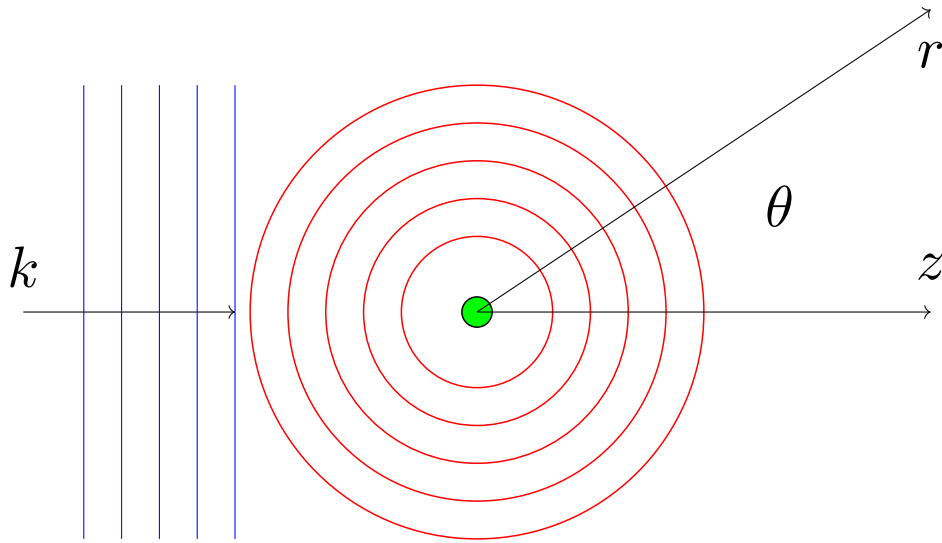
Figure 2.1.: Scattering of an incoming plane wave (blue) with momentum k on a target (●) resulting in an outgoing spherical wave (red).

outgoing wave function exists. So, the Møller operators are isometric and the outgoing wave function can be calculated directly from the incoming wave function by

$$|\psi_{\text{out}}\rangle = \Omega_-^\dagger \Omega_+ |\psi_{\text{in}}\rangle := S |\psi_{\text{in}}\rangle \,. \tag{2.2}$$

This combination of the Møller operators is typically referred to as the (unitary) scattering or S-matrix, $S = \Omega_-^\dagger \Omega_+$. It contains all information relevant to describe the scattering process. Note that the notation used in this overview is mainly reduced to presenting "operator equations". To prove the identities presented here, matrix elements of the operators in a given basis will be considered. While physically the in- and outgoing states are represented by wave packets, for practical derivations it is assumed that they are a superposition of plane waves.

So far, the ansatz includes the time explicitly (time-dependent scattering). In the following, different ways how to calculate the S-matrix are presented. This will be done in a time-independent scattering formalism.

To simplify the following derivations a decomposition of the S-matrix into two contributions is considered. On the one hand, the in- and outgoing state can be equivalent. This part is represented by an identity operator $\mathbb{1}$. On the other hand, a transition between two different states can take place. This contribution is taken care of by introducing the transition or T-matrix. Altogether, the S-matrix is given by

$$S = \mathbb{1} - 2\pi i T \,. \tag{2.3}$$

The prefactor of the T-matrix is a convention. Here, the convention by Taylor [96] is used. To derive a self-consistent equation for the T-matrix consider the two Green's operators,

$$\begin{aligned} G_0(z) &:= [z - H_0]^{-1} \,, \\ G(z) &:= [z - H]^{-1} \,. \end{aligned} \tag{2.4}$$

Scattering theory for few-body systems

They present a pole at the discrete eigenvalues of H_0 or H, respectively. In the case of scattering the spectrum of H is continuous, which results in a branch cut in the complex energy plane along the positive real axis from 0 to ∞. This branch cut will become central when the analytical continuation is discussed (cf. Chapter 5). Note that if we know $G(z)$ for all z, we have solved the eigenvalue problem for H. It can be connected to the free Green's operator by the so-called Lippmann-Schwinger equation (for $G(z)$) [85]

$$
\begin{aligned}
G(z) &= G_0(z) + G_0(z)VG(z) \, , \\
&= G_0(z) + G(z)VG_0(z) \, .
\end{aligned}
\tag{2.5}
$$

The T-matrix can be represented by the Green's operator,

$$
T(z) = V + VG(z)V \, .
\tag{2.6}
$$

Exploiting this connection allows to write down the Lippmann-Schwinger equation for the T-matrix

$$
T(z) = V + VG_0(z)T(z) \, .
\tag{2.7}
$$

We now switch from an "operator-like" discussion to an investigation of matrix elements of the operators. For an overview on the basis states and the conventions used within this work see Appendix A. While the previous results are basis-independent, here a first statement on the symmetries of the system should be made. The systems considered are translationally invariant, i.e. $[P, H] = 0$, where P is the operator of the total momentum. So, the Hamiltonian can be separated in a center-of-mass and a relative part. In the following the center-of-mass part is neglected, such that the energy of the system is given solely by the relative energy

$$
E_p = \frac{p^2}{2\mu} \, ,
\tag{2.8}
$$

where μ is the reduced mass of the system. A central part of the following discussion are the momentum-space plane wave eigenvectors $\left| \boldsymbol{p}_+ \right\rangle$ and $\left| \boldsymbol{p}_- \right\rangle$ of H, $H \left| \boldsymbol{p}_\pm \right\rangle = E_p \left| \boldsymbol{p}_\pm \right\rangle$. They are connected to the Møller operators by

$$
\left| \boldsymbol{p}_\pm \right\rangle = \Omega_\pm \left| \boldsymbol{p} \right\rangle \, .
\tag{2.9}
$$

It can be shown that the eigenvectors $\left| \boldsymbol{p}_\pm \right\rangle$ fulfill a Lippmann-Schwinger-like equation,

$$
\left| \boldsymbol{p}_\pm \right\rangle = \left| \boldsymbol{p} \right\rangle + G\left(E_p \pm i0\right) V \left| \boldsymbol{p} \right\rangle \, ,
\tag{2.10}
$$

where $G\left(E_p \pm i0\right) = \lim_{\varepsilon \downarrow 0} G\left(E_p \pm i\varepsilon\right)$. The $i\varepsilon$ term is necessary to obtain a well-defined, non-singular theory. This leads to a further important quantity, sometimes used as a definition of the T-matrix,

$$
T\left(E_p \pm i0\right) \left| \boldsymbol{p} \right\rangle = V \left| \boldsymbol{p}_\pm \right\rangle \, .
\tag{2.11}
$$

Combining the last two equations results in the Lippmann-Schwinger equation for $\left| \boldsymbol{p}_\pm \right\rangle$

$$
\left| \boldsymbol{p}_\pm \right\rangle = \left| \boldsymbol{p} \right\rangle + G_0\left(E_p \pm i0\right) V \left| \boldsymbol{p}_\pm \right\rangle \, ,
\tag{2.12}
$$

which finally allows to write down a Lippmann-Schwinger equation for the wave functions

$$
\left\langle \boldsymbol{r} | \boldsymbol{p}_\pm \right\rangle = \left\langle \boldsymbol{r} | \boldsymbol{p} \right\rangle + \int \frac{\mathrm{d}^3 r'}{(2\pi)^3} \left\langle \boldsymbol{r} \middle| G_0\left(E_p \pm i0\right) \middle| \boldsymbol{r}' \right\rangle V\left(\boldsymbol{r}'\right) \left\langle \boldsymbol{r}' | \boldsymbol{p}_\pm \right\rangle \, .
\tag{2.13}
$$

Here a local interaction, $\langle \boldsymbol{r}|V|\boldsymbol{r}'\rangle = (2\pi)^3\,\delta^{(3)}\left(\boldsymbol{r} - \boldsymbol{r}'\right)V\left(\boldsymbol{r}'\right)$, is assumed. Taking the limit r to infinity the wave function becomes

$$\langle \boldsymbol{r}|\boldsymbol{p}_\pm\rangle \xrightarrow{r\to\infty} e^{i\boldsymbol{p}\cdot\boldsymbol{r}} - 4\pi^2\mu \left\langle \pm p\hat{\boldsymbol{r}}\middle|V\middle|\boldsymbol{p}_\pm\right\rangle \frac{e^{\pm ipr}}{r}\,, \tag{2.14}$$

where $\hat{\boldsymbol{r}} = \boldsymbol{r}/|\boldsymbol{r}|$. It shows the superposition of an incoming plane wave and an outgoing/incoming spherical wave. Physically, an incoming spherical wave would be a wrong boundary condition. In the following, we will focus on the outgoing spherical wave or equivalently the +-sign. The full wave function can be derived from the previous result by considering a superposition of the plane-wave wave functions

$$\psi(\boldsymbol{r},t) \equiv \langle\boldsymbol{r}|U(t)|\psi\rangle = \langle\boldsymbol{r}|U(t)\Omega_+|\psi_{\text{in}}\rangle = \int \mathrm{d}^3p\,\underbrace{\phi(\boldsymbol{p})}_{\langle\boldsymbol{p}|\psi_{\text{in}}\rangle}\,e^{-iE_pt}\,\langle\boldsymbol{r}|\boldsymbol{p}_+\rangle$$

$$\xrightarrow{r\to\infty} \int \mathrm{d}^3p\,\phi(\boldsymbol{p})e^{-iE_pt}\left[e^{i\boldsymbol{p}\cdot\boldsymbol{r}} - 4\pi^2\mu\left\langle +p\hat{\boldsymbol{r}}\middle|V\middle|\boldsymbol{p}_+\right\rangle\frac{e^{+ipr}}{r}\right] \tag{2.15}$$

$$:= \psi_{\text{in}}(\boldsymbol{r},t) + \psi_{\text{scat}}(\boldsymbol{r},t)\,.$$

Figure 2.1 shows a sketch of the scattering process including the incoming plane wave $\psi_{\text{in}}(\boldsymbol{r},t)$ propagating in the z-direction as well as the outgoing spherical wave $\psi_{\text{scat}}(\boldsymbol{r},t)$. The prefactor of the outgoing spherical wave is commonly referred to as the scattering amplitude $f(p,\theta)$,

$$f(p,\theta) := -4\pi^2\mu\left\langle +p\hat{\boldsymbol{r}}\middle|V\middle|\boldsymbol{p}_+\right\rangle = -4\pi^2\mu\left\langle +p\hat{\boldsymbol{r}}\middle|T\left(E_p + i0\right)\middle|\boldsymbol{p}\right\rangle\,, \tag{2.16}$$

where θ is the angle between $\boldsymbol{p}$ and $\hat{\boldsymbol{r}}$. For the last equality, we applied Eq. (2.11). It shows that the scattering amplitude is proportional to the so-called on-shell T-matrix. In general a matrix element of the T-matrix $\langle\boldsymbol{k}|T(E)|\boldsymbol{p}\rangle$ can be

$$\text{on} - \text{shell} \longleftrightarrow |\boldsymbol{k}| = |\boldsymbol{p}| \quad\text{and}\quad E = \frac{k^2}{2\mu} = \frac{p^2}{2\mu}\,,$$

$$\text{off} - \text{shell} \longleftrightarrow |\boldsymbol{k}| \neq |\boldsymbol{p}| \quad\text{and}\quad \frac{k^2}{2\mu} \neq E \neq \frac{p^2}{2\mu}\,, \tag{2.17}$$

$$\text{half} - \text{on} - \text{shell} \longleftrightarrow |\boldsymbol{k}| \neq |\boldsymbol{p}| \quad\text{and}\quad E = \frac{k^2}{2\mu}\text{ or }E = \frac{p^2}{2\mu}\,.$$

Physical observables are only connected to on-shell matrix elements.

In the following the investigation is restricted to spherically symmetric potentials. Further, it is assumed that the angular momentum operator commutes with the Hamiltonian, $[L, H] = 0$. So the angular momentum is conserved. This allows us to expand $\boldsymbol{p}_+$ into a partial-wave basis $|plm\rangle$. Let us first consider the partial-wave expansion of a plane wave,

$$e^{i\boldsymbol{p}\cdot\boldsymbol{r}} = 4\pi\sum_{l=0}^{\infty} i^l j_l(pr) \sum_{m=-l}^{l} Y_{lm}^*\left(\hat{\boldsymbol{p}}\right) Y_{lm}\left(\hat{\boldsymbol{r}}\right)$$

$$\xrightarrow{r\to\infty} 4\pi\sum_{l=0}^{\infty} i^l \frac{1}{pr}\sin\left(pr - \frac{\pi}{2}l\right) \sum_{m=-l}^{l} Y_{lm}^*\left(\hat{\boldsymbol{p}}\right) Y_{lm}\left(\hat{\boldsymbol{r}}\right)\,, \tag{2.18}$$

where j_l are spherical Bessel functions and Y_{lm} are spherical harmonics. Choosing our coordinate system such that $\boldsymbol{r}||\hat{\boldsymbol{e}}_z$, this simplifies to

$$e^{ipr\cos\theta} = \sum_{l=0}^{\infty}\left(2l+1\right)i^l j_l(pr)P_l\left(\cos\theta\right) \xrightarrow{r\to\infty} \sum_{l=0}^{\infty}\left(2l+1\right)i^l \frac{1}{pr}\sin\left(pr - \frac{\pi}{2}l\right)P_l\left(\cos\theta\right)\,, \tag{2.19}$$

where $\theta \sphericalangle (\boldsymbol{p}, \boldsymbol{r})$. Together with the partial-wave expansion of the scattering amplitude,

$$f(p, \theta) = \sum_{l=0}^{\infty} (2l + 1)\, f_l(p) P_l (\cos \theta) \,, \tag{2.20}$$

it can be plugged in into the plane-wave wave function Eq. (2.14)

$$\langle \boldsymbol{r} | \boldsymbol{p}_+ \rangle \xrightarrow{r \to \infty} \sum_{l=0}^{\infty} (2l + 1) \frac{\overbrace{[1 + 2ipf_l(p)]}^{S_l(p)} e^{ipr} + (-1)^{l+1} e^{-ipr}}{2ipr} P_l (\cos \theta) \,. \tag{2.21}$$

Here, we defined the partial-wave S-matrix

$$S_l(p) := 1 + 2ipf_l(p) \,, \tag{2.22}$$

where $f_l(p)$ is the partial-wave scattering amplitude. Commonly the partial-wave S-matrix is parameterized by the phase shift δ_l,

$$S_l(p) := e^{2i\delta_l(p)} \,, \tag{2.23}$$

where the factor 2 is convention. This parameterization preserves the unitarity of the S-matrix. The name phase shift becomes more clear if the kernel of Eq. (2.21) is simplified,

$$\frac{S_l(p)e^{ipr} + (-1)^{l+1} e^{-ipr}}{2ipr} \sim \frac{e^{i\delta_l(p)}}{pr} \sin \left[pr - \frac{\pi}{2}l + \delta_l(p) \right] \,. \tag{2.24}$$

For a vanishing phase shift, the equation corresponds to the non-interacting case. So, the phase shift describes the shift of the phase of the wave relative to the free solution. A positive phase shift corresponds to an attractive potential, while a negative phase shift describes a repulsive potential. Due to the definition of the phase shift, it is only determined up to multiples of π. In general, the boundary conditions are chosen such that the phase shift goes to zero for $p \to \infty$. Together with the requirement of a continuous behavior, this determines the phase shift uniquely. Further, the phase shift fulfills Levinson's theorem

$$\delta_l(0) - \delta_l(\infty) = \begin{cases} \left(n_{\mathrm{b}} + \frac{1}{2} \right) \pi & \text{for} \quad l = 0 \,, \\ n_{\mathrm{b}} \pi & \text{for} \quad l > 0 \,, \end{cases} \tag{2.25}$$

where n_{b} is the number of bound states.

Exploiting the connection between S-matrix and scattering amplitude Eq. (2.22), the partial-wave scattering amplitude can be written as

$$f_l(p) = \frac{S_l(p) - 1}{2ip} = \frac{e^{i\delta_l(p)} \sin \delta_l(p)}{p} = \frac{1}{p \cot \delta_l(p) - ip} \,. \tag{2.26}$$

A common parametrization of the phase shift for a short-ranged potential is given by the so-called effective range expansion (ERE) [97–99]

$$p^{2l+1} \cot \delta_l(p) = -\frac{1}{a_l} + \frac{1}{2} r_l p^2 - P_l r_l^3 p^4 + \mathcal{O}\left(p^6\right) \,, \tag{2.27}$$

where the scattering length a_l, the effective range r_l, and the shape parameter P_l are introduced. Note that the names of the parameters are modified depending on the partial wave considered, e.g. the S-wave scattering length a_0 and the P-wave scattering volume a_1.

The scattering amplitude can further be connected to the differential cross section by

$$\frac{\mathrm{d}\sigma}{\mathrm{d}\Omega} = |f(p,\theta)|^2 \,. \tag{2.28}$$

Applying the general definition of cross section results in

$$\sigma = \int_{\Omega} \mathrm{d}\Omega \frac{\mathrm{d}\sigma}{\mathrm{d}\Omega} = \sum_{l=0}^{\infty} \sigma_l = \frac{4\pi}{p^2} \sum_{l=0}^{\infty} (2l+1)\sin^2\delta_l(p) \,. \tag{2.29}$$

The cross section is the quantity presented, which is closest to what is observable experimentally. It becomes maximal for the phase shift equal to odd multiples of $\pi/2$. This behavior is connected to a resonance as will be discussed in the next Section.

In the following, the analytic structure of the S-matrix as well as the connection of bound states, virtual states and resonances to poles of the S-matrix are investigated. The starting point is the radial Schrödinger equation

$$\left[\frac{\mathrm{d}^2}{\mathrm{d}r^2} - \frac{l(l+1)}{r^2} - U(r) + p^2 \right] \psi_{l,p}(r) = 0 \,, \tag{2.30}$$

where the modified potential $U(r) = 2\mu V(r)$ is defined. $\psi_{l,p}(r)$ is called the normalized radial function, which fulfills the boundary condition $\psi_{l,p}(0) = 0$. It can be written as

$$\psi_{l,p}(r) \xrightarrow{r \to \infty} \hat{j}_l(pr) + p f_l(p)\hat{h}_l^+(pr) = \frac{i}{2}\left[\hat{h}_l^-(pr) - S_l(p)\hat{h}_l^+(pr) \right] \,, \tag{2.31}$$

where $\hat{j}_l(z)$ and $\hat{h}_l^{\pm}(z)$ are the Riccati-Bessel and the Riccati-Hankel functions, respectively. The Riccati-Hankel functions are defined by

$$\hat{h}_l^{\pm}(z) = \hat{n}_l(z) \pm i\hat{j}_l(z) \,, \tag{2.32}$$

where $\hat{n}_l(z)$ is the Riccati-Neumann function. $\psi_{l,p}(r)$ is defined via the two boundary conditions at $r = 0$ and for $r \to \infty$. It is convenient to define a solution $\phi_{l,p}(r)$ that is defined by only one boundary condition,

$$\phi_{l,p}(r) \xrightarrow{r \to 0} \hat{j}_l(pr) \,. \tag{2.33}$$

The regular solution $\phi_{l,p}(r)$ differs from $\psi_{l,p}(r)$ only by normalization. It can be shown that for $r \to \infty$ it is given by

$$\phi_{l,p}(r) \xrightarrow{r \to \infty} \frac{i}{2}\left[\mathcal{F}_l(p)\hat{h}_l^-(pr) - \mathcal{F}_l^*(p)\hat{h}_l^+(pr) \right] \,, \tag{2.34}$$

where the Jost function $\mathcal{F}_l(p)$ is introduced. By comparison to the normalized radial function Eq. (2.31) a connection to the S-matrix is obtained,

$$S_l(p) = \frac{\mathcal{F}_l^*(p)}{\mathcal{F}_l(p)} = \frac{\mathcal{F}_l(-p)}{\mathcal{F}_l(p)} \Leftrightarrow \mathcal{F}_l(p) = |\mathcal{F}_l(p)|\, e^{-i\delta_l(p)} \,. \tag{2.35}$$

Based on this definition, we can motivate that a pole of the S-matrix with $\mathrm{Re}\, p = 0$ and $\mathrm{Im}\, p \geq 0$, $p := i\kappa$, corresponds to a bound state. For $S_l(p)$ to become singular $\mathcal{F}_l(p)$ has to vanish. In this case Eq. (2.34) simplifies to

$$\phi_{l,p}(r) \xrightarrow{r \to \infty} -\frac{i}{2}\mathcal{F}_l^*(p)\hat{h}_l^+(pr) = -\frac{i}{2}\mathcal{F}_l^*(p)e^{i\left(pr - \frac{\pi}{2}l\right)} = -\frac{i}{2}\mathcal{F}_l^*(p)e^{-\kappa r}e^{-i\frac{\pi}{2}l} \,. \tag{2.36}$$

Only the outgoing part of the wave function remains, which vanishes for $r \to \infty$. So, this can be identified with a bound state. It can further be shown, that $\mathcal{F}_l(p)$ for $\mathrm{Im}\, p \geq 0$ can only vanish on the imaginary axis. So, the only possible poles with $\mathrm{Im}\, p \geq 0$ are bound states.

Scattering theory for few-body systems

2.2. Resonances

Not only bound states, but also resonances can be connected to poles of the S-matrix or zeros of $\mathcal{F}_l(p)$. However, while $\mathcal{F}_l(p)$ is analytic for $\operatorname{Im} p \geq 0$ (beside the bound state poles), this is in general not true for $\operatorname{Im} p < 0$. In the following, we will consider a resonance located at a momentum

$$\bar{p} = p_{\mathrm{R}} - i p_{\mathrm{I}}\,, \qquad p_{\mathrm{R}}, p_{\mathrm{I}} \geq 0\,. \tag{2.37}$$

So, $\mathcal{F}_l(p)$ has a zero at $\bar{p}$ and can be represented by

$$\mathcal{F}_l(p) = \left.\frac{\mathrm{d}\mathcal{F}_l(p)}{\mathrm{d}p}\right|_{p=\bar{p}} (p - \bar{p}) + \mathcal{O}\left[(p - \bar{p})^2\right]\,. \tag{2.38}$$

The corresponding phase shift is given by (cf. Eq. (2.35))

$$\delta_l(p) = -\arg\left(\mathcal{F}_l(p)\right) \approx -\arg\left(\left.\frac{\mathrm{d}\mathcal{F}_l(p)}{\mathrm{d}p}\right|_{p=\bar{p}}\right) - \arg\left(p - \bar{p}\right) \tag{2.39}$$

$$:= \delta_{\mathrm{bg}} + \delta_{\mathrm{res}}(p)\,.$$

Here, a background phase shift δ_{bg} and the resonant part of the phase shift δ_{res} are defined. In general, the background phase shift could take any value. For resonances with a vanishing imaginary part it can be assumed to be small. The resonant part describes the rapid increase of the phase shift by π at the resonance momentum. This behavior becomes clear in Fig. 2.2. For $p \ll p_{\mathrm{R}}$, $\delta_{\mathrm{res}}(p)$ vanishes. Moving along the positive real momentum axis up to $p = p_{\mathrm{R}}$ the resonant part of the phase shift increases up to $\pi/2$. As shown above, this is the point where the cross section becomes maximal; the resonance energy E_{R} or resonance momentum p_{R}. Following the real axis further, $\delta_{\mathrm{res}}(p)$ increases up to the final value π. The closer the resonance to the positive real axis, the faster $\delta_{\mathrm{res}}(p)$ changes.
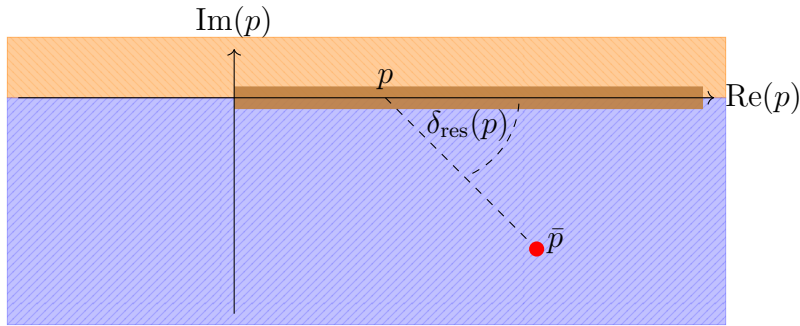
Figure 2.2.: The complex momentum plane showing a resonance at $\bar{p}$. The resonant part of the phase shift $\delta_{\mathrm{res}}(p)$ is connected to the angle between the momentum on the positive real axis and the resonance. At $\operatorname{Re} p = p_{\mathrm{R}}$ the angle takes the value $\pi/2$, while for $\operatorname{Re} p < p_{\mathrm{R}}(\operatorname{Re} p > p_{\mathrm{R}})$ the $\delta_{\mathrm{res}}(p)$ is smaller (larger) than $\pi/2$. The strength of the change of $\delta_{\mathrm{res}}(p)$ depends on the value of p_{I}. The closer it is located to the axis, the larger the slope at the resonance.

To investigate the behavior of the phase shift around the resonance energy closer, consider

$$
\begin{aligned}
\cot \delta_l(E_p) &= \underbrace{\cot \delta_l\left(E_{\mathrm{R}}\right)}_{=0} + \left.\frac{\mathrm{d}}{\mathrm{d}E_p}\cot \delta_l\left(E_p\right)\right|_{E_p=E_{\mathrm{R}}} (E_p - E_R) + \mathcal{O}\left[(E_p - E_R)^2\right] \\
&= \underbrace{\left.\frac{\mathrm{d}\delta_l}{\mathrm{d}E_p}\right|_{E_p=E_{\mathrm{R}}}}_{:=\frac{2}{\Gamma_{\mathrm{R}}}} (E_p - E_R) + \mathcal{O}\left[(E_p - E_R)^2\right] ,
\end{aligned}
\tag{2.40}
$$

where the resonance width is defined,

$$
\Gamma_{\mathrm{R}} = \frac{2}{\delta_l'\left(E_{\mathrm{R}}\right)} .
\tag{2.41}
$$

As the discussion of Fig. 2.2 revealed, the slope of the phase shift is connected to the imaginary part of the resonance momentum. This translates into a resonance in the complex energy plane located at

$$
E = \frac{\bar{p}^2}{2\mu} = E_{\mathrm{R}} - i\frac{\Gamma_{\mathrm{R}}}{2} .
\tag{2.42}
$$

The parameterization of the phase shift around the resonance energy can be plugged in into the definition of the cross section Eq. (2.29) resulting in the Breit-Wigner formula

$$
\sigma\left(E_p\right) = \frac{4\pi}{p^2}\sum_{l=0}^{\infty}(2l+1)\frac{\Gamma_{\mathrm{R}}^2/4}{\left(E_p - E_{\mathrm{R}}\right)^2 + \Gamma_{\mathrm{R}}^2/4} .
\tag{2.43}
$$

Here, a vanishing background phase shift is assumed.

All in all, a resonance is a nearly-bound state located in the fourth quadrant of the complex momentum or energy plane close to the real axis. It is defined by a resonance energy E_{R} and a resonance width Γ_{R}. The resonance width can be connected to a finite lifetime τ_{R} of the resonance (cf. next subsection) by the Heisenberg uncertainty principle $\Gamma_{\mathrm{R}}\tau_{\mathrm{R}} \geq 1$. A resonance corresponds to a rapid increase of the phase shift with a positive slope through odd multiples of $\pi/2$ or a peak in the cross section. Following the Breit-Wigner formula, the effect on the cross section is the bigger the closer the pole is located to the real axis. For poles far away from the axis, no effect is observable.

2.2.1. Time delay

So far, the resonant scattering process was investigated in a time-independent framework at $t = 0$. However, we could also consider Fig. 2.1 at a time $t > 0$. A sketch of the situation is shown in Fig. 2.3, where we see the unscattered outgoing plane wave as well as the scattered outgoing spherical wave. Between corresponding wavefronts of both waves a distance ξ can be defined. Due to the short-living resonant state the scattered wave lags this distance ξ behind the unscattered wave. It can be connected to the momentum at the resonance p_{R},

$$
\xi = \delta_l'(p_{\mathrm{R}}) = -\left.\frac{\mathrm{d}\delta_l}{\mathrm{d}p}\right|_{p=p_{\mathrm{R}}} = v_0\left.\frac{\mathrm{d}\delta_l}{\mathrm{d}E}\right|_{E=E_{\mathrm{R}}} ,
\tag{2.44}
$$

where $v_0 = p_R/\mu$ is the velocity of the incoming particles. Instead of speaking of the distance ξ, it is more common to introduce the so-called time delay τ by

$$\tau = \frac{\xi}{v_0} = \frac{1}{v_0}\frac{\mathrm{d}\delta_l}{\mathrm{d}p}\bigg|_{p=p_R} = \frac{\mathrm{d}\delta_l}{\mathrm{d}E}\bigg|_{E=E_R}. \tag{2.45}$$

For causality reasons, the time delay is bounded from below. Considering a target with a diameter d the earliest time the outgoing spherical wave can be emitted is the point, where the incoming plane wave hits the target. In this case, the spherical wave is ahead of the plane by a time

$$\tau = -\frac{d}{v_0} < 0. \tag{2.46}$$

Note that this causality bound results in an upper limit on the effective range, the famous Wigner bound [100].

The time delay defined by Eq. (2.45) possesses the complicating feature that it diverges at $p = 0$. So, a modified time delay defined by the Wigner-Smith matrix [101], τ_{WS}, is introduced:

$$\tau_{WS} = 2p\tau. \tag{2.47}$$
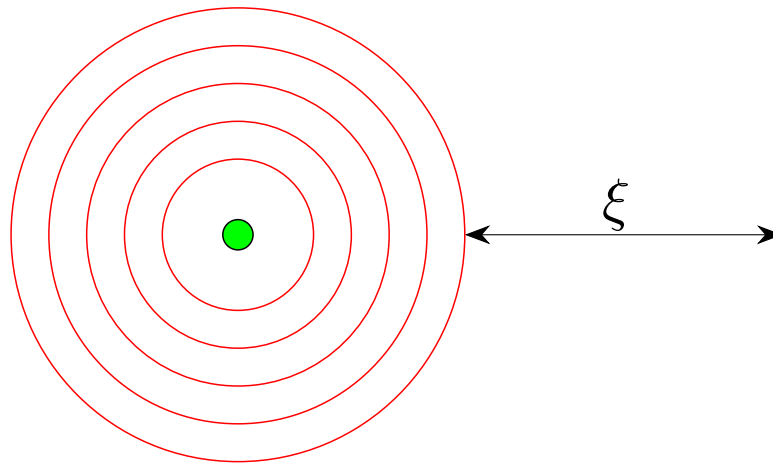
Figure 2.3.: The unscattered outgoing plane wave as well as the outgoing spherical wave after the scattering on a target (●). A distance ξ between the corresponding wave fronts of both waves is defined.

2.3. Sheet structure

During the recent investigations, momentum and energy were considered as two equivalent variables. However, the mapping from the momentum to the energy plane is not unique. Two momenta with opposite signs correspond to the same energy. To get a unique mapping a two-sheeted Riemann surface for the energy plane is introduced. While bound states live on the first or physical sheet with $\mathrm{Im}\,p > 0$, resonances are located on the second or unphysical sheet with $\mathrm{Im}\,p < 0$. So, the two momenta with

opposite signs are located on two different sheets. Both sheets are connected by a branch cut spanned along the positive real axis. The sheet structure for a two-body system is shown in Fig. 2.4. Besides the bound states and resonances a further state on the unphysical sheet is shown, a virtual state. A virtual state is no proper state as the wave function would diverge (cf. Eq. (2.36) for $\kappa \to -\kappa$). A virtual state only has a measurable effect if it is close to threshold. A prominent example is the virtual state in the n-p singlet channel at $a_0 = -23.7\,\text{fm}$.
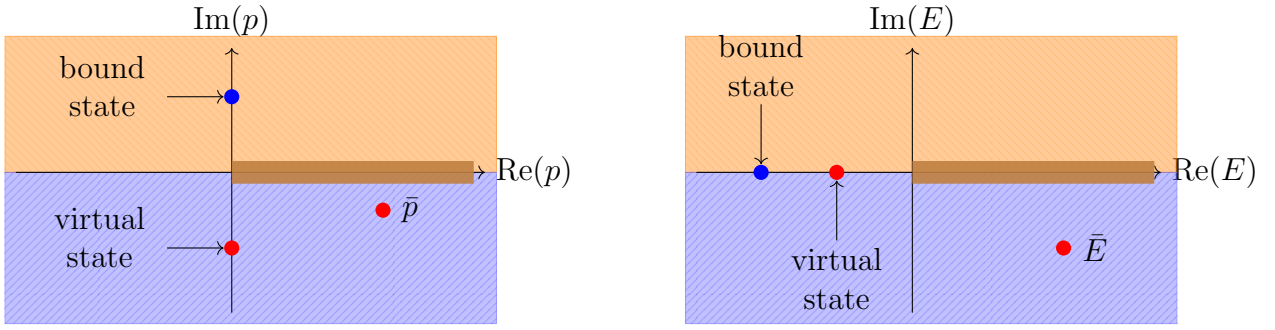
Figure 2.4.: The structure of the complex momentum and energy plane for two particles. Energies on the physical sheet translate to momenta on the physical part of the complex momentum plane with $\operatorname{Im} p > 0$. Energies on the unphysical sheet are mapped to the region of the momentum plane with $\operatorname{Im} p < 0$. Both sheets are connected by a branch cut starting at the branch point at the origin and the following the positive real axis up to infinity. For example a bound state on the physical sheet as well as a virtual state and a resonance $\bar{p}/\bar{E}$ on the unphysical sheet are shown.

2.4. Many-body systems

The introduction to scattering theory presented so far is restricted to the scattering of two particles. Many of the concepts presented can be extended to more particles. A concept relevant to this thesis is the sheet structure. Assuming a rotationally invariant system and an energy range, where only two-body channels are open, the system presents a sequence of N thresholds

$$W_1 < W_2 < \ldots < W_n < W_N. \tag{2.48}$$

At each threshold, a new channel opens. The thresholds correspond to branch points of the S-matrix, which are starting points of a branch cut following the real axis up to infinity. These cuts are commonly called unitarity cuts. Similar to the two-body system a physical sheet exists. All branch points are located on the physical sheet. Starting from the physical sheet and crossing any of the cuts another unphysical sheet is accessed. Figure 2.5 shows a sketch of the resulting sheet structure. To summarize, for N thresholds there are one physical and N unphysical sheets. Note that in comparison to the two-body system there is not only a single complex momentum plane, but there are N defined by

$$p_i = \sqrt{2\mu_i (E - W_i)}. \tag{2.49}$$
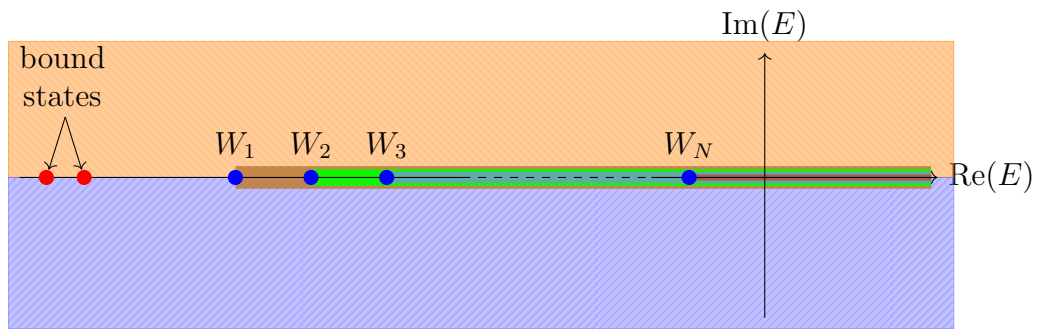
Figure 2.5.: The complex energy plane for a multi-particle system presenting only two-body breakup channels. At each threshold W_i a new unitarity cut, guiding to a different unphysical sheet, starts.

So far, only two-body breakup channels are included. In reality, the system also includes more-particle breakup channels. Each breakup channel results in a further branch cut. Altogether this results in a very complicated sheet structure.

3 Pionless EFT

This Chapter gives an introduction into the basic concepts of an effective field theory (EFT) with a focus on pionless EFT (EFT($\not\pi$)) [102–106]. The Lagrangians for two- and three-body systems with and without spin are presented. The three-body Lagrangians are used to derive the corresponding Feynman rules. These are applied to obtain the three-body scattering equations for a system of three spinless bosons, Section 3.3.1, the neutron-deuteron system in the quartet, Section 3.3.2.a and doublet-channel, Section 3.3.2.b, and for the three-neutron system Section 3.3.3. Finally, a different ansatz deriving an effective interaction potential from the EFT is presented. This potential will be used together with the Faddeev equations derived in the following Chapter in comparison to the scattering equations derived within this Chapter.

3.1. General introduction

The basic idea of an EFT is known to humanity already since the earliest times. People describe and characterize their environment by what they can see and resolve. They recognized that it helps to simplify everyday life by introducing hierarchies of scales. Over time the knowledge and capabilities improve. Theories and concepts that have been proposed by earlier generations show that they are only part of a whole. They are suitable for what they are designed for, but on another "scale" they present worse results or even fail. A prominent physical example is Newton's gravitational theory. It is perfectly suited describing everyday-life phenomena, like an apple falling from a tree, but for high-accuracy problems, e.g. GPS, it becomes necessary to include corrections from general relativity. This separation of scales, many physical systems present, is the starting point for the development of an EFT.

The procedure of deriving an EFT can in general be divided into three steps:

1. Determine the relevant degrees of freedom (DOF) of the theory,

2. Identify the symmetries of the system,

3. Find an expansion parameter and derive the power counting.

Following these three steps, it is possible to write down a general Lagrangian consistent with the symmetries of the system including all relevant DOF. This Lagrangian is valid up to the break-down scale Λ_b. The latter describes the appearance of new or unresolved physics. The restriction to energies or momenta lower than the break-down scale ensures the separation of scales. The procedure described so far is commonly referred to as the bottom-up ansatz.

If the high-energy theory is known and one wants to derive a simpler low-energy theory, a second procedure, the top-down ansatz, can be applied. Fields connected to DOF with a mass larger than the

break-down scale are integrated out. This results in a series of local contact interactions as well as nonlocal terms including derivatives.

In general, the EFT Lagrangian includes an infinite number of terms. These have to be ordered to allow a systematic approximation as well as error estimates to the system. This ordering is performed by introducing a power counting. It assigns a power of a small expansion parameter ϵ to every contribution, where ϵ is the value of two well-separated scales. Terms which have the same value of ϵ are equally important. The lowest non-vanishing order is denoted as leading order (LO), followed by the next higher order next-to-leading order (NLO), next-to-next-to-leading order (N^{2}LO), and so on. The theoretical error of the calculation can be approximated by the first neglected order. So, an EFT allows for a systematic error estimate. Moreover, the calculation can be improved up to the desired accuracy in a systematic expansion.

Figure 3.1 presents an overview of the (momentum) scales in a nuclear system. It starts with the smallest scale, the inverse $^1S_0$ and $^3S_1$ scattering lengths at a momentum in the range of 10 to 40 MeV, respectively. Within this thesis, we will restrict ourselves to momenta lower than the pion mass $m_\pi \approx 140$ MeV. The corresponding EFT is referred to as pionless EFT. Next higher scales are given by the virtual excitation of the nucleon to the Delta resonance at roughly $Q \approx 300$ MeV and by the high mass connected to the mass of non-Goldstone bosons at $Q \sim 1$ GeV.

$$0 \longmapsto\!\!\!\!\!\!\!\!\!\vert\!\!\!\!\!\!\!\!\!\vert\!\!\!\!\!\!\!\!\!\vert\!\!\!\!\!\!\!\!\!\vert\!\!\!\!\!\!\longrightarrow Q$$

$$\underset{a_{s/t}^{-1} \approx 10 - 40\,\text{MeV}}{} \quad \underset{m_\pi \approx 140\,\text{MeV}}{} \quad \underset{m_\Delta - m_N \approx 300\,\text{MeV}}{} \quad \underset{m_{\text{high}} \approx 1\,\text{GeV}}{}$$
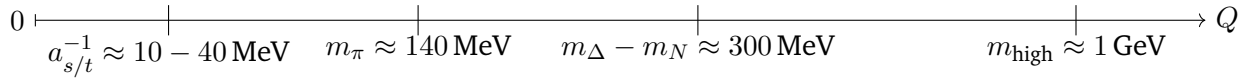
Figure 3.1.: The momentum scales relevant for the nucleon-nucleon force.

In general, it is possible to assign an EFT to one of two classes, a natural or an unnatural EFT [19, 20]. The more straightforward case is a natural theory, which is a theory with a single mass scale M. It is possible to derive the scaling of the theory from a naive dimensional analysis demanding a dimensionless action. All parameters are expected to scale in powers of the mass M according to their mass dimension. However, the more interesting and relevant case for this work is an unnatural EFT. The theory is so-called fine-tuned to have two scales, the scale M as well as further scale $\mathcal{N} \sim |a^{-1}| \ll M$. The small scale is for example set by shallow bound states, e.g. the deuteron. It changes the scaling of the theory and modifies at which order of the power counting terms are included.

3.2. Two-body system

Based on the pioneering work by van Kolck [20], the pionless EFT Lagrangian for a spinless two-body system is given by

$$
\begin{aligned}
\mathcal{L} = {}& \psi^\dagger \left(i\partial_0 + \frac{\boldsymbol{\nabla}^2}{2m} + \frac{\boldsymbol{\nabla}^4}{8m^3} + \dots \right) \psi \\
& - \frac{1}{2} C_0 \psi^\dagger \psi \psi^\dagger \psi \\
& - \frac{1}{8} \left(C_2 + C_2' \right) \left[\psi^\dagger \overleftrightarrow{\boldsymbol{\nabla}} \psi \cdot \psi^\dagger \overleftrightarrow{\boldsymbol{\nabla}} \psi - \psi^\dagger \psi \psi^\dagger \overleftrightarrow{\boldsymbol{\nabla}}^2 \psi \right] \\
& + \frac{1}{4} \left(C_2 - C_2' \right) \psi^\dagger \psi \, \boldsymbol{\nabla}^2 \left(\psi^\dagger \psi \right) + \dots ,
\end{aligned}
\tag{3.1}
$$

with the operator $\overleftrightarrow{\vec{\nabla}} = \vec{\nabla} - \overleftarrow{\vec{\nabla}}$. ψ represents the only degree of freedom, a propagating, non-relativistic field. The so-called low energy couplings (LECs) $C_{2n}, n \in \mathbb{N}_0$, include the details of the interaction at low energies. Terms with a higher number of fields ψ or terms containing derivatives are represented by the dots.

The whole formalism can be extended to particles containing spin, e.g. the nucleons. In leading order, the Lagrangian is given by [105]

$$
\begin{aligned}
\mathcal{L}_N = {} & N^\dagger \left(i\partial_0 + \frac{\nabla^2}{2M_N} + \dots \right) N \\
& - C_{0,s} \left(N^\dagger \mathcal{P}_s N \right)^\dagger \left(N^\dagger \mathcal{P}_s N \right) - C_{0,t} \left(N^\dagger \mathcal{P}_t N \right)^\dagger \left(N^\dagger \mathcal{P}_t N \right) + \dots ,
\end{aligned}
\tag{3.2}
$$

with the projectors

$$
(\mathcal{P}_t)^i = \frac{1}{\sqrt{8}} \sigma^2 \sigma^i \tau^2 , \qquad\qquad (\mathcal{P}_s)^i = \frac{1}{\sqrt{8}} \sigma^2 \tau^2 \tau^i .
\tag{3.3}
$$

N are the nucleon fields with mass M_N, which are doublets in spin and isospin space, $C_{0,s/t}$ are low-energy coupling constants and σ^i and τ^i, $i = 1, 2, 3$, denote the Pauli matrices in spin and isospin space, respectively. The indices s and t represent the singlet and triplet states, respectively.

3.3. Three-body system

We now proceed with the three-body system. Note that to be consistent with the common literature, the conventions within this and the following Sections are modified. Similar to the two-body problem, we first restrict ourselves to a system of spinless particles, three identical spinless bosons. A possible representation of the LO Lagrangian is given by [107, 108]

$$
\mathcal{L}_{3B} = \psi^\dagger \left(i\partial_0 + \frac{\boldsymbol{\nabla}^2}{2m} \right) \psi - \frac{g_2}{4} \left(\psi^\dagger \psi \right)^2 - \frac{g_3}{36} \left(\psi^\dagger \psi \right)^3 .
\tag{3.4}
$$

The Lagrangian includes a two-body interaction proportional to g_2 as well as a three-body interaction g_3. This system can be treated by applying the so-called dimer or diatom field trick [107, 109, 110] combining two particles into a composite particle, the dimer d. Introducing this new field, the Lagrangian can be written as

$$
\mathcal{L}_{3B}^d = \psi^\dagger \left(i\partial_0 + \frac{\boldsymbol{\nabla}^2}{2m} \right) \psi + \frac{g_2}{4} d^\dagger d - \frac{g_2}{4} \left(d^\dagger \psi^2 + \left(\psi^\dagger \right)^2 d \right) - \frac{g_3}{36} d^\dagger d \psi^\dagger \psi .
\tag{3.5}
$$

Both representations are equal up to order $\left(\psi^\dagger \psi \right)^3$ as shown in Ref. [108] using the equation of motion for d.

Nevertheless, the second Lagrangian does not contain a two-body contact interaction directly. It is "replaced" by the interaction of two dimer fields $d^\dagger d$ as well as the creation/annihilation of a dimer field from/to two fields.

A further notable feature is the non-existence of a spacial as well as a time derivative acting on the dimer field. So, it is not dynamic. The bare propagator of the dimer field is just the constant $4i/g_2$. However, the propagation of the dimer is incorporated considering corrections to the bare propagator represented

by the Dyson equation. It is a result of the unnatural scaling of pionless EFT. At LO all diagrams involving only a g_2 interaction are of equivalent importance and have to be resumed to all orders [20–22]. Without the resummation, the theory would not break down at the pion mass, but already at the lower scale $\mathcal{N}$. This feature can be understood in the way that a finite sum of non-singular terms cannot become singular.

Introducing the Feynman rules for the propagator of the field ψ

$$\text{————————} = \frac{i}{p_0 - \frac{\boldsymbol{p}^2}{2m} + i\varepsilon} := iS(p)\,, \qquad (3.6)$$

as well as for the bare dimer propagator

$$\text{════════} = \frac{4i}{g_2}\,, \qquad (3.7)$$

and for the vertex

$$\text{═══}\!\!<\quad = \quad >\!\!\text{═══} \quad = -\frac{ig_2}{2}\,, \qquad (3.8)$$

the Dyson equation for the full or dressed dimer propagator $iD(p_0, \boldsymbol{p})$ can be written as

$$\qquad (3.9)$$

$$iD(p_0, \boldsymbol{p}) \qquad = \qquad iD^0(p_0, \boldsymbol{p}) \qquad + \quad iD^0 \cdot \sum_{n=1}^{\infty} \left(-\Sigma D^0\right)^n$$

Equivalently, it can be represented by an integral equation by summing up the right-hand side of the equation

$$\qquad (3.10)$$

Here, $\Sigma(p_0, \boldsymbol{p})$ represents the self-energy. Using the geometric series, the full dimer propagator is written as

$$iD(p_0, \boldsymbol{p}) = iD^0 \cdot \sum_{n=0}^{\infty} \left[-\Sigma D^0\right]^n = \frac{iD^0}{1 - [-\Sigma D^0]} = \frac{i}{[D^0]^{-1} + \Sigma}\,. \qquad (3.11)$$

As a first step in calculating the full dimer propagator, a formula for the self-energy $i\Sigma(p_0, \boldsymbol{p})$ can be derived

$$
\begin{aligned}
\text{⬤} &= \frac{1}{2}\left(-\frac{ig_2}{2}\right) \int \frac{\mathrm{d}^3 q}{(2\pi)^3} \int \frac{\mathrm{d}q_0}{2\pi} \frac{i}{p_0 + q_0 - \frac{(\boldsymbol{p}+\boldsymbol{q})^2}{2m} + i\varepsilon} \frac{i}{-q_0 - \frac{\boldsymbol{q}^2}{2m} + i\varepsilon}\left(-\frac{ig_2}{2}\right) \\
&= \frac{1}{2}\left(-\frac{ig_2}{2}\right)^2 \int \frac{\mathrm{d}^3 k}{(2\pi)^3} \frac{im}{mp_0 - \frac{\boldsymbol{p}^2}{4} - \boldsymbol{k}^2 + i\varepsilon}, \qquad \text{with the substitution } \boldsymbol{k} = \boldsymbol{q} + \frac{\boldsymbol{p}}{2} \qquad (3.12) \\
&:= \frac{1}{2}\left(-\frac{ig_2}{2}\right)^2 I(p_0, \boldsymbol{p})\,.
\end{aligned}
$$

The remaining integral $I(p_0, \boldsymbol{p})$ is divergent. So, it has to be regularized. In general, there are different possible regularization schemes. Here, a regulator function will be introduced. The simplest choice for the regulator function is a Heaviside regulator. This corresponds to applying a fixed cutoff Λ to the integral,

$$
\begin{aligned}
I(p_0, \boldsymbol{p}) &= \int_0^\Lambda \frac{\mathrm{d}k}{2\pi} \underbrace{\int \frac{\mathrm{d}\Omega_k}{(2\pi)^2}}_{\pi^{-1}} k^2 \frac{im}{mp_0 - \frac{\boldsymbol{p}^2}{4} - \boldsymbol{k}^2 + i\varepsilon} \\
&= \frac{im}{2\pi^2} \left[-k \Big|_0^\Lambda + \left(mp_0 - \frac{\boldsymbol{p}^2}{4} + i\varepsilon \right) \int_0^\Lambda \mathrm{d}k \frac{1}{mp_0 - \frac{\boldsymbol{p}^2}{4} - \boldsymbol{k}^2 + i\varepsilon} \right] \\
&= \frac{im}{2\pi^2} \left[-\Lambda + \left(\frac{\boldsymbol{p}^2}{4} - mp_0 - i\varepsilon \right) \cdot \frac{1}{\sqrt{\frac{\boldsymbol{p}^2}{4} - mp_0 - i\varepsilon}} \underbrace{\mathrm{arctanh}\left(\frac{k}{\sqrt{\frac{\boldsymbol{p}^2}{4} - mp_0 - i\varepsilon}} \right) \Big|_0^\Lambda}_{\frac{\pi}{2} + \mathcal{O}(\Lambda^{-1})} \right] \\
&= \frac{im}{2\pi^2} \left[-\Lambda + \frac{\pi}{2} \sqrt{\frac{\boldsymbol{p}^2}{4} - mp_0 - i\varepsilon} + \mathcal{O}\left(\Lambda^{-1}\right) \right] .
\end{aligned}
\tag{3.13}
$$

Now, it is possible to present a formula for the full dimer propagator:

$$
iD(p_0, \boldsymbol{p}) = \frac{i}{[D^0]^{-1} + \Sigma} = \frac{i}{\frac{g_2}{4} - \frac{g_2^2 m}{16\pi^2} \left[-\Lambda + \frac{\pi}{2} \sqrt{\frac{\boldsymbol{p}^2}{4} - mp_0 - i\varepsilon} \right]} .
\tag{3.14}
$$

It still depends on the parameter g_2 of the Lagrangian as well as the regularization scale Λ. So, it has to be renormalized. This can either be done from a more fundamental theory (top-down ansatz) or from experimental data (bottom-up ansatz). We will follow the latter way and match our theory to the effective range expansion. The on-shell two-body T-matrix $it_0(k)$ can be derived from the dressed dimer propagator by adding external vertices:

$$
\times = \left(-\frac{ig_2}{2} \right) \cdot iD\left(p_0 = \frac{k^2}{m}, \boldsymbol{p} = 0 \right) \cdot \left(-\frac{ig_2}{2} \right) .
\tag{3.15}
$$

It is matched to

$$
t_0\left(k, E = \frac{k^2}{m} \right) = \frac{8\pi}{m} \frac{1}{k \cot \delta_0 - ik} .
\tag{3.16}
$$

This results in

$$
k \cot \delta_0 = -\frac{8\pi}{g_2 m} - \frac{2}{\pi} \Lambda .
\tag{3.17}
$$

Altogether, the renormalized dressed dimer propagator is given by

$$
D(p_0, \boldsymbol{p}) = \frac{32\pi}{g_2^2 m} \frac{1}{\frac{1}{a_0} - \sqrt{\frac{\boldsymbol{p}^2}{4} - mp_0 - i\varepsilon}} ,
\tag{3.18}
$$

where the first order effective range expansion Eq. (2.27) was applied.

So far, a spinless three-body system was considered. Now, spin and isospin are added to the theory. Again, we are able to introduce dimer fields representing dinucleons in the singlet $^1S_0$ (s) as well as triplet

$^3S_1$ (t) state. Regarding nucleons, these fields are commonly called dibaryon fields. The corresponding Lagrangian reads [105]

$$
\begin{aligned}
\mathcal{L}_N^d = {} & N^\dagger \left(i\partial_0 + \frac{\nabla^2}{2M_N} + \dots \right) N \\
& - t^{i\dagger} \left[g_t + \left(i\partial_0 + \frac{\nabla^2}{4M_N} \right) \right] t^i + y_t \left[t^{i\dagger} \left(N^\top \hat{P}_t^i N \right) + \text{h.c.} \right] \\
& - s^{\lambda\dagger} \left[g_s + \left(i\partial_0 + \frac{\nabla^2}{4M_N} \right) \right] s^\lambda + y_s \left[s^{\lambda\dagger} \left(N^\top \hat{P}_s^\lambda N \right) + \text{h.c.} \right] + \dots .
\end{aligned}
\tag{3.19}
$$

The new low-energy couplings are called $y_{s/t}$, while the bare dibaryon propagator is given by $i/g_{s/t}$.

First, we have to derive the relevant Feynman rules. In analogy to Eq. (3.6), the bare nucleon propagator is given by

$$
\alpha, a \;\rule[0.5ex]{3cm}{0.4pt}\; \beta, b \qquad = \frac{i\delta_\alpha^\beta \delta_a^b}{p_0 - \frac{\boldsymbol{p}^2}{2M_N} + i\varepsilon} ,
\tag{3.20}
$$

extending the spinless result by conserved spin (α, β) and isospin (a, b) indices.
Similar, the bare dibaryon propagators at LO for the singlet and triplet state are given by

$$
\begin{aligned}
\alpha, a \;\rule[0.5ex]{3cm}{1pt}\; \beta, b \qquad & = -\frac{i\delta_\alpha^\beta \delta_a^b}{g_s} , \\
\alpha, a \;\text{= = = = = = = =}\; \beta, b \qquad & = -\frac{i\delta_\alpha^\beta \delta_a^b}{g_t} ,
\end{aligned}
\tag{3.21}
$$

respectively. Finally, the dibaryon-nucleon vertices are given by

$$
\eta = \frac{iy_s}{\sqrt{8}} \left(\sigma_2 \right)_\alpha^\beta \left(\tau_2 \tau^\eta \right)_a^b ,
\tag{3.22}
$$

$$
\eta = \frac{iy_t}{\sqrt{8}} \left(\sigma_2 \sigma^\eta \right)_\alpha^\beta \left(\tau_2 \right)_a^b .
$$

The full dimer propagator can be derived analogously to the spinless case by taking care of the spin and isospin indices,

$$
iD_{s/t}(p_0, \boldsymbol{p}) = -\frac{1}{y_{s/t}^2} \frac{i}{\frac{g_{s/t}}{y_{s/t}^2} - \frac{M_N}{4\pi} \left(\frac{2}{\pi}\Lambda - \sqrt{\frac{\boldsymbol{p}^2}{4} - M_N p_0 - i\varepsilon} \right)} .
\tag{3.23}
$$

The matching to the physical two-body T-matrix results in

$$
k\cot\delta_0 = -\frac{1}{a_{s/t}} = -\frac{2}{\pi}\Lambda + \frac{4\pi}{M_N} \frac{g_{s/t}}{y_{s/t}^2} .
\tag{3.24}
$$

This shows that the values of $g_{s/t}$ and $y_{s/t}$ are not observable. The only physically relevant quantity is $g_{s/t}/y_{s/t}^2$. Typically one sets

$$y_{s/t}^2 \equiv \frac{4\pi}{M_N} \ .$$ (3.25)

3.3.1. Three-boson system

The Feynman rules presented in the previous Section will now be used to derive the Faddeev equation for a system of three identical spinless bosons in the particle-dimer picture. This system presents a range of various states on the physical as well as unphysical sheets of the complex energy plane. It will be used for benchmark calculations for methods applied in this work. The associated equation describing the diboson-boson scattering, following from the Lagrangian Eq. (3.5), is depicted in Fig. 3.2.
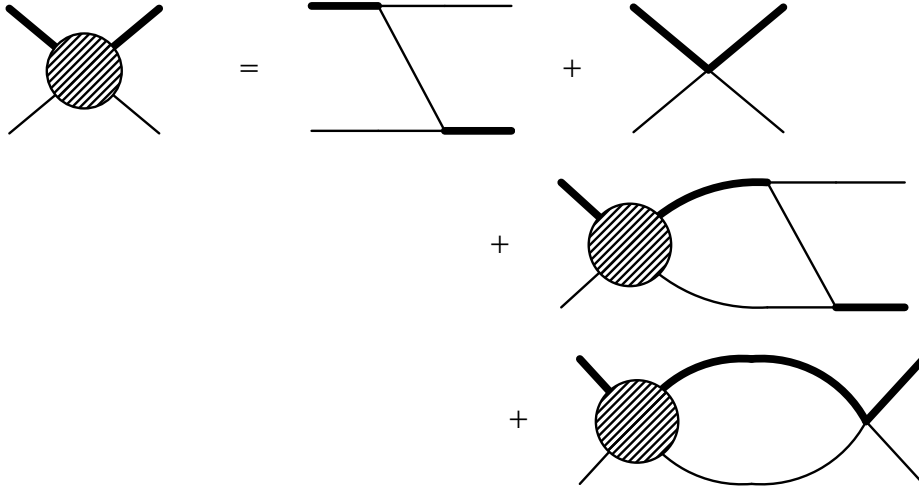
Figure 3.2.: Scattering equation for three spinless bosons. The T-matrix is represented by the blob, while thin (thick) lines represent bosons (dressed dimer propagators).

To transform the graphical representation into an equation, the following kinematics are chosen: the incoming momenta are chosen to be $\boldsymbol{k}$ and $-\boldsymbol{k}$ for the dimer and the single boson, respectively. The outgoing momenta are given by $\boldsymbol{p}$ and $-\boldsymbol{p}$. The energy of the incoming (outgoing) dimer is given by $E - E_d$ ($E - E_d'$), while the energy of the incoming (outgoing) boson is taken as E_d (E_d').

Applying the Feynman rules given in the previous Section one obtains

$$
\begin{aligned}
iT(\boldsymbol{k}, \boldsymbol{p}; E, E_d, E_d') =& \left(-i\frac{g_2}{2}\right)^2 iS\left(E - E_d - E_d', \boldsymbol{k} + \boldsymbol{p}\right) - i\frac{g_3}{36} \\
&+ \int \frac{\mathrm{d}^4 q}{(2\pi)^4} iT\left(\boldsymbol{k}, \boldsymbol{q}; E, E_d, q_0\right) iD\left(E - q_0, \boldsymbol{q}\right) iS\left(q_0, -\boldsymbol{q}\right) \\
&\times \left[iS\left(E - q_0 - E_d', \boldsymbol{q} + \boldsymbol{p}\right)\left(-i\frac{g_2}{2}\right)^2 - i\frac{g_3}{36}\right].
\end{aligned}
$$ (3.26)

The integral over the energy component q_0 is performed as usually using the residue theorem. This sets q_0 on-shell, $q_0 = \boldsymbol{q}^2/2m$. The equation can be further simplified by setting also the in- and outgoing

particles of the T-matrix on-shell, $E_d = \boldsymbol{k}^2/2m$, $E'_d = \boldsymbol{p}^2/2m$. Altogether, the resulting integral equation is given by

$$
\begin{aligned}
T\left(\boldsymbol{k}, \boldsymbol{p}; E, \frac{\boldsymbol{k}^2}{2m}, \frac{\boldsymbol{p}^2}{2m}\right) = &-m\frac{g_2^2}{4}\left[\frac{1}{mE - \boldsymbol{k}^2 - \boldsymbol{p}^2 - \boldsymbol{k}\cdot\boldsymbol{p} + i\varepsilon} + \frac{g_3}{9g_2^2 m}\right] \\
&-\int \frac{\mathrm{d}^3 q}{(2\pi)^3} T\left(\boldsymbol{k}, \boldsymbol{q}; E, \frac{\boldsymbol{k}^2}{2m}, \frac{\boldsymbol{q}^2}{2m}\right) 8\pi \frac{1}{-\frac{1}{a_0} + \sqrt{\frac{3}{4}\boldsymbol{q}^2 - mE - i\varepsilon}} \\
&\times \left[\frac{1}{mE - \boldsymbol{q}^2 - \boldsymbol{p}^2 - \boldsymbol{q}\boldsymbol{p} + i\varepsilon} + \frac{g_3}{9g_2^2 m}\right].
\end{aligned} \tag{3.27}
$$

For a vanishing three-body force, $g_3 = 0$, this equation is equivalent to the Skorniakov-Ter-Martirosian (STM) equation [111] proposed in 1957. It was shown that for three identical bosons a unique solution of the STM equation could be obtained by introducing a three-body force [112, 113]. The first calculations for a finite cutoff tuned to reproduce three-body observables were performed by Kharchenko [114] in 1973. Here, we apply the EFT formalism following the pioneering work by Bedaque *et al.* [110] in 1998. Similar to their work, we restrict our investigation to a total orbital angular momentum $L = 0$.

So, the S-wave projection has to be performed (cf. Appendix B.2, drop the last two arguments of T)

$$
\begin{aligned}
T_0\left(k, p; E\right) = &-m\frac{g_2^2}{4}\left[-\frac{1}{2kp}\log\left(\frac{k^2 + p^2 + kp - mE - i\varepsilon}{k^2 + p^2 - kp - mE - i\varepsilon}\right) + \frac{g_3}{9g_2^2 m}\right] \\
&-16\pi \int_0^\Lambda \frac{\mathrm{d}q}{(2\pi)^2} q^2 \frac{T_0\left(k, q; E\right)}{-\frac{1}{a_0} + \sqrt{\frac{3}{4}q^2 - mE - i\varepsilon}} \\
&\times \left[-\frac{1}{2qp}\log\left(\frac{q^2 + p^2 + qp - mE - i\varepsilon}{q^2 + p^2 - qp - mE - i\varepsilon}\right) + \frac{g_3}{9g_2^2 m}\right].
\end{aligned} \tag{3.28}
$$

Similar to the calculation of the self-energy, the integral is regularized by a hard momentum cutoff Λ.

The physical T-matrix is derived by multiplication with the wave function renormalization Z,

$$
T_0(k, p; E) \longrightarrow \sqrt{Z} T_0(k, p; E) \sqrt{Z}, \tag{3.29}
$$

where Z is given by

$$
Z^{-1} = i\partial_{p_0} \left(iD(p_0, \boldsymbol{p})\right)^{-1}\Big|_{\boldsymbol{p}=0, p_0 = -\frac{1}{ma_0^2}} = \frac{g_2^2 m^2 a_0}{64\pi}. \tag{3.30}
$$

This results in

$$
\begin{aligned}
T_0\left(k, p; E\right) = &\frac{16\pi}{ma_0}\left[\frac{1}{2kp}\log\left(\frac{k^2 + p^2 + kp - mE - i\varepsilon}{k^2 + p^2 - kp - mE - i\varepsilon}\right) - \frac{g_3}{9g_2^2 m}\right] \\
&+\frac{4}{\pi} \int_0^\Lambda \mathrm{d}q\, q^2 \frac{T_0\left(k, q; E\right)}{-\frac{1}{a_0} + \sqrt{\frac{3}{4}q^2 - mE - i\varepsilon}} \\
&\times \left[\frac{1}{2qp}\log\left(\frac{q^2 + p^2 + qp - mE - i\varepsilon}{q^2 + p^2 - qp - mE - i\varepsilon}\right) - \frac{g_3}{9g_2^2 m}\right].
\end{aligned} \tag{3.31}
$$

Furthermore, it is convenient to replace the three-body coupling constant by

$$g_3 = 9g_2^2 m \frac{H_0(\Lambda)}{\Lambda^2} \, . \tag{3.32}$$

To simplify the notation, a two-body interaction kernel

$$Z_{2,0}\left(k, p; E\right) = -\frac{1}{kp} \log\left(\frac{k^2 + p^2 + kp - mE - i\varepsilon}{k^2 + p^2 - kp - mE - i\varepsilon}\right) \tag{3.33}$$

and a three-body interaction kernel can be defined

$$Z_{3,0}\left(k, p; E\right) = 2\frac{H_0\left(\Lambda\right)}{\Lambda^2} \, . \tag{3.34}$$

Altogether the equation reads

$$
\begin{aligned}
T_0\left(k, p; E\right) = {} & -\frac{8\pi}{ma_0}\left[Z_{2,0}\left(k, p; E\right) + Z_{3,0}\left(k, p; E\right)\right] \\
& + \int_0^\Lambda \mathrm{d}q \, q^2 \tau_0\left(z\right)\left[Z_{2,0}\left(q, p; E\right) + Z_{3,0}\left(q, p; E\right)\right] T_0\left(k, q; E\right) \, ,
\end{aligned}
\tag{3.35}
$$

where

$$\tau_0\left(z\right) = -\frac{2}{\pi}\left[-\frac{1}{a_0} - i\sqrt{z}\right]^{-1} \, , \tag{3.36}$$

and $z = mE - 3/4q^2 + i\varepsilon$. The version of τ_0 introduced here is a modified/scaled version of the dressed dimer propagator, which will be used for the following Chapters.

3.3.2. Neutron-deuteron system

The next system to consider is the neutron-deuteron system. In comparison to the three-boson system, the particles contain spin now. The coupling of the neutron and deuteron spins results in two possible channels to consider, the quartet $\left(S = \frac{3}{2}\right)$ and the doublet $\left(S = \frac{1}{2}\right)$ channel.

3.3.2.a. Quartet channel

The first channel investigated is the quartet channel $\left(S = \frac{3}{2}\right)$ [115, 116]. Here, all spins of the three nucleons have to be aligned. So, the only possible intermediate state is a deuteron. Following the EFT formalism, the graphical representation of the Faddeev equation is shown in Fig. 3.3.

The graphical representation of the Faddeev equation can be transformed into the normal equation by applying the Feynman rules presented in the previous Section. This procedure is similar to the three-boson system. However, here spin and isospin have to be considered. The final equation reads

$$
\begin{aligned}
(iT^{rs})^{\beta b}{}_{\alpha a}(\boldsymbol{k}, \boldsymbol{p}; E) = {} & -\frac{iM_N y_t^2}{2}\left(\sigma^s \sigma^r\right)^\beta{}_\alpha \, \delta_a^b \frac{1}{\boldsymbol{k}^2 + \boldsymbol{k}\cdot\boldsymbol{p} + \boldsymbol{p}^2 - M_N E - i\varepsilon} \\
& + \int \frac{\mathrm{d}^3 q}{(2\pi)^3} D_t\left(E - \frac{\boldsymbol{q}^2}{2M_N}, \boldsymbol{q}\right)(iT^{rk})^{\gamma c}{}_{\alpha a}(\boldsymbol{k}, \boldsymbol{q}; E) \\
& \times \frac{M_N y_t^2}{2}\frac{\left(\sigma^s \sigma^k\right)^\beta{}_\gamma \, \delta_c^b}{\boldsymbol{q}^2 + \boldsymbol{q}\cdot\boldsymbol{p} + \boldsymbol{p}^2 - M_N E - i\varepsilon} \, ,
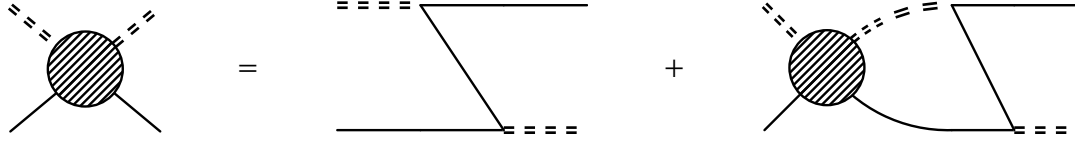\end{aligned}
\tag{3.37}
$$

Figure 3.3.: n-d quartet channel integral equation. The T-matrix is represented by the blob, while single (dashed double) lines represent neutrons (deuterons).

where the dressed dimer propagator D_t is defined by Eq. (3.23). Here, y_t is left explicitly. The notation is the following; the inner indices, e.g. r and s, represent the quantum numbers of the deuteron lines, while the outer lower and upper indices represent the spin and isospin for the incoming and outgoing neutron lines, respectively. The correct quantum numbers of the quartet channel are obtained for spins with a positive z-projection, $\alpha = \beta = 1$, as well as for the negative isospin projection of the neutrons, $a = b = 2$. Further, following Appendix C.1, the quantum numbers of the deuteron are included by choosing[1] $r = (1 - i2)/\sqrt{2}$ and $s = r^\dagger = (1 + i2)/\sqrt{2}$. All in all, the fully projected T-matrix is given by

$$T = \frac{1}{2}\left[T^{11} + T^{22} + i\left(T^{12} - T^{21}\right)\right]^{12}{}_{12} \, , \tag{3.38}$$

which is equivalent to the substitution

$$\left(\sigma^s \sigma^r\right)^\beta{}_\alpha \, \delta^b_a \to 2 \tag{3.39}$$

in the inhomogeneous as well as in the homogeneous term of Eq. (3.37). Plugging in the simplification $y_t^2 = 4\pi/M_N$ as well as performing the S-wave projection results in

$$T_0(k, p; E) = -4\pi Z_{2,0}\left(k, p; E\right) + \int_0^\Lambda \mathrm{d}q \, q^2 Z_{2,0}\left(q, p; E\right) \tau_0\left(z\right) T_0\left(k, q; E\right) \, , \tag{3.40}$$

where

$$
\begin{aligned}
Z_{2,0}\left(k, p; E\right) &= -\frac{1}{2}\int_{-1}^{+1}\mathrm{d}x \frac{1}{M_N E - k^2 - p^2 - kpx} \\
&= \frac{1}{2kp}\log\left(\frac{k^2 + p^2 - M_N E - i\varepsilon + kp}{k^2 + p^2 - M_N E - i\varepsilon - kp}\right) \, .
\end{aligned} \tag{3.41}
$$

3.3.2.b. Doublet channel

Besides the quartet channel, where all three spins couple to a total spin $S = \frac{3}{2}$, the spin of the deuteron and the neutron can be anti-parallel. This results in a total spin $S = \frac{1}{2}$, the doublet channel. The triton ^3H can be identified with this channel.

Here, also the $^1S_0$ state as an intermediate state is possible. This results in two coupled equations presented in Fig. 3.4.

---

[1]This notation is meant in the sense that $T^{rs} = \frac{1}{\sqrt{2}}\left(T^{1s} - iT^{2s}\right)$ for $r = (1 - i2)/\sqrt{2}$, and similarly for $s = (1 + i2)/\sqrt{2}$.
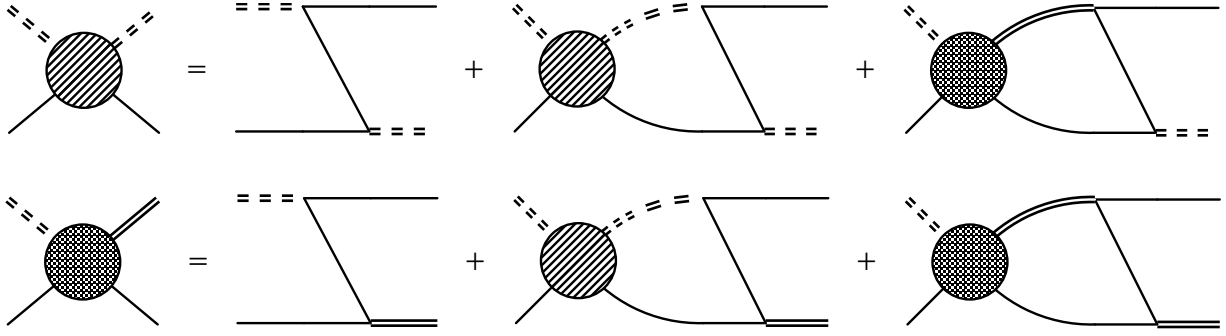
Figure 3.4.: n-d doublet channel integral equation. The components of the T-matrix are represented by the blobs, while single (dashed double) lines represent neutrons (deuterons). Additionally, the $^1S_0$-channel propagator is represented by a solid double line.

Similar to the quartet channel, a system of equations can be derived by applying the Feynman rules,

$$
\begin{pmatrix} T_t(k,p;E) \\ T_s(k,p;E) \end{pmatrix} = 2\pi \begin{pmatrix} Z_{2,0}(k,p;E) + Z_{3,0}(k,p;E) \\ -3Z_{2,0}(k,p;E) - Z_{3,0}(k,p;E) \end{pmatrix}
$$
$$
- \frac{1}{\pi} \int_0^\infty \mathrm{d}q \, q^2 \left[Z_{2,0}(q,p;E) \begin{pmatrix} 1 & -3 \\ -3 & 1 \end{pmatrix} + Z_{3,0}(q,p;E) \begin{pmatrix} 1 & -1 \\ -1 & 1 \end{pmatrix} \right] \qquad (3.42)
$$
$$
\begin{pmatrix} \mathrm{D}_t(q) & 0 \\ 0 & \mathrm{D}_s(q) \end{pmatrix} \begin{pmatrix} T_t(k,q;E) \\ T_s(k,q;E) \end{pmatrix},
$$

where the definition of the two-body interaction kernel of the quartet channel Eq. (3.41) is applied and a short-hand notation for the dibaryon propagator is introduced

$$
D_{t/s}(q) = D_{t/s}\left(E - \frac{q^2}{2M_N}, q \right) .
$$

Besides the two-body interaction kernel $Z_{2,0}$ the integral equation, similar to the three-boson system, contains a three-body force, which has to be included already at LO [117].

3.3.3. Three-neutron system

The last system to be considered is the three-neutron system. As in the previous cases, the Faddeev equation can be derived from the Lagrangian by applying the Feynman rules. However, based on the Faddeev equation for the quartet-channel neutron-deuteron system the equation can be derived simpler by applying the spin-isospin symmetry. While the deuteron is a spin-triplet and isospin-singlet state, the dineutron has to be a isospin-triplet and spin-singlet state. The corresponding projectors read

$$
\left(\mathcal{P}_s^\dagger \right)^i (\mathcal{P}_s)^j = \frac{1}{8} \tau^i \tau^2 \underbrace{\sigma^2 \sigma^2}_{\mathbb{1}} \tau^2 \tau^j = \frac{1}{8} \tau^i \underbrace{\tau^2 \tau^2}_{\mathbb{1}} \tau^j = \frac{1}{8} \tau^i \tau^j . \qquad (3.43)
$$

Again, one has to project onto the physical states by applying the substitutions $i = (1 - i2)/\sqrt{2}$ and $j = (1 + i2)/\sqrt{2}$,

$$
\left(\tau^i \tau^j \right)^b{}_a = \begin{pmatrix} 0 & 0 \\ 0 & 2 \end{pmatrix}^b{}_a . \qquad (3.44)
$$

The isospin state of the neutron is chosen by setting $a = b = 2$, which results in a factor of 2, similar to the neutron-deuteron quartet channel. So, the Faddeev equation for the three-neutron system is in-principle equivalent to the one for the neutron-deuteron quartet channel given by Eq. (3.40). However, while for the neutron-deuteron system a relative S-wave between the neutron and the deuteron was considered, for the three-neutron system a general partial wave l is needed. The corresponding Faddeev equation, following from Eq. (3.40), reads

$$T_l(k, p; E) = -4\pi Z_{2,l}(k, p; E) + \int_0^\Lambda \mathrm{d}q \, q^2 Z_{2,l}(q, p; E) \, \tau_l(z) \, T_l(k, q; E) \,, \tag{3.45}$$

where

$$Z_{2,l}(k, p; E) = -\frac{1}{2} \int_{-1}^{+1} \mathrm{d}x \frac{P_l(x)}{M_N E - k^2 - p^2 - kpx} \,. \tag{3.46}$$

3.4. Effective interaction potentials

Within the last Section, the Feynman rules obtained from the Lagrangian were used to derive the three-body scattering equations for different systems. Anyhow, the structure of the three-body force presented by this approach is not suitable for an analytical continuation. In the following, a second approach will be applied. We will follow Refs. [118, 119] and use the pionless EFT to construct an effective interaction potential, which will be used together with the Faddeev equations derived in the next Chapter. In general, the effective potential has the structure

$$V_{\mathrm{eff}} = \sum_{n=2}^\infty V_n \,, \tag{3.47}$$

where the index n represents a n-body interaction. Considering a system of N particles, interaction terms up to $n = N$ contribute. In the low-energy regime, higher-body interactions are typically suppressed. The potentials V_n are constrained by the symmetries of the system, e.g. Galilean invariance. Following the Galilean invariance, the interaction can only depend on the relative momenta of the incoming and outgoing particles. The interaction can be expressed in a momentum expansion of these relative momenta, which for a two-body interaction takes the form

$$\langle \boldsymbol{k}' | V_2 | \boldsymbol{k} \rangle = \underbrace{C_0 + \frac{C_2}{2} \left(\boldsymbol{k}'^2 + \boldsymbol{k}^2 \right)}_{\mathrm{S-wave}} + \underbrace{C_2' \boldsymbol{k} \cdot \boldsymbol{k}'}_{\mathrm{P-wave}} + \dots \,. \tag{3.48}$$

For simplicity regulator functions have been suppressed. Similar expressions can be derived for three- and higher-body interactions. The power counting is performed in even powers of Q/m_π, where $Q \sim k \sim k'$. At LO only the term C_0 contributes, while the terms proportional to C_2 and C_2' are order Q^2 and contribute at NLO. The exact form of the effective potential depends on the specific regularization scheme used. The low-energy observables, however, are independent of the regularization scheme (up to higher-order corrections) and one can choose a convenient scheme for practical calculations. Explicit forms for the effective potentials will be given in Section 5.3.

Finally, one is left with a theory depending on the low-energy couplings (LEC's) C_{2n}, which have to be determined. Similar to the previous Sections, the theory is matched to the effective range expansion.

First, the two-body T-matrix has to be derived. Therefore Eq. (3.48) can in general be written as

$$V_2 = C_{2n} |\zeta\rangle |g\rangle \langle g| \langle \zeta| \,, \tag{3.49}$$

where explicitly the two-body regulator function $|g\rangle$ and a projector to the correct two-body state $|\zeta\rangle$ were introduced. The projector will account for momentum dependencies, e.g. for C_2'

$$\langle plm|\zeta\rangle := p^l \delta_{l1} \,. \tag{3.50}$$

Combining the separable potential with the general representation of the Lippmann Schwinger equation Eq. (2.7),

$$t(z) = C_n |\zeta\rangle |g\rangle \langle g| \langle \zeta| + C_n |\zeta\rangle |g\rangle \langle g| \langle \zeta| G_0(z) t(z) \,, \tag{3.51}$$

an explicit representation of the two-body T-matrix can be derived

$$t(z) = \frac{|\zeta\rangle |g\rangle \langle g| \langle \zeta|}{C_n^{-1} - \langle g| \langle \zeta| G_0(z) |\zeta\rangle |g\rangle} := |\zeta\rangle |g\rangle \, \tau(z) \, \langle g| \langle \zeta| \,, \tag{3.52}$$

where

$$\tau(z) = \left[\frac{1}{C_n} - \langle g| \langle \zeta| G_0(z) |\zeta\rangle |g\rangle \right]^{-1} \,. \tag{3.53}$$

τ can be identified with the dressed dimer propagator introduced previously. Following this equation C_n can be determined by the condition

$$\frac{1}{C_n} = \langle g| \langle \zeta| G_0(z) |\zeta\rangle |g\rangle \bigg|_{z=(i\gamma)^2} \,, \tag{3.54}$$

where γ is the two-body binding momentum. It can be shown that C_0 is connected to the scattering length a_0, while C_2 and C_2' are connected to the effective range r_0 and the scattering volume a_1, respectively.

3.5. Uncertainty estimates

Finally, investigate the uncertainties presented by the pionless EFT. As was explained in the introduction, an EFT presents the possibility of a systematic error quantification by the expansion in a small parameter ϵ. The power of this parameter is connected to terms that are omitted in the EFT expansion. Within this thesis, only LO potentials will be considered. So, the terms order Q^2 are neglected. The uncertainties connected to these terms scale like

$$\mathcal{O}\left(\frac{Q^2}{\Lambda_b^2}\right) \,, \tag{3.55}$$

where $\Lambda_b = m_\pi$ is the breakdown scale of pionless EFT. Besides the uncertainty due to omitted terms also the regularization procedure introduces an error. It results from an expansion of the denominator of τ for small Q/Λ. For a LO calculation, it can be shown that an artificial effective range proportional to $1/\Lambda$ is introduced due to the finite cutoff. Altogether the EFT uncertainty scales like

$$\mathcal{O}\left[\max\left(\frac{Q^2}{\Lambda_b^2}, \frac{Q^2}{\Lambda^2}, \cdots\right)\right] \,. \tag{3.56}$$

The magnitude of the second type of uncertainties can be modified by changing Λ. If $\Lambda \geq \Lambda_b$ the error due to the regularization becomes negligible and the total error of the theory is given due to the EFT truncation.

4 Faddeev equations

Within Chapter 2 the scattering equation for two-body systems, the Lippmann-Schwinger equation, was presented. The main focus of this work is dedicated to three-body systems. The corresponding scattering equations were named after their developer Ludvig Faddeev as Faddeev equations [86].

This Chapter presents the derivation of a general single-channel Faddeev equation including two- and three-body interactions. This general Faddeev equation is used in the following Chapters to investigate the three-boson and the three-neutron system together with the effective interaction potentials discussed in the previous Chapter, Section 3.4. As will be shown below, the structure of the three-body force emerging from the Faddeev formalism is much more complicated than the constant one from the Lagrange formalism presented in the previous Chapter. Only this structure allows us to perform the analytical continuation correctly.

4.1. Derivation

The Faddeev equation can be derived based on the ordinary time-independent Schrödinger equation,

$$H \ket{\Psi} = E \ket{\Psi} \,, \tag{4.1}$$

where $\ket{\Psi}$ is the full relative three-body wave function. This wave function is decomposed into the three so-called Faddeev components $\ket{\psi_i}$ according to

$$\ket{\Psi} = \sum_{i=1}^{3} \ket{\psi_i} \equiv G_0 \left(\sum_{i=1}^{3} V_2^{(i)} + V_3 \right) \ket{\Psi} \,, \tag{4.2}$$

where $i = 1, 2, 3$ labels the three different pairs in the three-body system. The above definition includes the free Green's function Eq. (2.4)

$$G_0(z) = \frac{1}{z - H_0} \,, \tag{4.3}$$

where z is an arbitrary (in principle complex) energy. H_0 represents the relative kinetic part of the three-body Hamiltonian and the two-body pair interactions are given by $V_2^{(i)}$. Moreover, a three-body force V_3 is included here as well to keep the equation sufficiently general.

If the three particles are identical, one can simplify the Faddeev equation by introducing the permutation operator

$$P = P_{12}P_{23} + P_{13}P_{23} \,, \tag{4.4}$$

which allows to express the full state by only one component

$$|\Psi\rangle = (1 + P) |\psi_1\rangle \ . \tag{4.5}$$

The index 1 is dropped in the following.

Altogether, the leading-order representation of the Faddeev equation is given by [120]

$$|\psi\rangle = G_0 t P |\psi\rangle + \frac{1}{3} \left(G_0 + G_0 t G_0\right) V_3 \left(1 + P\right) |\psi\rangle \ , \tag{4.6}$$

where t is the two-body T-matrix.

Within this thesis, only separable two- and three-body interactions are applied,

$$
\begin{aligned}
V_2 &= C_n |\zeta\rangle |g\rangle \langle g| \langle \zeta| \ , \\
V_3 &= D_n |\eta\rangle |\xi\rangle \langle \xi| \langle \eta| \ ,
\end{aligned}
\tag{4.7}
$$

where C_n and D_n are the interaction strength, $|g\rangle$ and $|\xi\rangle$ are the two- and three-body regulator functions and $|\zeta\rangle$ and $|\eta\rangle$ project onto the two- and three-body states of interest, respectively. For further information on the interactions used within this work see Section 3.4.

To solve the Faddeev equation presented above, one has to choose a basis. A common choice are the momentum-space three-body Jacobi coordinates,

$$
\begin{aligned}
\boldsymbol{u}_1 &= \mu_{12} \left(\frac{\boldsymbol{k}_1}{m_1} - \frac{\boldsymbol{k}_2}{m_2} \right) \ , \\
\boldsymbol{u}_2 &= \mu_{(12)3} \left[\frac{\boldsymbol{k}_3}{m_3} - \frac{1}{M_{12}} \left(\boldsymbol{k}_1 + \boldsymbol{k}_2 \right) \right] \ ,
\end{aligned}
\tag{4.8}
$$

where $\boldsymbol{k}_1, \boldsymbol{k}_2$, and $\boldsymbol{k}_3$ are the momenta of the particles and $\mu_{ij} := \left(m_i m_j\right) / \left(m_i + m_j\right), \mu_{(ij)k} := \left(M_{ij} m_k\right) / \left(M_{ij} + m_k\right)$, and $M_{ij} = m_i + m_j$. Here, $\boldsymbol{u}_1$ represents the relative momentum between the first two particles, while the relative momentum between the third particle and the center of mass of the first two particles is given by $\boldsymbol{u}_2$. The relative kinetic energy of the three-body system simplifies to

$$H_0 |\boldsymbol{u}_1 \boldsymbol{u}_2\rangle = \left(\frac{u_1^2}{2\mu_{12}} + \frac{u_2^2}{2\mu_{(12)3}} \right) |\boldsymbol{u}_1 \boldsymbol{u}_2\rangle = \left(\frac{u_1^2}{m} + \frac{3}{4m} u_2^2 \right) |\boldsymbol{u}_1 \boldsymbol{u}_2\rangle \ . \tag{4.9}$$

Within the last step, it was assumed that all three particles have the same mass as used within this work. Together with the appropriate angular momentum, spin, and isospin quantum numbers, which are summarized in the multi-index $|\text{i}\rangle$, we define our basis as $|u_1 u_2 \text{i}\rangle$. This work uses a jj coupling scheme, for which the set of quantum numbers is given by

$$|\text{i}\rangle = |(\lambda s) j (l s_3) I J\rangle \ , \tag{4.10}$$

with the relative orbital angular momentum λ between the first two particles and the orbital angular momentum l relative to the third particle. s is the coupled spin of the first two particles, which couples with λ to j. Similarly, the spin of the third particle s_3 couples with l to I, which itself is coupled with j to the total angular momentum J.

Following the definition of the basis states, the identity operator of the system is defined by

$$\mathbb{1} = \sum_{\text{i}} \int \mathrm{d}u_1 \, u_1^2 \int \mathrm{d}u_2 \, u_2^2 \, |u_1 u_2 \text{i}\rangle \langle u_1 u_2 \text{i}| := \sum_{\text{i}} \int \mathcal{D}u \, u^2 \, |u_1 u_2 \text{i}\rangle \langle u_1 u_2 \text{i}| \ , \tag{4.11}$$

where the sum runs over all channels i considered. In the following, the investigation is restricted to a single-channel problem. The extension to a larger number of channels is straightforward and follows directly from the derivation presented.

Now, the derivation of the partial-wave projected Faddeev equation can be performed by projecting Eq. (4.6) onto the single-channel basis,

$$\langle u_1 u_2 \mathrm{i}|\psi\rangle := \psi_{\mathrm{i}}\left(u_1, u_2\right) = \langle u_1 u_2 \mathrm{i}|G_0 t P|\psi\rangle + \langle u_1 u_2 \mathrm{i}|\frac{1}{3}\left(G_0 + G_0 t G_0\right) V_3 \left(1 + P\right)|\psi\rangle\,. \tag{4.12}$$

The right-hand side of the equation can be evaluated by inserting several identity operators. To simplify the resulting matrix elements we exploit that the free Green's function G_0 is diagonal in all variables,

$$\langle u_1' u_2' \mathrm{i}'|G_0(E)|u_1 u_2 \mathrm{i}\rangle$$
$$= G_0\left(E; u_1, u_2\right) \frac{\delta\left(u_1' - u_1\right)}{u_1' u_1} \frac{\delta\left(u_2' - u_2\right)}{u_2' u_2} \delta_{\mathrm{i}\mathrm{i}'}\,, \tag{4.13}$$

with

$$G_0(E; u_1, u_2) = \left(E - \frac{u_1^2}{m} - \frac{3}{4m} u_2^2\right)^{-1}\,. \tag{4.14}$$

The two-body T-matrix for the separable two-body potential Eq. (4.7) is given by Eq. (3.52),

$$\langle u_1' u_2' \mathrm{i}'|t(E)|u_1 u_2 \mathrm{i}\rangle = \langle u_1'|g\rangle\, \tau_{\mathrm{i}}\left(z\right) \langle g|u_1\rangle \langle u_1' \mathrm{i}'|\zeta\rangle \langle \zeta|u_1 \mathrm{i}\rangle\, \frac{\delta\left(u_2' - u_2\right)}{u_2' u_2} \delta_{\mathrm{i}\mathrm{i}'}\,, \tag{4.15}$$

with the energy of the first pair of particles $z = E - \frac{3}{4} m u_2'^2$. Representations of τ_{i} for different regulators are presented in Section 5.3.

Furthermore, the matrix element of the permutation operator has to be defined. It is given by

$$\langle u_1' u_2 \mathrm{i}|P|u_1'' u_2'' \mathrm{i}''\rangle = \int_{-1}^{+1} \mathrm{d}x \frac{\delta(u_1' - \pi_1)}{u_1'^{\lambda+2}} \frac{\delta(u_1'' - \pi_2)}{u_1''^{\lambda''+2}} G_{\mathrm{i}\mathrm{i}''}(u_2 u_2'' x)\,, \tag{4.16}$$

with

$$\pi_1 = \sqrt{u_2''^2 + \frac{1}{4} u_2^2 + u_2 u_2'' x}\,,$$
$$\pi_2 = \sqrt{\frac{1}{4} u_2''^2 + u_2^2 + u_2 u_2'' x}\,, \tag{4.17}$$

and

$$G_{\mathrm{i}\mathrm{i}''}(u_2 u_2'' x) = \sum_k P_k(x) \sum_{\lambda_1 + \lambda_2 = \lambda} \sum_{\lambda_1'' + \lambda_2'' = \lambda''} u_2^{\lambda_2 + \lambda_2''} u_2''^{\lambda_1 + \lambda_1''} g_{\mathrm{i}\mathrm{i}''}^{k\,\lambda_1 \lambda_2 \lambda_1'' \lambda_2''}\,. \tag{4.18}$$

$g_{\mathrm{i}\mathrm{i}''}^{k\,\lambda_1 \lambda_2 \lambda_1'' \lambda_2''}$ is a purely geometrical factor. Further information on the geometrical factor is given in Appendix D.1.

Combining all matrix elements together with the explicit representation of the three-body interaction Eq. (4.7), the Faddeev equation can be written as

$$
\psi_i(u_1, u_2) = G_0(E; u_1, u_2) \left[\int_{-1}^{+1} dx \int du_2' u_2'^2 \; \langle u_1|g\rangle \, \tau_i\left(E - \frac{3}{4}mu_2^2\right) \langle g|\pi_1\rangle \right.
$$

$$
\times \frac{\langle u_1 i|\zeta\rangle \langle \zeta|\pi_1 i\rangle}{\pi_1^\lambda \pi_2^{\lambda'}} G_{ii}(u_2 u_2' x)\psi_i(\pi_2, u_2')
$$

$$
+ \int \mathcal{D}u' u'^2 \; D_0 \langle u_1 u_2 i|\eta\rangle \langle u_1 u_2 i|\xi\rangle \langle \xi|u_1' u_2' i\rangle \langle \eta|u_1' u_2' i\rangle \psi_i(u_1', u_2')
$$

$$
+ \int du_1'' u_1''^2 \int \mathcal{D}u' u'^2 \; G_0(E; u_1'', u_2) \langle u_1|g\rangle \, \tau_i\left(E - \frac{3}{4}mu_2^2\right) \langle g|u_1''\rangle \langle u_1 i|\zeta\rangle \langle \zeta|u_1'' i\rangle
$$

$$
\left. \times D_0 \langle u_1'' u_2 i|\eta\rangle \langle u_1'' u_2 i|\xi\rangle \langle \xi|u_1' u_2' i\rangle \langle \eta|u_1' u_2' i\rangle \psi_i(u_1', u_2') \right].
$$

(4.19)

Note that the factor $1 + P$ within the term connected to three-body force in Eq. (4.6) cancels against the factor $1/3$.

Finally, since we are working with separable interactions, it is possible and convenient to transform the Faddeev equations by defining

$$
\psi_i(u_1, u_2) = G_0(E; u_1, u_2) \langle u_1|g\rangle \langle u_1|\zeta\rangle \, \tau_i\left(E - \frac{3}{4}mu_2^2\right) F_i(u_2),
$$

(4.20)

where $F_i(u_2)$ is the so-called reduced Faddeev component. Instead of the full Faddeev component the reduced component only depends on one momentum variable reducing the numerical effort to solve the problem.

The final Faddeev equation for general two- and three-body regulators reads

$$
F_i(u_2) = \int du_2' u_2'^2 \tau_i\left(E - \frac{3}{4}mu_2'^2\right) F_i(u_2')
$$

$$
\times \left[\int_{-1}^{+1} dx \frac{\langle g|\pi_1\rangle \langle \zeta|\pi_1 i\rangle}{\pi_1^\lambda \pi_2^{\lambda'}} G_{ii}(u_2 u_2' x) G_0(E; \pi_2, u_2') \langle \pi_2|g\rangle \langle \pi_2 i|\zeta\rangle \right.
$$

$$
+ \int du_1' u_1'^2 \; G_0(E; u_1', u_2') \langle u_1'|g\rangle D_0 \langle \xi|u_1' u_2' i\rangle \langle \eta|u_1' u_2' i\rangle \langle u_1' i|\zeta\rangle
$$

(4.21)

$$
\times \left\{ \frac{\langle u_1 u_2 i|\xi\rangle}{\langle u_1|g\rangle \langle u_1 i|\zeta\rangle \, \tau_i\left(E - \frac{3}{4}mu_2^2\right)} \langle u_1 u_2 i|\eta\rangle \right.
$$

$$
\left. \left. + \int du_1'' u_1''^2 \; G_0(E; u_1'', u_2) \langle u_1'' u_2 i|\eta\rangle \langle g|u_1''\rangle \langle \zeta|u_1'' i\rangle \langle u_1'' u_2 i|\xi\rangle \right\} \right].
$$

The terms connected to the three-body force still present a very complicated structure, which is to be simplified in the following. Applying the general definition of the dimer propagator for $z = E - \frac{3}{4}mu_2^2$ [1],

$$
\tau_i(z) = \left[\frac{1}{C_i} - \int_0^\infty dq \; q^2 \, \langle \zeta|q i\rangle \langle g|q\rangle \, G_0(z; q) \langle q|g\rangle \langle q i|\zeta\rangle \right]^{-1},
$$

(4.22)

---

[1] Note the changed definition of C_i in comparison to Eq. (4.7), where the index now represents the multi-index of the dimer.

results in the following expression for the terms within the curly bracket

$$
\frac{\langle u_1 u_2 \mathrm{i}|\xi\rangle \langle u_1 u_2 \mathrm{i}|\eta\rangle}{\langle u_1|g\rangle \langle u_1 \mathrm{i}|\zeta\rangle} \left[\frac{1}{C_\mathrm{i}} - \int_0^\infty \mathrm{d}q\, q^2 \langle \zeta|q\mathrm{i}\rangle \langle g|q\rangle\, G_0(z;q) \langle q|g\rangle \langle q\mathrm{i}|\zeta\rangle \right]
$$

$$
+ \int \mathrm{d}u_1'' u_1''^2\, G_0\left(E; u_1'', u_2\right) \langle u_1'' u_2 \mathrm{i}|\eta\rangle \langle g|u_1''\rangle \langle \zeta|u_1''\mathrm{i}\rangle \langle u_1'' u_2 \mathrm{i}|\xi\rangle
$$

$$
= \frac{\langle u_1 u_2 \mathrm{i}|\xi\rangle \langle u_1 u_2 \mathrm{i}|\eta\rangle}{\langle u_1|g\rangle \langle u_1 \mathrm{i}|\zeta\rangle} \frac{1}{C_\mathrm{i}} + \int \mathrm{d}u_1'' u_1''^2\, \langle g|u_1''\rangle\, G_0\left(E; u_1'', u_2\right) \langle \zeta|u_1''\mathrm{i}\rangle
$$

$$
\times \left[-\frac{\langle u_1 u_2\, \mathrm{i}|\xi\rangle \langle u_1 u_2 \mathrm{i}|\eta\rangle}{\langle u_1|g\rangle \langle u_1 \mathrm{i}|\zeta\rangle} \langle u_1''|g\rangle \langle u_1'' \mathrm{i}|\zeta\rangle + \langle u_1'' u_2 \mathrm{i}|\eta\rangle \langle u_1'' u_2 \mathrm{i}|\xi\rangle \right] . \tag{4.23}
$$

To renormalize the theory properly, we choose

$$
\frac{1}{C_\mathrm{i}} = \int_0^\infty \mathrm{d}q\, q^2 \langle \zeta|q\mathrm{i}\rangle \langle g|q\rangle\, G_0(z;q) \langle q|g\rangle \langle q\mathrm{i}|\zeta\rangle \Bigg|_{z=(i\gamma)^2} , \tag{4.24}
$$

where γ is the two-body binding momentum. Introducing the short-hand notation for the integral

$$
I_\mathrm{i}(z;q) := \int_0^\infty \mathrm{d}q\, q^2 \langle \zeta|q\mathrm{i}\rangle \langle g|q\rangle\, G_0(z;q) \langle q|g\rangle \langle q\mathrm{i}|\zeta\rangle , \tag{4.25}
$$

the terms related to the three-body force are given by

$$
D_0 \int \mathrm{d}u_2' u_2'^2 \tau_\mathrm{i}\left(E - \frac{3}{4}mu_2'^2\right) F_\mathrm{i}(u_2')\, I_\mathrm{i}\left(E - \frac{3}{4}mu_2'^2; u_1'\right) \frac{\langle \xi|u_1' u_2'\mathrm{i}\rangle \langle \eta|u_1' u_2'\mathrm{i}\rangle}{\langle g|u_1'\rangle \langle \zeta|u_1'\mathrm{i}\rangle}
$$

$$
\times \Bigg\{ \frac{\langle u_1 u_2 \mathrm{i}|\xi\rangle \langle u_1 u_2 \mathrm{i}|\eta\rangle}{\langle u_1|g\rangle \langle u_1 \mathrm{i}|\zeta\rangle} I_\mathrm{i}\left((i\gamma)^2; q\right)
$$

$$
+ I_\mathrm{i}\left(E - \frac{3}{4}mu_2^2; u_1''\right) \left[-\frac{\langle u_1 u_2 \mathrm{i}|\xi\rangle \langle u_1 u_2 \mathrm{i}|\eta\rangle}{\langle u_1|g\rangle \langle u_1 \mathrm{i}|\zeta\rangle} + \frac{\langle u_1'' u_2 \mathrm{i}|\xi\rangle \langle u_1'' u_2 \mathrm{i}|\eta\rangle}{\langle u_1''|g\rangle \langle u_1''\mathrm{i}|\zeta\rangle} \right] \Bigg\} . \tag{4.26}
$$

Note that this equation structure can be simplified using a separable regulator.

Altogether, the general single-channel Faddeev equation for the reduced Faddeev component is given by

$$
F_\mathrm{i}(u_2) = \int \mathrm{d}u_2' u_2'^2 \left[Z_{2,\mathrm{i}}\left(u_2', u_2; E\right) + Z_{3,\mathrm{i}}\left(u_2', u_2; E\right) \right] \tau_\mathrm{i}\left(E - \frac{3}{4}mu_2'^2\right) F_\mathrm{i}(u_2') , \tag{4.27}
$$

where a two-body interaction kernel

$$
Z_{2,\mathrm{i}}\left(u_2', u_2; E\right) = \int_{-1}^{+1} \mathrm{d}x\, \frac{\langle g|\pi_1\rangle \langle \zeta|\pi_1\mathrm{i}\rangle\, G_{\mathrm{ii}}(u_2 u_2' x) G_0(E; \pi_2, u_2') \langle \pi_2|g\rangle \langle \pi_2 \mathrm{i}|\zeta\rangle}{\pi_1^\lambda \pi_2^{\lambda'}} \tag{4.28}
$$

and three-body interaction kernel

$$
Z_{3,\mathrm{i}}\left(u_2', u_2; E\right) = D_0 I_\mathrm{i}\left(E - \frac{3}{4}mu_2'^2; u_1'\right) \frac{\langle \xi|u_1' u_2'\mathrm{i}\rangle \langle \eta|u_1' u_2'\mathrm{i}\rangle}{\langle g|u_1'\rangle \langle \zeta|u_1'\mathrm{i}\rangle} \Bigg\{ \frac{\langle u_1 u_2 \mathrm{i}|\xi\rangle \langle u_1 u_2 \mathrm{i}|\eta\rangle}{\langle u_1|g\rangle \langle u_1 \mathrm{i}|\zeta\rangle} I_\mathrm{i}\left((i\gamma)^2; q\right)
$$

$$
+ I_\mathrm{i}\left(E - \frac{3}{4}mu_2^2; u_1''\right) \left[-\frac{\langle u_1 u_2 \mathrm{i}|\xi\rangle \langle u_1 u_2 \mathrm{i}|\eta\rangle}{\langle u_1|g\rangle \langle u_1 \mathrm{i}|\zeta\rangle} + \frac{\langle u_1'' u_2 \mathrm{i}|\xi\rangle \langle u_1'' u_2 \mathrm{i}|\eta\rangle}{\langle u_1''|g\rangle \langle u_1''\mathrm{i}|\zeta\rangle} \right] \Bigg\} \tag{4.29}
$$

were defined.

5 Analytical continuation

The Chapter on the introduction to the scattering theory for few-body systems, Chapter 2, presented the sheet structure of the complex energy plane and gave an introduction to the poles that can be found on the unphysical sheets; resonances and virtual states. Artifacts of these states can be detected, performing calculations on the physical sheet, if they are not far away from the physical sheet. An example given in the Chapter on scattering theory is the calculation of the phase shifts (cf. Eq. (2.23)). This type of calculation represents the first group of methods to find poles on the unphysical sheets. The second group includes methods of performing an analytical continuation through the branch cut and doing calculations directly on the unphysical sheet. Both types of methods have advantages as well as disadvantages. While the calculation on the physical sheet is simpler, the extrapolation to the unphysical sheet can be delicate or even questionable. Direct searches of resonance poles on the unphysical sheet are much more complex, both numerically and conceptually, but generally lead to more robust results.

This Chapter presents two types of methods part of the second group. First, the analytical continuation in the coupling constant (ACCC), following the work by Kukulin *et al.* [80–84], is considered. Further, the analytical continuation of the two- and three-body scattering equations for the T-matrix is presented. The prerequisites performing the analytical continuation are discussed and the equations for an explicit and implicit contour deformation are derived. Further, the correct representation of the dimer propagator on the whole complex momentum plane for different regulators is derived. Finally, the choice of the correct branch of the complex square root for the different methods applied within this work is discussed.

5.1. Analytical continuation in the coupling constant (ACCC)

In the following, the connection between states on the physical and on the unphysical sheet and their evolution into each other is investigated. First, the Hamiltonian H is replaced by a Hamiltonian $H(\lambda)$, where $H(\lambda) \to H$ for $\lambda \to 1$. λ is a real factor modifying the interaction strength. Assume for a moment that for $\lambda = 1$ a bound state close to threshold exists. By changing λ the potential can be tuned to be more attractive, i.e. the bound state stays on the physical sheet and moves away from the cut. Alternatively, it can be tuned to be less attractive or even repulsive. In the latter case, the bound state moves through the branch cut at the branch point located at the origin onto the unphysical sheet. To follow the moving poles the analyticity of the Jost function in p and λ is exploited by expanding the Jost function, Eq. (2.35), around $p = 0$ (for a fixed value of λ)

$$\mathcal{F}_l(\lambda, p) = 1 + \sum_{n=0}^{\infty} \left[\alpha_{2n} p^{2n} + i p^{2l+1} \beta_{2n} p^{2n} \right] . \tag{5.1}$$

This equation can further be expanded in λ. After setting the resulting equation equal to zero (to get a pole for the S-matrix) and solving for $p(\lambda)$ one obtains [121]

$$p_l(\lambda) = \sum_{n=1}^{l} \alpha_n \, (\lambda - \lambda_0)^{n-\frac{1}{2}} + \sum_{n=2l}^{\infty} \beta_n \, (\lambda - \lambda_0)^{n/2} \, , \tag{5.2}$$

where the offset λ_0 is introduced. It is determined by the transition point $p_l(\lambda) = 0$. For $l = 0$ only the second term contributes

$$p_0(\lambda) = \sum_{n=0}^{\infty} \beta_n \, (\lambda - \lambda_0)^{n/2} = \beta_0 + \beta_1 \sqrt{\lambda - \lambda_0} + \mathcal{O}\left[(\lambda - \lambda_0)^{3/2} \right] \, . \tag{5.3}$$

For $l > 0$ the dominant contribution is

$$p_l(\lambda) = \pm\alpha_1 \sqrt{\lambda - \lambda_0} \, . \tag{5.4}$$

The notation can be simplified by introducing the variable $x := \sqrt{\lambda - \lambda_0}$.

In general, we can now apply the ACCC by fitting the coefficients of Eq. (5.2) to bound state data on the physical sheet. However, this ansatz presents some disadvantages, as presented in the following Section, such that we will apply the Padé approximation as proposed by Kukulin *et al.* [80–84] instead.

5.1.1. Padé approximation

We consider an function $g(z)$ analytic in the vicinity of $z = 0$. So, it can be expended in a power series (around $z = 0$)

$$g(z) = \sum_{n=0}^{\infty} c_n z^n \, . \tag{5.5}$$

An approximation to this power series includes only the first N terms of the series. This approximation can describe the behavior of the function including zeros for small z, but it is not able to reproduce poles. A more general approximation to the function is given by the Padé approximation. A Padé approximant $g^{[N,M]}(z)$ of the function can be defined by

$$g^{[N,M]}(z) = \frac{P_N(z)}{Q_M(z)} = g(z) + \mathcal{O}\left(z^{N+M+1} \right) \, , \tag{5.6}$$

where $P_N(z)$ and $Q_M(z)$ are polynomials in z of the degree N and M, respectively. The Padé approximant is a convergent representation of the function on the whole domain of analyticity as well as it allows to reproduce poles by a vanishing denominator. We will only consider the case where $N = M$ as it conserves the unitarity of the S-matrix. These approximants are called diagonal Padé approximants.

5.1.2. Application of Padé approximants

First, a λ-dependent Hamiltonian $H(\lambda)$ has to be defined. In general, there are two different possibilities. Either an external potential V_{ext} can be introduced,

$$H(\lambda) = H + (\lambda - 1) \, V_{\text{ext}} \, , \tag{5.7}$$

or the existing potential can be modified

$$H(\lambda) = H_0 + \lambda V \,. \tag{5.8}$$

For the latter case, further modifications are possible, e.g. a partial scaling of the potential

$$H(\lambda) = H_0 + \lambda V_0 + V_1 \,. \tag{5.9}$$

Crucial in the application of the ACCC is the accurate determination of the value of λ_0. It can easily be determined by the condition $p_l(\lambda_0) = 0$. So, we only have to find a bound-state pole on the physical sheet with a vanishing binding energy.

Now the Padé approximant for $p_l(x)$ can be determined. Following Eq. (5.6) it is given by

$$p_l(x) \approx p_l^{[N,M]}(x) = i\frac{P_N(x)}{Q_M(x)} = i\frac{\sum_{n=0}^{N} c_n x^n}{\sum_{n=0}^{M} d_n x^n} \,, \tag{5.10}$$

where all coefficients c_n, d_n are real as they are fitted to (real) bound-state data.

Note that during the derivation it was assumed that $x \in \mathbb{R}$ for $\lambda \geq \lambda_0$. This is only true for an attractive potential. So, for a repulsive potential x is defined by $\sqrt{\lambda_0 - \lambda}$.

5.2. Analytical continuation of scattering equations

The ACCC discussed in the last Section represents, in principle, an exact formalism to analytically continue the pole trajectory to the unphysical sheets. Nevertheless, for practical purposes, the method has some shortcomings. First, the potential has to be modified to create a bound state trajectory on the physical sheet without introducing additional cuts. For an increasing number of particles, this can become very complicated or even impossible. Further, the method is only exact for treating polynomials of infinite orders. Applying the formalism with polynomials of finite orders results in an uncertainty for the pole location.

In the following, the analytical continuation of the scattering equations for two (Lippmann-Schwinger) and three particles (Faddeev) is presented. While there is a large effort for the analytical continuation, the application of the analytically-continued equation is straightforward. Methods equivalent to those applied to the equations on the physical sheet can be used, such that the methodical error of the results vanishes.

The mathematical foundation necessary to perform the analytical continuation goes back to the work by Gel'fand *et al.* proposing the so-called rigged Hilbert spaces [122]. The general idea of this formalism is to deform the integration path of the scattering equation. By deforming the integration path the cut is deformed, too. The aim is to show that it is possible to deform the cut such that the third and fourth quadrant of the complex energy plane becomes part of the accessible region. Figure 5.1 shows the principle idea of the formalism. The two virtual states enclosed between the cut and the positive real axis are accessible, while the resonance is outside the area of applicability.

Already 1964, Lovelace proposed the method of contour rotation to analytically continue the Faddeev equation to the unphysical sheets [123]. This formalism was extended independently to general integration contours by Glöckle [44], as well as by Möller [40–43, 48]. Furthermore, these works introduced a
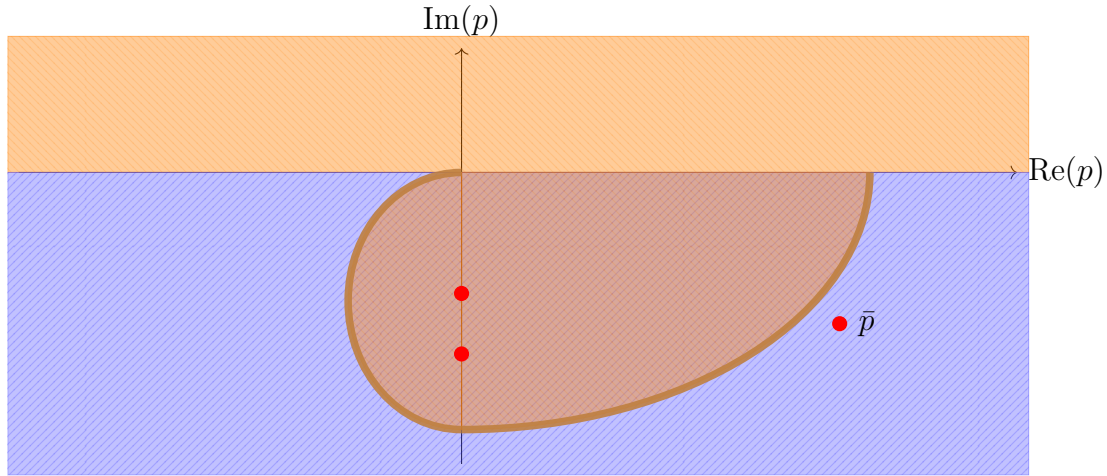
Figure 5.1.: A sketch showing the deformation of the integration contour/ cut onto the unphysical sheet. The area between the cut and the positive real axis (▨) becomes accessible. Using this integration contour the two virtual states can be found, while the resonance is not accessible.

modified equation structure that is simpler to use. The basic idea by Lovelace of a rotated contour was extended by Pearce and Afnan and applied to several systems [87–91]. It is conceptually equivalent to the complex scaling method [124–128], which performs a rotation in coordinate space.

We will apply both methods, the simplified equation structure by Glöckle and Möller as well as the explicit contour rotation proposed by Afnan. Both methods have advantages as well as disadvantages, which will be discussed together with the formalism itself in the following Sections.

5.2.1. Two-body systems - The Lippmann-Schwinger equation

The scattering equation for two particles is the Lippmann-Schwinger equation, Eq. (2.7). By inserting appropriate basis states the partial-wave projected Lippmann-Schwinger equation can be derived (cf. Appendix B.1),

$$T_l(k, p; E) = V_l(k, p) + \int_0^\infty \mathrm{d}q \; q^2 V_l(q, p) G_0(q; E) T_l(k, q; E) \,, \tag{5.11}$$

where $V_l(k, p)$ is the partial-wave projected potential and $G_0(q; E)$ the free Green's function,

$$G_0(q; E) = \frac{1}{E - \frac{q^2}{2\mu} + i\varepsilon} \,. \tag{5.12}$$

As shown in the previous Chapter the free Green's function presents a cut along the positive real axis of the complex energy plane.

5.2.1.a. Explicit contour deformation

First, an explicit contour deformation applying the type of contours proposed by Afnan is considered. These contours are derived from the contour along the real axis, $q \in [0, \infty)$, by applying the coordinate

transformation

$$q \longrightarrow q e^{-i\varphi} , \qquad \varphi > 0 . \tag{5.13}$$

It represents one of the simplest type of contours as it only depends on a single variable, the rotation angle φ. The rotation angle is defined by the position of the poles on the unphysical sheet which should be included in the calculation. Assuming a resonance at a momentum $\bar{p}$ it has to fulfill the condition

$$\varphi > \Phi = \arctan \left| \frac{\operatorname{Im} \bar{p}}{\operatorname{Re} \bar{p}} \right| = \frac{1}{2} \arctan \frac{0.5\Gamma}{E_{\mathrm{R}}} . \tag{5.14}$$

The defining angles and the rotated contour are sketched in Fig. 5.2. The rotation is solely restricted by singularities of the potential.
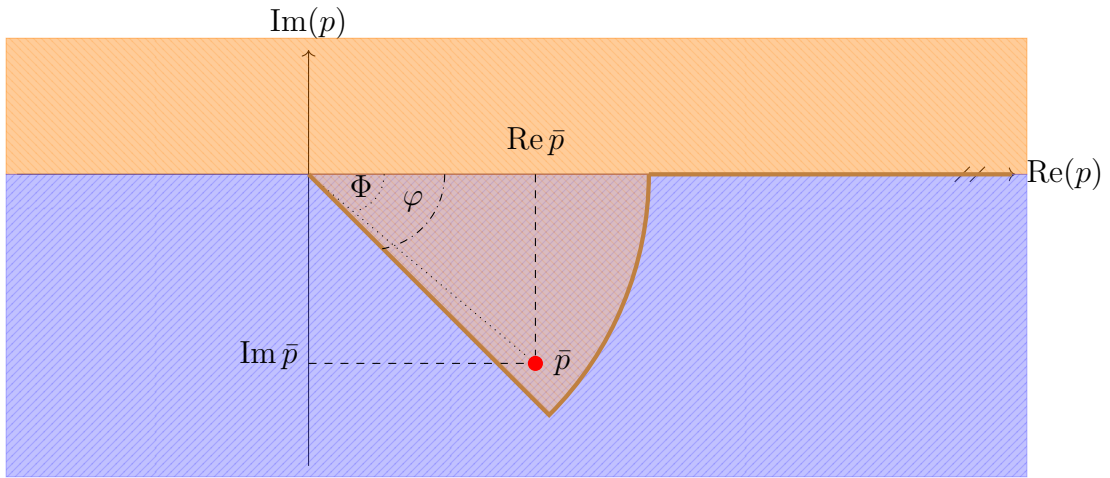
Figure 5.2.: The angle Φ connected to the pole on the unphysical sheet and the rotation angle φ. To perform the analytical continuation $\varphi > \Phi$ must hold. A possible rotated contour and the accessible region of the unphysical sheet are shown.

5.2.1.b. Implicit contour deformation

Besides an explicit contour deformation, it is also possible to derive a Lippmann-Schwinger equation on the unphysical sheet that is equivalent to the Lippmann-Schwinger equation on the physical sheet with a modified potential in the homogeneous term. This derivation can be performed on a mathematical basis following the theory of rigged Hilbert spaces. We will apply a more physical ansatz following the work by Glöckle [44] and Orlov [129]. The derivation starts at the partial-wave expanded Lippmann Schwinger equation on the physical sheet Eq. (5.11),

$$T_l(k,p;E) = V_l(k,p) + \int_0^\infty \mathrm{d}q \ q^2 V_l(q,p) G_0(q;E) T_l(k,q;E) . \tag{5.15}$$

It presents only one moving singularity due to the free Green's function located at $q \equiv q_0 = \sqrt{2\mu (E + i\varepsilon)}$. This pole should now be shifted downwards onto the unphysical sheet. First, it has to be assumed that the T-matrix has no poles along the positive real axis of the q-plane. This can in general be achieved. Further, the integral kernel has to be analytic in some region on the unphysical sheet. The analyticity

of the kernel depends on the potential and has to be checked for every potential used independently. Finally, the most important rule is that while continuing the integral to the unphysical sheet the moving singularities should not touch or cross the cut. So, while shifting the pole, the integration contour has to be deformed simultaneously. The resulting contour is denoted $C_{\mathbb{C}}$. Figure 5.3 shows the pole q_0 on the unphysical sheet as well as several possible contours.
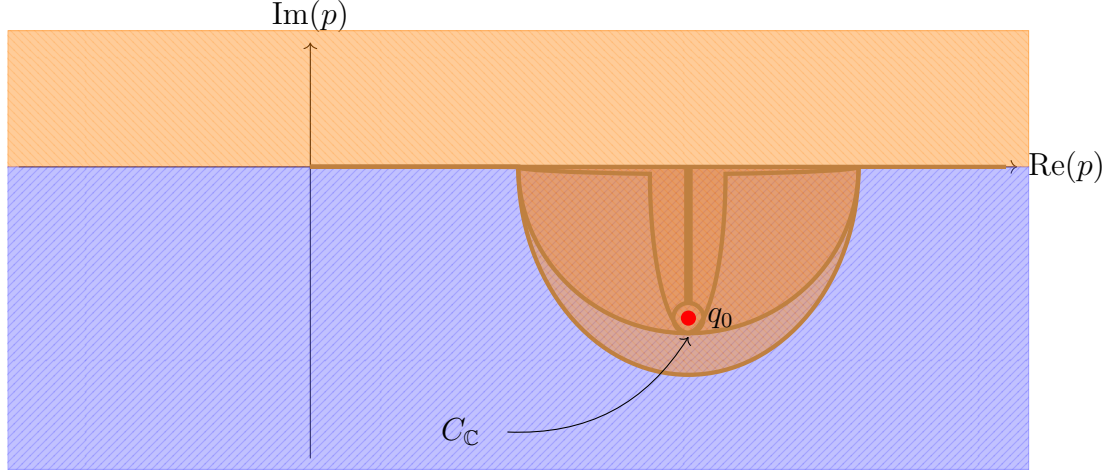

Figure 5.3.: The pole of the free Green's function q_0 on the unphysical sheet together with several possible integration contours. Poles on the unphysical sheet located between the integration contours and the positive real axis are accessible by the analytical continuation. As shown by the most inner contour, it is possible to perform an integration along the real axis and include the pole q_0 explicitly by applying the residue theorem.

It is convenient to use a contour as close as possible to the pole to avoid possible (unknown) singularities of the T-matrix. Considering Fig. 5.3 this assumption corresponds to the most inner contour. It is given by the contour along the real axis $C_{\mathbb{R}}$ and a contribution of the pole q_0. The two paths parallel to the imaginary axes cancel each other. The contribution of the pole is included by applying the residue theorem

$$
\begin{aligned}
\int_{C_{\mathbb{C}}} \mathrm{d}q K_l(q,p;E) T_l(k,q;E) &= \int_{C_{\mathbb{R}}} \mathrm{d}q K_l(q,p;E) T_l(k,q;E) + \oint_{q_0} \mathrm{d}q K_l(q,p;E) T_l(k,q;E) \\
&= \int_{C_{\mathbb{R}}} \mathrm{d}q K_l(q,p;E) T_l(k,q;E) + 2\pi i N_{q_0} \operatorname{Res}_{q_0} K_l(q,p;E) T_l(k,q;E) ,
\end{aligned}
\tag{5.16}
$$

where $K_l(q,p;E) = q^2 V_l(q,p) G_0(q;E)$ is the kernel of the Lippmann-Schwinger equation, $N_{q_0} = 1$ the winding number and $\operatorname{Res}_{q_0} K_l(q,p;E) T_l(k,q;E)$ the residue at the pole q_0. The calculation of the residue of the kernel reduces to the calculation of the residue of the free Green's function as the remaining kernel is non-singular at q_0. It can be calculated by applying the definition of the residue of a pole of first order,

$$
\operatorname{Res}_{q_0} G_0(q;E) = \lim_{q \to q_0} (q - q_0) G_0(q;E) = -2\mu \lim_{q \to q_0} (q - q_0) \frac{1}{q - q_0} \frac{1}{q + q_0} = -\frac{\mu}{q_0} .
\tag{5.17}
$$

Altogether, the Lippmann Schwinger equation on the unphysical sheet is given by

$$
\begin{aligned}
T_l(k,p;E) = V_l(k,p) &+ \int_{C_{\mathbb{R}}} \mathrm{d}q \; q^2 V_l(q,p) G_0(q;E) T_l(k,q;E) \\
&- 2\pi i \mu q_0 V_l(q_0,p) T_l(k,q_0;E) .
\end{aligned}
\tag{5.18}
$$

At the pole the T-matrix factorizes into the singularity and the residue R. The inhomogeneous potential term is finite at the pole and will be neglected in the following. This results in the equation

$$R_l(k, p; E) = \int_{C_{\mathbb{R}}} \mathrm{d}q \ q^2 V_l(q, p) G_0(q; E) R_l(k, q; E) - 2\pi i \mu q_0 V_l(q_0, p) R_l(k, q_0; E) \,. \tag{5.19}$$

Physically, it is already possible to use this equation to search for poles on the unphysical sheet. Numerically, it is more convenient to consider the half-on-shell equation of Eq. (5.19) at $p = q_0$,

$$R_l(k, q_0; E) = \int_{C_{\mathbb{R}}} \mathrm{d}q \ q^2 V_l(q, q_0) G_0(q; E) R_l(k, q; E) - 2\pi i \mu q_0 V_l(q_0, q_0) R_l(k, q_0; E)$$

$$\Leftrightarrow R_l(k, q_0; E) = [1 + 2\pi i \mu q_0 V_l(q_0, q_0)]^{-1} \int_{C_{\mathbb{R}}} \mathrm{d}q \ q^2 V_l(q, q_0) G_0(q; E) R_l(k, q; E) \,, \tag{5.20}$$

and combine both equations to

$$R_l(k, p; E) = \int_{C_{\mathbb{R}}} \mathrm{d}q \ q^2 G_0(q; E) R_l(k, q; E) \left[V_l(q, p) - \frac{2\pi i \mu q_0 V_l(q_0, p) V_l(q, q_0)}{1 + 2\pi i \mu q_0 V_l(q_0, q_0)} \right] \,. \tag{5.21}$$

It is equivalent to the Lippmann Schwinger equation for the residue on the physical sheet for an energy-dependent potential

$$V_l(q, p; E) := V_l(q, p) - \frac{2\pi i \mu q_0 V_l(q_0, p) V_l(q, q_0)}{1 + 2\pi i \mu q_0 V_l(q_0, q_0)} \,, \tag{5.22}$$

whereby the energy dependence is due to the pole momentum $q_0 = \sqrt{2\mu (E + i\varepsilon)}$.

5.2.2. Three-body systems - The Faddeev equation

Now, a third particle is added to the two-body system. This increases the complexity enormously by introducing new cuts. Note that in the following, only systems of three identical particles are considered.

A general, partial-wave projected three-body Faddeev equation has the structure

$$T_l(k, p; E) = Z_l(k, p; E) + \int \mathrm{d}q \, q^2 Z_l(q, p; E)\tau_l(z)T_l(k, q; E) \,, \qquad (5.23)$$

with a potential-like interaction kernel

$$Z_l(k, p; E) = Z_{2,l}(k, p; E) + Z_{3,l}(k, p; E) \,,$$
$$Z_{2,l}(k, p; E) = \int_{-1}^{+1} \mathrm{d}x \frac{g(\pi_1) \, g(\pi_2) \, P_l(x)}{2\mu E - k^2 - p^2 - kp \cdot x + i\varepsilon} \,, \qquad (5.24)$$

and the LO dimer propagator

$$\tau_l(z) = \frac{2}{\pi} \frac{1}{\gamma_l + i\sqrt{2\mu z}} \,. \qquad (5.25)$$

The interaction kernel $Z_l(k, p; E)$ separates into a contribution from two-body $Z_{2,l}(k, p; E)$ as well as three-body interactions $Z_{3,l}(k, p; E)$. The explicit structure of the three-body interaction kernel depends on the regulator used. However, within this work, it does not present any singularities and will not be considered explicitly for the derivation of the analytical continuation. The dimer propagator can be identified with the two-body T-matrix. So, it becomes singular at the energy of the two-body bound state,

$$z = -\frac{\gamma_l^2}{2\mu} = -B_2 \,. \qquad (5.26)$$

Further, it creates a square-root branch cut starting at the two-body binding energy, the two-body branch point, and following the real axis through zero along the positive real axis up to infinity,

$$q = q_0 := \sqrt{\frac{4}{3}\left(2\mu E + \gamma_l^2\right)} \,. \qquad (5.27)$$

The two-body interaction kernel corresponds to the free Green's function in the two-body system. Similar to the two-body case, it introduces a cut along the positive real energy axis from zero to infinity. Performing the partial-wave projection in Eq. (5.24) by integrating over x results in a logarithmic structure. Similar to the square root, the complex logarithm is a multivalued function: it does not change if an integer multiple of $2\pi i$ is added to its argument. Therefore, this branch cut leads to an infinite number of unphysical sheets. Physically, only the one adjacent to the lower rim of the physical sheet is relevant as it affects measurable quantities such as the cross section. Note that the regulator can also generate an artificial cut. Within this work, only the Yamaguchi model used for comparison has this feature.

The cut starting at the two-body branch point will be called two-body cut, while the cut resulting from the free Green's function will be called three-body cut. Accordingly, the sheets accessed through the cuts are called two- and three-body sheets, respectively. The sheet structure of the Faddeev equation is shown in Fig. 5.4.
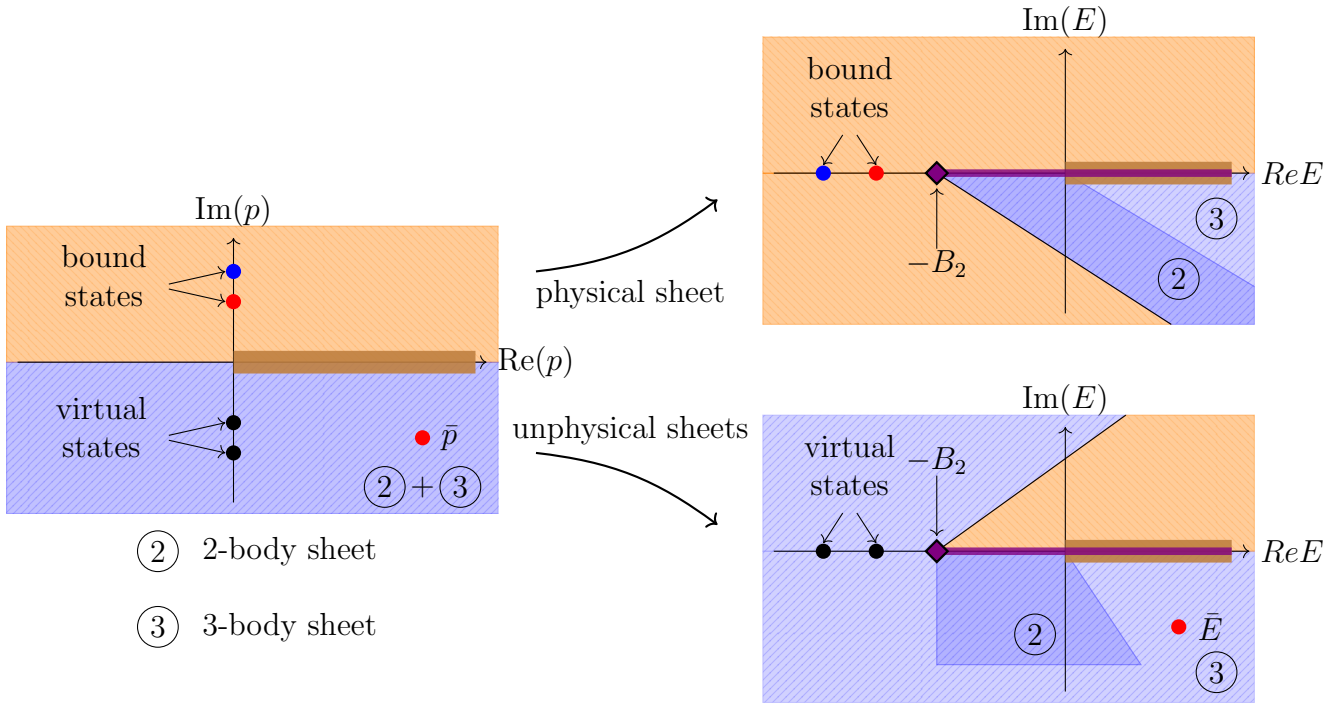
Figure 5.4.: The structure of the complex momentum and energy plane for three particles defined by the energy-momentum relation $E = \frac{3}{4}p^2 - B_2$, where B_2 is the two-body binding energy. Energies on the physical sheet (upper right plot) translate to momenta on the physical part of the momentum plane with $\text{Im}(p) > 0$ (shading [orange]). Energies on the unphysical sheets (lower right plot) are mapped to the region of the complex momentum plane with $\text{Im}(p) < 0$ (shading [blue]). The physical and unphysical sheets are connected by two branch cuts; the three-body cut starting at the origin and following the positive real axis and the two-body cut starting at the two-body binding energy B_2 (◆) and following the real axis, too. The complex energy plane shows two unphysical sheets, the one accessible through the cut starting at the two-body threshold (2-body sheet, darker shaded) and the one accessible through the three-body threshold (3-body sheet, lighter shaded). Both unphysical sheets extend further than sketched here. Note that the position of the two-body branch point depends on the two-body interaction strength. While bound states are located on the physical sheet, virtual states and resonances $\bar{p}/\bar{E}$ live on the unphysical sheets. This is also true for the corresponding areas on the complex momentum plane.

The two-body cut is only present if the two-body system is bound. Otherwise, only the three-body cut has to be considered. These will be the two cases to investigate in the following.

5.2.2.a. Analyticity of the kernel

The analytical continuation of the kernel is restricted by its singularities. In the two-body system the procedure was trivial. Assuming that the potential is non-singular, only the singularity of the free Green's function has to be considered. Here, this investigation is much more complicated.

In the following, the forbidden areas resulting from the zeros of the denominator of the two-body interaction kernel will be investigated,

$$2\mu E - q^2 - p^2 - qp \cdot x = 0\,, \qquad x \in [-1, +1]\,. \tag{5.28}$$

The analytical continuation is performed due to a transformation of the contour of integration. So, the singularities in the momentum plane for q have to be determined. Solving Eq. (5.28) for q results in

$$\begin{aligned}
q &= -\frac{p}{2}x \pm \sqrt{2\mu E - p^2\left(1 - \frac{x^2}{4}\right)} \\
&= -\frac{p}{2}x \pm i\sqrt{-2\mu E + p^2\left(1 - \frac{x^2}{4}\right)}\,.
\end{aligned} \tag{5.29}$$

While for $\mathrm{Im}\,E \geq 0$ both representations agree, for $\mathrm{Im}\,E < 0$ the first (second) equation has to be applied for $\mathrm{Re}\,E > 0$ ($\mathrm{Re} < 0$), respectively. This equation can now be investigated for complex energies in the third and fourth quadrant. Depending on the method which is applied, q is to be evaluated differently. Applying an explicit contour deformation we use $q \to q\exp(-i\varphi)\,, q \in [0, \infty)$. In the case of the implicit deformation q is either evaluated on the positive real momentum axis or it is substituted by q_0.

Similar to the two-body system, first an analytical continuation through the positive real axis is considered. We start at a state located on the physical sheet at the upper rim of the cut, e.g. $E = (1 + 0.1i)$ MeV. Figure 5.5 shows the two areas the two-body interaction kernel is singular defined by Eq. (5.29) as well as the singularities of the dimer propagator defined by Eq. (5.27) for various values of $\gamma_l > 0$. It further shows the integration contour for $\varphi = 0$.
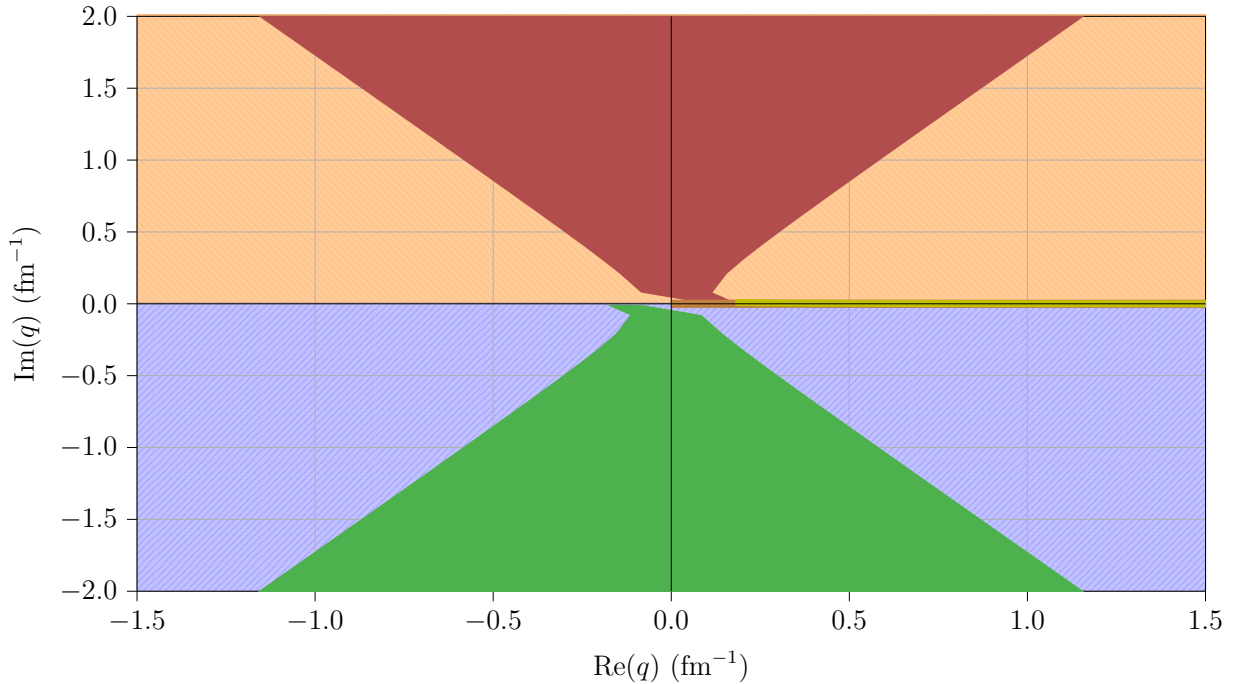
Figure 5.5.: The complex momentum plane for the integration variable q and an energy $E = (1 + 0.1i)$ MeV. The singular areas of the two-body interaction kernel Eq. (5.29) (red/ green areas) and the singularity path of the dimer propagator Eq. (5.27) (for various values of $\gamma_l > 0$, yellow line) are shown together with the integration contour for $\varphi = 0$ (brown line).

The energy is now shifted into the fourth quadrant of the complex momentum plane, $E = (1 - 0.1i)\,$MeV. Simultaneously, the integration contour is transformed to an angle $\varphi = \pi/4 + 0.1$. The resulting singularities of the kernel are shown in Fig. 5.6.
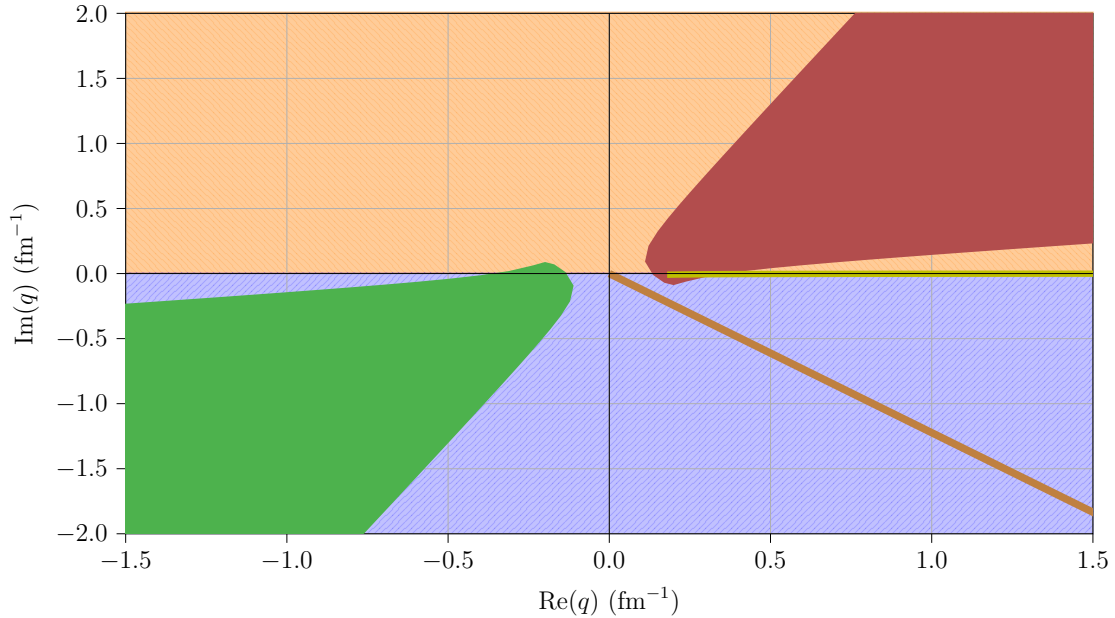
Figure 5.6.: A plot similar to Fig. 5.5 for an energy $E = (1 - 0.1i)\,$MeV and a rotation angle $\varphi = \pi/4 + 0.1$.

This procedure can be repeated until the energy reaches the area of interest. Figure 5.7 shows a contour rotated to $\varphi = \pi/2 + 0.1$ for an energy $E = -i\,$MeV. It allows to find all poles on the third and fourth quadrant of the complex energy plane.
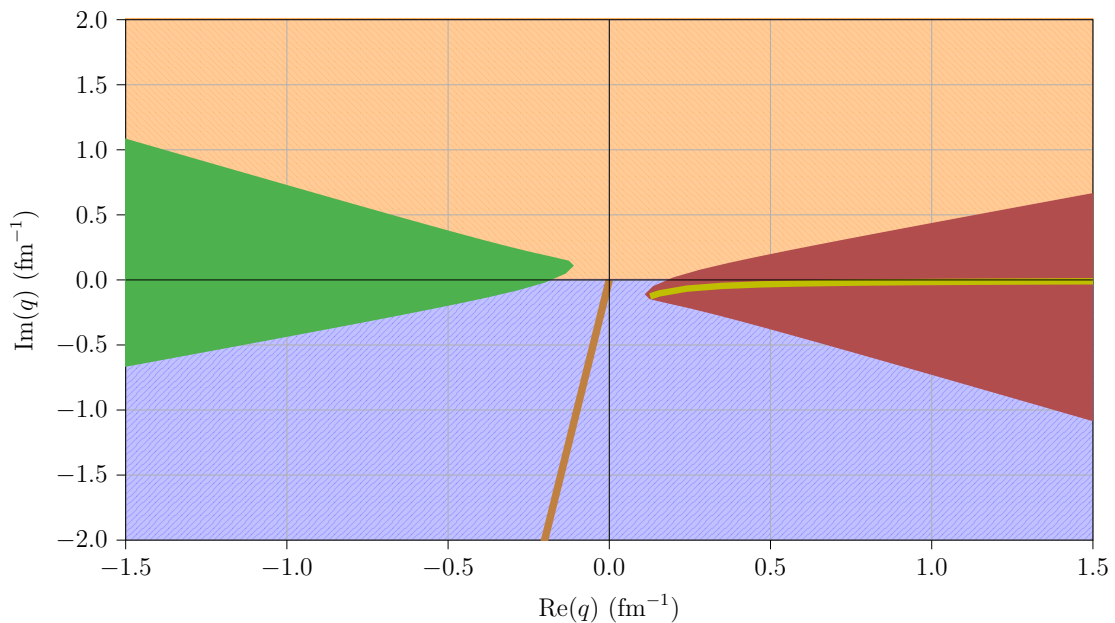
Figure 5.7.: A plot similar to Fig. 5.5 for an energy $E = -1.0i\,$MeV and a rotation angle $\varphi = \pi/2 + 0.1$.

Besides an analytical continuation through the positive real axis, it is also possible to perform an analytical continuation through the two-body branch cut at negative energies. This procedure results in singularities equivalent to those shown for an analytical continuation through the positive real axis.

Finally, the analyticity for momenta used for an implicit contour deformation is investigated. Here, considering energies in the third and fourth quadrant, the propagator can only become singular due to complex q_0. So, Eq. (5.29) becomes

$$
\begin{aligned}
q &= -\frac{q_0}{2}x \pm \sqrt{2\mu E - q_0^2 \left(1 - \frac{x^2}{4}\right)} \\
&= -\frac{q_0}{2}x \pm i\sqrt{-2\mu E + q_0^2 \left(1 - \frac{x^2}{4}\right)}.
\end{aligned}
\tag{5.30}
$$

Using the definition of q_0, Eq. (5.27), the branch cut starts at, $x = -1$,

$$
q = \frac{q_0}{2} \pm i\gamma_l, \qquad \gamma_l > 0,
\tag{5.31}
$$

and ends at , $x = +1$,

$$
q = -\frac{q_0}{2} \pm i\gamma_l.
\tag{5.32}
$$

q_0 is located in the fourth quadrant. So, considering the upper sign the trajectory can start in the fourth or first quadrant and ends in the second quadrant. In the case of the lower sign, the trajectory starts in the fourth quadrant and ends in the third or second quadrant. It can be shown that if the trajectories cross the real axis, the upper-sign trajectory is the one crossing the contour of integration at positive real energies. This results in the condition

$$
\text{Im}\left(\frac{q_0}{2} + i\gamma_l\right) > 0.
\tag{5.33}
$$

Further, deriving a closed set of equations, both momenta of the potential are evaluated at q_0. The resulting singularities follow from Eq. (5.30) together with $p = q_0$

$$
2\mu E = 4\gamma_l^2 \frac{2 - x}{3 - 4(2 - x)}.
\tag{5.34}
$$

This cut is present for energies with $-4\gamma_l^2 \le 2\mu E \le -4\gamma_l^2/3$.

5.2.2.b. Explicit contour deformation

Again, first an explicit contour deformation is considered. The application for a three-body system does not differ that much from the two-body system. However, due to the two-body substructure, there are two cases that can be considered; a bound and an unbound two-body subsystem.

Unbound two-body subsystem

The simpler case is an unbound subsystem. The behavior of the system is similar to the two-body problem as there is only one cut along the positive real axis created by the free Green's function. So, the formulas presented for the two-body system in Section 5.2.1.a can be applied to the Faddeev equation, too. Figure 5.8 shows a possible pole trajectory in the complex momentum and energy planes. Starting at a given bound state and decreasing the interaction strength the pole moves towards the three-body branch point at the origin, where it crosses the cut becoming a resonance.
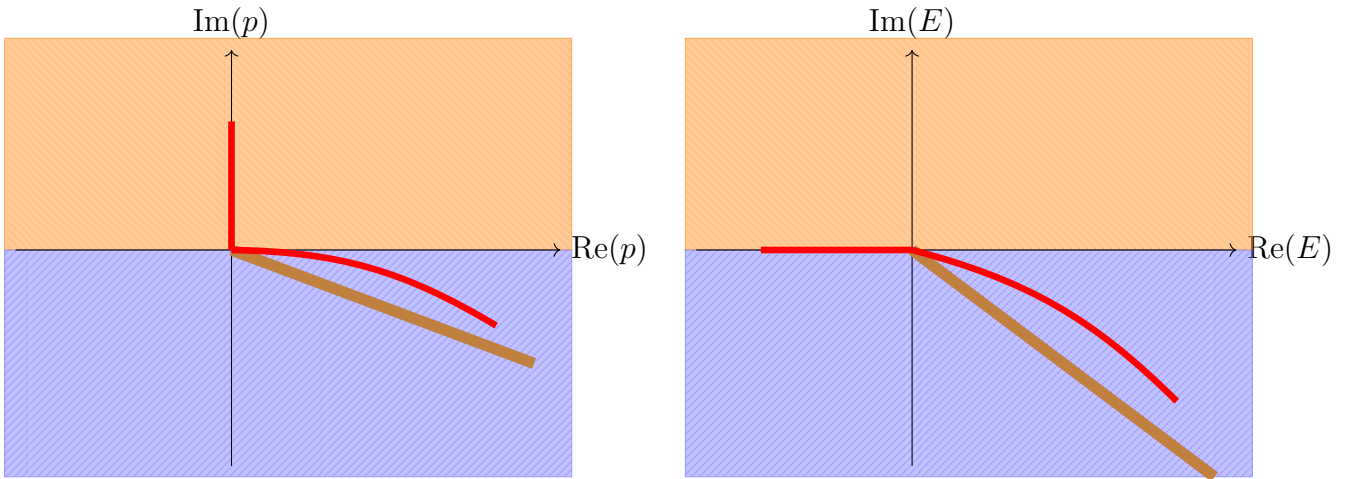
Figure 5.8.: The evolution of a bound state (red) into a resonance for an unbound two-body subsystem in the complex momentum and energy planes together with a rotated three-body cut/ integration contour (brown).

Bound two-body subsystem

In the following, the two-body subsystem is bound. This increases the complexity of the problem by introducing the two-body cut. Again, the procedure is to follow a bound state from the physical to the unphysical sheet as the two-body interaction strength is decreased. By decreasing the interaction strength the two-body binding energy decreases, too. So, also the two-body branch point moves closer to the origin. This can in general result in two situations: either the two-body branch point arrives at the origin before the three-body bound state or the two-body branch point is caught up by the three-body bound state. The first situation is trivial as the analytical continuation can be performed for an unbound subsystem. So, we will focus on the second situation.

Figure 5.9 shows the situation shortly before the three-body bound state (★) overtakes the two-body bound state (two-body branch point, ●). Note that the momentum plane considered is the one connected to the relative energy, $E - E_2$, where $2\mu E_2 = -\gamma_l^2$ is the energy of the two-body system.

As soon as the three-body bound state overtakes the two-body bound state, it moves from the physical sheet through the two-body cut to the unphysical sheet next to it. These complex energies in the third quadrant are now accessed by applying the contour rotation to the integration contour resulting in a rotation of the two-body as well as the three-body cut, too. The rotation angle is calculated relative to
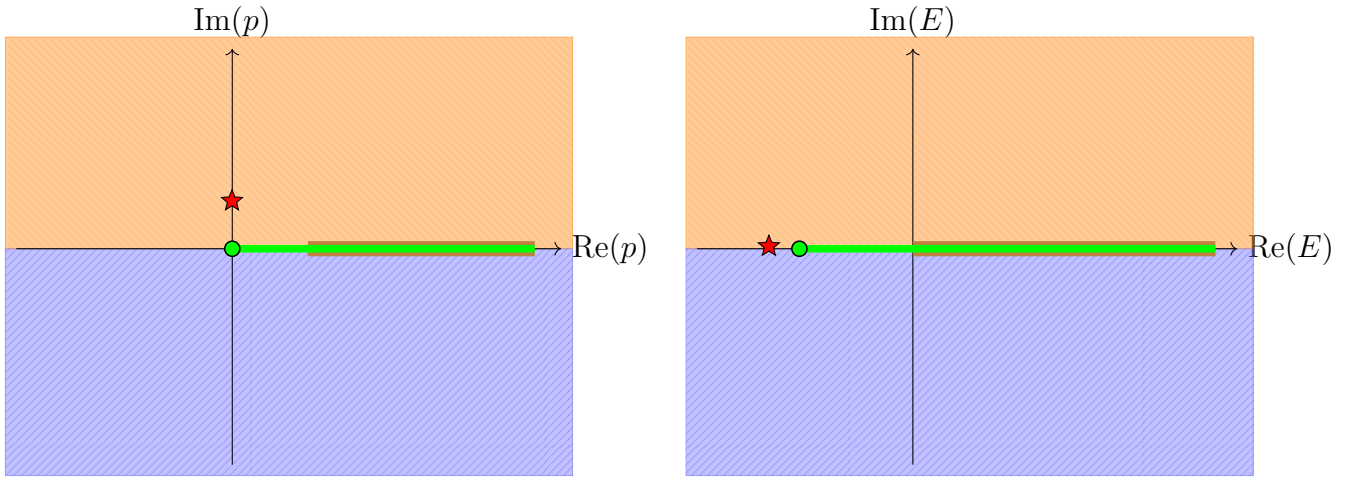
Figure 5.9.: A bound state (★) next to the two-body branch point (●) in the complex momentum and energy planes together with the two- (green line) and three-body cuts (brown line). The complex momentum plane is defined by the relative energy plane, $p = \sqrt{E - E_2}$. So, the two-body branch point in the complex momentum plane is located at the origin, while the three-body branch point is shifted towards positive energies.

the two-body branch point by

$$\tan\left(2\varphi\right) = -\frac{\operatorname{Im} E}{\operatorname{Re} E - E_2} > 0\,. \tag{5.35}$$

For practical calculations always an angle slightly larger than the limiting angle φ is chosen as the cut presents a finite width. Figure 5.10 sketches the situation right after the analytical continuation.

Still, the two-body cut and the contour of integration coincide. The three-body cut represents the border of this unphysical sheet. Crossing the cut another unphysical sheet is accessed. So, the angle connected to the three-body cut presents the upper limiting angle,

$$\tan\left(2\tilde{\varphi}\right) = -\frac{\operatorname{Im} E}{\operatorname{Re} E} > 0\,. \tag{5.36}$$

Following the trajectory further, the real part of the complex three-body energy may be overtaken by the two-body binding energy, again. The resulting pole in the relative energy plane is now located in the third quadrant resulting in

$$\tan\left(2\varphi - \frac{\pi}{2}\right) = \frac{\operatorname{Re} E - E_2}{\operatorname{Im} E} > 0\,. \tag{5.37}$$

As shown in Fig. 5.11 this restricts the possible range of angles even further.
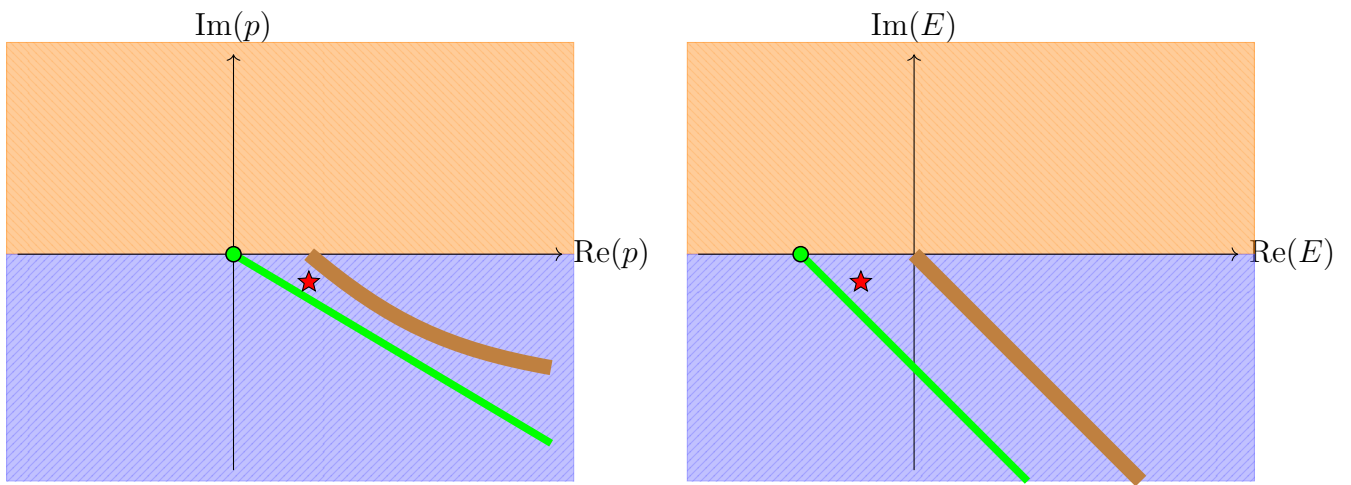
Figure 5.10.: Decreasing the two-body interaction strength relative to Fig. 5.9 the pole moves through the two-body cut becoming a resonance (★) on the unphysical 2-body sheet. The resonance is located between the two rotated cuts.
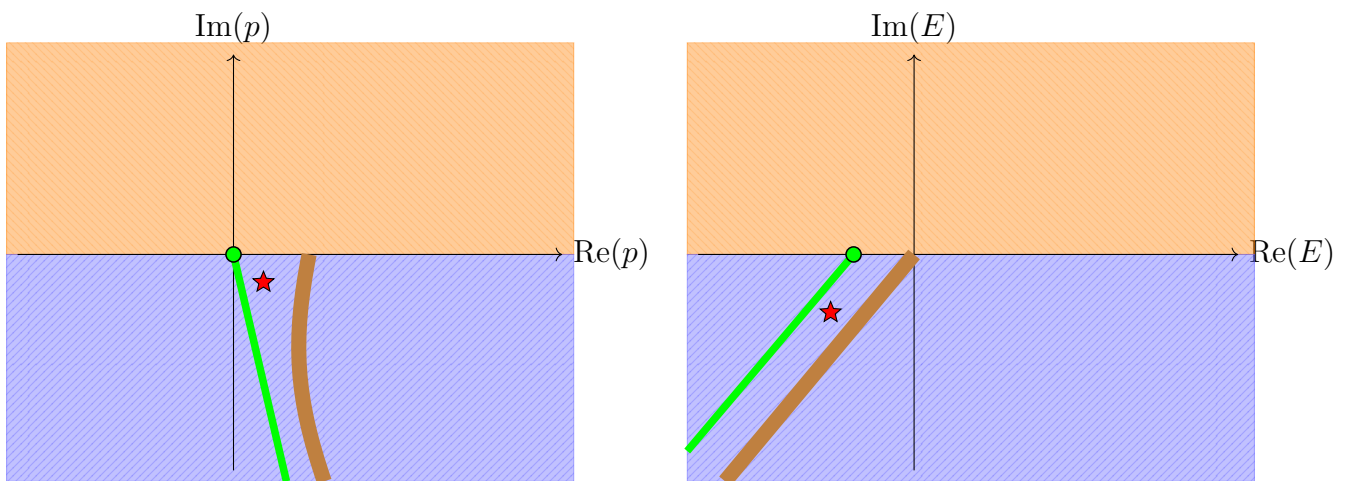
Figure 5.11.: Decreasing the interaction strength in Fig. 5.10 further it is possible that the two-body bound states "overtakes" the resonance. The resonance is now located in the third quadrant of the complex relative energy plane reducing the possible range of the rotation angle even further.

5.2.2.c. Implicit contour deformation

Within the last Section, the analytical continuation using a rotated contour was considered. This only presents one specific type of contours. Similar to the two-body system a contour close to the pole and the cuts can be used. It allows to treat the singularities explicitly, such that only an integration along the positive real axis remains.

Unbound two-body subsystem

First, an unbound two-body subsystem is considered [130]. Here, the dimer propagator can not become singular and we are only left with the branch cut resulting from the two-body interaction kernel. Figure 5.12 shows the two branch cuts defined by Eq. (5.29) for a fixed value of $p < \sqrt{2\mu E}$. The left-hand side of the figure presents the situation for an energy on the physical sheet right above the cut. Moving down the energy on the unphysical sheet also the cut move downwards. So, the contour of integration has to be transformed, too. The final situation is shown on the right-hand side of the figure. While the vertical paths cancel, we are left with the integration over the real axis ($C_{\mathbb{R}}$) and a contribution from the integral discontinuity along the cut (C_{disc}),

$$
\begin{aligned}
T_l\left(k,p;E\right) = Z_l\left(k,p;E\right) &+ \int_{C_{\mathbb{R}}} \mathrm{d}q \; q^2 Z_l\left(q,p;E\right) \tau_l(z) T_l\left(k,q;E\right) \\
&+ \int_{C_{\mathrm{disc}}} \mathrm{d}q \; q^2 \mathrm{disc}\, Z_l\left(q,p;E\right) \tau_l(z) T_l\left(k,q;E\right) \; .
\end{aligned}
\tag{5.38}
$$
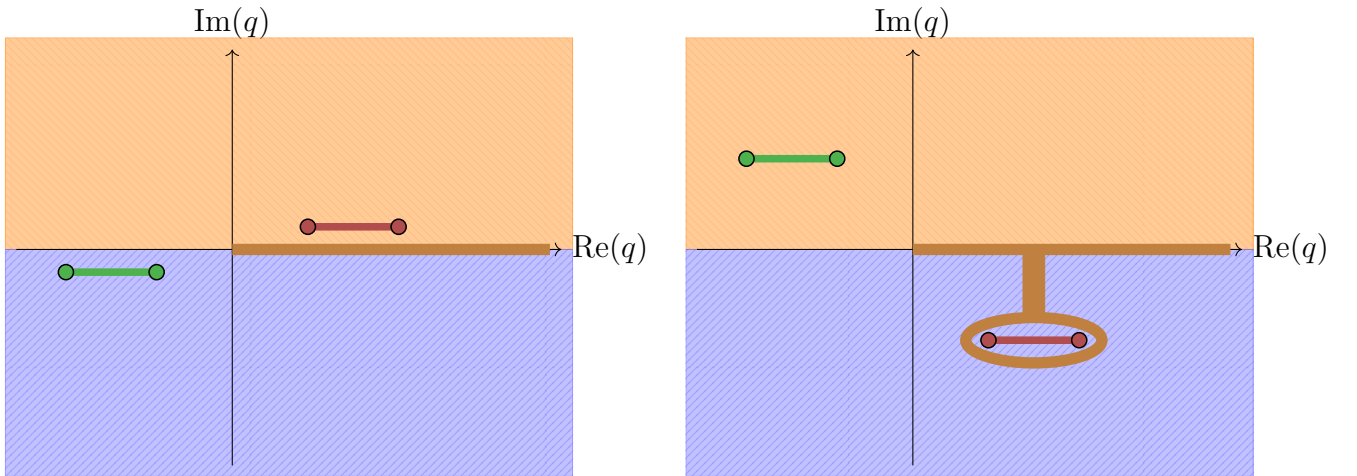
Figure 5.12.: The two branch cuts of the two-body interaction kernel Eq. (5.29) for a fixed value of $p < \sqrt{2\mu E}$ (green/ red lines) in the complex momentum plane of the integration variable q. The left-hand side of the figure shows the situation for an energy on the physical sheet with $\mathrm{Re}\, E > 0$. Moving the energy down onto the unphysical sheet the relevant branch cut moves downwards, too. So, the integration contour (brown line) is deformed as shown on the right-hand side of the figure. This results in an integration along the real axis and a contribution of the integral discontinuity along the branch cut.

The integral discontinuity of the two-body interaction kernel along the cut is defined by

$$
\begin{aligned}
\text{disc } Z_{2,l}\left(k,p;E\right) &= \int_{-1}^{+1} \mathrm{d}x \left[\frac{g\left(\pi_1\right)g\left(\pi_2\right)P_l(x)}{2\mu E - k^2 - p^2 - kp \cdot x + i\varepsilon} - \frac{g\left(\pi_1\right)g\left(\pi_2\right)P_l(x)}{2\mu E - k^2 - p^2 - kp \cdot x - i\varepsilon} \right] \\
&= \mathcal{P} \int_{-1}^{+1} \mathrm{d}x \left[\frac{g\left(\pi_1\right)g\left(\pi_2\right)P_l(x)}{2\mu E - k^2 - p^2 - kp \cdot x} - \frac{g\left(\pi_1\right)g\left(\pi_2\right)P_l(x)}{2\mu E - k^2 - p^2 - kp \cdot x} \right] \\
&\quad + 2i\pi \frac{1}{kp} g\left(\pi_1\right)g\left(\pi_2\right)P_l\left(\frac{2\mu E - k^2 - p^2}{kp} \right) \\
&= 2i\pi \frac{1}{kp} g\left(\pi_1\right)g\left(\pi_2\right)P_l\left(\frac{2\mu E - k^2 - p^2}{kp} \right).
\end{aligned}
\tag{5.39}
$$

Note that so far only the case $p < \sqrt{2\mu E}$ was considered. For larger momenta, the cuts cross the imaginary axis as shown in Fig. 5.13. Performing the analytical continuation the cut structure, as well as the integration contour, become very complicated. It is not possible anymore to represent the equation on the unphysical sheet by an integration over the real axis plus additional terms.
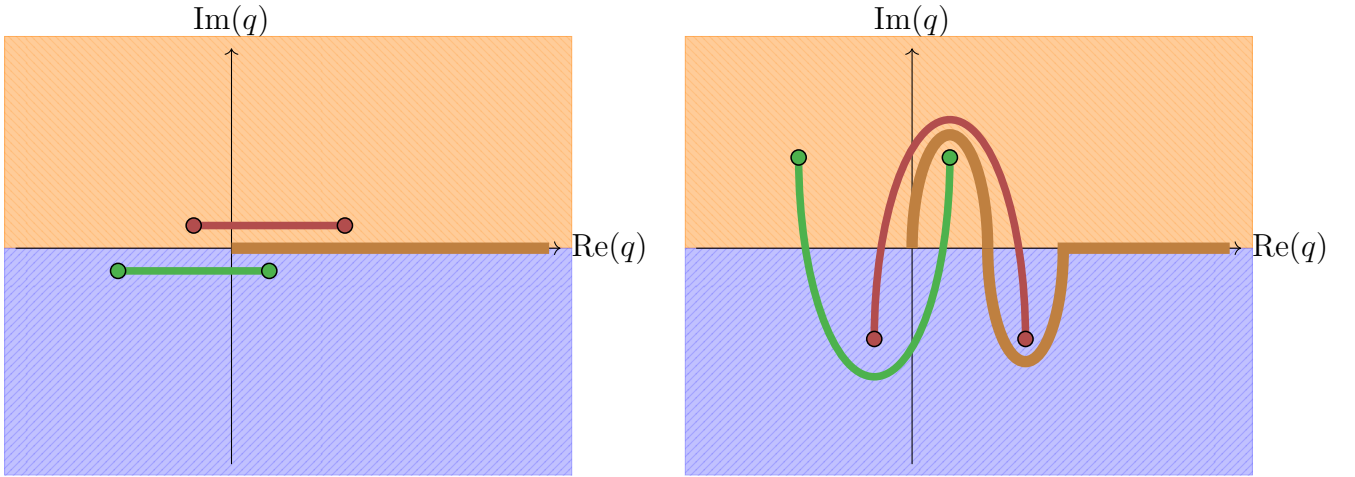
Figure 5.13.: A sketch analog to Fig. 5.12 for $p > \sqrt{2\mu E}$. The branch cuts cross the imaginary axis resulting in a very complicated branch cut structure after the analytical continuation as shown on the right-hand side of the figure.

Bound two-body subsystem

Now, we consider the in-principle more complicated analytical continuation through the two-body cut [44]. Beside the branch cuts originating from the two-body interaction kernel, we also have to consider the pole due to the dimer propagator at

$$
q_0 = \sqrt{\frac{4}{3}\left(2\mu E + \gamma_l^2\right)}.
\tag{5.40}
$$

We start right at the beginning with the case $p > \sqrt{2\mu E}$, which presented the more complicated branch cut structure in the unbound system. In opposite to energies with a positive real part, for a negative real part the cuts move not along the imaginary but along the real axis (cf. Fig. 5.14). So, the cuts never get
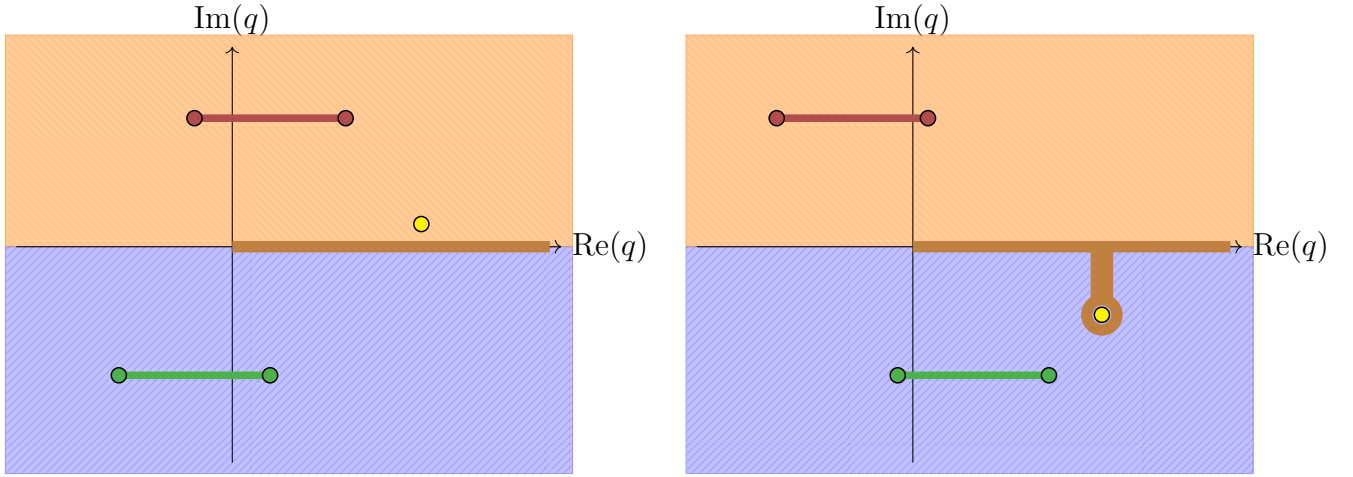
Figure 5.14.: A sketch similar to Fig. 5.12 for a bound two-body subsystem. Beside the branch cuts connected to the two-body interaction kernel, also the singularity of the dimer propagator (○) has to be considered. Here, the analytical continuation is performed through the two-body cut, i.e. $\mathrm{Re}\, E < 0$. While moving down the energy onto the unphysical sheet the branch cuts move mainly horizontally. So, they never get close to the integration contour and can be neglected while the analytical continuation. This results, analogous to the two-body system, in an integration contour along the real axis and a contribution from the residue of the dimer propagator.

close to the integration contour and can be neglected while the analytical continuation. Similar to the two-body system, we are only left with the residue of the dimer propagator,

$$
\begin{aligned}
T_l\left(k,p;E\right) = Z_l\left(k,p;E\right) + \int_{C_{\mathbb{R}}} \mathrm{d}q\ q^2 Z_l\left(q,p;E\right) \tau_l(z) T_l\left(k,q;E\right) \\
- 2\pi i q_0^2 N_{q_0} Z_l\left(q_0,p;E\right) T_l\left(k,q_0;E\right) \mathrm{Res}_{q_0}\, \tau_l(z)\, .
\end{aligned}
\tag{5.41}
$$

Similar to the two-body system, the T-matrix separates into the residue R and the singularity in the vicinity of the pole. Following similar steps as for two particles, the final equation reads

$$
\begin{aligned}
R_l\left(k,p;E\right) = \int_{C_{\mathbb{R}}} \mathrm{d}q\ q^2 \tau_l(z) R_l\left(k,q;E\right) \\
\times \left[Z_l\left(q,p;E\right) + \frac{2\pi i q_0^2 Z_l\left(q_0,p;E\right) Z_l\left(q,q_0;E\right) \mathrm{Res}_{q_0}\, \tau_l(z)}{1 - 2\pi i q_0^2 Z_l\left(q_0,q_0;E\right) \mathrm{Res}_{q_0}\, \tau_l(z)} \right].
\end{aligned}
\tag{5.42}
$$

5.3. Regulators & two-body T-matrices

Within the previous Sections, several equations were derived assuming general regulators. In the following, the regulators used within this work as well as the resulting equations on the physical and unphysical sheets are derived.

The quantity to consider is Eq. (4.25)

$$I_{\mathrm{i}}(z;q) = \int_0^\infty \mathrm{d}q \; q^2 \, \langle \zeta | q\mathrm{i} \rangle \, \langle g|q \rangle \, G_0(z;q) \, \langle q|g \rangle \, \langle q\mathrm{i}|\zeta \rangle \;. \tag{5.43}$$

It depends on the two-body regulator $|g\rangle$ as well as on the projector $|\zeta\rangle$. In the following a leading-order two-body S-wave potential is assumed. This results in $\langle \zeta|q\mathrm{i} \rangle = \langle q\mathrm{i}|\zeta \rangle = 1$ for i equaling the multi-index of the concrete interaction channel. An extension to higher orders and further partial waves is straightforward and results in additional powers of q within the integral kernel, e.g. a potential proportional to C_2' leads to a further factor of q^2.

This work uses a sharp cutoff (Heaviside regulator) and a smooth Gaussian regulator. Further, the Yamaguchi model is applied. It can be interpreted as a regulator, too. The procedure for every regulator is the following. First, the integral is solved for an energy $mz = mE + i\varepsilon = p^2 + i\varepsilon$ on the physical sheet. Together with the renormalized dimer propagator

$$\tau_{\mathrm{i}}(z) = \left[I_{\mathrm{i}} \left((i\gamma_{\mathrm{i}})^2 ; q \right) - I_{\mathrm{i}} \left(z; q \right) \right]^{-1} \tag{5.44}$$

the analytical continuation for energies on the unphysical sheets is discussed.

5.3.1. Heaviside regulator

First, a Heaviside regulator similar to the one applied within the Lagrangian formalism is investigated. It is defined by $\langle q|g \rangle := \Theta \left(\Lambda - q \right)$. The integral $I_{\mathrm{i}}(z;q)$ can be solved generally for an additional power $2n$ of q,

$$
\begin{aligned}
I_{\mathrm{i}}(z;q) &= \int_0^\infty \mathrm{d}q \; q^2 \, \langle g|q \rangle \, G_0(z;q) \, \langle q|g \rangle \, q^{2n} = \int_0^\Lambda \mathrm{d}q \; q^2 \, G_0(z;q) q^{2n} \\
&= \int_0^\Lambda \mathrm{d}q \; q^{2+2n} \frac{1}{mz - q^2} = \int_0^\Lambda \mathrm{d}q \; q^{2+2n} \frac{1}{p^2 - q^2 + i\varepsilon} \\
&= \frac{q^{3+2n}}{(3+2n)\,p^2} {}_2F_1 \left(1, \frac{2n+3}{2}, \frac{2n+5}{2}, \frac{q^2}{p^2} \right) \Bigg|_0^\Lambda ,
\end{aligned}
\tag{5.45}
$$

where ${}_2F_1$ is the Gaussian hypergeometric function. For $n = 0$ it simplifies to

$$I_{\mathrm{i}}(z;q) = -\Lambda + p \operatorname{arctanh} \left(\frac{\Lambda}{p} \right) \;. \tag{5.46}$$

So, for a Heaviside regulator, the renormalized dimer propagator on the physical sheet is given by

$$\tau_{\mathrm{i}}(z) = \left[i\gamma_{\mathrm{i}} \operatorname{arctanh} \left(-i\frac{\Lambda}{\gamma_{\mathrm{i}}} \right) - p \operatorname{arctanh} \left(\frac{\Lambda}{p} \right) \right]^{-1} \;. \tag{5.47}$$

It can be motivated that this structure is only valid on the physical sheet by using the property $\operatorname{arctanh}(z) = -\operatorname{arctanh}(-z)$. This shows that the given representation is independent of the sign of γ_{i} and p.

To figure out the correct analytical continuation all functional dependence on γ_{i} and p has to be dropped. This goal is reached in the limit $\Lambda \longrightarrow \infty$,

$$\tau_{\mathrm{i}}(z) = -\frac{2}{\pi} \left[-\gamma_{\mathrm{i}} - ip \right]^{-1} \;. \tag{5.48}$$

The expansion of the integral has to reproduce this behavior on the physical as well as on the unphysical sheet. So, the correct representation for both sheets is given by

$$
I_{\mathrm{i}}(z;q) + \Lambda =
\begin{cases}
p \operatorname{arctanh}\left(\frac{\Lambda}{p}\right) = -\frac{\pi}{2}\underbrace{\sqrt{-p^2}}_{+ip} + \frac{p^2}{\Lambda} + \mathcal{O}\left(\Lambda^{-3}\right) & \text{for } \operatorname{Im} p > 0, \\
p \operatorname{arctanh}\left(-\frac{\Lambda}{p}\right) = +\frac{\pi}{2}\underbrace{\sqrt{-p^2}}_{-ip} - \frac{p^2}{\Lambda} + \mathcal{O}\left(\Lambda^{-3}\right) & \text{for } \operatorname{Im} p < 0.
\end{cases}
\tag{5.49}
$$

Altogether the correct representation of the renormalized propagator is given by

$$
\tau_{\mathrm{i}}(z) = \left[i\gamma_{\mathrm{i}} \operatorname{arctanh}\left(-i\frac{\Lambda}{|\gamma_{\mathrm{i}}|}\right) - p \operatorname{arctanh}\left(\pm\frac{\Lambda}{p}\right) \right]^{-1},
\tag{5.50}
$$

where the upper (lower) sign represents a state with $\operatorname{Im} p > 0$ ($\operatorname{Im} p < 0$).

5.3.2. Gaussian regulator

The second regulator to consider is a Gaussian regulator,

$$
\langle q|g\rangle := \exp\left(-\frac{q^2}{\Lambda^2}\right).
\tag{5.51}
$$

Here, the integral becomes

$$
\begin{aligned}
I_{\mathrm{i}}(z;q) &= \int_0^\infty \mathrm{d}q\, q^2 \langle g|q\rangle\, G_0(z;q)\, \langle q|g\rangle = \int_0^\infty \mathrm{d}q\, q^2 G_0(z;q) \exp\left(-2\frac{q^2}{\Lambda^2}\right) \\
&= \int_0^\infty \mathrm{d}q\, q^2 \frac{\exp\left(-2\frac{q^2}{\Lambda^2}\right)}{mz - q^2} = \int_0^\infty \mathrm{d}q\, q^2 \frac{\exp\left(-2\frac{q^2}{\Lambda^2}\right)}{p^2 - q^2 + i\varepsilon} \\
&= -\frac{i\pi}{2p} p^2 \exp\left(-2\frac{p^2}{\Lambda^2}\right) - \mathcal{P} \int_0^\infty \mathrm{d}q\, q^2 \frac{\exp\left(-2\frac{q^2}{\Lambda^2}\right)}{q^2 - p^2} \\
&= -\sqrt{\frac{\pi}{2}}\frac{\Lambda}{2} - \frac{i\pi}{2} p \exp\left(-2\frac{p^2}{\Lambda^2}\right) \operatorname{erfc}\left(-i\frac{\sqrt{2}p}{\Lambda}\right),
\end{aligned}
\tag{5.52}
$$

where $\operatorname{erfc}(z)$ represents the complementary error function

$$
\operatorname{erfc}(z) = 1 - \operatorname{erf}(z) = \frac{2}{\sqrt{\pi}} \int_z^\infty \mathrm{d}t\, e^{-t^2}.
\tag{5.53}
$$

Following this result, the renormalized dimer propagator on the physical sheet for a Gaussian regulator is given by

$$
\tau_{\mathrm{i}}(z) = \left[\frac{\pi}{2}\gamma_{\mathrm{i}} \exp\left(2\frac{\gamma_{\mathrm{i}}^2}{\Lambda^2}\right) \operatorname{erfc}\left(\frac{\sqrt{2}\gamma_{\mathrm{i}}}{\Lambda}\right) + \frac{i\pi}{2} p \exp\left(-2\frac{p^2}{\Lambda^2}\right) \operatorname{erfc}\left(-i\frac{\sqrt{2}p}{\Lambda}\right) \right]^{-1}.
\tag{5.54}
$$

Following the definition of the error function $\operatorname{erf}(z) = -\operatorname{erf}(-z)$ it is independent of the sign of γ_{i} and p, too.

Similar to the Heaviside regulator the expansion in Λ^{-1} is used to find the correct analytical continuation,

$$\mathrm{erf}\left(\mp i \frac{\sqrt{2} p}{\Lambda}\right) = \mp 2i\sqrt{\frac{2}{\pi}} \frac{p}{\Lambda} + \mathcal{O}\left(\frac{1}{\Lambda^3}\right) = \mathcal{O}\left(\frac{1}{\Lambda}\right). \tag{5.55}$$

In comparison to the Heaviside regulator the correction is not at order $\mathcal{O}\left(\Lambda^0\right)$. So, it can not be determined by matching to the leading order term as for the Heaviside regulator. However, based on the correct analytical continuation of the integral for a Heaviside regulator

$$I_\mathrm{i}(z; q) \sim p \cdot \mathrm{arctanh}\left(\pm\frac{\Lambda}{p}\right)$$
$$= -\frac{\pi}{2} i p \pm \frac{p^2}{\Lambda} \pm \frac{1}{3}\frac{p^4}{\Lambda^3} + \mathcal{O}\left(\frac{1}{\Lambda^4}\right) \tag{5.56}$$

we can figure out the analytical continuation for the Gaussian regulator from the order $\mathcal{O}\left(\Lambda^{-1}\right)$

$$I_\mathrm{i}(z; q) = -\frac{\pi}{2} i p \exp\left(-2\frac{p^2}{\Lambda^2}\right) \mathrm{erfc}\left(\mp i\sqrt{2}\frac{p}{\Lambda}\right)$$
$$= -\frac{\pi}{2} i p \pm \sqrt{2\pi}\frac{p^2}{\Lambda} + i\pi\frac{p^3}{\Lambda^2} \mp \frac{4}{3}\sqrt{2\pi}\frac{p^4}{\Lambda^3} + \mathcal{O}\left(\frac{1}{\Lambda^4}\right), \tag{5.57}$$

where the upper (lower) sign represents a state with $\mathrm{Im}\,p > 0$ ($\mathrm{Im}\,p < 0$).

Altogether, the correct representation of the renormalized dimer propagator is given by

$$\tau_\mathrm{i}(z) = -\frac{2}{\pi}\left[-\gamma_\mathrm{i} \exp\left(2\frac{\gamma_\mathrm{i}^2}{\Lambda^2}\right) \mathrm{erfc}\left(\sqrt{2}\frac{|\gamma_\mathrm{i}|}{\Lambda}\right) - ip \exp\left(-2\frac{p^2}{\Lambda^2}\right) \mathrm{erfc}\left(\mp i\sqrt{2}\frac{p}{\Lambda}\right)\right]^{-1}. \tag{5.58}$$

5.3.3. Yamaguchi regulator

Finally, the Yamaguchi formfactor is considered,

$$\langle q|g\rangle := \frac{1}{q^2 + \beta^2}. \tag{5.59}$$

The structure of the Yamaguchi-type regulator function is special. It introduces the parameter β, which not only regulates the integral for high momenta, as Λ does, but also has an effect on "physical quantities" (cf. Section 10.3). Again, the integral can be solved for a general additional power of $2n$

$$I_\mathrm{i}(z; q) = \int_0^\infty \mathrm{d}q \, q^2 \, \langle g|q\rangle \, G_0(z; q) \, \langle q|g\rangle \, q^{2n} = \int_0^\infty \mathrm{d}q \, q^2 G_0(z; q) \left[q^2 + \beta^2\right]^{-2} q^{2n}$$
$$= \int_0^\infty \mathrm{d}q \, q^{2+2n} \frac{\left[q^2 + \beta^2\right]^{-2}}{mz - q^2} = \int_0^\infty \mathrm{d}q \, q^{2+2n} \frac{\left[q^2 + \beta^2\right]^{-2}}{p^2 - q^2 + i\varepsilon}$$
$$= \frac{q^{2n+1}}{2n+1}\frac{1}{\beta^2}\frac{1}{(p^2 + \beta^2)^2}\left[\beta^2 \, {}_2F_1\left(1, \frac{2n+1}{2}, \frac{2n+3}{2}, \frac{q^2}{p^2}\right)\right. \tag{5.60}$$
$$+ p^2 \, {}_2F_1\left(1, \frac{2n+1}{2}, \frac{2n+3}{2}, -\frac{q^2}{p^2}\right)$$
$$\left.- (p^2 + \beta^2) \, {}_2F_1\left(2, \frac{2n+1}{2}, \frac{2n+3}{2}, -\frac{q^2}{p^2}\right)\right]\Bigg|_0^\infty.$$

For $n = 0$ this result simplifies to

$$I_\text{i}(z; q) = \frac{\pi}{4\beta} \frac{1}{(p + i\beta)^2} \,. \tag{5.61}$$

In comparison to the other formfactors, the momentum p does not appear within any other function (e.g. $\text{arctanh}, \exp, \text{erfc}$). So, there is no analytical continuation needed and this representation of the integral can be used on all sheets.

5.4. Square root branch cuts

Within the previous Section, the different representations for the dimer propagator on the physical and unphysical sheet were derived by comparison to the fully expanded version Eq. (5.48). The final results depend only on the imaginary part of the momentum p. However, the correct representation of the momentum as a function of the energy has to be derived, too.

Within the Faddeev formalism, the relevant momentum is the momentum of the first pair of particles k. For a bound state on the physical sheet ($q \in \mathbb{R}^+$) it is given by

$$\begin{aligned} k = \sqrt{z} &= \sqrt{2\mu E - \frac{3}{4}q^2 + i\varepsilon} \\ &= i\sqrt{-2\mu E + \frac{3}{4}q^2 - i\varepsilon} \,. \end{aligned} \tag{5.62}$$

Both representations of the square root are equivalent and the $i\varepsilon$ term is explicitly needed to determine the correct branch. Performing the analytical continuation it has to be required that k is continuous, too. Note that for complex energies the $i\varepsilon$ is not necessary anymore and will be dropped.

5.4.1. Formalism by Glöckle

First, the formalism by Glöckle is considered. Here, the energies are located on the unphysical sheet, $\text{Im}\, E < 0$, while the momenta are given by the integration contour along the positive real axis, $q \in \mathbb{R}^+$. The formalism by Glöckle can only be applied to three-body systems with a bound subsystem. So, the pole trajectory crosses the two-body cut and the energy is located on the third quadrant of the complex energy plane, $\text{Re}\, E < 0, \text{Im}\, E < 0$. Simultaneously, the momentum k moves from the location $k \equiv i\kappa, \kappa > 0$ to the second (fourth) quadrant of the complex momentum plane for the second (first) representation of Eq. (5.62). So, the second representation results in a continuous pole trajectory and has to be applied for this case, while the first does not. Following the pole trajectory the energy can move to the fourth quadrant, $\text{Re}\, E > 0, \text{Im}\, E < 0$. Applying the same argument as before, it can be concluded that again the second representation results in a continuous trajectory.

5.4.2. Formalism by Afnan

Further, the method by Afnan can be applied. Here, the two cases of a bound and unbound two-body subsystem have to be considered. Furthermore, in addition to a complex energy, the integration contour becomes complex ($q \in \mathbb{C}$), too.
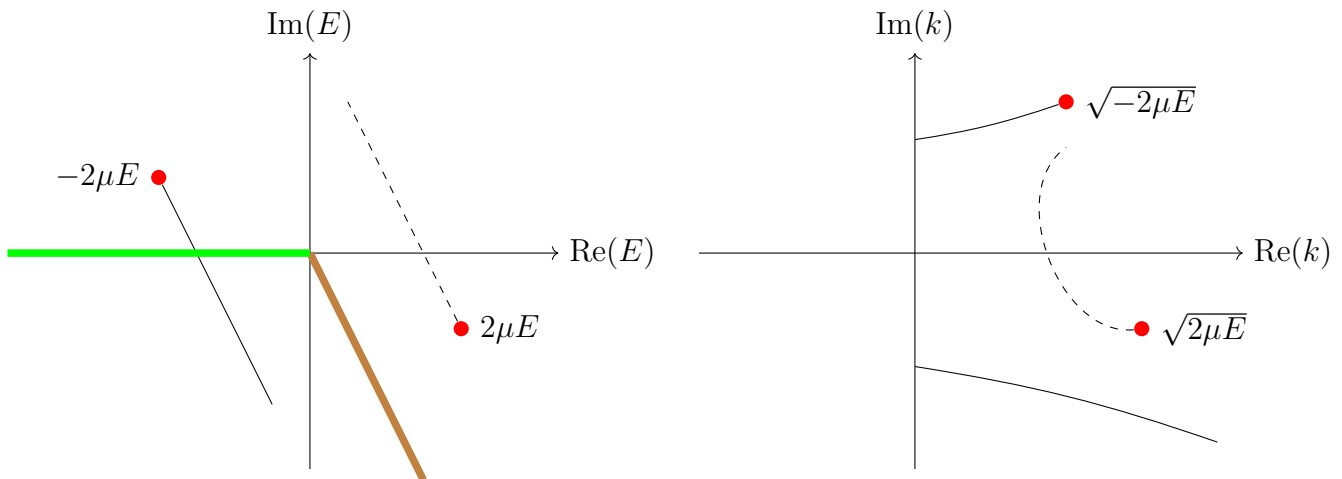
Figure 5.15.: Both representations of Eq. (5.62) shown in the complex momentum and energy plane. The momenta are chosen along the contour of integration indicated by the brown line. The complex energy plane shows the square root branch cut along the negative real axis. The trajectory starting at $-2\mu E$ crosses the square root branch cut resulting in a discontinuity, which becomes visible in the complex momentum plane. The trajectory starting at $2\mu E$ is continuous and should be applied for practical calculations.

5.4.2.a. Unbound two-body subsystem

First, the simpler case of an unbound subsystem is investigated. So, there is only the three-body cut left and an analytical continuation results in a state on the fourth quadrant of the complex energy plane. The limiting rotation angle is determined by Eq. (5.36). Choosing this angle the arguments of Eq. (5.62) would cross the origin. However, for practical calculations the angle is chosen slightly larger. The corresponding situation for both representations of Eq. (5.62) is shown in Fig. 5.15 in the complex momentum and energy planes. For momenta along the contour of integration, the first representation of Eq. (5.62) crosses the real axis at positive values resulting in a continuous trajectory. In comparison, the second representation crosses the square-root branch cut at negative real energies, which results in a discontinuity.

Following the pole trajectory on the unphysical sheet, the energy may move onto the third quadrant of the complex energy plane. Applying the same argumentation as before, it can be shown that again the first representation has to be applied as it does not cross the square root branch cut.

5.4.2.b. Bound two-body subsystem

A more complicated situation occurs if the two-body subsystem is bound. Here, not only the three-body but also the two-body cut contributes. This case will be investigated in the following. Note that due to the two-body bound state the rotation angle is determined by Eq. (5.35). It depends on the two-body binding energy, which results in further cases to consider.

Similar to the formalism by Glöckle, we follow the pole trajectory from the physical sheet to an energy on the unphysical sheet on the third quadrant of the complex energy plane. Usually, this energy is located on the fourth quadrant of the relative energy plane. This restricts the rotation angle to $\varphi < \pi/4$. Again, an investigation similar to the unbound subsystem can be performed. It shows that the first representation would cross the square-root branch cut, while the second does not.

There is the possibility that the energy moves to the third quadrant of the relative energy plane. These energies accessed by angles in the range $\pi/4 < \varphi < \pi/2$, which are determined by Eq. (5.37). If the limiting angles are applied the first (second) representation crosses the real axis at $E_2 < 0$ $(-E_2 > 0)$, respectively. So, the first representation would cross the square root branch cut. However, due to numerical reasons, the angles are chosen slightly larger than the limiting angle, which results in the shift $\delta(\varphi)$,

- $k = \sqrt{2\mu E - \frac{3}{4}q^2} \longrightarrow \operatorname{Im} E = 0 \Leftrightarrow \operatorname{Re} E = E_2 + \delta(\varphi)$,

- $k = i\sqrt{-2\mu E + \frac{3}{4}q^2} \longrightarrow \operatorname{Im} E = 0 \Leftrightarrow \operatorname{Re} E = -E_2 - \delta(\varphi)$.

Here, it is not possible to make a general statement. The correct representation has to be chosen dependent on the rotation angle φ.

5.5. Numerical procedure

So far, it was described how to derive the scattering equations for the T-matrix for two- and three-body systems on the physical as well as unphysical sheets. As was shown in Chapter 2 physical states can be connected to poles of the S-matrix, or equivalently the T-matrix. So, the question arises of how to determine these poles.

In general, the most straightforward way is to solve the scattering equation for the T-matrix and investigate its value in the complex energy plane. However, there is a numerically much faster and simpler formalism. The Lippmann-Schwinger, as well as the Faddeev equation, are mathematically given by a so-called Fredholm equation of the second kind. On the physical sheet, the kernel is Hermitian and it can be shown (e.g. Ref. [88]) that the T-matrix can be expanded in a basis given by the solutions of the homogeneous Lippmann-Schwinger and Faddeev equations, respectively. The coefficients of the expansion are proportional to

$$\frac{1}{1 - \lambda_n}, \tag{5.63}$$

with the eigenvalues of the homogeneous equation λ_n.

This expansion was extended to non-Hermitian kernels by Afnan [88]. So, to find poles on the unphysical sheet one has to search for eigenvalues equal to one of the homogeneous scattering equations along the rotated contour. The first step of the procedure is now similar to the search for a bound state on the physical sheet. The kernel is expanded in a momentum space basis derived by a Gauss-Legendre mesh. Now, these momenta are substituted by the rotated momenta. Here, also the weight in the integral has to be transformed correctly. Following the expansion, the next step would be to search for eigenvalues equal to one as a function of the complex energy. However, mathematically equivalent but numerically easier and faster is the search for zeros of the characteristic polynomial for eigenvalues equal to 1. In comparison to the search for a bound-state pole, this corresponds to two-dimensional root

finding. Mathematically, this is much more advanced and it cannot be guaranteed that the corresponding numerical routines will find all poles. So, before applying the root-finding routines it is recommended to plot the absolute value of the characteristic polynomial as a function of the complex energy. This plot largely depends on the numerical parameters used within the derivation of the kernel matrix. The only physically relevant part are the zeros, which are used as starting values for the root-finding routines.

Analytical Continuation

6 Two-body systems

In the end, we want to search for states on the unphysical sheets in three-body systems making use of different techniques. As preparation, we test these techniques at different two-body systems. Two-body systems posses the simplest sheet structure possible, a physical and an unphysical sheet. So, they are perfectly suited for this purpose. All methods presented in the following are based on the momentum-space Lippmann-Schwinger equation.

Within this Chapter different toy potentials created to show bound states, virtual states, and resonances are investigated. All toy potentials are designed in coordinate space and Fourier-transformed to momentum space. We start with the simplest type of potential possible, an attractive Gaussian presenting bound and virtual states. In a second step, the attractive Gaussian is combined with a repulsive Gaussian wall. This potential additionally exhibits resonances. The pole structure of both potentials is investigated by calculating the phase shifts and time delays, applying the ACCC and the analytical continuation. By comparing these results the advantages and shortcomings of the different methods become evident. We will show that the most stable and clearest definition of the pole structure is only possible using the analytical continuation.

6.1. Attractive Gaussian

The first toy potential investigated is a spherically-symmetric, attractive Gaussian,

$$V_{\mathrm{B}}(r)\delta^{(3)}\left(\boldsymbol{r}'-\boldsymbol{r}\right) := \left\langle\boldsymbol{r}'\middle|V_{\mathrm{B}}\middle|\boldsymbol{r}\right\rangle = V_0 e^{-\alpha_0 r^2}\delta^{(3)}\left(\boldsymbol{r}'-\boldsymbol{r}\right), \quad \text{where} \quad r := |\boldsymbol{r}|. \tag{6.1}$$

It only depends on the relative distance r between both particles. Figure 6.1 shows a sketch of this potential for the parameters

$$\begin{aligned} V_0 &= -200\,\mathrm{MeV}\,, \\ \alpha_0 &= 1\,\mathrm{fm}^{-2}\,. \end{aligned} \tag{6.2}$$

For this set of parameters, the potential presents a bound state at $E = -14.725\,\mathrm{MeV}$. Applying the Fourier transform, the S-wave projected momentum-space representation of our toy potential Eq. (6.1) is given by

$$V_{\mathrm{B}}(k,k') := \left\langle k'\underbrace{00}_{l'm'}\middle|V_{\mathrm{B}}\middle|k\underbrace{00}_{lm}\right\rangle = \frac{1}{2kk'\sqrt{\pi\alpha_0}}V_0\left(e^{-\frac{1}{4\alpha_0}k_-^2} - e^{-\frac{1}{4\alpha_0}k_+^2}\right), \tag{6.3}$$
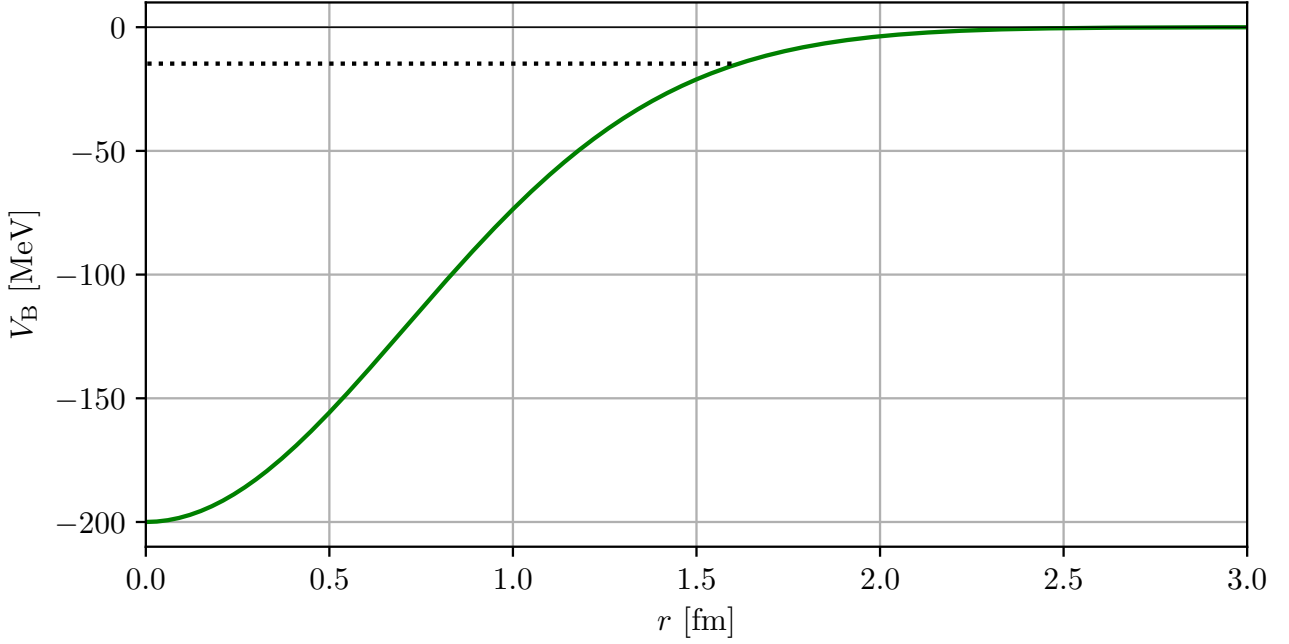
Figure 6.1.: The attractive Gaussian potential in coordinate space described by Eq. (6.1). The parameters are given by $V_0 = -200\,\text{MeV}$ and $\alpha_0 = 1\,\text{fm}^{-2}$. The potential shows a bound state at $E = -14.725\,\text{MeV}$ indicated by the dotted line.

where $k_\pm = k \pm k'$. Note that this potential is not only a toy potential. Deriving the leading order pionless EFT S-wave potential for two nucleons coupling to a spin-singlet results in

$$\langle k'00|V_{0,s}|k00\rangle = \frac{\Lambda}{2\pi m k k'} C_{0,s}^\Lambda \left(e^{-\frac{k_-^2}{\Lambda^2}} - e^{-\frac{k_+^2}{\Lambda^2}} \right) , \tag{6.4}$$

where Λ is a regulator parameter and $C_{0,s}^\Lambda$ is the regulator-dependent low-energy coupling. In practice, the toy potential can be interpreted as an EFT potential if we identify the width of the Gaussian α_0 with the regulator parameter Λ. This potential can be used to investigate for example the dineutron system [62].

In the following, we want to investigate pole trajectories as a function of the potential parameters. For a fixed width α_0 the existence of bound and virtual states depends only on the value of V_0. Decreasing the absolute value of V_0 the bound state moves further to the threshold, finally becoming a virtual state. As will be shown later, the transition takes place at $V_0 := V_0^{\text{bp}} = -111.232\,\text{MeV}$. The pole trajectory in the momentum as well as energy plane is sketched in Fig. 6.2. We will present three methods to extract the energies of the bound and virtual states; phase shifts, ACCC, and analytical continuation. The calculations are performed for fixed $\alpha_0 = 1\,\text{fm}^{-2}$ for V_0 in the range $-200\,\text{MeV}$ to $-80\,\text{MeV}$.
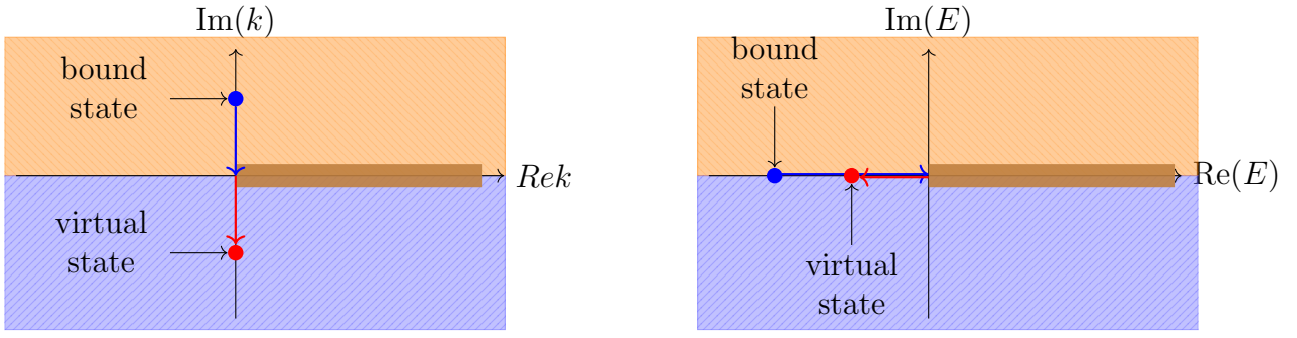
Figure 6.2.: The pole trajectory of the attractive Gaussian potential Eq. (6.3) in the complex momentum (left) and energy plane (right). Decreasing the interaction strength V_0 the bound state moves towards the branch point at the origin becoming a virtual state.

6.1.1. Phase shifts & time delays

The first and simplest method is the calculation of the phase shifts by solving the partial-wave projected Lippmann-Schwinger equation Eq. (B.4) for the on-shell T-matrix elements. The technical details of the numerical solution are presented in Appendix E.1. The phase shift is connected to the on-shell T-matrix by Eq. (2.16),

$$
\begin{aligned}
f(p, \theta) &= -4\pi^2 \mu \langle \boldsymbol{p}|T(E_p + i0)|\boldsymbol{p}\rangle \\
&= -4\pi^2 \mu \sum_{l,m} \langle plm|T(E_p + i0)|plm\rangle Y_{lm}(\Omega_p) Y_{lm}^*(\Omega_p) \\
&= 4\pi \sum_{l,m} f_l(p) Y_{lm}(\Omega_p) Y_{lm}^*(\Omega_p) ,
\end{aligned}
\tag{6.5}
$$

where for the last equality Eq. (2.20) was applied. Altogether the phase shift is given by

$$
p^{2l+1} \cot \delta_l - ip = -\frac{1}{\pi\mu} \frac{1}{T_l(p, p; E_p)} .
\tag{6.6}
$$

Figure 6.3 shows the phase shifts for eight different interaction strength in the range $V_0 = -200\,\text{MeV}$ to $-80\,\text{MeV}$. The first five phase shifts exhibit a bound state. Following Levinson's theorem Eq. (2.25), this becomes visible by a phase shift starting at $\text{Re}\,\delta = 180°$ for $k = 0\,\text{fm}^{-1}$. Decreasing the interaction strength V_0 the slope for small momenta increases up to the point the bound state pole moves from the physical to the unphysical sheet becoming a virtual state. At this point the phase shift flips from $\text{Re}\,\delta = 180°$ to $\text{Re}\,\delta = 0°$ at $k = 0\,\text{fm}^{-1}$. Decreasing V_0 further the slope for small momenta starts to decrease. In the limit V_0 going to zero, the phase shift is constantly zero as there is no interaction left.

Based on the phase shifts the time delays can be calculated. Interpolating the phase shift data and calculating their derivative the (Wigner-Smith) time delay τ_{WS} (cf. Eq. (2.47)) is presented in Fig. 6.4. The attractive Gaussian considered presents almost no structures in the phase shifts. For a bound state the phase shift monotonically decreases from $\text{Re}\,\delta = 180°$ at $k = 0\,\text{fm}^{-1}$ to $\text{Re}\,\delta = 0°$ at $k \longrightarrow \infty\,\text{fm}^{-1}$. The purely negative time delay behaves symmetrically: it increases monotonically until it reaches the zero. The bound state time delays for different V_0 mainly differ in their behavior for small k. At $k = 0\,\text{fm}^{-1}$ the value of τ_{WS} increases for poles closer to the transition point V_0^{bp}. For the transition $V_0 = V_0^{\text{bp}} - \varepsilon$ to $V_0 = V_0^{\text{bp}} + \varepsilon$, $\varepsilon \longrightarrow 0$, the time delay flips from $-\infty$ to $+\infty$. Considering the virtual state poles, the peak
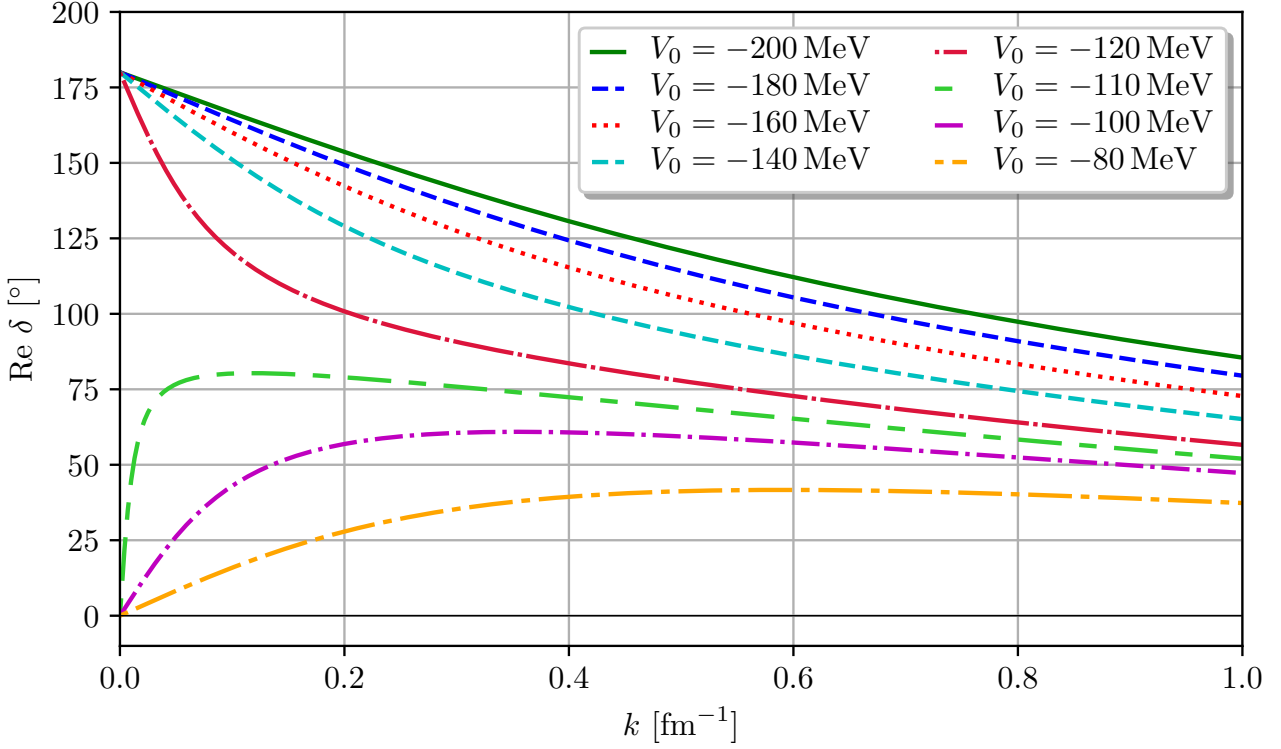
Figure 6.3.: The phase shifts for the attractive Gaussian potential Eq. (6.3) for eight different interaction strength V_0 and $\alpha_0 = 1\,\mathrm{fm}^{-2}$. From top to bottom the interaction strength decreases from $V_0 = -200\,\mathrm{MeV}$ to $V_0 = -80\,\mathrm{MeV}$. The upper five trajectories correspond to a bound state. Following Levinson's theorem they start at $\mathrm{Re}\,\delta = 180°$ for $k = 0\,\mathrm{fm}^{-1}$. The lower three trajectories correspond to a virtual state. At $V_0^{\mathrm{bp}} = -111.232\,\mathrm{MeV}$ the bound state pole moves from the physical to the unphysical sheet becoming a virtual state. Simultaneously, the phase shift flips from $\mathrm{Re}\,\delta = 180°$ to $\mathrm{Re}\,\delta = 0°$ at $k = 0\,\mathrm{fm}^{-1}$. This flip results in a high slope for small momenta for V_0 close to the transition point.

of the time delay at $k = 0\,\mathrm{fm}^{-1}$ is located at positive values and decreases for values of V_0 further away from V_0^{bp}. At some k the time delay moves from the positive to the negative half-plane going smoothly to zero in the limit $k \longrightarrow \infty$.

Finally, the bound and virtual-state energies are determined from the phase shifts. Therefore the phase shifts are fitted by the S-wave effective range expansion Eq. (2.27)

$$k \cot \delta_0(k) = -\frac{1}{a_0} + \frac{1}{2} r_0 k^2 + \mathcal{O}\left(k^4\right) . \qquad (6.7)$$

The bound- and virtual-state energy is connected to the scattering length a_0 and effective range r_0 by

$$E = -\frac{1}{2\mu} \frac{2}{r_0^2} \left[1 - \frac{r_0}{a_0} - \sqrt{1 - 2\frac{r_0}{a_0}} \right] . \qquad (6.8)$$

Table 6.1 shows the results of the fits as well as the energies of the bound and virtual states for different V_0 along the trajectory.
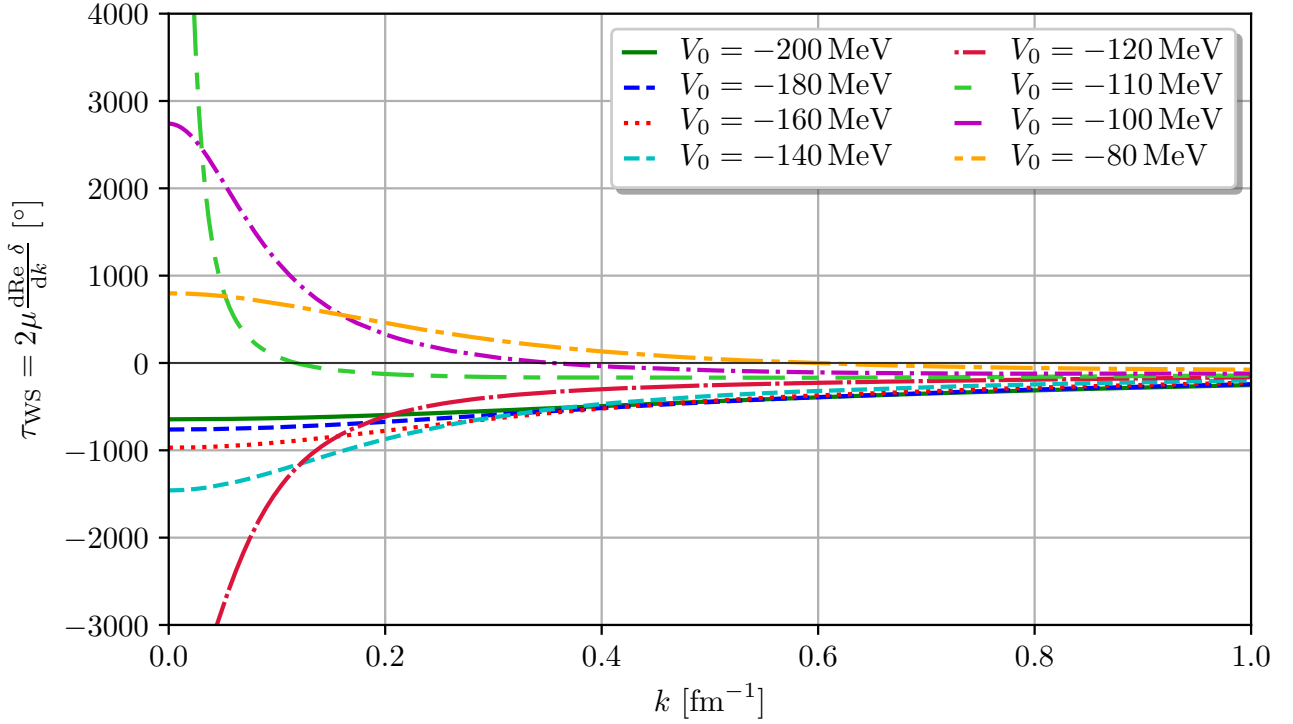
Figure 6.4.: The time delays for the attractive Gaussian toy potential Eq. (6.3) derived from the phase shifts shown in Fig. 6.3. The first five curves corresponding to a bound state show a purely negative time delay. They differ mainly in the behavior for small k. Poles close to threshold show a larger time delay at the origin. The three curves connected to the virtual states show a positive time delay for small momenta and a negative time delay for larger k.

V_0 [MeV]	a_0 [fm]	r_0 [fm]	Re E [MeV]	Im E [MeV]
-200.0	2.363	0.991	-15.126	0.0
-180.0	2.791	1.063	-9.604	0.0
-160.0	3.553	1.146	-5.156	0.0
-140.0	5.345	1.246	-1.937	0.0
-120.0	15.214	1.373	-0.197	0.0
-110.0	-101.634	1.451	-0.004	0.0
-100.0	-10.061	1.544	-0.357	0.0
-80.0	-2.926	1.793	-3.119	0.0

Table 6.1.: The pole trajectory for the attractive Gaussian potential Eq. (6.3) for V_0 in the range –200 MeV to –80 MeV derived from a fit of the effective range expansion Eq. (6.7) to the phase shifts. The table shows, for a given V_0, the scattering length a_0, the effective range r_0 as well as the energy calculated from Eq. (6.8). The color-coding is chosen equivalently to Fig. 6.2. Orange rows indicate states on the physical sheet (bound states), while blue rows represent states on the unphysical sheet (virtual states).

6.1.2. ACCC

While the phase shifts only indicate effects from the regions of the unphysical sheets close to the branch cuts to the physical sheets, the ACCC allows to find poles further away from the physical sheet. Therefore the pole trajectory on the physical sheet is fitted by a Padé approximation. The fit is based on 18 bound state poles for V_0 in the range $-200\,\text{MeV}$ to $-115\,\text{MeV}$ as well as the three values $V_0 = -114, -113$ and $-112\,\text{MeV}$. The binding energies are determined by searching for poles of the T-matrix Lippmann-Schwinger equation. Table 6.2 shows the results for data on the physical as well as on the unphysical sheet for different orders of the Padé approximation. A graphical representation of the pole trajectories in comparison to the results derived by the analytical continuation in the following Section can be found in Fig. 6.5.
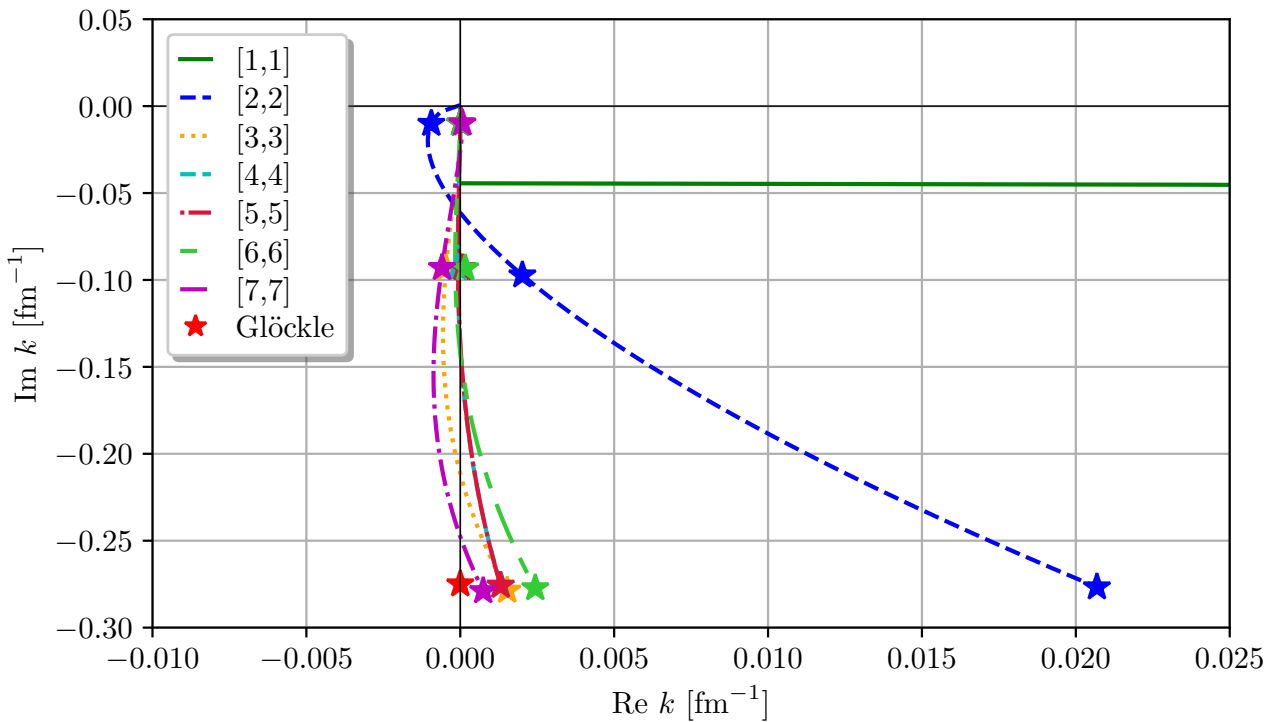
Figure 6.5.: The ACCC method applied to the attractive Gaussian potential in comparison to the results derived from the analytical continuation applying the formalism by Glöckle. The first seven equal-order Padé approximations are shown. Along the Padé approximations stars indicate the values the calculation by Glöckle (★) can be compared to. While the first order [1,1] fails to reproduce the pole trajectory, the higher-order approximations reproduce the imaginary part of the momentum very well. The second-order approximation leads to a large over-estimation of the real part of the momentum. For the higher orders, the difference in the real part of the momentum to the correct result, $\text{Re}\,k = 0\,\text{fm}^{-1}$, depends on the value of V_0.

	V_0 [MeV]	-200.0	-180.0	-160.0	-140.0	-120.0	-110.0	-100.0	-80.0
Input	Re E [MeV]	-14.725	-9.444	-5.109	-1.928	-0.196			
[1,1]	Re E [MeV]	-15.285	-9.219	-4.929	-2.014	-0.269	-0.025	0.392	1.027
	Im E [MeV]	0.0	0.0	0.0	0.0	0.0	0.153	0.622	1.493
[2,2]	Re E [MeV]	-14.723	-9.446	-5.109	-1.928	-0.197	-0.004	-0.392	-3.155
	Im E [MeV]	0.0	0.0	0.0	0.0	0.0	-0.001	-0.016	0.474
[3,3]	Re E [MeV]	-14.725	-9.444	-5.109	-1.928	-0.196	-0.004	-0.359	-3.217
	Im E [MeV]	0.0	0.0	0.0	0.0	0.0	0.0	-0.004	0.035
[4,4]	Re E [MeV]	-14.725	-9.444	-5.109	-1.928	-0.196	-0.004	-0.359	-3.152
	Im E [MeV]	0.0	0.0	0.0	0.0	0.0	0.0	-0.001	0.030
[5,5]	Re E [MeV]	-14.725	-9.444	-5.109	-1.928	-0.196	-0.004	-0.356	-3.204
	Im E [MeV]	0.0	0.0	0.0	0.0	0.0	0.0	-0.002	0.023
[6,6]	Re E [MeV]	-14.725	-9.444	-5.109	-1.928	-0.196	-0.004	-0.357	-3.231
	Im E [MeV]	0.0	0.0	0.0	0.0	0.0	0.0	-0.005	0.001
[7,7]	Re E [MeV]	-14.725	-9.444	-5.109	-1.928	-0.196	-0.004	-0.359	-3.225
	Im E [MeV]	0.0	0.0	0.0	0.0	0.0	0.0	-0.005	0.024

Table 6.2.: The first seven equal-order Padé approximations for the attractive Gaussian toy potential Eq. (6.3). For comparison a set of bound state data used as input for the fits is shown. These data are reproduced latest by the third-order approximation. Regarding the poles on the unphysical sheet, the results show that the closer they are to physical sheet, the lower the order of the Padé approximation has to be to produce converged results. While the pole at $V_0 = -110.0$ MeV is already reproduced by the second order, the poles at $V_0 = -100.0$ MeV and $V_0 = -80.0$ MeV are almost converged for the third-order approximation.

6.1.3. Analytical continuation

Finally, an analytical continuation to the unphysical sheet to search for the virtual-state poles directly is performed. Here, only the formalism by Glöckle (cf. Section 5.2.1.b) could be applied. A contour rotation following the method by Afnan would result in a diverging potential for $\varphi > \pi/4$ due to the exponential functions,

$$
\exp\left[-\frac{k_\pm^2}{4\alpha_0}\right] \xrightarrow{\text{Afnan}} \exp\left[-\frac{k_\pm^2}{4\alpha_0}e^{-i2\varphi}\right]
$$
$$
= \exp\left[-\frac{k_\pm^2}{4\alpha_0}\underbrace{\cos\left(2\varphi\right)}_{<0 \text{ for } \varphi>\pi/4}\right]\exp\left[i\frac{k_\pm^2}{4\alpha_0}\sin\left(2\varphi\right)\right] \xrightarrow{k_\pm\to\infty} \infty. \tag{6.9}
$$

The procedure is the following. First, we calculate contour plots of the absolute value of the determinant of the identity matrix minus the kernel of Eq. (B.4) for poles on the physical sheet and of Eq. (5.21) for poles on the unphysical sheet, respectively. These contour plots are shown in Fig. 6.6. Following Eq. (5.21) a zero within these contour plots correspond to a pole, either a bound or a virtual state.

Table 6.3 shows energies along the pole trajectory for V_0 in the range -200 MeV to -80 MeV. At $V_0^{\text{bp}} = -111.232$ MeV the bound state pole moves through the branch point at the origin becoming a virtual state.

V_0 [MeV]	Re E [MeV]	Im E [MeV]
-200.0	-14.725	0.0
-180.0	-9.444	0.0
-160.0	-5.109	0.0
-140.0	-1.928	0.0
-120.0	-0.196	0.0
-110.0	-0.004	-1.082×10^{-9}
-100.0	-0.358	-6.073×10^{-9}
-80.0	-3.133	-7.203×10^{-10}

Table 6.3.: The pole trajectory for the attractive Gaussian potential Eq. (6.3) for V_0 in the range -200 MeV to -80 MeV. On the unphysical sheet the calculation was performed using the formalism by Glöckle.
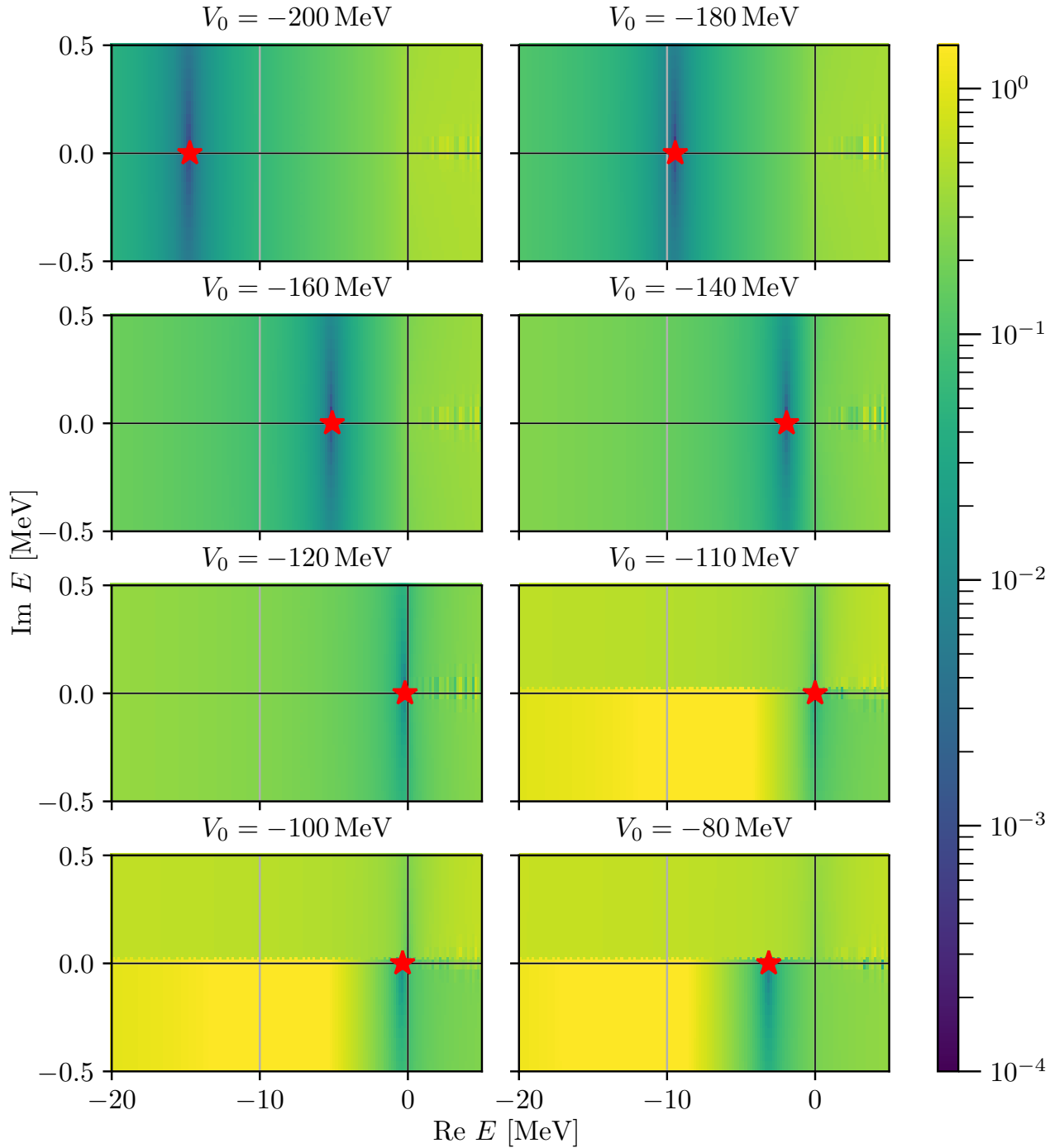
Figure 6.6.: Contour plots of $|\det \mathbb{1} - K|$, where K is the kernel of the Lippmann-Schwinger equation Eq. (B.4) for poles on the physical sheet or the kernel of the analytically-continued Lippmann-Schwinger equation Eq. (5.21) for poles on the unphysical sheet, respectively. The contour plots are calculated in the complex energy plane for different V_0 indicated above the plots. Following Eq. (5.21), a zero within these plots corresponds to a pole of the Lippmann-Schwinger equation. These zeros are indicated by a red star ($\star$). Following the plots from the top left to the bottom right, the pole trajectory starts at a bound state at $E = -14.725$ MeV. It moves towards the branch point at the origin when decreasing V_0. For $V_0 = V_0^{\text{bp}} = -111.232$ MeV it crosses the cut at the branch point. Decreasing V_0 further, the pole becomes a virtual state following the negative real axis to $E = -3.133$ MeV for $V_0 = -80$ MeV in the bottom right plot.

6.1.4. Comparison

Within the previous Sections three methods to derive the pole trajectory on the physical and unphysical sheet were applied; phase shifts, ACCC (only unphysical sheet), and the analytical continuation. The results of all three methods are presented in Table 6.4. Altogether, all three methods present very well agreeing results. The energies on the physical sheet can only be compared between the phase-shift calculation and the search for poles of the T-matrix ("analytical continuation"). Taking the latter as a benchmark, the energies of the phase shift calculation agree the better the closer they are to the branch point. A similar result can be found on the unphysical sheet. Here, also the results of the ACCC can be compared to. For simplicity, assuming that the Padé approximation $E^{[N,N]}$ converges in the limit $N \to \infty$, the highest order calculated is taken for comparison. Using the analytical continuation as a reference all three methods agree very well, too. The phase-shift calculation presents results closer than the ACCC to the ones derived by analytical continuation for energies further away from the branch point. Practically both calculations, the phase shift as well as the ACCC, can be improved by taking further orders of the effective range expansion or higher Padé approximants, respectively.

V_0 [MeV]	Phase shift		ACCC, [7,7]		Analytical continuation	
	Re E [MeV]	Im E [MeV]	Re E [MeV]	Im E [MeV]	Re E [MeV]	Im E [MeV]
-200.0	-15.126	0.0	-14.725	0.0	-14.725	0.0
-180.0	-9.604	0.0	-9.444	0.0	-9.444	0.0
-160.0	-5.156	0.0	-5.109	0.0	-5.109	0.0
-140.0	-1.937	0.0	-1.928	0.0	-1.928	0.0
-120.0	-0.197	0.0	-0.196	0.0	-0.196	0.0
-110.0	-0.004	0.0	-0.004	0.0	-0.004	0.0
-100.0	-0.357	0.0	-0.359	-0.005	-0.358	0.0
-80.0	-3.119	0.0	-3.225	0.024	-3.133	0.0

Table 6.4.: The results for the bound and virtual state energies for the attractive Gaussian potential for all three methods discussed. The energies of the ACCC on the physical sheet are those used as input for the fits and therefore agree exactly with the ones derived from the poles of the T-matrix in the analytical continuation column. Altogether, all two (three) methods on the physical (unphysical) sheet agree very well with each other. For energies further away from the branch point the discrepancy increases to the benchmark calculation using the analytical continuation.

6.2. Attractive Gaussian & repulsive Gaussian wall

Based on the experience gained with the first toy potential, another toy potential is investigated. Besides bound and virtual states, it further exhibits resonances. The complexity is extended from an effective one-dimensional problem (along the imaginary momentum axis) to a two-dimensional problem. Following physical intuition, in addition to the attractive Gaussian at the origin, the second potential includes a repulsive Gaussian wall,

$$V_{\mathrm{R}}(r)\delta\left(r - r'\right) := \left\langle r' \underbrace{00}_{l'm'} \middle| V_{\mathrm{R}} \middle| r \underbrace{00}_{lm} \right\rangle = \left(V_1 e^{-\frac{r^2}{\alpha_1^2}} + V_2 e^{-\frac{(r-r_2)^2}{\alpha_1^2}} \right) \delta\left(r - r'\right) . \tag{6.10}$$

Similar to the first potential, it is spherically symmetric and projected to S-wave. A sketch of the potential is shown in Fig. 6.7.
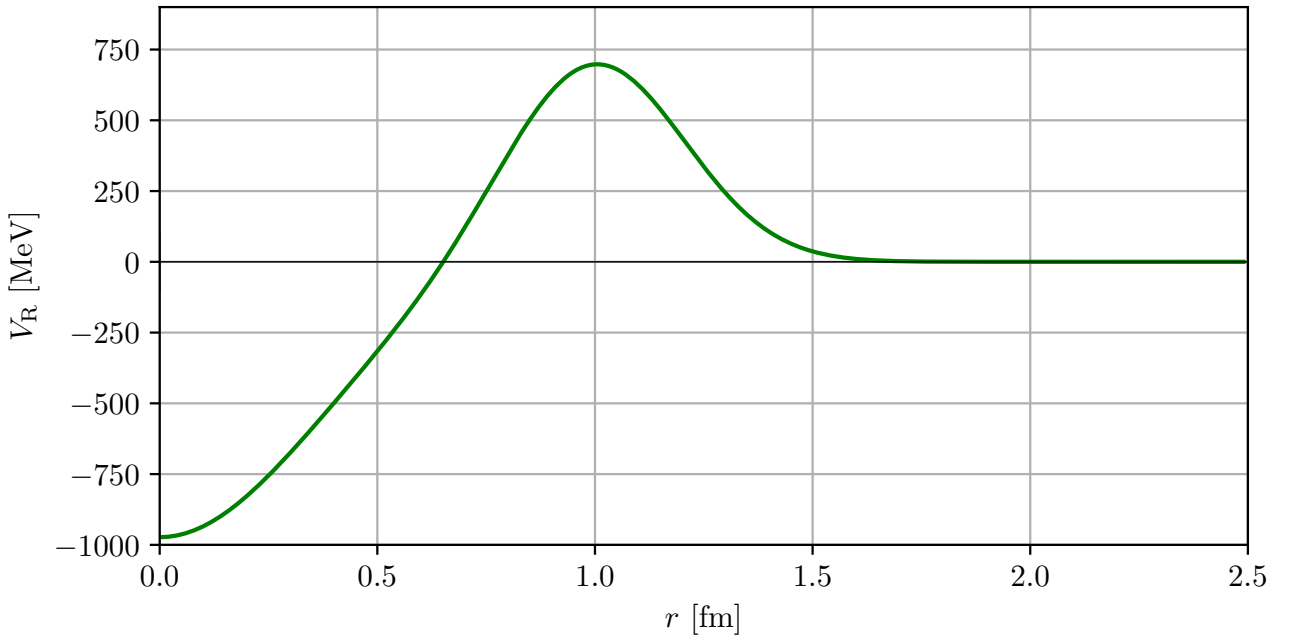
Figure 6.7.: The resonant toy-potential Eq. (6.10) consisting of an attractive Gaussian at the origin and a repulsive Gaussian wall. The sketch shown is done for the parameters given in Eq. (6.13).

The momentum-space representation of the potential is given by

$$
\begin{aligned}
V_{\mathrm{R}}(k, k') &:= \left\langle k'00 \middle| V_{\mathrm{R}} \middle| k00 \right\rangle \\
&= \frac{1}{2\sqrt{\pi}kk'} \alpha_1 V_1 \left(e^{-\frac{\alpha_1^2}{4}k_-^2} - e^{-\frac{\alpha_1^2}{4}k_+^2} \right) \\
&\quad + \frac{1}{2\sqrt{\pi}kk'} \alpha_2 V_2 \left[\cos\left(r_2 k_-\right) e^{-\frac{k_-^2 \alpha_2^2}{4}} \operatorname{Re} \operatorname{erfc}\left(-\frac{1}{2\alpha_2}\left(2r_2 + i\alpha_2^2 k_-\right) \right) \right. \\
&\qquad\qquad \left. - \cos\left(r_2 k_+\right) e^{-\frac{k_+^2 \alpha_2^2}{4}} \operatorname{Re} \operatorname{erfc}\left(-\frac{1}{2\alpha_2}\left(2r_2 + i\alpha_2^2 k_+\right) \right) \right],
\end{aligned}
\tag{6.11}
$$

where $k_\pm = k \pm k'$. The contribution of the repulsive wall is proportional to the complementary error function

$$\text{erfc}(z) = 1 - \text{erf}(z) = \frac{2}{\sqrt{\pi}} \int_z^\infty \mathrm{d}t \, e^{-t^2} \,. \tag{6.12}$$

Fixing the widths of the Gaussian potentials, α_1 and α_2, as well as the position of the barrier r_2 the appearance of bound states, virtual states, and resonances only depends on the ratio of V_1 and V_2. For our calculations, we decided to keep V_1 fixed and only change V_2.

The starting point of our investigation is a resonance at $E = 2.449 \, \text{MeV} - 0.271i \, \text{MeV}$ for the set of parameters

$$\begin{aligned} V_1 &= -973 \, \text{MeV}, & \alpha_1 &= 0.4981 \, \text{fm}, \\ V_2 &= 715 \, \text{MeV}, & \alpha_2 &= 0.292 \, \text{fm}, & r_2 &= 0.9972 \, \text{fm}. \end{aligned} \tag{6.13}$$

Based on these parameters, the transition to a broader as well as the transition to a smaller resonance is investigated. The latter case presents some interesting features. These features can only be observed when applying the analytical continuation. To better understand the shortcomings of the phase shift and the ACCC results let us discuss the pole structure for the latter case first:

Starting at the given resonance and decreasing V_2 the resonance energy moves towards the branch point at the origin. However, the pole trajectory never crosses this branch point. It stays on the unphysical sheet becoming a virtual state with a vanishing negative imaginary part, $E = E_v^1 - i\varepsilon$. At a value of V_2 close to this transition point a bound and a virtual state with a vanishing positive imaginary part, $E = E_v^2 + i\varepsilon$, appear at the origin. Decreasing V_2 further, the binding as well as the two virtual state energies increase, too.

6.2.1. Phase shifts & time delays

Similar to the single attractive Gaussian, first the phase shifts and time delays along the pole trajectory are investigated.

Starting at the given resonance, we first investigate the transition to a broader resonance by increasing the value of V_2. The corresponding phase shifts are shown in Fig. 6.8. All phase shifts start at $\text{Re}\,\delta = 0°$ for $k = 0 \, \text{fm}^{-1}$ with a negative slope. Around the resonance momentum, the phase shifts rapidly increase by approximately $180°$, following the definition of resonance. The large momentum behavior beyond the resonance is independent of the values of V_2 applied. Increasing V_2 the slope of the phase shifts around the resonance momentum increases, too. However, the inverse slope of the phase shift multiplied with the resonance momentum increases. This results in a larger resonance width. Note that for increasing resonance width absolute value of the background phase shift increases, too. This results in a shift of the resonance momentum (the inflection point of the phase shift) away from the phase shift $\text{Re}\,\delta = 90°$.
The time delays derived from these phase shifts are shown in Fig. 6.9. They present the expected peak structure around the resonance momentum. For momenta lower and higher than the momentum range connected to the resonance, the time delays become negative. For small momenta, this can be explained by the negative background phase shift, while for larger momenta the boundary condition $\text{Re}\,\delta \longrightarrow 0°$ for $k \longrightarrow \infty$ has to be fulfilled. The increasing slope of the phase shift around the resonance momentum for increasing V_2 becomes visible in the peak height becoming larger for larger V_2.
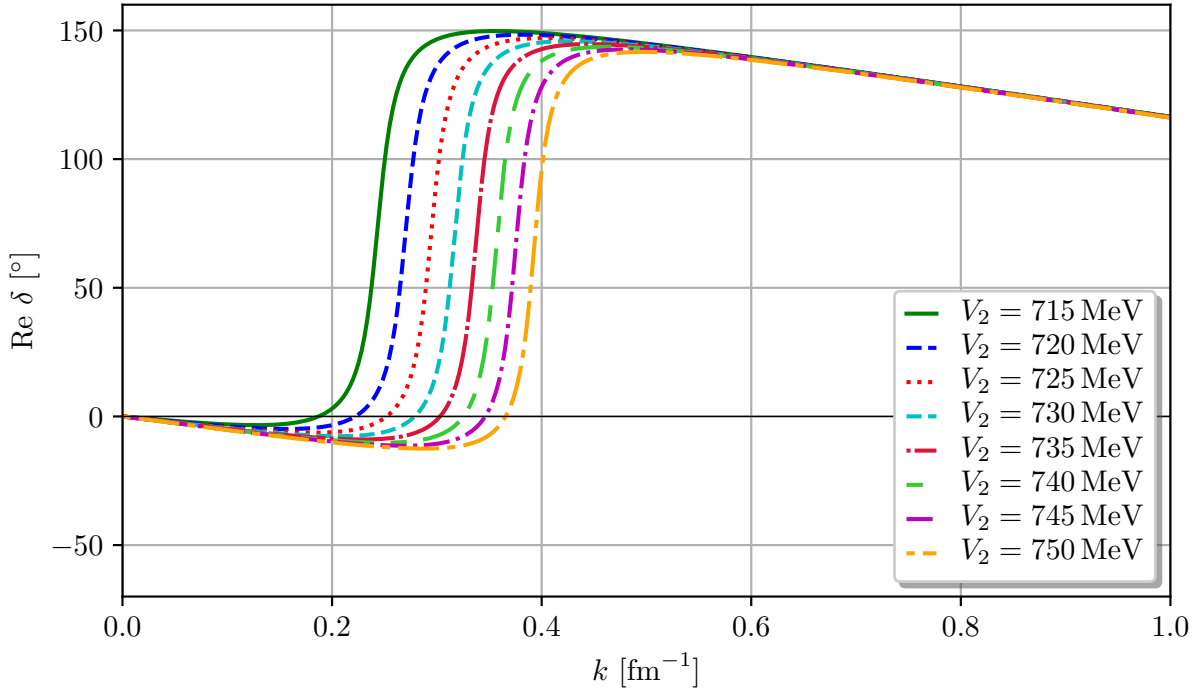
Figure 6.8.: The phase shifts for the potential Eq. (6.11). Starting at the set of parameters given in Eq. (6.13), we keep all parameters fixed and only increase V_2. Following physical intuition this results in an increasing resonance momentum and width. All phase shifts show the expected increase by $180°$ around the resonance momentum. Due do a negative background phase shift the phase shifts do not rise up to $180°$ resulting in an asymmetric behavior around $\mathrm{Re}\,\delta = 90°$.

Figure 6.9.: The time delays derived from the phase shifts presented in Fig. 6.8. They show the expected peak structure around the resonance momentum. Due to the higher slope for larger V_2 the peak height increases, too. The negative background phase shift results in time delays negative for small momenta. For momenta larger than the resonance momentum the time delay becomes negative, too.

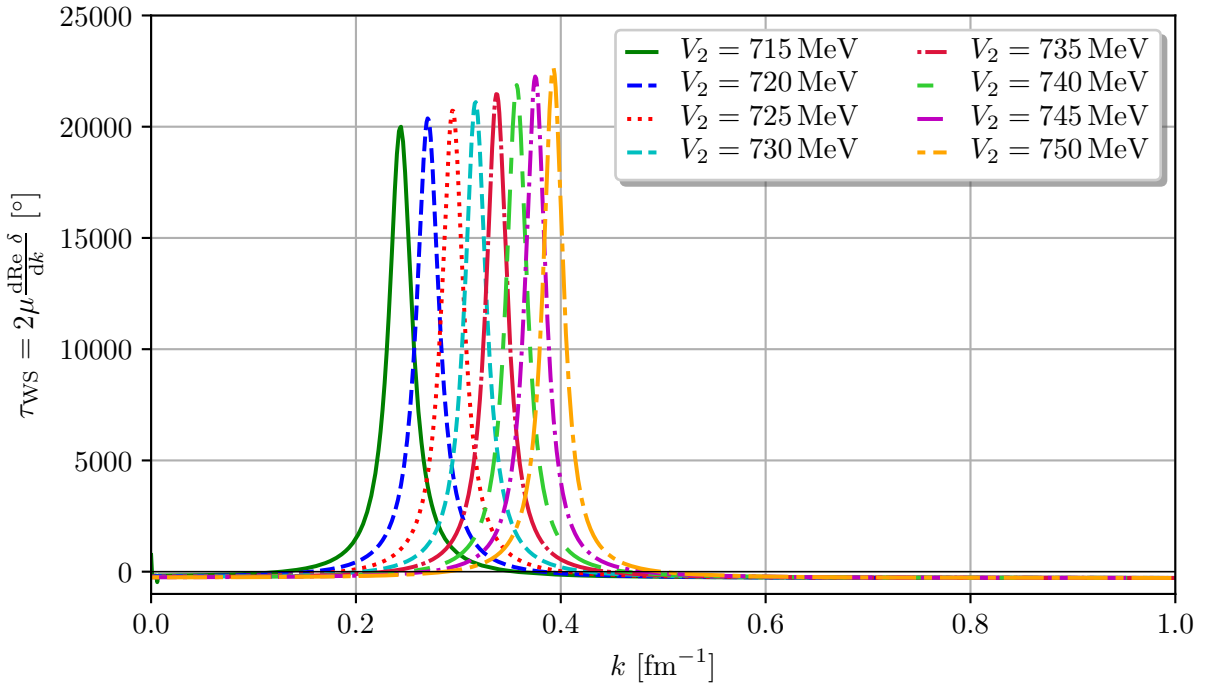| V_2 [MeV]	Re E [MeV]	Im E [MeV]
715.0	2.454	−0.275
720.0	3.019	−0.299
725.0	3.586	−0.321
730.0	4.151	−0.339
735.0	4.712	−0.355
740.0	5.272	−0.369
745.0	5.828	−0.381
750.0	6.382	−0.392

Table 6.5.: The resonances energies and widths as a function of V_2 for the second toy potential Eq. (6.11) extracted from the phase shifts shown in Fig. 6.8.

Based on the phase shifts we can extract reference values for the resonance energies and widths. The real part of the resonance energy is determined by the inflection point of the sharp rise of the phase shift, while the imaginary part of the resonance energy is given by Eq. (2.41),

$$\Gamma = 2 \left[\frac{\mathrm{d}\delta}{\mathrm{d}E} \bigg|_{E=E_{\mathrm{R}}} \right]^{-1}. \tag{6.14}$$

The extracted values are presented in Table 6.5.

Instead of increasing the value of V_2, we now decrease it from 715.0 MeV to 680.0 MeV. The corresponding phase shifts for V_2 along this trajectory are shown in Fig. 6.10. The first three curves for $V_2 =$ 715.0 MeV, 700.0 MeV and 695.0 MeV show the expected resonance behavior. Similar to the previous case, the resonance momentum moves closer to the origin and the slope at the resonance momentum decreases. The next two curves for $V_2 =$ 693.8 MeV and 693.7 MeV already present a different behavior. The left tail of the rising resonance structure is not is visible anymore. This could be interpreted as a resonance close to the origin. However, in comparison to the previous trajectories the slope does not decrease further with decreasing V_2, it increases. As we will see later these two phase shifts correspond to the transition of the resonance into a virtual state like structure. Decreasing V_2 to 693.6 MeV, the phase shift at the origin flips from $0°$ to $180°$, indicating the existence of a bound state. This feature remains for even lower values of V_2. Due to the continuity of the phase shifts in V_2 a valley at small k arises, which is filled if V_2 is decreased further. The time delays calculated for these phase shifts are shown in Fig. 6.11. They present the expected structures investigated already in the discussion of the phase shifts. The three values for V_2 corresponding to a resonance become visible by their peak structure. Only for $V_2 = 715.0$ MeV the left tail of the resonance becomes negative. This indicates the negative background phase shift, which disappears for smaller V_2. The time delays clearly shows the change in the evolution of the peak height for the resonances in comparison to the two virtual-state curves. Finally, the negative time delays at the origin connected to the bound-state curves become visible.
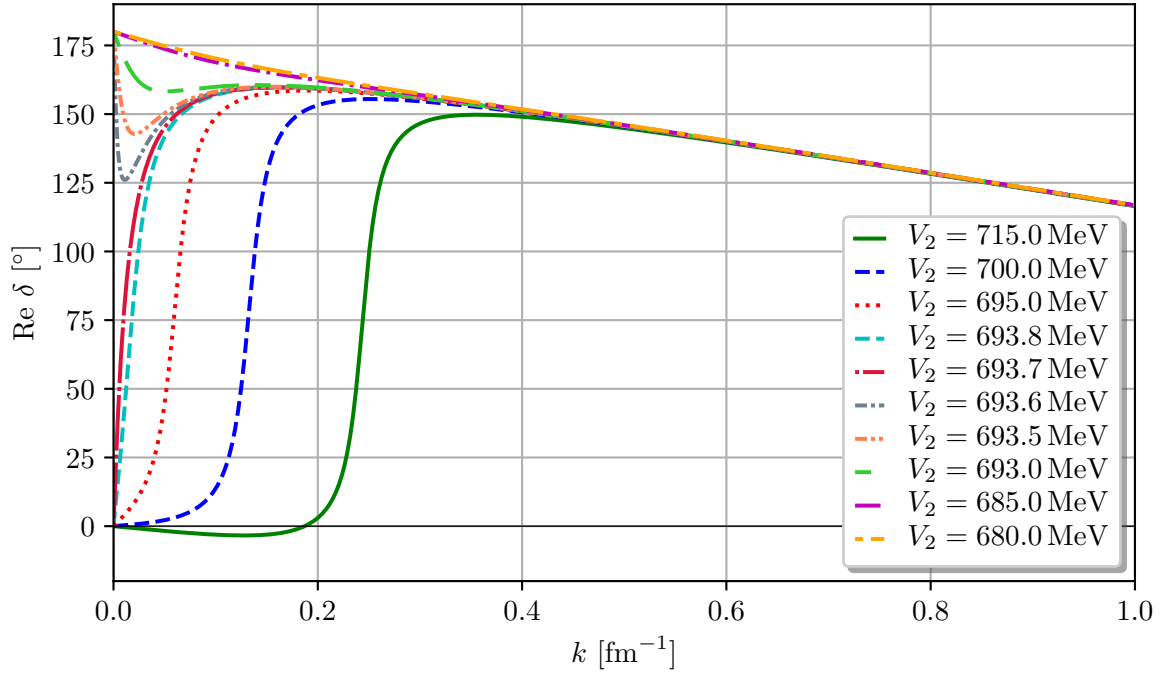
Figure 6.10.: The phase shifts for the second toy potential Eq. (6.11) as function of V_2. Starting at large V_2, the first three curves show the expected behavior for a resonance moving towards the origin. The fourth and five curve, although they could be interpreted as a resonance close to the origin, correspond to a virtual state. This becomes visible by comparing the evolution of the slope to the previous resonance curves. The remaining five curves show the existence of a bound state following Levinson's theorem. The phase shifts evolve continuously from the resonant to the bound curves resulting in a valley for small k, which is filled when V_2 further decreases.

Figure 6.11.: The time delays derived from the phase shifts shown in Fig. 6.10. The three resonance curves for large V_2 as well as the five bound-state curves for small V_2 become visible. The time delay clearly allows to differentiate between the three resonance and the two virtual-state curves by investigating the evolution of their peak height.

V_2 [MeV]	Re E [MeV]	Im E [MeV]
715.0	2.454	−0.275
700.0	0.722	−0.157
695.0	0.141	−0.071

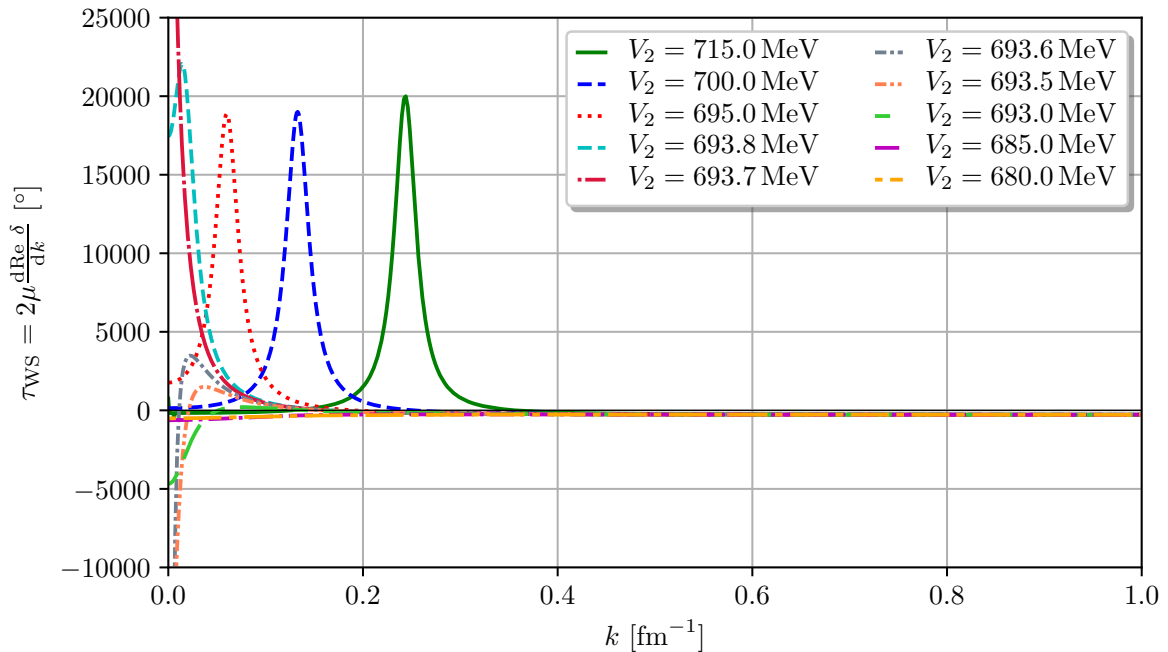Table 6.6.: The resonance energies and widths extracted from the phase shifts shown in Fig. 6.10.

Similar to the evolution to a broader resonance, the phase shifts can be used to extract the resonance energies and widths. The extracted values are shown in Table 6.6. However, trying to extract the bound- and virtual-state energies analog to the attractive Gaussian toy potential presents no valid results. As will be shown later this results from the simultaneous existence of two virtual and one bound state.

6.2.2. ACCC

The ACCC is applied as it would be done, if there is no knowledge on the correct pole trajectories on the unphysical sheets. So, the input for the fits is given by the bound state poles on the physical sheet. We consider bound state poles for V_2 in the range 670 MeV to 693.6 MeV. The results for the pole trajectories are shown in Fig. 6.12. They show the transition of the bound states into resonances. Without further knowledge on the correct results these pole trajectories present valid results. Let us compare them to the phase shift calculations, ignoring that we know of the virtual states we could only gather due to our knowledge from the analytical continuation. Figure 6.12 shows for comparison results obtained from the analytical continuation in the next Section. The resonant part of these results agree very well with the results derived from the phase shift calculations as shown in the previous Section. A comparison of the different Padé orders shown indicates that already the fourth order presents converged results agreeing well with the "correct" results. Note that even orders, i.e. [4,4] and [6,6], as well as odd orders, i.e. [5,5] and [7,7], yield similar results. The difference between even and odd orders becomes visible further away from the origin, where even-order trajectories better describe the results derived from analytical continuation. For a better comparison, Table 6.7 presents selected results along the resonant part of the pole trajectory.

V_2 [MeV]		695.0	700.0	710.0	720.0	730.0	740.0	750.0
[1,1]	Re E [MeV]	0.136	0.646	1.664	2.676	3.683	4.685	5.681
	Im E [MeV]	-0.045	-0.122	-0.272	-0.442	-0.632	-0.841	-1.068
[2,2]	Re E [MeV]	0.139	0.714	1.866	3.018	4.170	5.322	6.474
	Im E [MeV]	-0.071	-0.161	-0.271	-0.359	-0.438	-0.514	-0.588
[3,3]	Re E [MeV]	0.141	0.723	1.849	2.953	4.052	5.148	6.242
	Im E [MeV]	-0.075	-0.146	-0.224	-0.296	-0.379	-0.466	-0.558
[4,4]	Re E [MeV]	0.141	0.722	1.876	3.019	4.153	5.277	6.390
	Im E [MeV]	-0.072	-0.156	-0.242	-0.297	-0.336	-0.365	-0.387
[5,5]	Re E [MeV]	0.141	0.723	1.876	3.016	4.141	5.253	6.352
	Im E [MeV]	-0.072	-0.156	-0.239	-0.289	-0.326	-0.353	-0.376
[6,6]	Re E [MeV]	0.141	0.722	1.876	3.019	4.154	5.279	6.394
	Im E [MeV]	-0.072	-0.156	-0.243	-0.298	-0.338	-0.368	-0.389
[7,7]	Re E [MeV]	0.141	0.723	1.876	3.016	4.142	5.254	6.354
	Im E [MeV]	-0.072	-0.156	-0.239	-0.289	-0.326	-0.354	-0.376

Table 6.7.: Resonance energies derived by the ACCC using the bound state energies as input.
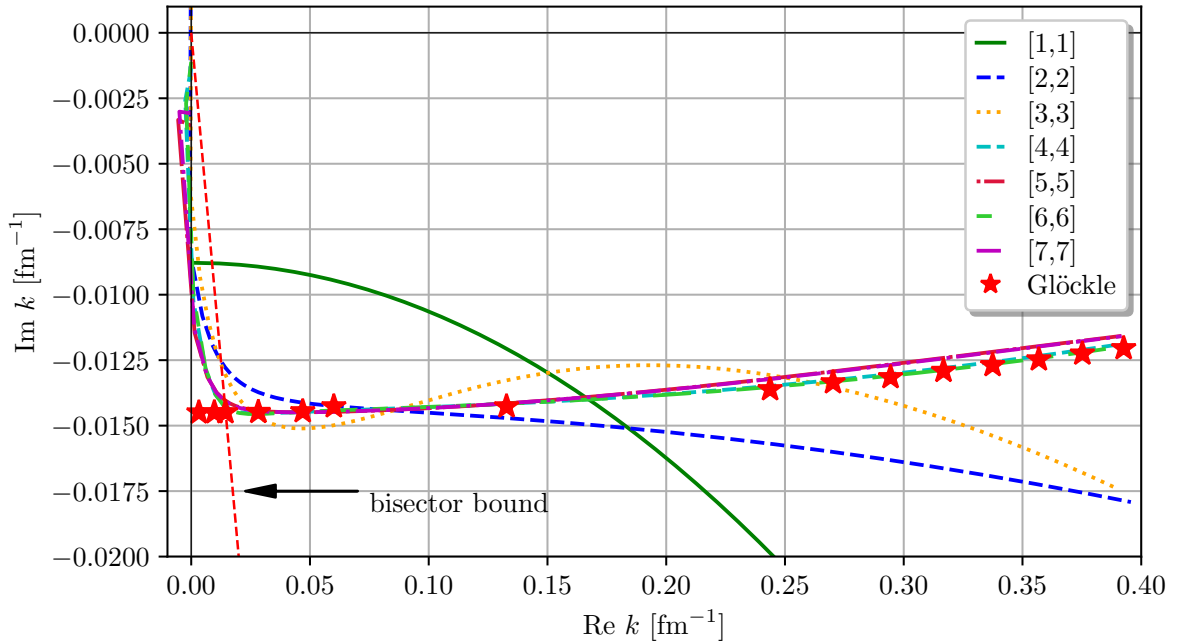
Figure 6.12.: The resonance momentum according to the ACCC applied to the bound state data on the physical sheet in comparison to results derived using the analytical continuation formalism by Glöckle. Neglecting the range up to $k \approx 0.03\,\mathrm{fm}^{-1}$ already the third-order Padé approximant presents results very-well agreeing with the analytical continuation. These results are located in the upper bisector of the fourth quadrant of the complex momentum plane indicated by the red dashed line. So, they can be identified by resonances following the formal definition.

6.2.3. Analytical continuation

Finally, the analytical continuation is applied. In comparison to the previous toy potential the formalism by Afnan can be applied to the resonant part of the trajectory, too. As far as possible the calculations have been performed using the methods by Glöckle and Afnan. Both methods present equivalent results, such that we do not differentiate between them. For the virtual-state part of the trajectory only the formalism by Glöckle was applied.

Similar to the previous toy potential, the first step in investigating the pole structure is the calculation of contour plots. These plots are shown in Fig. 6.13 for various values of V_2 along the pole trajectory. They show the transition of the resonance into to a virtual state like state with negative imaginary part at $V_2 = 693.791$ MeV and $E = -0.017i$ MeV. Close to this transition point at $V_2 = 693.642$ MeV a bound state on the physical sheet and a virtual state like state with a vanishing positive imaginary on the unphysical sheet arise. Similar to Fig. 6.13 the moving pole trajectory of the bound state on the physical sheet can be investigated by performing contour plots of the physical Lippmann-Schwinger equation. The energies of the states on the physical and unphysical sheet are shown in Table 6.8.

V_2 [MeV]	Re E [MeV]	Im E [MeV]
750.0	6.383	-0.386
745.0	5.828	-0.377
740.0	5.271	-0.364
735.0	4.712	-0.350
730.0	4.150	-0.335
725.0	3.586	-0.317
720.0	3.019	-0.296
715.0	2.449	-0.271
700.0	0.722	-0.156
695.0	0.141	-0.072
693.8	0.001	-0.018
693.7	6.390×10^{-6}	-2.719×10^{-8}
693.6	-0.044	-5.903×10^{-6}
693.6	-7.222×10^{-5}	1.126×10^{-8}
693.6	-0.001	0.0
693.5	-0.064	-6.103×10^{-6}
693.5	-0.001	5.184×10^{-8}
693.5	-0.004	0.0
693.0	-0.146	-7.216×10^{-6}
693.0	-0.012	5.139×10^{-7}
693.0	-0.038	0.0
685.0	-1.225	-1.405×10^{-6}
685.0	-0.449	8.509×10^{-6}
685.0	-0.836	0.0
680.0	-1.869	-1.618×10^{-5}
680.0	-0.749	1.254×10^{-5}
680.0	-1.372	0.0

Table 6.8.: The resonance, bound- and virtual-state energies for different values of V_2 along the trajectory.
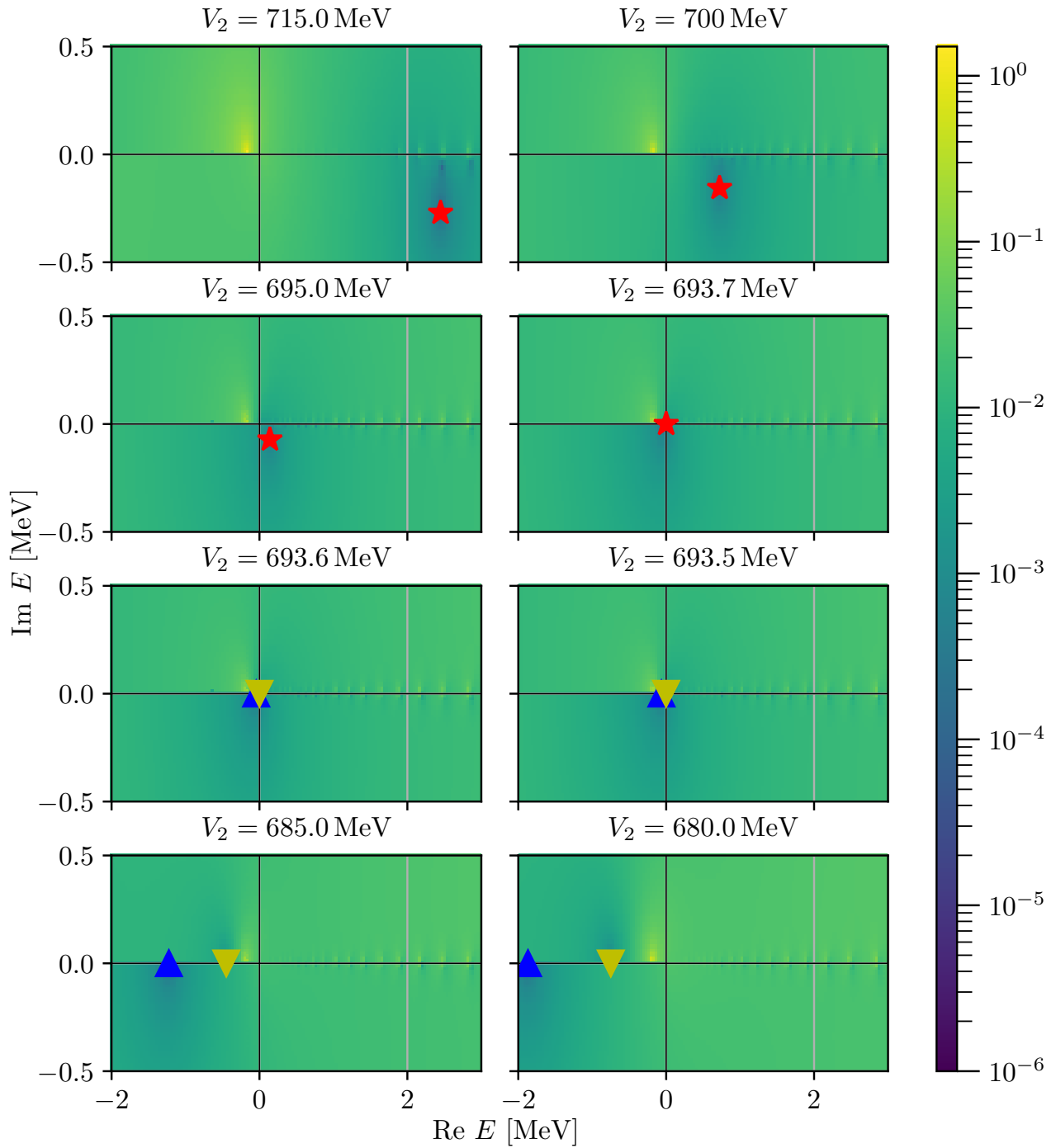
Figure 6.13.: The determinant of the identity matrix minus the kernel of the Lippmann-Schwinger equation on the unphysical sheet, $|\det \mathbb{1} - K|$, for various values of V_2 along the trajectory. A zero within these plots indicates a pole of the T-matrix. The corresponding values determined by a root-finding are indicated by symbols. Up to $V_2 = 693.7\,\mathrm{MeV}$ there is only the resonant state (★) located in the fourth quadrant. For larger values the resonance turns into a virtual state like state with a vanishing negative imaginary part (▲). Close to this transition point a pair of a bound (not shown) and a virtual state like state with vanishing positive imaginary part (▽) arise.

6.2.4. Comparison

The comparison of the three methods can be divided into two cases. On the one hand, there is the resonant part of the trajectory. It can be calculated using all three methods. Table 6.9 shows the good agreement between all three methods. Note that for the ACCC this is somewhat surprising as the resonance part of the trajectory is not connected to the bound part of the trajectory. On the other hand, there is the range of V_2, where a bound state exists parallel to two virtual state like states. Here, a comparison of the methods shows the restricted applicability of the phase shift and ACCC method. The derivation of the energies from the phase shift calculations fails as there are more than one state in parallel. The application of the ACCC method to the bound-state trajectory reproduces the resonant part of the trajectory, while physically it is connected to a virtual state with a vanishing positive imaginary part. Only the analytical continuation allows to derive the energies of both poles on the unphysical sheet.

V_2 [MeV]	Phase shift		ACCC, [7,7]		Analytical continuation	
	Re E [MeV]	Im E [MeV]	Re E [MeV]	Im E [MeV]	Re E [MeV]	Im E [MeV]
750.0	6.382	-0.392	6.354	-0.376	6.383	-0.386
740.0	5.272	-0.369	5.254	-0.354	5.271	-0.364
730.0	4.151	-0.339	4.142	-0.326	4.150	-0.335
720.0	3.019	-0.299	3.016	-0.289	3.019	-0.296
710.0	1.875	-0.237	1.876	-0.239	1.876	-0.242
700.0	0.722	-0.157	0.723	-0.156	0.722	-0.156
695.0	0.141	-0.071	0.141	-0.072	0.141	-0.072

Table 6.9.: The resonance energies for all three methods used.

7 The three-boson system - Analytical continuation

Within this Chapter, the first three-body system considered within this work, a system of three identical, spinless bosons with short-range S-wave interactions, is discussed. First, the Efimov effect and its predictions for the three-boson system are discussed. Further, the Faddeev equation for this system is derived applying the Faddeev formalism. It is compared against the Faddeev equation derived from the Lagrange formalism. Next, the renormalization of the three-body force is discussed. In the following, another representation of the Faddeev equation derived by Bringas *et al.* [95] is presented. It is used for the comparison to the subsequent application of the analytical continuation for unbound two-boson subsystems. Finally, the Efimov trajectory for a bound two-boson subsystem is calculated.

Parts of this Chapter have been published in this or similar form in Phys. Rev. C, vol. 105, no. 6, p. 064002 [68].

7.1. Efimov effect

The history of the Efimov effect dates back to the year 1970, when Efimov discovered a discrete scaling in the spectrum of three-body systems [131, 132]. This effect takes place in systems with attractive short-range interactions, e.g. systems with a large two-body S-wave scattering length. For a recent review on Efimov physics see Ref. [133].

In the following, the Efimov effect is motivated for the three-boson system based on the Faddeev equation Eq. (3.35). In the limit $\Lambda \to \infty$, for a finite $H(\Lambda)$, the three-body force term vanishes and the scattering equation presents a continuous scaling symmetry,

$$
\begin{aligned}
a &\longrightarrow \nu a\,, \\
E &\longrightarrow \nu E\,.
\end{aligned}
\tag{7.1}
$$

Reducing the cutoff to a finite value leads to a breaking of the continuous scaling symmetry to a discrete subgroup of scaling transformations,

$$
\begin{aligned}
a &\longrightarrow \nu^n a\,, \\
E &\longrightarrow \nu^{-2n} E\,,
\end{aligned}
\tag{7.2}
$$

where n is an integer and ν is the discrete scaling factor. This discrete scaling symmetry leads to a universal spectrum of three-body states, the Efimov effect. In the unitary limit ($a \longrightarrow \pm\infty$) the binding energies of two consecutive states are connected by

$$
E_{n+1} = \nu^2 E_n\,.
\tag{7.3}
$$

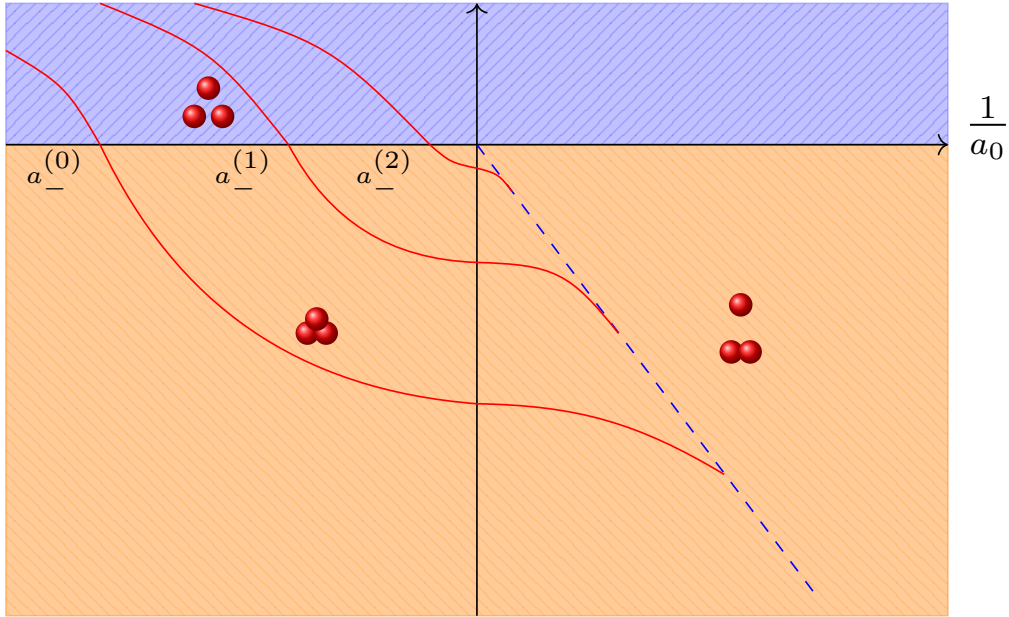$$\mathrm{sign}(\mathrm{Re}\ E) \cdot \sqrt{|\mathrm{Re}\ E|}$$

Figure 7.1.: The so-called Efimov plot displaying the Efimov effect. The x-axis presents the inverse scattering length, while the y-axis shows the square root of the real part of the energy multiplied by its sign. The dashed-blue line indicates the binding energy of the dimer $B_2 = 1/a^2$. In the area right to the dashed blue line the three-body system presents a virtual state, while the dimer is bound. Crossing the line, the three-body system becomes bound, too, until a negative scattering length $a_-^{(n)}$ is reached. Here, the pole moves from the physical sheet (orange/light shaded) to the unphysical sheet adjacent the positive real axis (blue/dark shaded) becoming a resonance.

Here, the counting starts at the deepest bound state accessible within the EFT. Similarly, it is possible to connect the scattering lengths at which the pole trajectory moves from the physical to the unphysical sheet by

$$a_-^{(n)} = \nu a_-^{(n+1)}. \tag{7.4}$$

These discrete scaling symmetries are evident in Fig. 7.1, the so-called Efimov plot. It shows the square root of the real part of the energy multiplied by its sign as a function of the inverse two-body scattering length. The discrete scaling symmetry is not only present along the axis, but also for all states along a straight line at a fixed angle.

Based on the Efimov structure all pole trajectories for the three-boson system are presented in units of a_-. Besides for small Λ, where physically relevant momenta are cut off, or for large Λ, where the theory is not valid anymore, all Efimov states are located at the same energies using this unit scheme.

7.2. Faddeev equation

Within this work, two different approaches to derive the Faddeev equations are discussed. Either one can use the Faddeev formalism together with a potential derived from pionless EFT, or one can apply the Feynman rules derived from the pionless EFT Lagrangian. Only the first formalism results in a representation of the Faddeev equation, that can be used for the analytical continuation. In the following, both representations of the Faddeev equation are derived and their crucial difference is discussed.

7.2.1. Faddeev formalism

The Faddeev equation for the three-boson system following from the Faddeev formalism, Eq. (4.27), is given by

$$
F_0(u_2) = \int \mathrm{d}u_2' u_2'^2 \tau_0 \left(E - \frac{3}{4} u_2'^2 \right) F_0(u_2') \left[\int_{-1}^{+1} \mathrm{d}x \, \langle g|\pi_1 \rangle \, G_0(E; \pi_2, u_2') \, \langle \pi_2|g \rangle \right.
$$
$$
+ D_0 I_0 \left(E - \frac{3}{4} u_2'^2; u_1' \right) \frac{\langle \xi|u_1' u_2' \rangle}{\langle g|u_1' \rangle} \left\{ \frac{\langle u_1 u_2|\xi \rangle}{\langle u_1|g \rangle} I_0 \left((i\gamma)^2; q \right) \right.
$$
$$
\left. \left. + I_0 \left(E - \frac{3}{4} u_2^2; u_1'' \right) \left[-\frac{\langle u_1 u_2|\xi \rangle}{\langle u_1|g \rangle} + \frac{\langle u_1'' u_2|\xi \rangle}{\langle u_1''|g \rangle} \right] \right\} \right],
\tag{7.5}
$$

where $G_{00}(u_2 u_2' x) = P_0(x) = 1$ was used. The simplest representation of this equation can be derived for a Gaussian type regulator,

$$
\langle u_1|g \rangle = g(u_1) = \exp \left(-\frac{u_1^2}{\Lambda^2} \right),
$$
$$
\langle u_1 u_2|\xi \rangle = \xi(u_1, u_2) = \exp \left(-\frac{u_1^2 + \frac{3}{4} u_2^2}{\Lambda^2} \right) = g(u_1) g \left(\frac{\sqrt{3}}{2} u_2 \right).
\tag{7.6}
$$

The final equation reads

$$
F_0(u_2) = \int \mathrm{d}u_2' u_2'^2 \tau_0 \left(E - \frac{3}{4} u_2'^2 \right) F_0(u_2') \left[\int_{-1}^{+1} \mathrm{d}x \, g(\pi_1) \, G_0(E; \pi_2, u_2') g(\pi_2) \right.
$$
$$
\left. + D_0 I_0 \left(E - \frac{3}{4} u_2'^2; u_1' \right) g \left(\frac{\sqrt{3}}{2} u_2' \right) g \left(\frac{\sqrt{3}}{2} u_2 \right) I_0 \left((i\gamma)^2; q \right) \right]
\tag{7.7}
$$
$$
= \int \mathrm{d}u_2' u_2'^2 \tau_0(z) \underbrace{\left[Z_{2,0}(u_2, u_2'; E) + Z_{3,0}(u_2, u_2'; E) \right]}_{Z_0(u_2, u_2'; E)} F_0(u_2') ,
$$

with $z = E - \frac{3}{4} u_2'^2$. For convenience, a dimensionless coupling $H(\Lambda) = D_0 \Lambda^4$ is introduced.

7.2.2. Lagrange formalism

The Faddeev equation derived in the Faddeev formalism can be compared to the representation derived from the Lagrange formalism, Eq. (3.35). Within this work, we are only interested in the difference of

the homogeneous representations of the Faddeev equations. The crucial difference of both equations is in the structure of the three-body force applied. While the Faddeev equation derived from the Lagrange formalism presents a momentum- and energy-independent three-body force

$$Z_{3,0}\left(u_2, u_2'; E\right) = \frac{H_0\left(\Lambda\right)}{\Lambda^2} , \tag{7.8}$$

the structure within the Faddeev formalism is much more advanced

$$Z_{3,0}\left(u_2, u_2'; E\right) = \frac{H_0\left(\Lambda\right)}{\Lambda^4} I_0\left(E - \frac{3}{4}u_2'^2; u_1'\right) g\left(\frac{\sqrt{3}}{2}u_2'\right) g\left(\frac{\sqrt{3}}{2}u_2\right) I_0\left((i\gamma)^2; q\right) . \tag{7.9}$$

One can expand the latter result for large Λ resulting in

$$Z_{3,0}\left(u_2, u_2'; E\right) = \frac{H_0\left(\Lambda\right)}{\Lambda^4}\left[\frac{\pi\Lambda^2}{8} - \sqrt{\frac{\pi}{2}}\frac{\pi\Lambda}{4}\left(\sqrt{\frac{3}{4}u_2'^2 - mE} + \frac{1}{a}\right)\right] + \mathcal{O}\left(\Lambda^{-4}\right) . \tag{7.10}$$

This functional dependence on the momenta and energy occurring in the higher order terms in $1/\Lambda$ only makes it possible to apply the analytical continuation. So, within this Chapter the representation of the Faddeev equation derived within the Faddeev formalism is applied.

7.3. Renormalization of $H(\Lambda)$

The three-body force $H(\Lambda)$ is renormalized such that at $\gamma_0 = a_0^{-1} = 0\,\text{fm}^{-1}$ the energy of the shallowest three-body bound state keeps fixed when varying the regulator scale Λ [108, 110]. Within this work, two different regularization prescriptions are applied. On the one hand, the three-body force $H(\Lambda)$ is chosen such that it reproduces the energy of the three-body bound state for any natural value of Λ. On the other, we fix $H(\Lambda) = 0$ and determine Λ such that the pole is reproduced. An example of the three-body force for the first case as a function of the cutoff is shown in Fig. 7.2. Furthermore, the values of Λ used for the second approach can be read off the plot as its zeros.

Both renormalization prescriptions present indistinguishable results such that in the following only one pole trajectory is presented.

7.4. Method by Bringas *et al.* [95]

Beside the Faddeev equations presented in the previous sections a further version applied to this problem by Bringas *et al.* [95] will be investigated in the following. Their equation, applying a subtractive regularization scheme, reads [134]

$$\begin{aligned} F_0\left(u_2\right) = \int \mathrm{d}u_2' u_2'^2 \int_{-1}^{+1} \mathrm{d}x &\left[\frac{1}{mE - u_2^2 - u_2'^2 - u_2 u_2' x} - \frac{1}{-m\mu^2 - u_2^2 - u_2'^2 - u_2 u_2' x}\right] \\ &\times \tau_0\left(E - \frac{3}{4}u_2'^2\right) F_0\left(u_2'\right) , \end{aligned} \tag{7.11}$$

where μ is the subtraction point. For practical purposes μ is set to 1 fm. Similar to this work, Bringas *et al.* apply a contour rotation following the formalism by Afnan.
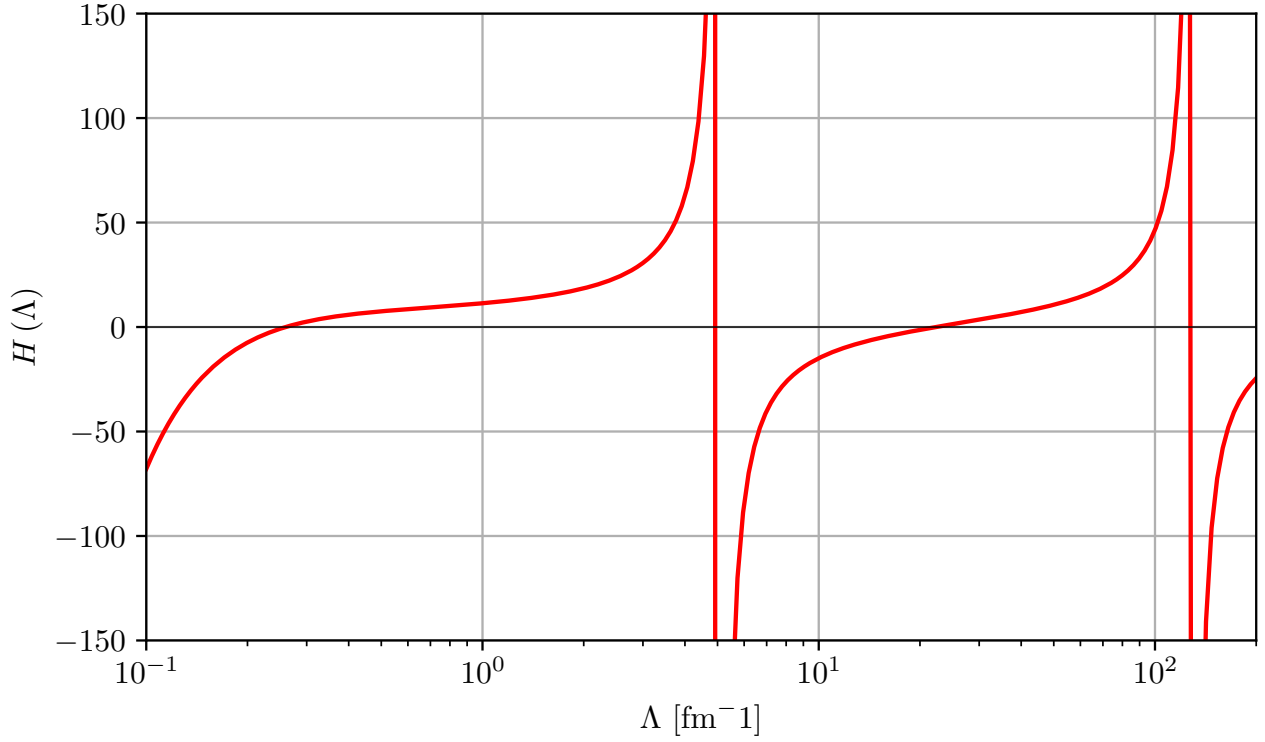
Figure 7.2.: The running of the three-body force $H(\Lambda)$ as function of the regulator parameter Λ.

7.5. Analytical continuation

The three-boson system presents a very rich pole structure. Beside bound states on the physical sheet there are also virtual states on the unphysical sheet adjacent to the two-body cut as well as resonances on the unphysical sheet next to the three-body cut. Analytical continuation is a formalism well suited to explore these structures.

7.5.1. Bound two-body subsystem

First, the three-boson system for a bound subsystem is investigated. Here, it is possible to apply the implicit contour transformation given by Eq. (5.42),

$$
\begin{aligned}
R_0\left(k, p; E\right) &= \int_{C_{\mathbb{R}}} \mathrm{d}q\, q^2 \tau_0(z) R_0\left(k, q; E\right) \\
&\quad \times \left[Z_0\left(q, p; E\right) + \frac{2\pi i q_0^2 Z_0\left(q_0, p; E\right) Z_0\left(q, q_0; E\right) \mathrm{Res}_{q_0} \tau_0(z)}{1 - 2\pi i q_0^2 Z_l\left(q_0, q_0; E\right) \mathrm{Res}_{q_0} \tau_l(z)} \right] \\
&\equiv \int_{C_{\mathbb{R}}} \mathrm{d}q\, \mathcal{K}_0\left(q, p; E\right) R_0\left(k, q; E\right) ,
\end{aligned}
\tag{7.12}
$$

where $q_0 = -\sqrt{\frac{4}{3}\left(mE + \frac{1}{a_0^2}\right)}$. This equation allows to find virtual state poles between the two-body branch point E_2 and the end point of the cut defined in Eq. (5.34), $4/3E_2$. This interval is shown in Fig. 7.3 for a scattering length $a_0 = 1.25$ fm together with the virtual state pole.
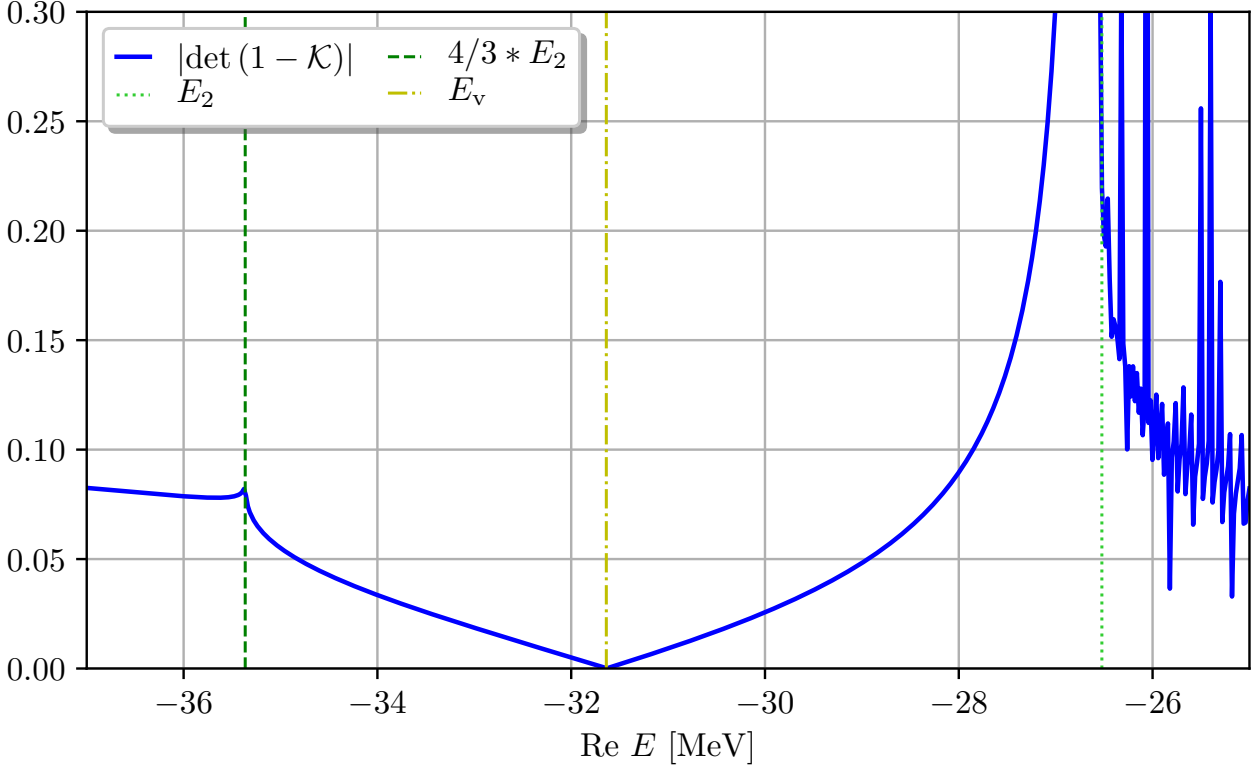

Figure 7.3.: The absolute value of $\det(\mathbb{1} - \mathcal{K})$ for $a_0 = 1.25$ fm, where $\mathcal{K}$ is defined in Eq. (7.12). The three-boson virtual state is located at $E_\mathrm{v} = -31.638$ MeV. At this point the determinant vanishes. The range of applicability of the analytical continuation is restricted to the left by the energy $E = 4/3E_2$, while for energies larger than the dimer energy E_2 no further virtual state poles are possible.

The pole trajectory can be followed from an unbound two-body subsystem, $a^{-1} = 0$ fm^{-1}, to the transition point from a bound to a virtual three-boson system up to the end of the range of applicability, $E = 4/3E_2$. This trajectory is shown in units of a_- in Fig. 7.4. Close to the origin the three-boson system is bound. Decreasing the scattering length, the three-boson binding energy evolves slower than the two-boson binding energy such that three-boson and two-boson energy agree at one point. Here, the pole trajectory moves through the two-body branch point on the unphysical sheet becoming virtual. Following this point the virtual state energy is always larger than the binding energy of the dimer up to the end of the trajectory at $E = 4/3E_2$.

Qualitatively, these results can be compared to a calculation by Yamashita *et al.* [134]. They applied the Faddeev equation Eq. (7.11) together with a contour rotation presenting a good agreement with the results of this work.
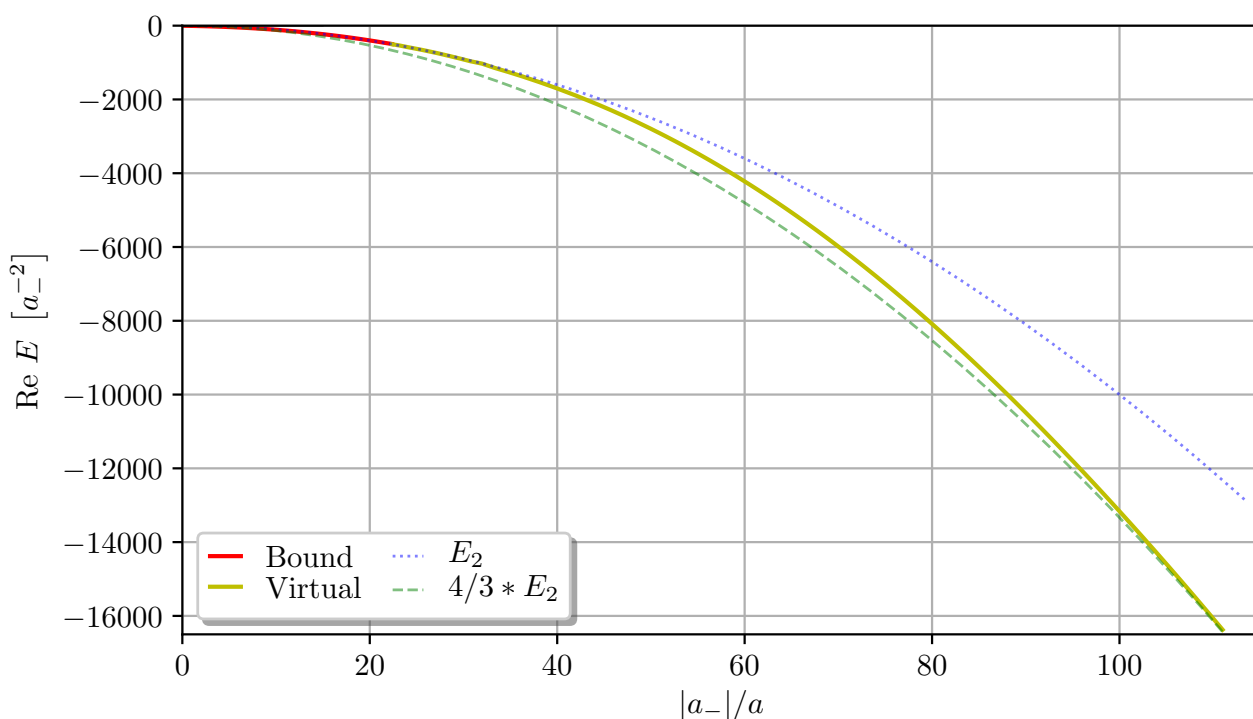
Figure 7.4.: The three-boson trajectory for positive scattering length. For large scattering lengths the three-boson system is bound. Decreasing the scattering length the three-boson system becomes virtual up to the point the energy reaches the end of applicability at $E = 4/3E_2$. Along the whole trajectory the energy is restricted to the range $4/3E_2 \leq E \leq E_2$.

7.5.2. Unbound two-body subsystem

The more interesting case is an unbound two-body subsystem. Here, the three-boson system presents a resonance. This case is comparable to the situation for the three-neutron system as for both systems the existence of a resonance for an unbound two-body subsystem is investigated. In comparison to the previous case, the application of an implicit contour rotation is not possible. So, an explicit contour rotation has to be performed. Similar to the previous section, the first step is a plot of the absolute value of the characteristic polynomial. However, as a resonance is defined by a real and an imaginary part of the energy, Fig. 7.3 has to be extended from the real axis to a contourplot of the complex energy plane. This plot of the fourth quadrant of the complex energy plane for an arbitrary value of the scattering length is shown in Fig. 7.5. Along the negative imaginary axis the rotated three-body cut becomes visible. The resonance is clearly visible as a zero within the middle of the fourth quadrant. Using this value as a starting point for the root finding formalism the exact resonance energy can be determined. Performing similar calculations for various scattering lengths results in the pole trajectory shown in Fig. 7.6. These results can be compared to the results by Bringas *et al.* [95], Section 7.4, and Deltuva [135]. The calculations by Bringas *et al.* can be performed by ourselves. The results by Deltuva are taken from his paper. He solved the Faddeev equations for the transition operators for several short-range force models on the physical sheet and matched it to an expansion of the transition operator into a power series near the resonance pole. The derived pole trajectory is fitted by a lowest- and a higher-order approximation. A comparison of all four pole trajectories shows a very good agreement (cf. Fig. 7.6).

A further qualitative comparison is possible with the results by Jonsell [136], who investigates the three-boson system using a hyperspherical formalism together with the CSM, and with the work of Hyodo *et al.* [137], who calculate the pole trajectories using a contour rotation. The behavior of the pole trajectory derived within this work is consistent with both of these calculations.

All in all, the three-boson system presents a sheet structure similar to the one of the three-neutron system. Applying the contour rotation it was possible to calculate the evolution of the three-boson bound state pole into a resonance. So, this calculation serves as a benchmark for our formalism for the subsequent application to the three-neutron system.
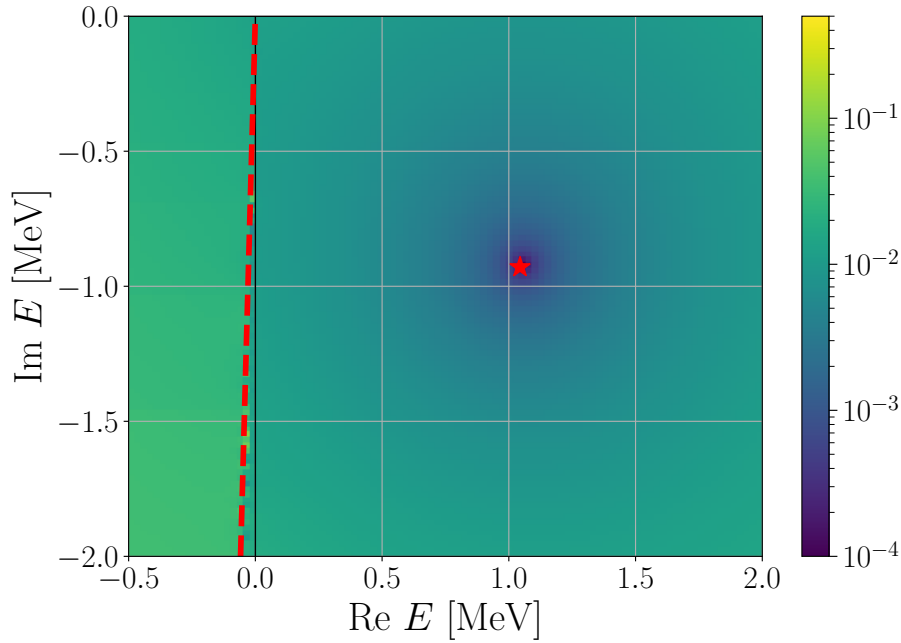
Figure 7.5.: The absolute value of the characteristic polynomial for a scattering length $a = -2.47 \, \text{fm}$ (chosen arbitrarily) on the unphysical sheet adjacent to the three-body cut. The calculation is performed using a rotation angle $\varphi = 0.8 \, \text{rad}$ (45.84°). As a consequence the three-body cut (dashed line) appears at an angle $2\varphi = 1.6 \, \text{rad}$ (91.67°) close to the negative imaginary axis. The value where the characteristic polynomial becomes zero is indicated by a star. This energy corresponds to a three-boson resonance. Similar plots can be created for the other scattering length values along the pole trajectory.
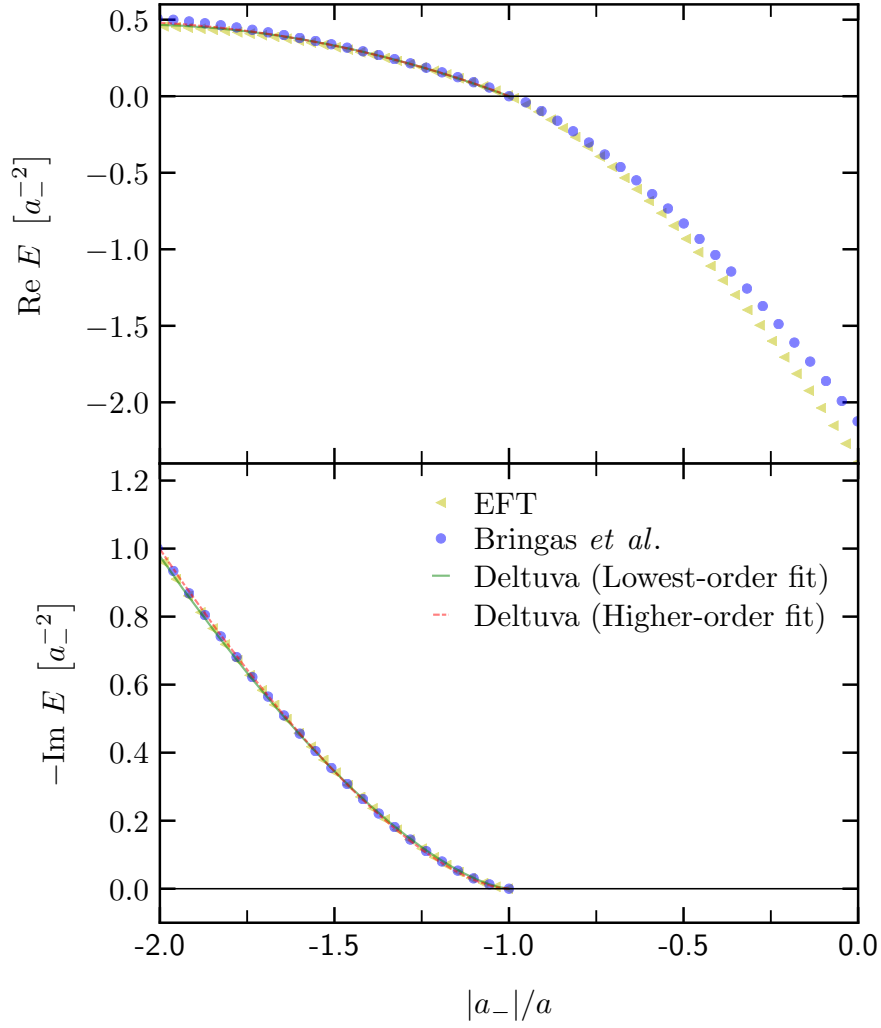
Figure 7.6.: Trajectories for the real (upper) and imaginary (lower) part of the three-boson pole energies. The trajectories are presented in units of a_- such that the transition from the physical to the unphysical sheet takes places at $|a_-|/a = -1$. The results derived in this work are compared to a calculation using the formalism by Bringas *et al.* [95] and two fits by Deltuva [135]. The latter ones are only present on the unphysical sheet.

8 The neutron-deuteron system

In the following Chapter, the neutron-deuteron (n-d) system is investigated. It is the only system investigated within this work consisting of different constituents, the neutron and the proton. Within the following calculations it is assumed that both nucleons have the same mass, the mass of the neutron.

The n-d system shows many interesting effects to be considered. In general it can be divided into two channels. The spin of the deuteron of 1 can couple with the spin-1/2 neutron to a total spin of 3/2 and 1/2. These channels are named according to their multiplicity quartet and doublet channel, respectively. The Faddeev equation for the quartet channel is equivalent to the one of the three-neutron system as shown in Section 3.3.3. The Faddeev equation of the doublet channel presents a more complicated structure. Similar to the three-boson system, it includes a three-body force, which has to be renormalized. Further, it not only includes the deuteron as an intermediate state, but also the $^1S_0$ state. Due to the structure of the n-d system consisting of two channels, effects appearing in only one channel do not inevitably effect observables as will be shown below by the phase shift anomaly. The phase shifts for both channels have been calculated before applying the same formalism, see for example Ref. [138]. However, they have never been investigated with the focus on the phase shift anomaly.

8.1. Phase shift anomaly

The doublet channel presents an anomaly of the phase shift close to the deuteron breakup threshold [139–143]. This anomaly originates from the large singlet scattering length $a_s = -23.714$ fm. It causes an effective long-range three-nucleon interaction of the range $|a_s|$.

This threshold anomaly will be investigated in the following for two different triplet scattering length $a_t = 4.3$ fm and $a_t = 5.4$ fm. While the latter value is the physical neutron-proton scattering length, the first value corresponds to the scattering length derived from the deuteron binding energy at LO in pionless EFT. Further, different energies the doublet channel three-body force is fitted to are applied, $E = -8.0$ MeV, -8.4818 MeV and -9.0 MeV. The physical triton has a binding energy $B_3 = 8.4818$ MeV [144]. In addition, a value slightly larger and a value slightly smaller are used to examine the dependence of the effect on the value of the three-body force.

To investigate the anomaly, the phase shifts have to be derived. For the quartet channel this done on the basis of Eq. (3.40),

$$\underbrace{T_{t,0}(k,p;E)}_{:=T_0^Q} = -4\pi Z_{2,0}\left(k,p;E\right) + \int_0^\Lambda \mathrm{d}q\; q^2 Z_{2,0}\left(q,p;E\right)\tau_0\left(z\right)T_{t,0}\left(k,q;E\right) , \tag{8.1}$$

while the doublet channel Faddeev equation is given by Eq. (3.42):

$$
\underbrace{\begin{pmatrix} T_{t,0}(k,p;E) \\ T_{s,0}(k,p;E) \end{pmatrix}}_{:=T_0^D} = 2\pi \begin{pmatrix} Z_{2,0}(k,p;E) + Z_{3,0}(k,p;E) \\ -3Z_{2,0}(k,p;E) - Z_{3,0}(k,p;E) \end{pmatrix}
$$

$$
- \frac{1}{\pi} \int_0^\infty \mathrm{d}q \, q^2 \left[Z_{2,0}(q,p;E) \begin{pmatrix} 1 & -3 \\ -3 & 1 \end{pmatrix} + Z_{3,0}(q,p;E) \begin{pmatrix} 1 & -1 \\ -1 & 1 \end{pmatrix} \right] \tag{8.2}
$$
$$
\begin{pmatrix} \mathrm{D}_t(q) & 0 \\ 0 & \mathrm{D}_s(q) \end{pmatrix} \begin{pmatrix} T_{t,0}(k,q;E) \\ T_{s,0}(k,q;E) \end{pmatrix} .
$$

These equations are solved for the on-shell T-matrices. Up to the break-up of the deuteron, these equations are solved applying the formalism presented in Appendix E.1. For higher energies the formalism by Hetherington & Schick given in Appendix E.2 has to be used. Based on the on-shell T-matrices, the corresponding phase shifts are defined by [138]

$$
T_l^Q (k,k;E_k) = \frac{2\pi}{\mu} \frac{1}{k \cot \delta_l^Q - ik} ,
$$
$$
T_l^{D,x} (k,k;E_k) = \frac{2\pi}{\mu} \frac{1}{k \cot \delta_l^{D,xy} - ik} , \tag{8.3}
$$

where x labels the singlet and triplet matrix elements, respectively.

The results for the doublet channel phase shifts are shown in Fig. 8.1. They present a small kink around the deuteron breakup momentum. This kink manifests the threshold anomaly. It is the more dominant the larger the ratio $|a_s|/a_t$ becomes.

The anomaly should also have an effect on the n-d scattering cross section. It includes contributions from the quartet as well as the doublet channel [138]

$$
\frac{\mathrm{d}\sigma}{\mathrm{d}\Omega} = \frac{1}{3} \left[\left| \sum_{l=0}^\infty (2l+1) \frac{P_l(\cos\theta)}{k \cot \delta_l^{D,tt} - ik} \right|^2 + 2 \left| \sum_{l=0}^\infty (2l+1) \frac{P_l(\cos\theta)}{k \cot \delta_l^Q - ik} \right|^2 \right] . \tag{8.4}
$$

Within this work, only a relative S-wave is considered, $l = 0$. The quartet channel phase shift used for the calculation of the cross section is shown in Fig. 8.2, while Fig. 8.3 shows the cross section. Around the position of the anomaly the quartet channel phase shifts are much larger than the doublet channel phase shifts. Due to this difference in the order of magnitude, the quartet channel dominates the cross section. So, it does not present any visible structure of doublet channel threshold anomaly. This investigation shows that even if there are structures in the T-matrix, it does not necessarily lead to effects on observables.
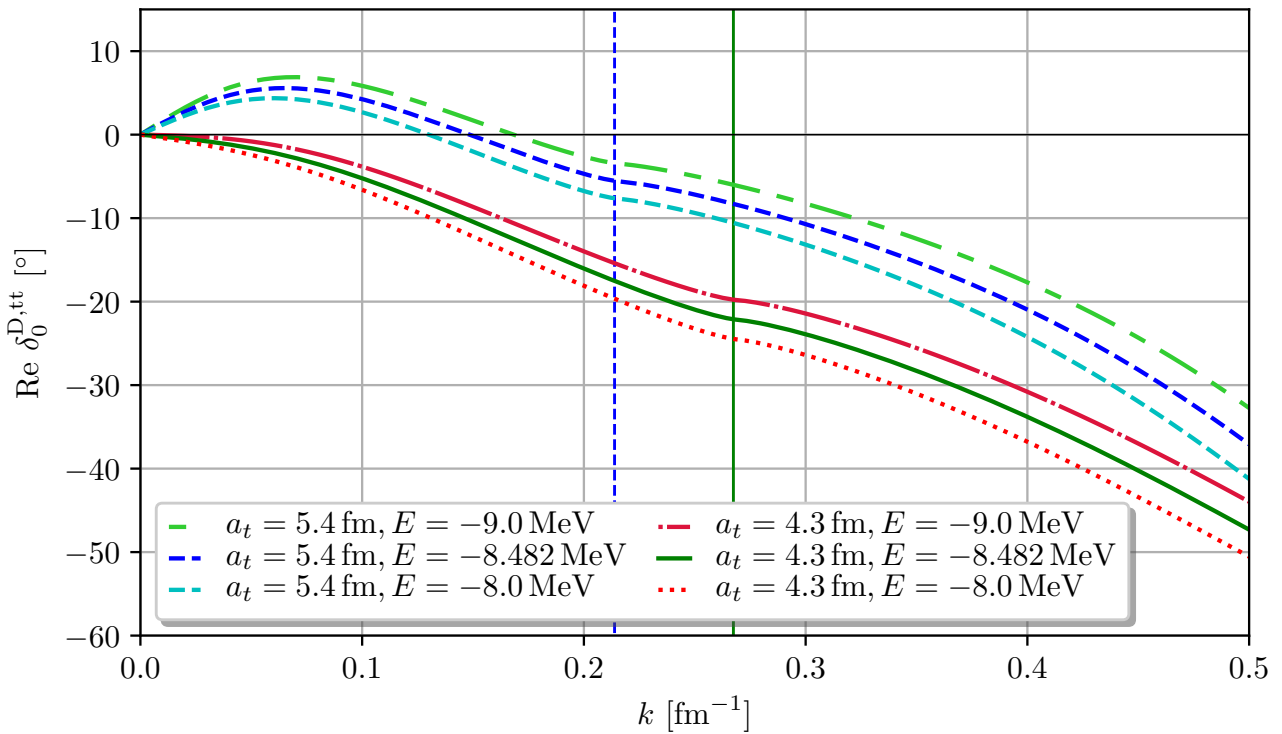
Figure 8.1.: The triplet component of the doublet channel n-d phase shift for different a_t and for three-body forces fitted to different three-body energies E. The breakup of the deuteron is indicated by a dashed (solid) vertical line for $a_t = 5.4\,\mathrm{fm}$ ($a_t = 4.3\,\mathrm{fm}$). Around the breakup the phase shifts present a small kink corresponding to the threshold anomaly. The effect of the different three-body forces is negligible for the structure of the anomaly.
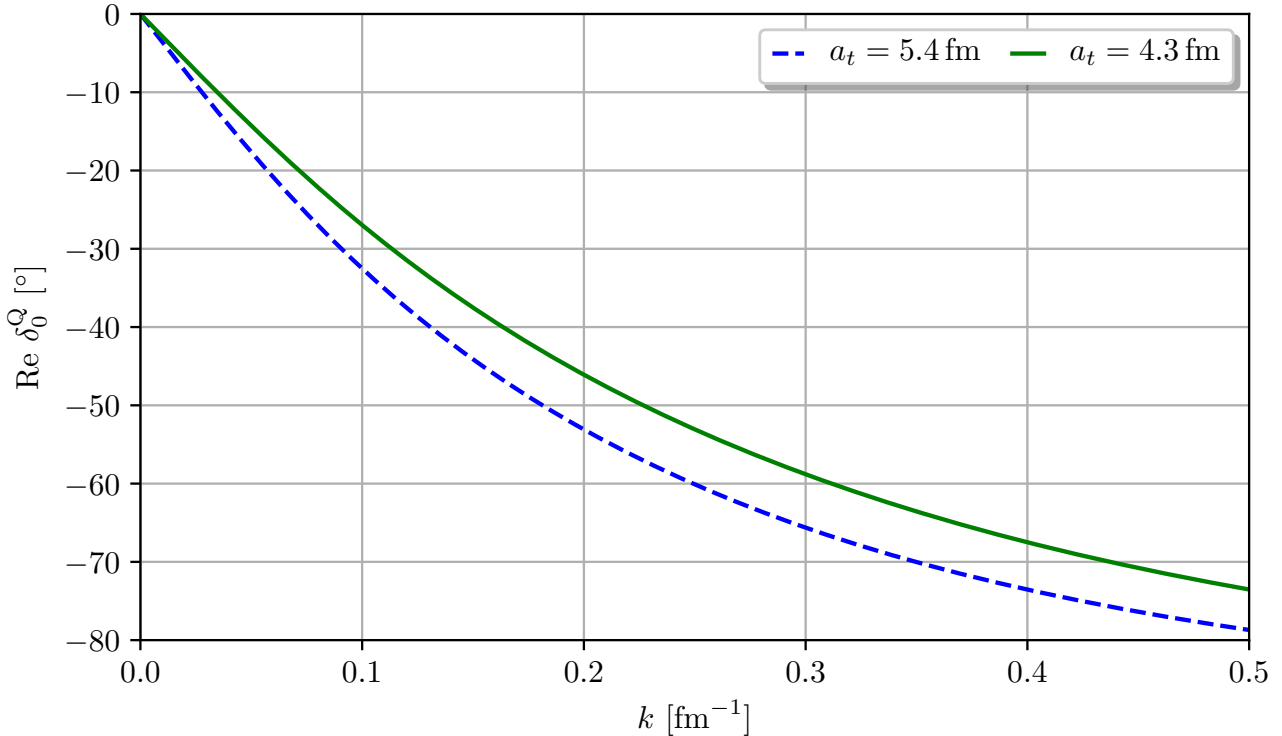
Figure 8.2.: The n-d quartet channel phase shifts for both values of the triplet scattering length a_t considered.
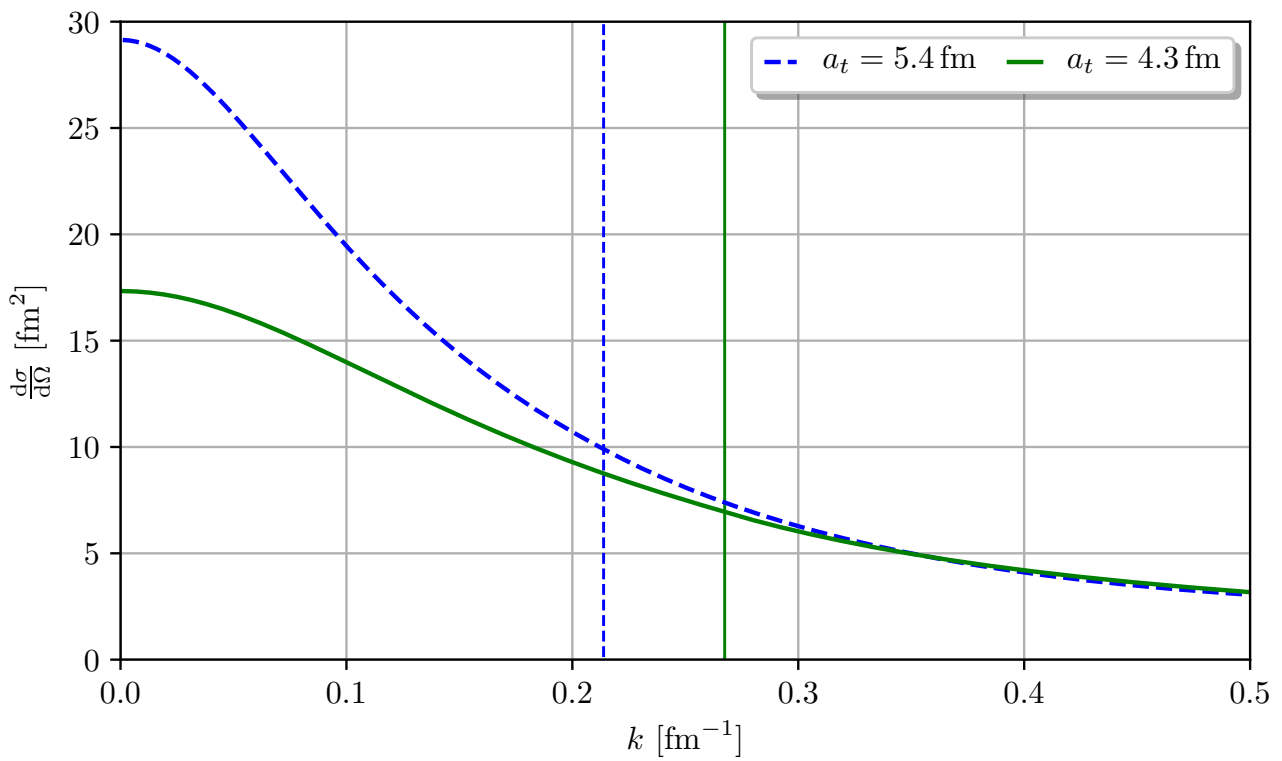
Figure 8.3.: The n-d scattering cross section following Eq. (8.4). The deuteron breakup is indicated by a dashed (solid) vertical line for $a_t = 5.4\,\text{fm}$ ($a_t = 4.3\,\text{fm}$). Due to the dominant contribution of the quartet channel, the doublet channel threshold anomaly is not visible in the cross section. Both cross sections show a smooth behavior around the break-up of the deuteron.

9 The three-neutron system - Phase shifts & time delay

In Chapter 6, the phase shift and time delay formalism was applied to different two-body toy potentials. It was used to extract the properties of various states on the physical and unphysical sheets. Within this Chapter, it will be applied to the three-neutron system. However, the (physical) three-neutron system consists of three particles, while in general phase shifts are only defined for effective two-body systems. So, the phase shifts will be calculated for an unphysically bound dineutron system and extrapolated to the physical neutron-neutron scattering length. On the basis of the phase shifts for positive scattering length, universal relations for the ERE can be defined. These relations are valid up to the breakupof the dineutron. Within this Chapter, these relations are determined for the third neutron in a relative S-, P- and D-wave and compared to previous calculations as far as they are existent. In the following, different possible models to extrapolate the phase shifts are discussed, compared and applied. The extrapolated phase shifts are discussed and compared to the work by Higgins *et al.* performing a similar calculation using the adiabatic hyperspherical formalism [64, 65].

9.1. Bound dineutron - $a_0 > 0$ fm

The basis of the following investigation are the phase shifts for a set of eight positive scattering lengths $a_0 = 4.318$ fm, 5.0 fm, 6.67 fm, 10.0 fm, 15.0 fm, 20.0 fm, 50.0 fm and 100.0 fm. First, the phase shifts for these eight scattering lengths and for the third neutron in a relative S-, P- and D-wave are calculated. These calculations were performed for a cutoff $\Lambda = 15$ fm$^{-1} \approx 3000$ MeV.

The basis for these phase shift calculations is the inhomogeneous Faddeev equation given by Eq. (3.45) and Eq. (3.46),

$$
T_l(k, p; E) = -4\pi Z_{2,l}(k, p; E) + \int_0^\Lambda \mathrm{d}q\ q^2 Z_{2,l}(q, p; E)\, \tau_l(z)\, T_l(k, q; E)\ ,
$$
$$
Z_{2,l}(k, p; E) = -\frac{1}{2} \int_{-1}^{+1} \mathrm{d}x \frac{P_l(x)}{M_N E - k^2 - p^2 - kpx}\ .
$$

$$(9.1)$$

Up to the breakupof the dineutron, this equation is solved applying the formalism presented in Appendix E.1. For higher energies the formalism by Hetherington & Schick given in Appendix E.2 is to be applied. The resulting on-shell T-matrix is connected to the phase shifts by

$$
T_l(k, k; E_k) = \frac{2\pi}{\mu} \frac{1}{k \cot \delta_l - ik} = \frac{3\pi}{M_N} \frac{1}{k \cot \delta_l - ik}\ .
$$

$$(9.2)$$

Note that above the breakup of the dineutron a three-body channel is created. To keep the S-matrix unitary and conserve the probability a further term in the T-matrix is needed. Instead of introducing this term, the effect is parametrized by allowing the phase shifts to become complex.

The real part of the phase shifts are shown in Fig. 9.1 for a third neutron in a relative S-wave, in Fig. 9.2 for a relative P-wave, and in Fig. 9.3 for the D-wave.
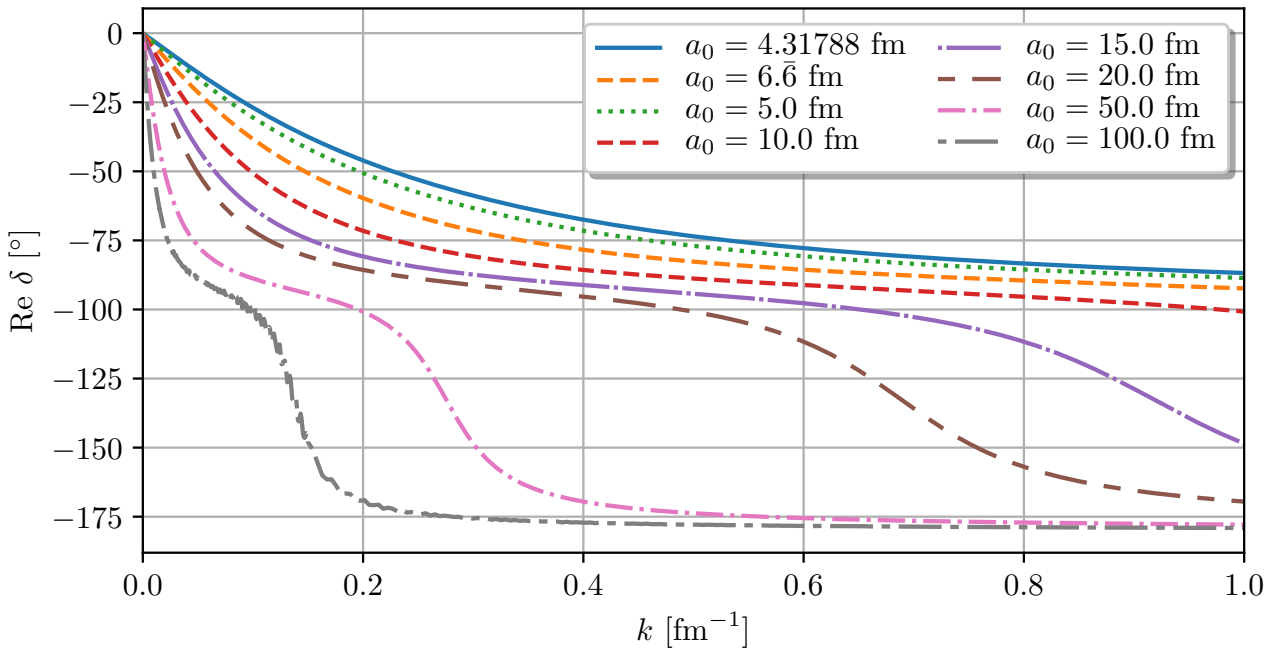

Figure 9.1.: The real part of the phase shifts for the third neutron in a relative S-wave and for the eight different scattering lengths considered. The phase shifts are negative over the whole momentum range considered. So, the channel investigated has a repulsive character. Increasing the scattering length this effect becomes more dominant for even smaller momenta.

Comparing the phase shifts for the three different partial waves shows that the overall magnitude decreases for higher partial waves. For a third neutron in a relative S- and D-wave the phase shifts are negative over the whole momentum range considered. This indicates the repulsive structure of these channels. In comparison, the channel with the third neutron in a relative P-wave has an attractive interaction as the phase shifts are positive. Increasing the scattering length a_0 or equivalently decreasing the binding momentum of the dineutron the maximum of the phase shifts is shifted to smaller momenta for all three partial waves considered. This effect can be connected to the three-neutron pole on the unphysical sheet, which moves closer towards the origin of the complex momentum and energy planes, as will be shown in the next Chapter (cf. Section 10.4).
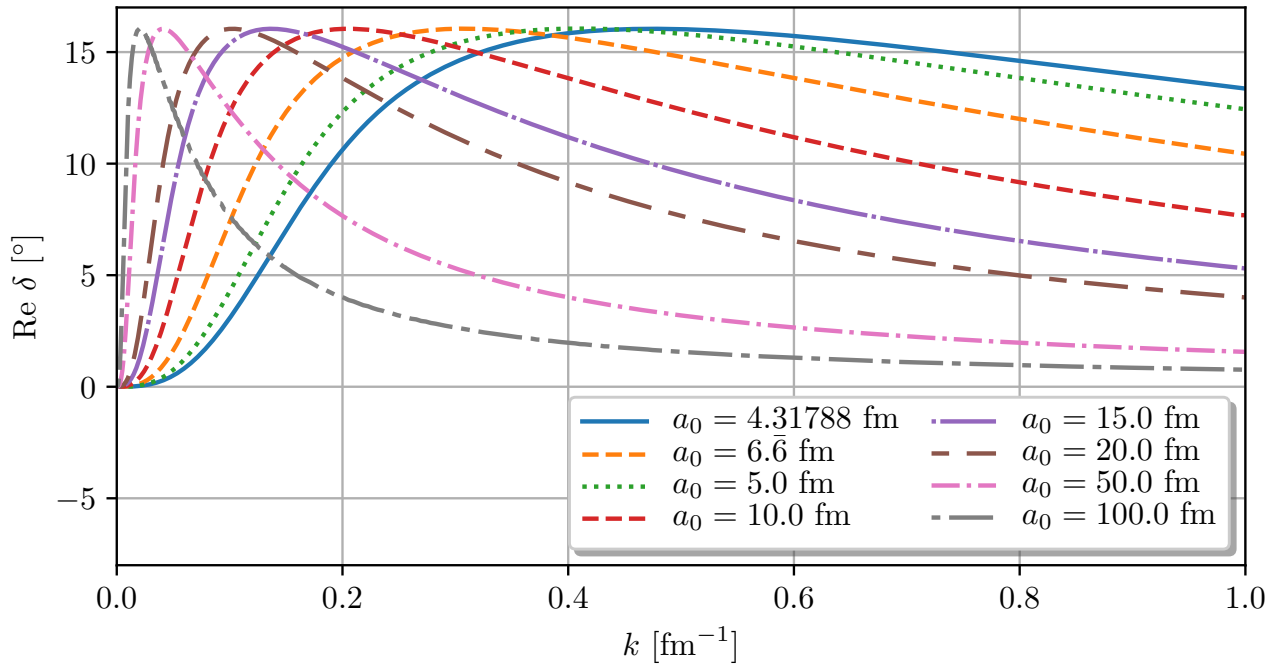
Figure 9.2.: The same curves as in Fig. 9.1 shown for the third neutron in a relative P-wave. The phase shifts are positive, indicating the attractive character of this channel. Increasing the scattering length the maximum is shifted to smaller momenta.
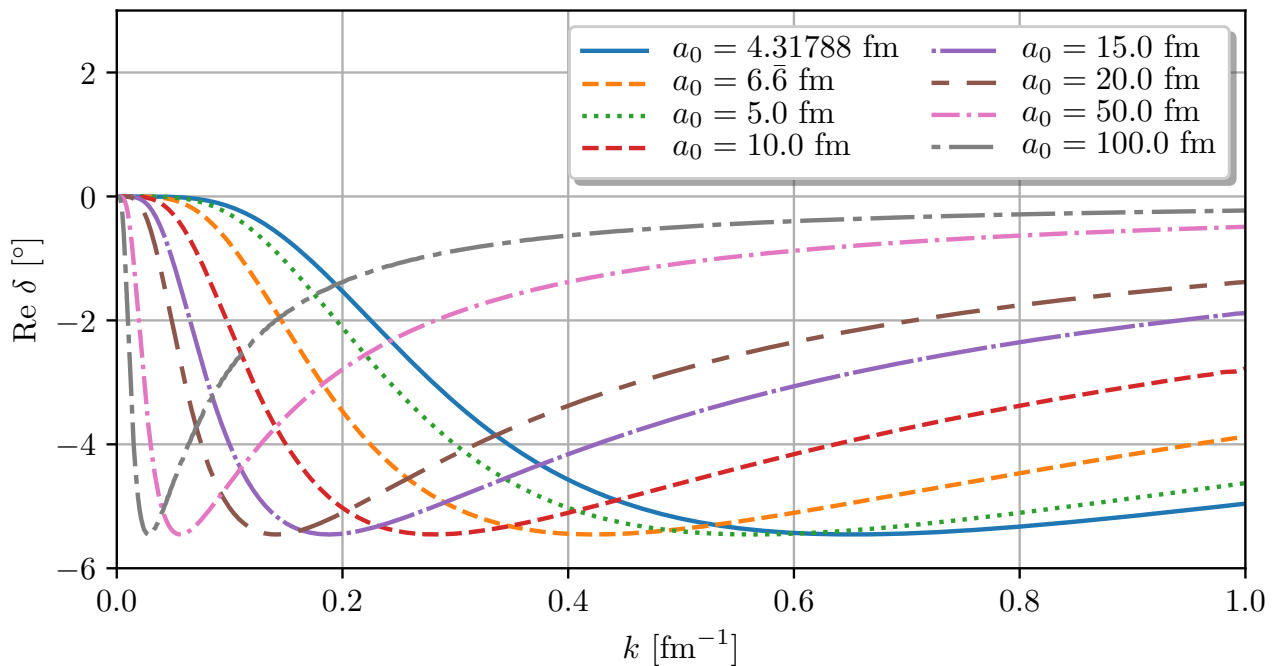
Figure 9.3.: The real part of the phase shifts for the third neutron in a relative D-wave for the eight different scattering length also considered in Fig. 9.1 and Fig. 9.2. Again, the phase shift is negative showing the repulsive character of this channel. In comparison to Fig. 9.1 the overall magnitude of the curves is much smaller.

9.1.1. Universal relation

In the limit of a shallow dineutron binding energy, up to the breakup of the dineutron, the dineutron-neutron scattering parameters of the ERE follow universal relations. They can be written as a constant times the dimer binding momentum $\gamma = a_0^{-1}$. In the following, we will derive these relations and fit the parameters by our phase shifts for the third neutron in a relative S-, P- and D-wave.

The investigation in which the third neutron is considered in a relative S-wave has been performed different times before. The first work was carried out by Skorniakov and Ter-Martirosian in 1957 [111]. Further calculations have been done at the beginning of this century by Petrov *et al.* [145, 146]. All three coincided in the result $a_{nn-n}\gamma \approx 1.2$. A work applying an epsilon expansion lead to the value $a_{nn-n}\gamma \approx 1.11$ [147]. Further studies applying a correlated Gaussian basis-set expansion technique [148] and a momentum space integral equation approach [149, 150] resulted in the coefficient $a_{nn-n}\gamma \approx 1.18$. A similar result was found in the work by Tan [151], $a_{nn-n}\gamma \approx 1.1790662349$. Finally, applying the same ansatz as within this work, Bour *et al.* [152] obtained a value $a_{nn-n}\gamma \approx 1.17907(1)$. While all results for the scattering length are almost equal, this is not true for the effective range. The work using the correlated Gaussian basis-set expansion technique [148] obtained a value $r_{nn-n}\gamma \approx 0.08(1)$. This value is in contrast to the result by Bour *et al.* [152], $r_{nn-n}\gamma \approx -0.0383(3)$. Beside the solution of the integral equation, Bour *et al.* [152] apply a lattice formalism. This technique gives the values $a_{nn-n}\gamma \approx 1.174(9)$ and $r_{nn-n}\gamma \approx -0.029(13)$.

First, consider the ERE, Eq. (2.27),

$$k^{2l+1} \cot \delta_l(k) = -\frac{1}{a_l} + \frac{1}{2}r_l k^2 - P_l r_l^3 k^4 + d_{4,l} k^6 + \mathcal{O}\left(k^8\right) \, , \tag{9.3}$$

which in general has the unit $(\text{fm}^{-1})^{2l+1}$. Based on the unit of the ERE, the scaling of the ERE parameters as functions of the scattering length can be derived:

$$
\begin{aligned}
[a_l] &= \text{fm}^{2l+1} \Rightarrow a_l \sim a_0^{2l+1} \, , \\
[r_l] &= \text{fm}^{-2l+1} \Rightarrow r_l \sim a_0^{-2l+1} \, , \\
[P_l] &= \text{fm}^{4l} \Rightarrow P_l \sim a_0^{4l} \, , \\
[d_{4,l}] &= \text{fm}^{-2l+5} \Rightarrow d_{4,l} \sim a_0^{-2l+5} \, .
\end{aligned}
\tag{9.4}
$$

Altogether, the "universal representation" of the ERE only dependent on the scattering length reads,

$$k^{2l+1} \cot \delta_l(k) = -\frac{c_1}{a_0^{2l+1}} + \frac{c_2}{2}a_0^{-2l+1}k^2 - c_3 a_0^{-2l+3}k^4 + c_4 a_0^{-2l+5}k^6 + \mathcal{O}\left(k^8\right) \, . \tag{9.5}$$

where the coefficients c_i will be fitted to phase-shift data. Note that for any partial wave at some order the ERE becomes proportional to a_0, such that it diverges for $a_0 \to \infty$. This effect will become problematic for the extrapolation to an unbound dineutron system discussed in the next Section.

To determine the universal relations the phase shifts are used to derive the representation $k^{2l+1} \cot \delta_l(k)$. For each partial wave and scattering length these representations are fitted to the ERE, Eq. (9.5). For a

given partial wave the different fits are averaged. This results in the three universal relations:

$$
\begin{aligned}
\text{S} - \text{wave}: \qquad & k \cot \delta_0 = -\frac{1}{1.17694(9)a_0} + \frac{0.0523(4)a_0}{2}k^2 + \mathcal{O}\left(k^4\right) , \\[6pt]
\text{P} - \text{wave}: \qquad & k^3 \cot \delta_1 = -\frac{-1.0499(1)}{a_0^3} + \frac{4.3859(11)}{2a_0}k^2 + 1.3338(6)a_0 k^4 + \mathcal{O}\left(k^6\right) , \\[6pt]
\text{D} - \text{wave}: \qquad & k^5 \cot \delta_2 = -\frac{2.8258(6)}{a_0^5} + \frac{-21.345(21)}{2a_0^3}k^2 - \frac{11.422(24)}{a_0}k^4 \\
& \qquad\qquad\qquad - 2.061(13)a_0 k^6 + \mathcal{O}\left(k^8\right) .
\end{aligned}
\tag{9.6}
$$

The representation for a third neutron in a relative S-wave can be compared to the results of previous works. The leading term connected to the scattering length, $a_{nn-n}\gamma \approx 1.17694(9)$, is in very good agreement with the other published values. However, considering the term connected to the effective range, $r_{nn-n}\gamma \approx 0.0523(4)$, shows a discrepancy to the work by von Stecher $et\ al.$ [148] ,$r_{nn-n}\gamma \approx 0.08(1)$, and Bour $et\ al.$ [152] , $r_{nn-n}\gamma \approx -0.0383(3)$. While the absolute value has the same order of magnitude, the sign of this work and the work by von Stecher $et\ al.$ differs in comparison to the result by Bour $et\ al.$. This small difference in the results of this work and the work by Bour $et\ al.$ can be explained by the implicit contribution of an neutron-neutron effective range due to the finite cutoff $\Lambda = 15$ fm^{-1} applied within this work. As was shown for example in Ref. [153] the contribution of this effective range results in an increasement of the dineutron-neutron effective range.

9.2. Extrapolation to the physical dineutron - $a_0 < 0$ fm

Now, the phase shifts are to be extrapolated in a_0^{-1} to the regime of an unbound dineutron. The problematic point of this extrapolation is the value $a_0^{-1} = 0$ fm^{-1}. As shown in the previous Section, the ERE scales like $\mathcal{O}\left(k^n\right) \sim a_{nn}^{n-2l-1}, n = 0, 2, 4, \ldots$. So, independent of the partial wave considered, it diverges for n large enough at this transition point from a bound to an unbound dineutron. This singularity complicates the fitting procedure.

In the following, different models for the extrapolation will be discussed. The first model considered is the modified effective range expansion

$$
\text{Model 1}: \qquad k^{2l+1} \cot \delta_l = -\frac{c_1}{a_0^{2l+1}} + \frac{c_2}{2}k^2 + \mathcal{O}\left(k^4\right) .
\tag{9.7}
$$

In comparison to the universal representation the singular dependence on a_0 in the k^2 term is dropped. So, this representation is non-singular at the transition point. It presents the simplest model applied within this work. Further, we will consider the unmodified universal representation derived in the previous Section

$$
\text{Model 2}: \qquad k^{2l+1} \cot \delta_l = -\frac{c_1}{a_0^{2l+1}} + \frac{c_2}{2}a_0^{-2l+1}k^2 - c_3 a_0^{-2l+3}k^4 + \mathcal{O}\left(k^6\right) .
\tag{9.8}
$$

To circumvent the singularity at the transition point, the inverse universal representation is considered as another model,

$$
\text{Model 3}: \qquad \left[k^{2l+1} \cot \delta_l\right]^{-1} = \left[-\frac{c_1}{a_0^{2l+1}} + \frac{c_2}{2}a_0^{-2l+1}k^2 - c_3 a_0^{-2l+3}k^4 + \mathcal{O}\left(k^6\right)\right]^{-1} .
\tag{9.9}
$$

However, in the limit $k \to 0$ it scales as a_0^{2l+1}. So, for small k this equation becomes hard to fit, too. Therefore, as a final model we consider:

$$\text{Model 4}: \qquad a_0^{-2l-1}\left[k^{2l+1}\cot\delta_l\right]^{-1} = \left[-c_1 + \frac{c_2}{2}a_0^2 k^2 - c_3 a_0^4 k^4 + \mathcal{O}\left(k^6\right)\right]^{-1}. \qquad (9.10)$$

By scaling with singularity this model shows a smoother behavior around the transition point. The last three models are shown in Fig. 9.4 for the universal relation by Bour *et al.* [152],

$$k\cot\delta_0 = -\frac{1}{1.17907(1)a_0} + \frac{-0.0383(3)a_0}{2}k^2 + \mathcal{O}\left(k^4\right), \qquad (9.11)$$

and an arbitrary momentum $k = 0.1\,\text{fm}^{-1}$. This plot illustrates the advantages and complicating features of the models as discussed previously.
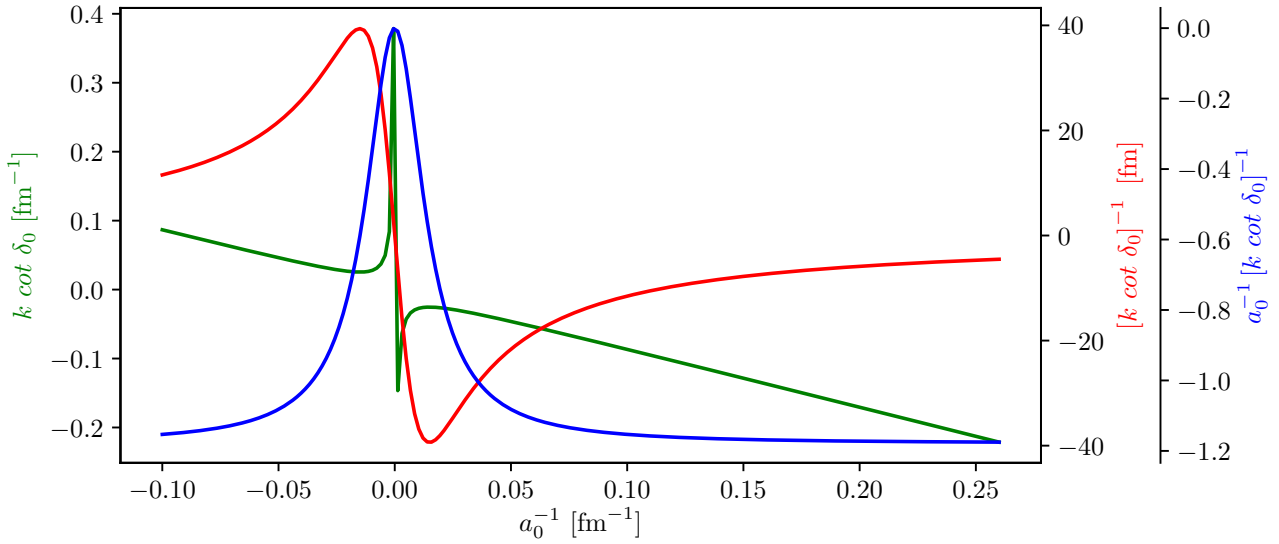

Figure 9.4.: The three different models 1, 2 and 3 based on the universal relation by Bour *et al.* [152] for $k = 0.1\,\text{fm}^{-1}$. The universal relation presents, as described, a singularity at $a_0^{-1} = 0\,\text{fm}^{-1}$. This singularity can be bypassed by considering the inverse universal relation. Anyhow, also this representation becomes large in the neighborhood of $a_0^{-1} = 0\,\text{fm}^{-1}$ for small k. One can correct for this behavior by considering the inverse universal relation multiplied by the singularity a_0^{-1}.

For practical purposes an application of the fits show that the results for the third and fourth model are equivalent. However, the fitting procedure for model 4 is simpler, such that model 3 will not be considered further.

Now, the phase shifts can be extrapolated to the physical neutron-neutron scattering length $a_0 = -18.9\,\text{fm}$. First, for each partial wave and each momentum bin the eight different scattering length are fitted by the different models. Within this work, we consider 300 momentum bins in the momentum range from zero to $k = 0.5\,\text{fm}^{-1}$. So, for every partial wave and model there are 300 different fits that are extrapolated. These different fits are combined to obtain the real part of the phase shifts as a function of the momentum. Note the difference between the universal relation and model 2. While the universal relations were fitted for a fixed scattering length as function of the momentum, model 2 is fitted for a fixed momentum as a

function of the scattering length.

Section 9.2 shows the result for the phase shifts for the third neutron in a relative S-wave together with the error bands due to the fitting. The calculation is compared to the universal relation derived by Bour *et al.* [152] and to the universal relation derived within this work, Eq. (9.6). Further, the three models 1, 2 and 4 in the representation up to $\mathcal{O}\left(k^4\right)$ are presented. The results by model 2 and 4 as well as the universal relation derived within this work agree pretty well. Also the phase shifts from model 1 and the work by Bour *et al.* are in agreement with each other. For small momenta, up to $k = 0.05\,\mathrm{fm}^{-1}$ all curves are in very good agreement with each other. While the uncertainty due to the extrapolation for models 2 and 4 is rather small, the uncertainty for the simpler model 1 increases for larger momenta. In comparison to the positive scattering length region, the phase shifts are now positive indicating the attractive character of the channel. This effect can be motivated by the dependence of the universal relations on odd powers of a_0, only. So, it is also present for the third neutron in a relative P-wave, Fig. 9.6. Here, only the more advanced models 2 and 4 up to order $\mathcal{O}\left(k^6\right)$ are shown together with the universal relation derived within this work. Again, all curves agree pretty well up to momenta of the order $k = 0.05\,\mathrm{fm}^{-1}$. The following structure seems to be harder to be described as indicated by the larger error bands. Nevertheless, all three curves show a similar behavior only differing in their magnitude. For larger momenta, the results of both models agree well, again. Finally, the results for the third neutron in a relative D-wave are shown in Fig. 9.7. Here, beside the universal relation, only model 2 (up to order $\mathcal{O}\left(k^8\right)$) for illustrative reasons is presented. The uncertainty of the extrapolation is so large, that no statement on the curve can be made. However, comparing the curve with the universal relation, and ignoring the uncertainty band, shows a good agreement between both.
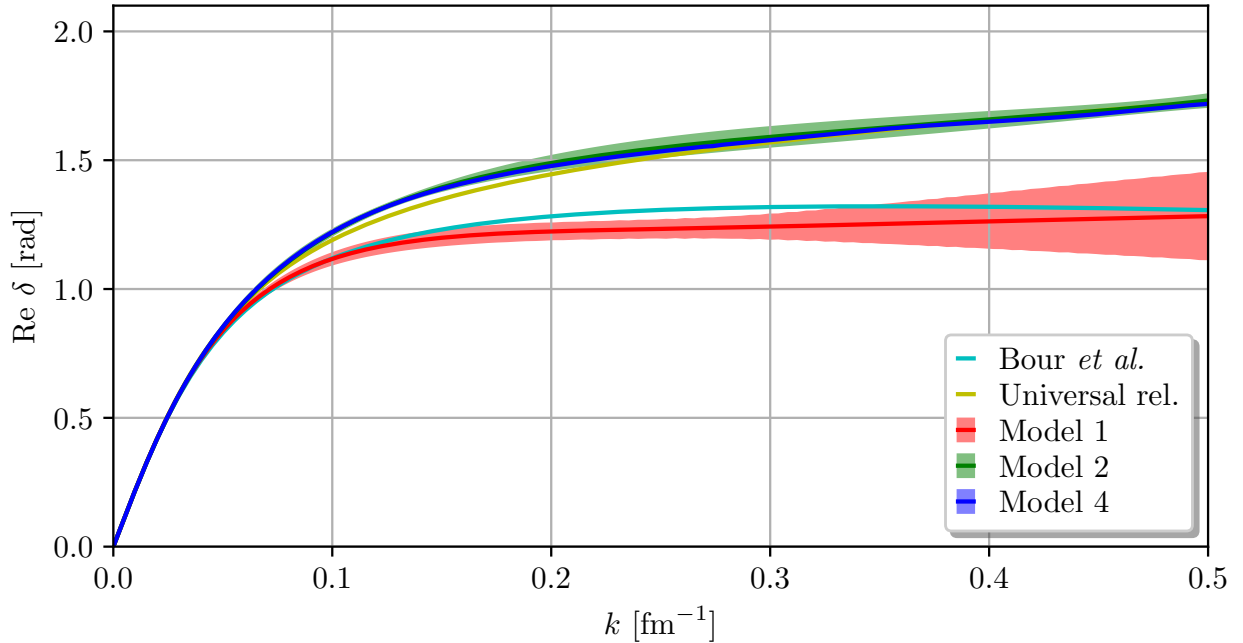
Figure 9.5.: The extrapolated phase shifts at $a_0 = -18.9\,\mathrm{fm}$ for the third neutron in a relative S-wave. The universal relations by Bour *et al.* [152] and the one derived within this work, Eq. (9.6), are shown. Further, the models 1, 2 and 4 up to $\mathcal{O}\left(k^4\right)$ are presented together with their error bands due to the extrapolation. Models 2 and 4 and the universal relation derived within this work show a very good agreement. Also the universal relation by Bour *et al.* and model 1 are in agreement with each other. However, the two groups of results show a different behavior for momenta larger than $k = 0.05\,\mathrm{fm}^{-1}$.
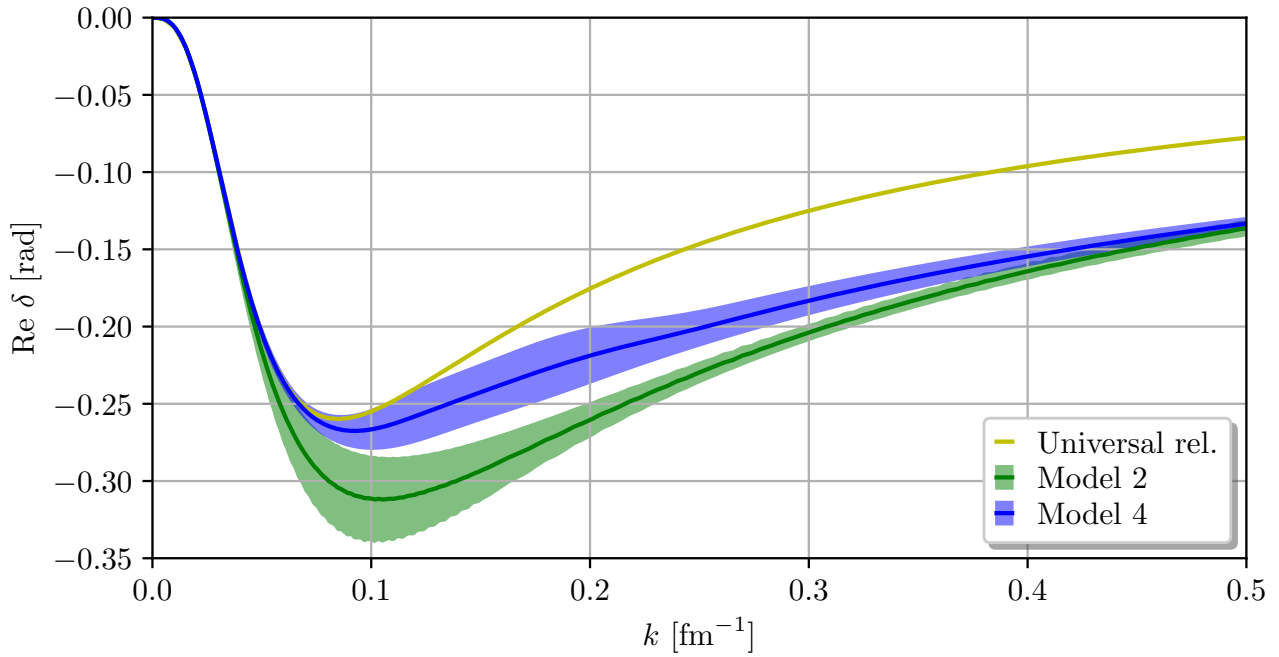
Figure 9.6.: The universal relation, Eq. (9.6), and the models 2 and 4 up to order $\mathcal{O}\left(k^6\right)$ for the third neutron in a relative P-wave. While the structure at $k = 0.1\,\text{fm}^{-1}$ is harder to describe, the models agree pretty well for small and larger momenta. The universal relation is only in agreement with the models for small momenta. Nevertheless, all results show a similar behavior.
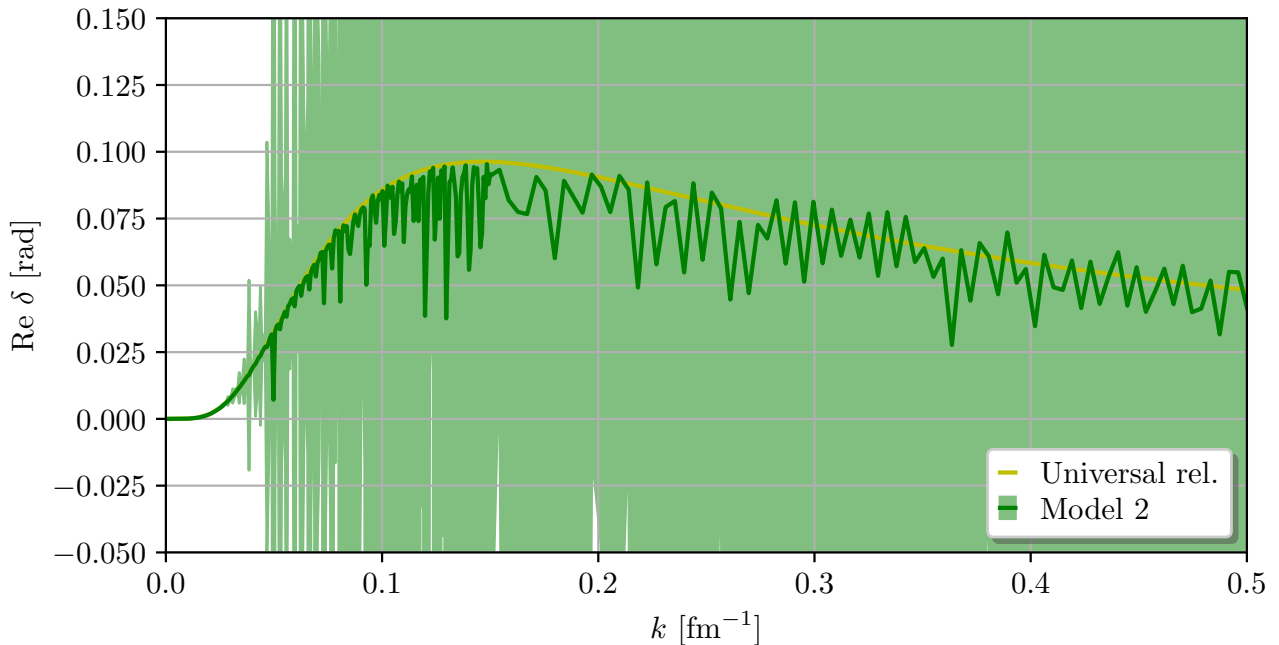
Figure 9.7.: The real part of the extrapolated phase shift for the third neutron in a relative D-wave. The universal relation is shown together with model 2. The uncertainty band of model 2 is that large, that no statement on the correct curve can be made.

The three-neutron system - Phase shifts & time delay

These phase shifts can now be compared to the work by Higgins *et al.* using the adiabatic hyperspherical formalism [64, 65]. Within their formalism they investigated the phase shifts and time delays for the three- and four-neutron systems. However, note that to their three-neutron phase shifts all channels with $J^\pi = 3/2^-$ contribute. So, only a rather qualitative comparison is possible. Their three- as well as four-neutron phase shifts start a $\delta = 0°$ for $k = 0\,\text{fm}^{-1}$ and rapidly rise to almost $\delta = 90°$ for the three-neutron and to almost $\delta = 180°$ for the four-neutron system. This rapid increase results in a peak of the time delay at $k = 0\,\text{fm}^{-1}$. Within the three partial waves considered within this Chapter only the P-wave case corresponds to the quantum numbers $J^\pi = 3/2^-$. As can be seen in Fig. 9.6, the phase shifts are negative over the whole momentum range shown. So, considering only this channel the results are in disagreement with the work by Higgins *et al.*. However, beside a neutron-neutron interaction in the $^1S_0$ channel also interactions in a P-wave channel contribute. These interactions would result in the third neutron in an even partial wave, e.g. a S- or D-wave. Comparing the S-wave phase shifts shown in Section 9.2 with the results by Higgins *et al.* they show a very similar behavior. Together with further corrections, e.g. the $^1S_0$ channel with a third neutron in a relative P-wave, it is possible to derive phase shifts with qualitatively very good agreement to the results using the adiabatic hyperspherical formalism.

10 The three-neutron system - analytical continuation

The main part of this work deals with the three-neutron system. Within this Chapter, the formalism of analytical continuation is applied to search for resonances and virtual states in this system. First, the Faddeev equations derived in the Lagrange and Faddeev formalism are presented and compared with each other. Due to the Pauli principle, the neutron-neutron interaction can only be in the $^1S_0$ channel. In the following, there will be different relative partial waves of the third neutron discussed. The most probable channel, following previous studies [67], is a relative P-wave ($l = 1$). It results in the possible states $J^\pi = \frac{1}{2}^-$ and $\frac{3}{2}^-$, which are degenerate in leading-order pionless EFT. Further, we will discuss a relative S-wave ($l = 0$), which results in the state $J^\pi = \frac{1}{2}^+$. As a first step, it is shown that the three-neutron system at LO does not present any bound state. To be comparable to the benchmark calculation of the three-boson system, the Yamaguchi model is introduced. It allows to create a bound three-neutron state, which can be transformed to a resonance reducing the interaction strength. However, note that this calculation is performed for an unphysically modified three-neutron system. Nevertheless, parts of this resonance trajectory can be reproduced by the LO pionless EFT potential for large, positive scattering lengths. So, the Yamaguchi model is used as a further benchmark for this work.

Parts of this Chapter have been published in this or similar form in Phys. Rev. C, vol. 105, no. 6, p. 064002 [68].

10.1. Faddeev equation

First, we compare the two different representations for the Faddeev equation derived within this work. The homogeneous Faddeev equation for the three-neutron system, following from the Lagrange formalism, is given by Eq. (3.45) and Eq. (3.46),

$$
R_l(p; E) = \int_0^\Lambda \mathrm{d}q \, q^2 Z_{2,l}\left(q, p; E\right) \tau_l\left(z\right) R_l\left(q; E\right) ,
$$
$$
Z_{2,l}\left(k, p; E\right) = -\frac{1}{2} \int_{-1}^{+1} \mathrm{d}x \frac{P_l(x)}{M_N E - k^2 - p^2 - kpx} .
$$

(10.1)

It can be compared to the Faddeev equation following from the Faddeev formalism, Eq. (4.27) and Eq. (4.28),

$$F_l\left(u_2\right) = \int \mathrm{d}u_2' u_2'^2 Z_{2,l}\left(u_2', u_2; E\right) \tau_l\left(z\right) F_l\left(u_2'\right),$$

$$Z_{2,l}\left(u_2', u_2; E\right) = -\frac{1}{2} \int_{-1}^{+1} \mathrm{d}x \frac{\langle g|\pi_1\rangle P_l(x) \langle \pi_2|g\rangle}{M_N E - u_2'^2 - u_2^2 - u_2' u_2 x}.$$

(10.2)

Here, it was used that $\lambda = 0$ and $G_{\mathrm{ii}}(u_2 u_2' x) = -0.5 P_l(x)$. Both representations are mainly equivalent. However, the two-body interaction kernel $Z_{2,l}$ derived from the Faddeev formalism further includes the two regulator functions in the numerator. To be consistent with the calculation for the three-boson system, here also the Faddeev equation derived from the Faddeev formalism will be applied. Further, similar to the three-boson system, the integral equation will be regulated by a Gaussian regulator $\langle p|g\rangle = \exp\left(-p^2/\Lambda^2\right)$.

10.2. 3n bound state

In the following, the aim is to proceed as for the three-boson system. So, we start at a three-neutron bound state for some unphysical scattering length. Then we reduce the interaction strength and follow the pole trajectory to the unphysical sheet. However, it can be shown using the structure of the Faddeev equation that no three-neutron bound state is possible. Investigating Eq. (10.2) in the limit $\Lambda \to \infty$ shows that the equation contains only one parameter, the S-wave scattering length a_0. So, it is possible to rescale all momenta with the absolute value of the scattering length and express the energy as a function of the squared scattering length

$$F_l(u_2) = -\frac{1}{\pi} \int \mathrm{d}u_2' u_2'^2 \int_{-1}^{+1} \mathrm{d}x \frac{\langle g|\pi_1\rangle P_l(x) \langle \pi_2|g\rangle}{M_N \tilde{E} - u_2'^2 - u_2^2 - u_2' u_2 x} \frac{F_l(u_2')}{\pm 1 + i\sqrt{M_N \tilde{E} - \frac{3}{4} u_2'^2}},$$

(10.3)

with $\tilde{E} = |a_0|^2 E$. The upper sign corresponds to positive scattering length, while the lower sign represents negative scattering length.

This procedure is similar to the three-boson system, where all pole trajectories in the Efimov plot are located on top of each other, if they are expressed in units of a_-. Note that in the three-boson system there is a second parameter, the three-body force, that had to be fixed first.

So, in the three-neutron system we have to distinguish two cases. On the one hand, there is the physical case with a negative scattering length and on the other hand one has to consider a positive scattering length. The region around $1/a_0 = 0\,\mathrm{fm}^{-1}$ is hard to investigate using this formalism as the corresponding energies $\tilde{E}$ would be close to infinity. However, this region can also be excluded using the continuity of the pole trajectory if there is no pole for all other scattering length. So, solving Eq. (10.3) for positive as well as negative a_0, the upper and the lower sign, shows no evidence for a possible three-neutron bound state at leading order. Finite range effects as well as higher-order corrections cannot change this conclusion as they are included perturbatively. Reducing the regulator parameter Λ to a finite value, it is still possible to exclude possible bound states with energies well below the regulator parameter, $|E| \ll \Lambda^2$.

10.3. Yamaguchi model

As shown in the previous Section, the three-neutron system presents no bound state using pionless EFT. This presents a complicating feature performing the analytical continuation. To verify the results derived from pionless EFT, the Yamaguchi model [154, 155] is used. This work follows the representation by Glöckle [44], who previously applied the Yamaguchi model to the three-neutron system. It presents the two-body interaction

$$V_2\left(k,p\right) = -\kappa g(p)g(k)\,,$$
$$g(p) = \frac{1}{p^2 + \beta^2}\,, \tag{10.4}$$

where the Yamaguchi formfactor $g(p)$ can be interpreted as a regulator. This behavior becomes clearer if the potential is redefined to

$$V_2\left(k,p\right) = -\tilde{\kappa}\tilde{g}(p)\tilde{g}(k)\,,$$
$$\tilde{g}(p) = \frac{\beta^2}{p^2 + \beta^2}\,. \tag{10.5}$$

The redefined formfactor fulfills the limits defining a regulator,

$$\tilde{g}(0) = 1\,,$$
$$\lim_{p \to \infty} \tilde{g}(p) = 0\,. \tag{10.6}$$

Nevertheless, to be comparable to the work by Glöckle the first representation is applied.

The Yamaguchi formfactor implements a further parameter β. Together with the parameter κ from the definition of the two-body potential it is possible to reproduce not only the scattering length, but also higher effective range parameters. This will be shown in the following. The Faddeev equation for the three-neutron system applying the Yamaguchi model is given by Eq. (10.2), where τ follows from Eq. (5.61),

$$\tau(z) = \left[-\frac{1}{\kappa} - \frac{\pi}{4\beta} \frac{1}{\left(\sqrt{z} + i\beta\right)^2} \right]^{-1}$$
$$= \frac{-\kappa\left(\sqrt{z} + i\beta\right)^2}{\left[\sqrt{z} + i\beta + i\sqrt{\frac{\kappa\pi}{4\beta}}\right]\left[\sqrt{z} + i\beta - i\sqrt{\frac{\kappa\pi}{4\beta}}\right]}\,. \tag{10.7}$$

To compare the Yamaguchi model to a pionless EFT calculation the parameters κ and β has to be connected to the parameters of the ERE. This is done by using the definitions

$$t_l\left(k,p;E\right) = \frac{1}{2\mu}g\left(k\right)g\left(p\right)\tau_l\left(z\right)\,, \tag{10.8}$$

and Eq. (6.6)

$$k^{2l+1}\cot\delta_l - ik = -\frac{1}{\pi\mu}\frac{1}{t_l\left(k,k;E_k\right)}\,. \tag{10.9}$$

So, one obtains

$$k\cot\delta_0 - ik = \frac{2}{\pi}\left(k^2 + \beta^2\right)^2 \frac{\left[\sqrt{2\mu E_k} + i\beta + i\sqrt{\frac{\kappa\pi}{4\beta}}\right]\left[\sqrt{2\mu E_k} + i\beta - i\sqrt{\frac{\kappa\pi}{4\beta}}\right]}{\kappa\left(\sqrt{2\mu E_k} + i\beta\right)^2}$$
$$= \frac{2}{\pi}\frac{1}{\kappa}\left[\beta^4 - \frac{\kappa\pi\beta}{4} + k^2\left(2\beta^2 + \frac{\kappa\pi}{4\beta}\right) + k^4 - i\frac{\kappa\pi}{2}k\right]\,. \tag{10.10}$$

The imaginary part cancels as expected. So, a comparison leads to,

$$-\frac{1}{a_0} = \frac{2}{\pi}\frac{1}{\kappa}\left(\beta^4 - \frac{\kappa\pi\beta}{4}\right),$$
$$\frac{r_0}{2} = \frac{2}{\pi}\frac{1}{\kappa}\left(2\beta^2 + \frac{\kappa\pi}{4\beta}\right), \tag{10.11}$$
$$-P_0 r_0^3 = \frac{2}{\pi}\frac{1}{\kappa}.$$

This comparison shows that the Yamaguchi model includes the first three terms of the ERE non-perturbatively, while all higher orders vanish.

To be comparable to the work by Glöckle [44], the parameters are fixed such that one reproduces the scattering length $a_0 = -23.47\,\text{fm}$ and the effective range $r_0 = 2.401\,\text{fm}$. This corresponds to the values $\kappa = 2.65\,\text{fm}^{-3}$ and $\beta = 1.304\,\text{fm}^{-1}$. Further, in the Yamaguchi model, similar to the work by Glöckle, we only consider a relative P-wave for the third neutron, $l = 1$. In the following, the parameter β will be kept fixed, while the interaction strength κ is varied. Note that for κ larger than $2.823\,\text{fm}^{-3}$ the corresponding scattering length is positive. For large κ the three-neutron system presents a bound state. Reducing the interaction strength, the three- as well as the two-body binding energy decrease. At $\kappa = 11.18\,\text{fm}^{-3}$ both values agree and the three-neutron bound states moves through the two-body branch cut onto the fourth quadrant of the relative energy plane, becoming a resonance. At this point either the explicit or the implicit contour deformation can be applied. Both formalisms result in indistinguishable results, such that we will not explicitly differentiate between them. Decreasing the value of κ further, the resonance performs the trajectory shown in Fig. 10.1. Finally at $\kappa = 2.823\,\text{fm}^{-3}(a_0^{-1} = 0\,\text{fm}^{-1})$ the trajectory arrives at the origin of the complex energy plane. Decreasing the interaction strength further, the dineutron system becomes unbound and the pole trajectory continues onto an unphysical sheet different from the one adjacent the lower rim of the physical sheet. This behavior can be motivated by investigating contour plots of the relevant unphysical sheet of the complex energy plane. These plots show no effect of a resonance or a virtual state. So, based on the continuity of the pole trajectory, the pole trajectory has to continue on a different unphysical sheet far away from the lower rim of the physical sheet and any effect on observables vanishes.
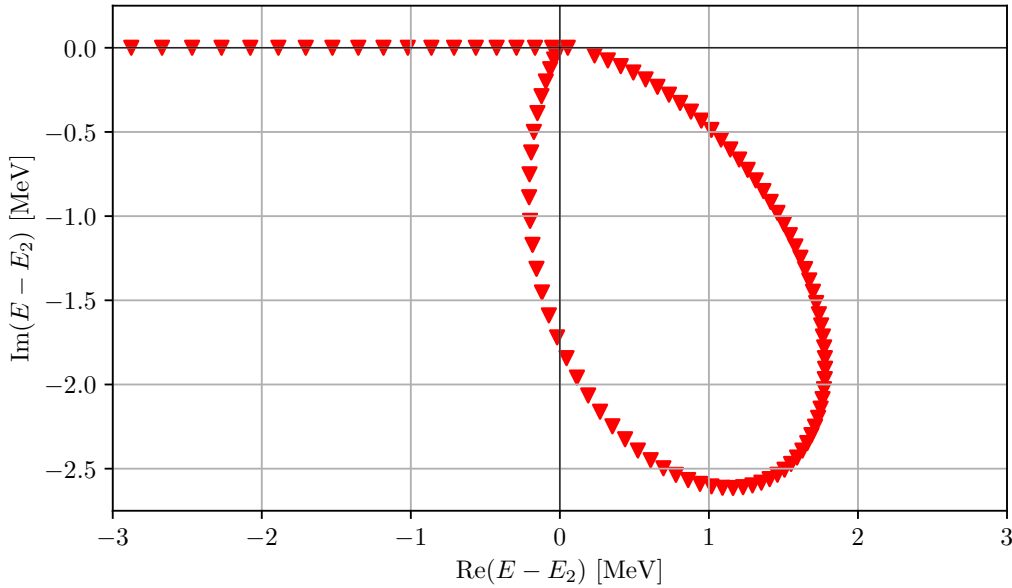

Figure 10.1.: The three-neutron pole trajectory calculated using the Yamaguchi model

10.4. Pionless EFT

Following the pionless EFT power counting, we are able to reproduce the pole trajectory in the Yamaguchi model next to the origin for r_0/a_0 going to zero. Performing a similar calculation as for the Yamaguchi model results in the plot shown in Fig. 10.2. It shows the pole trajectory in the Yamaguchi model in comparison to the LO pionless EFT trajectory together with the LO error band next to the origin on the unphysical sheet accessible through the two-body cut. Along both trajectories selected values of the scattering length are indicated.
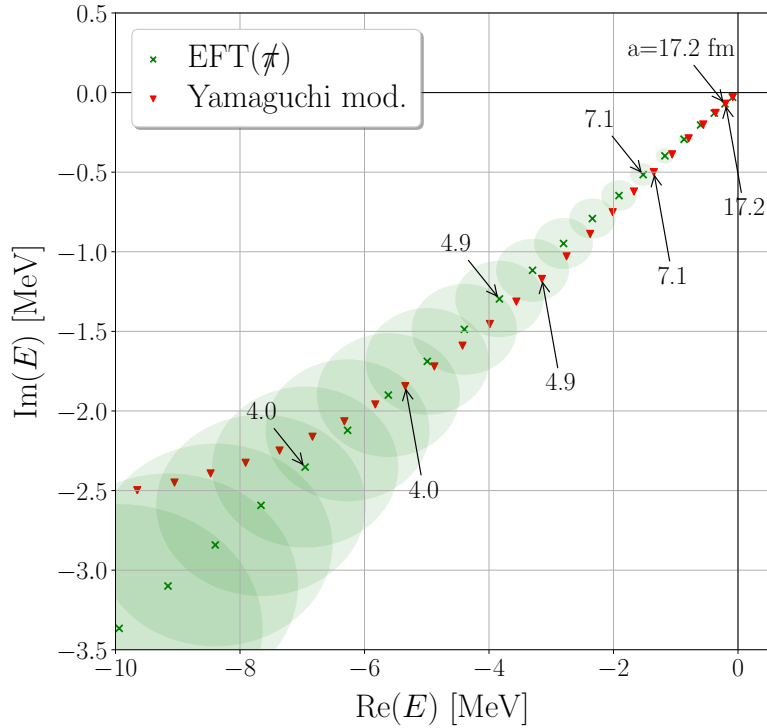
Figure 10.2.: The pole trajectory of the three-neutron system ($J^\pi = \frac{1}{2}^-$ and $J^\pi = \frac{3}{2}^-$) for positive scattering length for a pionless EFT interaction together with the LO error bands in comparison to a calculation using the Yamaguchi model. The values of the scattering length in fm for selected points are given by the numbers and arrows. The lower half-plane shows the unphysical sheet accessed through the two-body cut. Within the region where EFT($\not\pi$) is valid, both trajectories agree within the EFT error indicated by the LO circles.

Now, we can continue the trajectory towards the physical neutron-neutron scattering length considering an unbound dineutron system. As explained in the previous Section, the pole trajectory in the Yamaguchi model continues on an unphysical sheet different from the one adjacent to the lower rim of the physical sheet. To investigate the behavior for the pionless EFT potential, we perform a similar calculation as for the Yamaguchi model reducing the scattering length from $a_0 = -\infty$ fm to the physical value $a_0 = -18.9$ fm. First, the third neutron in a relative P-wave should be considered. Along this trajectory, the determinant of $\mathbb{1}$ minus the kernel of the Faddeev equation Eq. (10.2) is investigated, similar as it was done for example for the three-boson system. An example of a contourplot of the fourth quadrant of the complex energy plane for a scattering length along this path is shown in Fig. 10.3. Beside the rotated

three-body cut next to the negative imaginary axis, no behavior that can be connected to a resonance is visible. Beside the search for a resonance, we can further look for a virtual state. So, the cut has to be rotated into the second quadrant of the complex energy plane. An example of contourplot for this calculation is shown in Fig. 10.4. Similar to the fourth quadrant, it shows no structure connected to a virtual state.

These findings are also supported by the power counting. Around the transition point from a bound to an unbound dineutron system, r_0/a_0 is small and we should be able to recover the results of the Yamaguchi type regulator.
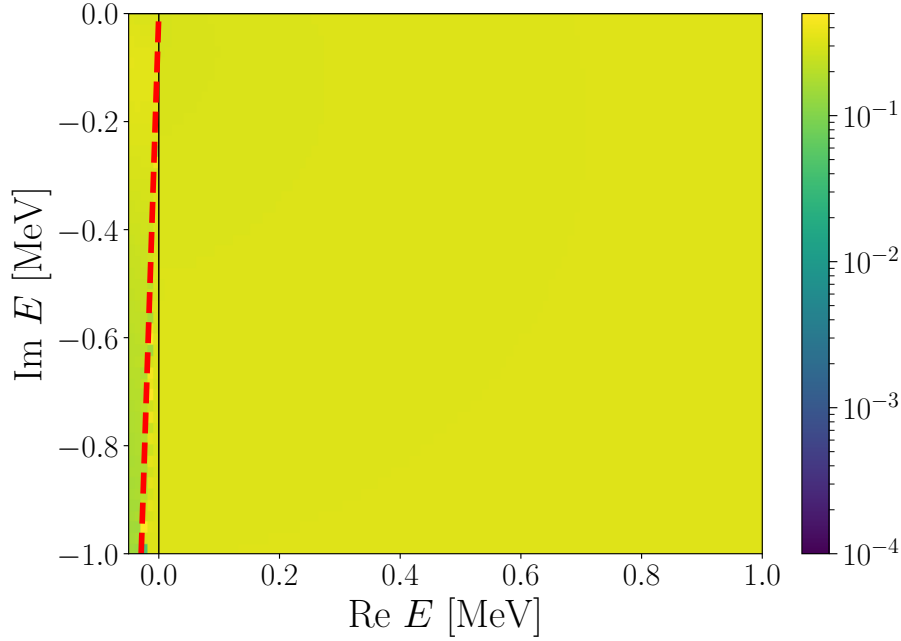
Figure 10.3.: A contour plot presenting the absolute value of the determinant of $\mathbb{1}$ minus the kernel of Eq. (10.2) on the unphysical sheet adjacent the positive real energy axis. A zero within this plot is equivalent to an eigenvalue equal to one of Eq. (10.2), which itself corresponds to a possible physical state. This calculation was performed for $a_0 = -18.77$ fm and a rotation angle $\varphi = 0.8$. The rotation angle becomes evident at the structure left to the negative imaginary axis, which corresponds to the rotated three-body cut.
Note that the order of magnitude of the data within this plot contains no physical content. It only depends on the parameters used for the numerical solution of the problem. Physically, the only relevant values are zeros.
So, this plot presents no evidence for a possible three-neutron resonance.

Finally, the third neutron in a relative S-wave, $J^\pi = \frac{1}{2}^+$ can be considered. The findings for this case are similar to those presented for a relative P-wave. Also here, a resonance or a virtual state in the three-neutron system can be excluded.
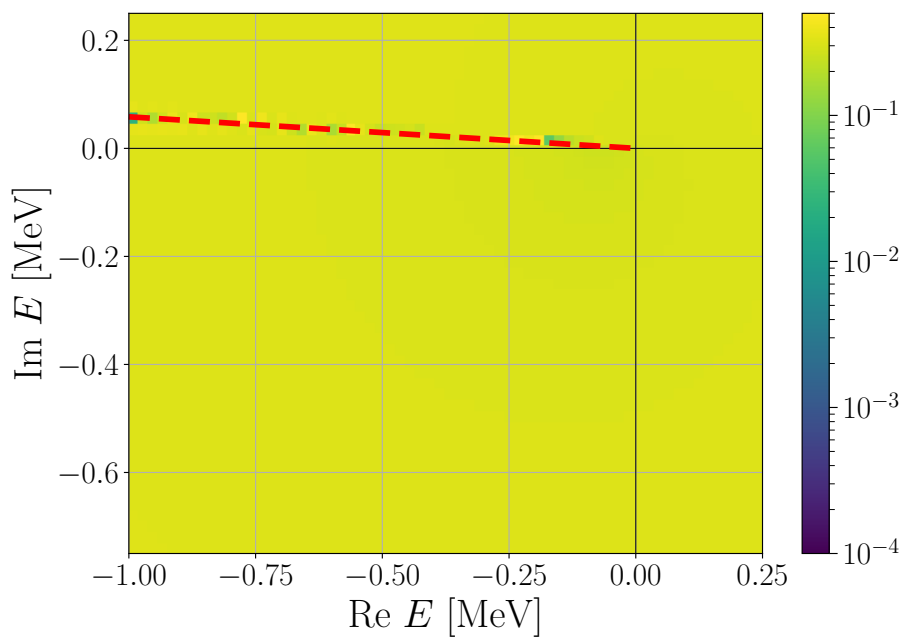
Figure 10.4.: A contour plot presenting same quantity as in Fig. 10.3. Here, the calculation was performed for $a_0 = -18.77$ fm and a rotation angle $\varphi = 1.6$. Again, the three-body cut is visible next to the negative real axis. It is indicated by the red dashed line. Similar to Fig. 10.3, this plot shows no evidence for a possible state of the three-neutron system on the unphysical sheet. Here, a possible virtual state can be excluded.

11 Point creation

Within this Chapter, the point production of the three-boson, the three-neutron and the four-neutron systems is investigated. In comparison to the scattering equations considered in the previous Chapters, the inhomogeneous term has to be replaced by a point source. The solution of these equations results in an amplitude with a dimer in the final state. These dimers are broken up and through appropriate symmetrization or anti-symmetrization, respectively, the corresponding equations for the point production amplitudes are derived. The point production amplitude is a quantity similar to the cross section. It is used to investigate the existence of resonances. Similar to the methods applied previously within this work, the three-boson system serves as a benchmark for the following investigation of the three-neutron system. Here, the point production amplitude is calculated and the existence of the resonance peak is shown. The point production amplitudes of the three- and four-neutron systems can further be described by the framework of nonrelativistic conformal field theory. It is shown that the point production amplitude of the three-neutron system follows these predictions, which rule out the existence of a resonance structure. Finally, the predictions of the nonrelativistic conformal field theory for the four-neutron system are presented. It is discussed, that they do not show a peak structure connected to a possible resonance.

11.1. Three bosons

The first system to be considered is the three-boson system. Similar to Chapter 7, it will be used as a benchmark for the three-neutron system. The aim is to derive an equation for the point production amplitude $R(E)$, a quantity which is proportional to the cross section. As we are not interested in the overall normalization, it contains the same physical content and can be used equivalently to the cross section.

The derivation is based on a Faddeev equation for the amplitude $\Gamma_l(E; p)$ (cf. Fig. 11.1). In comparison to the previous Chapters, the three-body force is explicitly set to zero. Its effect is incorporated by varying the cutoff Λ of the integral equation. Applying the Feynman rules the Faddeev equation reads

$$i\Gamma_l(E; p) = ig_{3,l}p^l + \int_0^\infty \mathrm{d}q \; q^2 Z_{2,l}(E; q, p) \, \tau_l(E; q) \, i\Gamma_l(E; q) \;,$$

$$\tau_l(E; q) = \left[\frac{1}{a_l} - \sqrt{\frac{3}{4}\boldsymbol{q}^2 - mE - i\varepsilon} \, \exp\left(-2\frac{mE - \frac{3}{4}\boldsymbol{q}^2}{\Lambda^2}\right) \mathrm{erfc}\left(\frac{\sqrt{-2\left(mE - \frac{3}{4}\boldsymbol{q}^2\right)}}{\Lambda}\right) \right]^{-1} \;. \qquad (11.1)$$

It describes the amplitude for the point creation of a diboson and a single boson, where $g_{3,l}$ is the point source in a given partial wave l. In the following, it will be set to one. Together with further factors
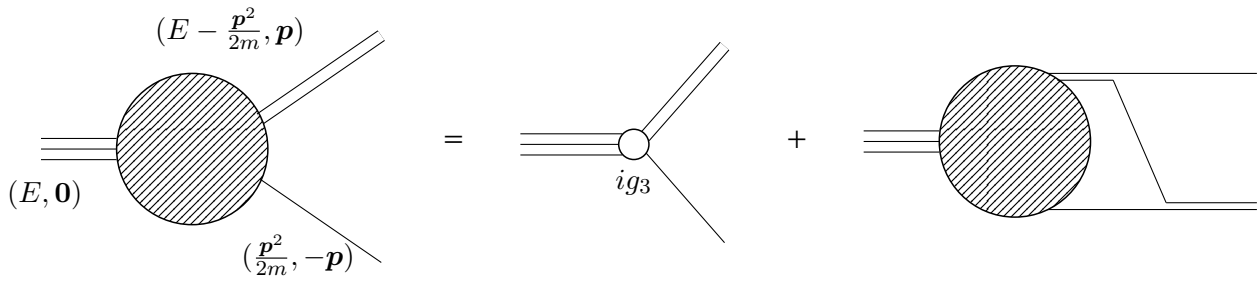
Figure 11.1.: Scattering equation for the point creation of a three-boson system.

appearing later in the derivation it can be summarized as a parameter of the theory that represents an overall normalization and has to be fitted to (experimental) data. Furthermore, a different renormalization condition (compare to Eq. (5.58)) is applied to be consistent to the code by König [156] used for benchmark reasons. This results in the modified representation of τ. However, we are not interested in a diboson-boson but a three-boson final state. So, the diboson has to be broken up. The corresponding amplitude is denoted by $\bar{\Gamma}_l$. Due to the bosonic structure of the system, it is defined by the symmetrized sum of all possible permutations, cf. Fig. 11.2, where it is implicitly assumed that all lines are on-shell.

Figure 11.2.: Symmetrized equation for the three-boson amplitude $\bar{\Gamma}_l$.

In general, for three distinguishable particles, there are $3! = 6$ permutations. However, three of the six

permutations are equivalent to the remaining ones, such that only three terms have to be considered,

$$
i\bar{\Gamma}_l\left(E;\boldsymbol{p},-\frac{\boldsymbol{p}}{2}+\boldsymbol{k}\right) = \left(\sqrt{Z}\right)^{-1}\frac{g_2^2}{\#}\left[i\Gamma_l\left(E;\boldsymbol{p}\right)\tau\left(E;-\boldsymbol{p}\right)P_l\left(\cos\theta_{\boldsymbol{p},\boldsymbol{k}}\right)\right.
$$
$$
+\, i\Gamma_l\left(E;-\frac{\boldsymbol{p}}{2}+\boldsymbol{k}\right)\tau\left(E;\frac{\boldsymbol{p}}{2}-\boldsymbol{k}\right)P_l\left(\cos\theta_{-\frac{\boldsymbol{p}}{2}+\boldsymbol{k},\boldsymbol{k}}\right)
$$
$$
\left.+\, i\Gamma_l\left(E;-\frac{\boldsymbol{p}}{2}-\boldsymbol{k}\right)\tau\left(E;\frac{\boldsymbol{p}}{2}+\boldsymbol{k}\right)P_l\left(\cos\theta_{-\frac{\boldsymbol{p}}{2}-\boldsymbol{k},\boldsymbol{k}}\right)\right],
$$

$$
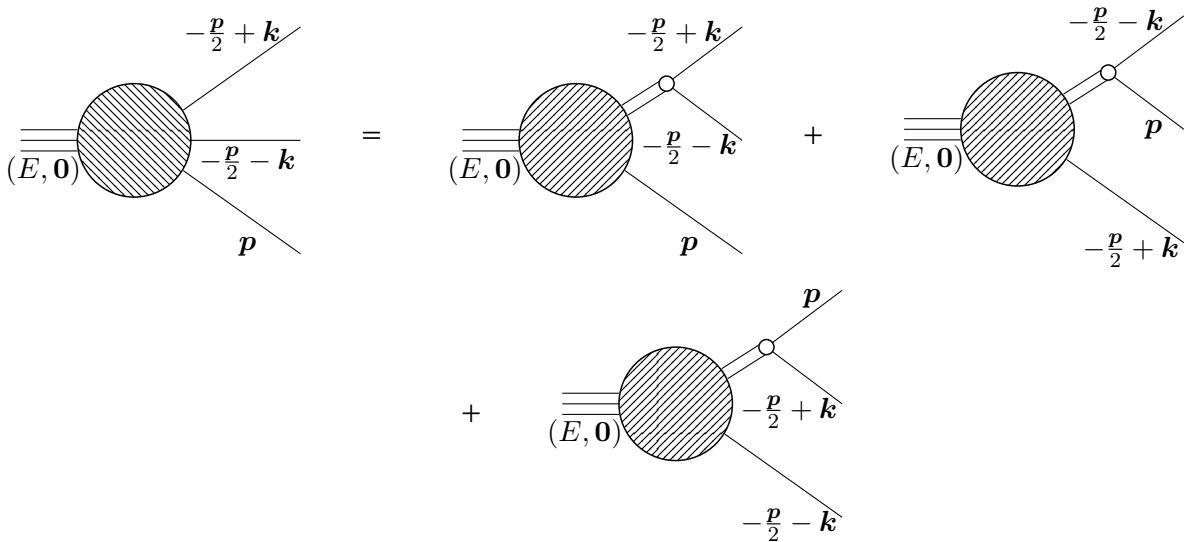\bar{\Gamma}\left(E;\boldsymbol{p},-\frac{\boldsymbol{p}}{2}+\boldsymbol{k}\right) := \sum_l (2l+1)\bar{\Gamma}_l\left(E;\boldsymbol{p},-\frac{\boldsymbol{p}}{2}+\boldsymbol{k}\right).
$$

(11.2)

The symmetrized amplitude includes several contributions. The inverse diboson wave function renormalization Z, which cancels the wave function renormalization contained in Γ_l, as well as the diboson-bb coupling g_2. The equation further contains a combinatorial factor $\#$, which is included in the factor fitted to (experimental) data. So, it is omitted for practical calculations. Note the modified definition of the partial-wave amplitude, here. In comparison to the usual definition, the Legendre polynomial is included within the definition of partial-wave projected amplitude $\bar{\Gamma}_l$, such that it does not depend on the magnitude of the momenta only.

Finally, the symmetrized amplitude can be used to calculate the point production amplitude $R(E)$. It is defined as the phase-space integral of $|\bar{\Gamma}|^2$,

$$
R(E) = \int \frac{\mathrm{d}^3 k}{(2\pi)^3} \int \frac{\mathrm{d}^3 p}{(2\pi)^3} \left|\bar{\Gamma}\left(E;\boldsymbol{p},-\frac{\boldsymbol{p}}{2}+\boldsymbol{k}\right)\right|^2 2\pi\delta\left[E - E_{\boldsymbol{p}} - E_{-\frac{\boldsymbol{p}}{2}+\boldsymbol{k}} - E_{-\frac{\boldsymbol{p}}{2}-\boldsymbol{k}}\right],
$$

(11.3)

where the δ-function ensures the energy conservation of the three outgoing bosons. The energy conserving δ-function can be simplified by applying the variable transformation for δ-distributions,

$$
\delta\left[g\left(x\right)\right] = \sum_n \frac{\delta\left(x - x_n\right)}{|g'\left(x_n\right)|}, \qquad g\left(x_n\right) = 0.
$$

(11.4)

This results in

$$
\delta\left[E - E_{\boldsymbol{p}} - E_{-\frac{\boldsymbol{p}}{2}+\boldsymbol{k}} - E_{-\frac{\boldsymbol{p}}{2}-\boldsymbol{k}}\right] = \delta\left[E - \frac{1}{2m}\left(\frac{3}{2}p^2 + 2k^2\right)\right] = \frac{\delta\left[k - \sqrt{mE - \frac{3}{4}p^2}\right]}{\left|-\frac{2}{m}\sqrt{mE - \frac{3}{4}p^2}\right|}.
$$

(11.5)

Note that the energy conservation sets a limit on the maximum value of p, $p \leq \sqrt{\frac{4}{3}mE}$.

The point production amplitude can be interpreted as a cross section (cf. Eq. (2.28)). So, it is sensitive to resonances and virtual states close to the physical sheet.

To derive the point production amplitude, the integral equation Eq. (11.1) for Γ_l has to be solved. In the following, to search for resonances, this is done for an unbound diboson system. So, the integral equation presents a branch cut along the positive real energy axis. The effect of this cut on the results can be avoided by calculating Γ_l not on the real axis, but slightly shifted onto the first quadrant of the complex energy plane, $E \to E + i\varepsilon$. Finally, one has to extrapolate to $\varepsilon = 0$. The third boson is to be considered in a relative S-wave, i.e. $l = 0$. So, the sum within Eq. (11.2) restricts to the contribution of one partial wave. Figure 11.3 shows the resulting point production amplitude for different imaginary parts of the

complex energy. For small imaginary parts, close to the physical sheet, a peak close to threshold becomes visible. This peak corresponds to a resonant state derived previously using the analytical continuation (cf. Section 7.5.2). Again, the three-boson system serves as a benchmark showing the applicability of the formalism to the search for resonances in the three-neutron system.
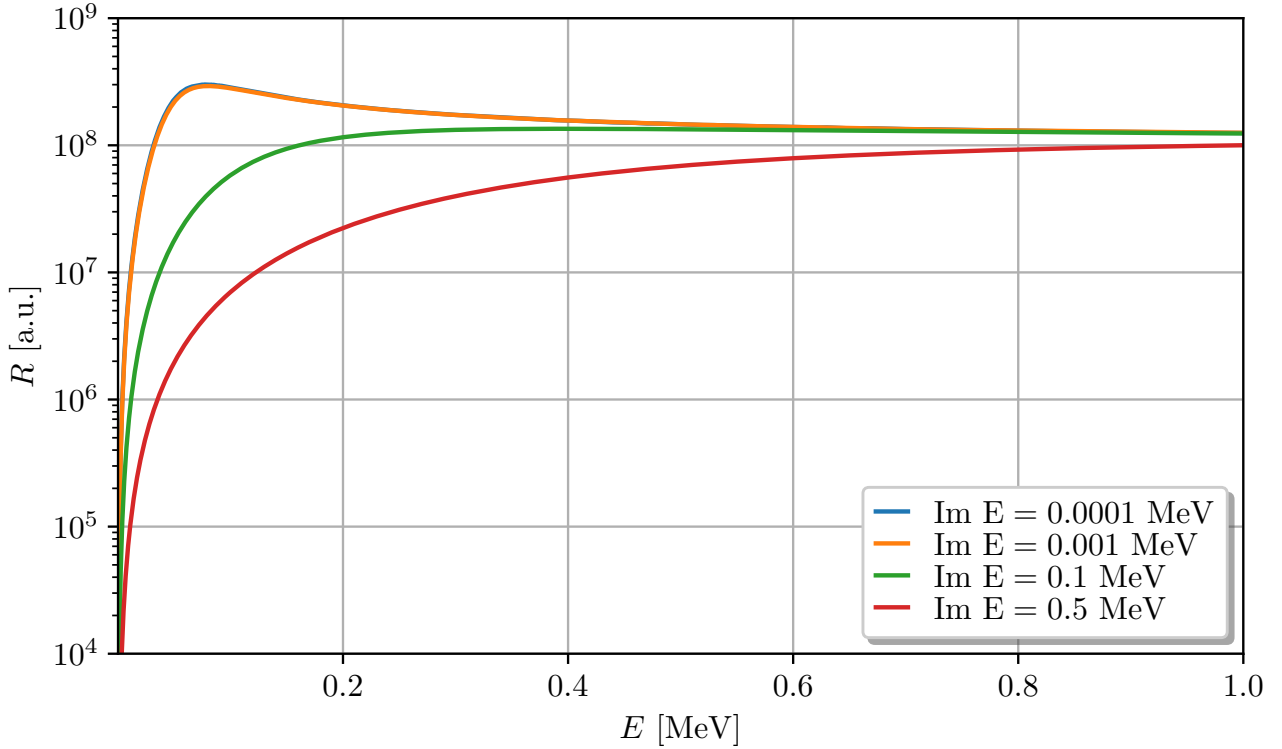
Figure 11.3.: The point production amplitude for the three-boson system for different imaginary parts of the energy. In the limit Im E → 0 the physical result is obtained. Here, the effect of the resonance close to threshold becomes visible as a peak in the amplitude.

11.2. Conformal symmetry

While the three-boson system at LO is determined by two scales, the scattering length and the three-body force, the systems that will be considered in the following present only one scale at leading order, the scattering length. So, it is possible to describe these systems as so-called "unparticles" or "unnuclei", which are fields in conformal field theory. The idea was originally proposed by Georgi [157] and extended to nonrelativistic systems by Hammer *et al.* [92]. A field in a nonrelativistic field theory is characterized by two parameters, a scaling dimension Δ and its mass M [93]. The energy dependence of the quantities calculated in the following is solely determined (up to an overall normalization) by the scaling dimension. An overview of the relevant scaling dimensions is presented in Table 11.1.

Following Ref. [92], nonrelativistic conformal field theory is applicable for center-of-mass energies in the range

$$\frac{1}{ma_0^2} \ll E \ll \frac{1}{mr_0^2} \,. \tag{11.6}$$

Within this energy range, the on-shell amplitude can be represented by

$$\Gamma_l\left(E;p\right) := cE^{\frac{\Delta-3.5}{2}}\,, \tag{11.7}$$

where c is a constant, that has to be fitted to data. Within this work, the production amplitude R is calculated. The scaling of the production amplitude follows from the scaling of the amplitude squared,

$$\left|\Gamma_l\left(E;p\right)\right|^2 \sim E^{\Delta-\frac{7}{2}}\,, \tag{11.8}$$

times an energy-dependent factor. Considering a three-body final state, the scaling is modified by the phase space integration as well as the dimer propagator. So, R scales as

$$R(E) \sim E^{\Delta-\frac{5}{2}}\,. \tag{11.9}$$

Besides the energy range predicted by conformal field theory, it is further possible to make a statement for small energies, where the particles can be assumed to be non-interacting. A free field is characterized by a scaling dimension $\Delta = 3/2$. Analogously to the conformal energy range, a representation of the point production amplitude for N particles can be derived

$$R(E) \sim E^{\Delta_{\text{free}}}\,,$$
$$\Delta_{\text{free}} = \frac{3N-5}{2} + \#\boldsymbol{\nabla} + \#\partial_t\,. \tag{11.10}$$

The terms $\#\boldsymbol{\nabla}$ and $\#\partial_t$ represent the number of spacial and time derivatives included in the operator $\mathcal{O}$, respectively. An overview of the corresponding values for systems up to four particles is given in Table 11.1.

N	S	L	$\mathcal{O}$	Δ	Δ_{free}
2	0	0	$\psi_\uparrow\psi_\downarrow$	2	0.5
3	0.5	0	$\psi_\uparrow\psi_\downarrow\partial_t\psi_\uparrow$	4.66622	3
3	0.5	1	$\psi_\uparrow\psi_\downarrow\boldsymbol{\nabla}\psi_\uparrow$	4.27272	3
3	0.5	2	$\psi_\uparrow\psi_\downarrow\boldsymbol{\nabla}^2\psi_\uparrow$	5.60498	4
4	0	0	$\psi_\uparrow\psi_\downarrow\boldsymbol{\nabla}\psi_\uparrow\cdot\boldsymbol{\nabla}\psi_\downarrow$	5.07(1)	5.5

Table 11.1.: An overview of the scaling dimension for different systems up to four particles in the conformal [93, 158] as well as the free energy range.

11.3. Three neutrons

The first system described by conformal symmetry to be considered is the point creation of a three-neutron system. The graphical representation of the corresponding scattering equation is equivalent to the one of the three-boson system presented in Fig. 11.1. Similarly, the Faddeev equation is equivalent to the one of the three-boson system, only differing by a factor -0.5. In comparison to the three-boson system, three neutrons are fermionic. So, the amplitude has to be antisymmetrized. The corresponding
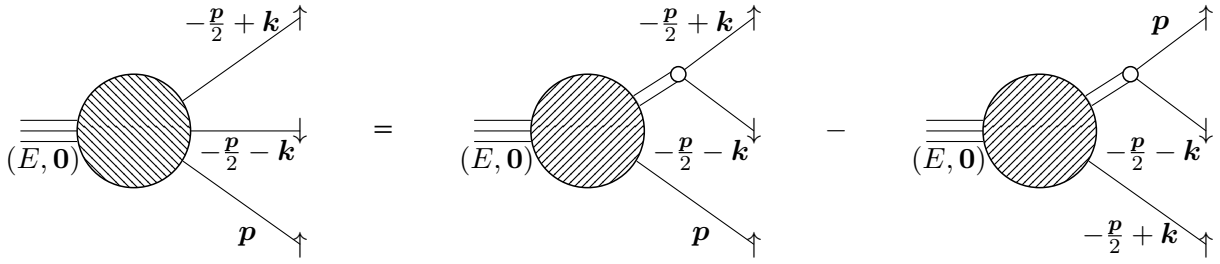
Figure 11.4.: Scattering equation for the point creation of a 3n system.

antisymmetrized scattering equation is shown in Fig. 11.4, where it is implicitly assumed that all lines are on-shell.

This equation transforms into

$$i\bar{\Gamma}_l\left(E; \boldsymbol{p}, -\frac{\boldsymbol{p}}{2} + \boldsymbol{k}\right) = \left(\sqrt{Z}\right)^{-1} \frac{g_2^2}{\#} \left[i\Gamma_l\left(E; \boldsymbol{p}\right) \tau_l\left(E; -\boldsymbol{p}\right) P_l\left(\cos\theta_{\boldsymbol{p},\boldsymbol{k}}\right) \right.$$
$$\left. - i\Gamma_l\left(E; -\frac{\boldsymbol{p}}{2} + \boldsymbol{k}\right) \tau_l\left(E; \frac{\boldsymbol{p}}{2} - \boldsymbol{k}\right) P_l\left(\cos\theta_{-\frac{\boldsymbol{p}}{2}+\boldsymbol{k},\boldsymbol{k}}\right) \right], \tag{11.11}$$

where similar to the three-boson system $\bar{\Gamma}$ and Γ represent the amplitude for three single neutrons or a neutron and dimer in the final state, respectively. Γ is to be calculated using Eq. (11.1) together with a factor -0.5 in the homogeneous term of the integral equation.

Again, the production amplitude is to be calculated. It is defined analogously to the three-boson system by Eq. (11.3). However, the situation becomes more complicated here as there will be not only a S-wave but also higher partial waves up to the D-wave. Introducing the definition $\boldsymbol{q} = -\frac{\boldsymbol{p}}{2} + \boldsymbol{k}$ the partial-wave expansions of the two amplitudes Γ are given by

$$\Gamma\left(E; \boldsymbol{p}\right) = \sum_l (2l + 1) \Gamma_l\left(E, p\right) P_l\left(\cos\theta_{\boldsymbol{p},\boldsymbol{z}}\right) ,$$
$$\Gamma\left(E; \boldsymbol{q}\right) = \sum_l (2l + 1) \Gamma_l\left(E, q\right) P_l\left(\cos\theta_{\boldsymbol{q},\boldsymbol{z}}\right) , \tag{11.12}$$

where $\theta_{\boldsymbol{p},\boldsymbol{z}}(\theta_{\boldsymbol{q},\boldsymbol{z}})$ is the angle between $\boldsymbol{p}(\boldsymbol{q})$ and the z-axis of the coordinate system, respectively. The coordinate system is chosen such that $\boldsymbol{k}||\boldsymbol{e}_z$. So, the angle of the second amplitude is given by

$$\cos\theta_{\boldsymbol{q},\boldsymbol{z}} = \cos\theta_{\boldsymbol{q},\boldsymbol{k}} = \frac{\boldsymbol{q}\cdot\boldsymbol{k}}{|\boldsymbol{q}||\boldsymbol{k}|} = \frac{-\frac{p}{2}k\cos\theta_{\boldsymbol{p},\boldsymbol{k}} + k^2}{k\sqrt{\frac{p^2}{4} + k^2 - pk\cos\theta_{\boldsymbol{p},\boldsymbol{k}}}} . \tag{11.13}$$

Calculating the absolute value squared of $\bar{\Gamma}$ an infinite sum of products of different partial waves contributes. In the following, only contributions up to the D-wave will be considered. First, for simplicity, the coupling between different partial waves is neglected such that a production amplitude for a given partial wave can be defined by

$$R_l\left(E\right) = \frac{1}{4\pi^3} \int_0^\infty \mathrm{d}p\, p^2 \left(mE - \frac{3}{4}p^2\right) \int_{-1}^{+1} \mathrm{d}\cos\theta_{\boldsymbol{p},\boldsymbol{k}} \frac{\left|(2l + 1)\bar{\Gamma}_l\left(E; \boldsymbol{p}, -\frac{\boldsymbol{p}}{2} + \boldsymbol{k}\right)\right|^2}{\left|-\frac{2}{m}\sqrt{mE - \frac{3}{4}p^2}\right|} . \tag{11.14}$$

Note that the interaction strength $g_{3,l}$ for each partial-wave is chosen to be equivalent ($g_{3,l} = 1$). The resulting production amplitudes are shown in a double-logarithmic plot in Fig. 11.5 (S-wave), Fig. 11.6 (P-wave) and Fig. 11.7 (D-wave). Besides the point production amplitude, a fit of the form $R(E) = aE^b$ to the small (E=0 MeV) as well as the large (E=100 MeV) energy range is shown. It allows to compare to the predictions for free particles and by nonrelativistic conformal field theory, respectively. Following Eq. (11.6) the point production amplitude is described by nonrelativistic conformal field theory for energies in the range

$$\frac{1}{ma_0^2} \approx 0.1\,\text{MeV} \ll E \ll \frac{1}{mr_0^2} \approx 5\,\text{MeV}\,, \tag{11.15}$$

where $a_0 = -18.9\,\text{fm}$ and $r_0 = 2.7\,\text{fm}$. Note that within this work a pionless EFT interaction at LO is applied. So, the effective range r_0 effectively takes the value zero and the range extends up to the breakdown of our EFT.

All in all, for all three partial-wave channels the results for the point production amplitude agree pretty well with these predictions.
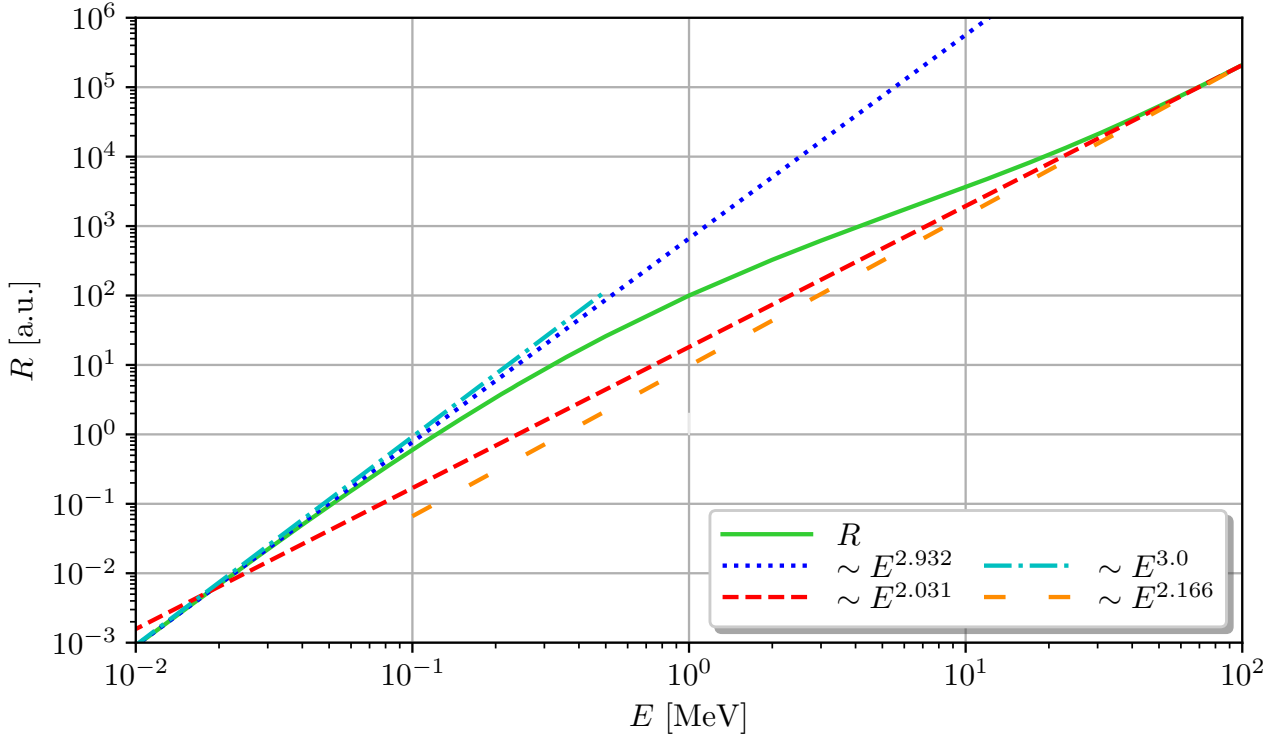
Figure 11.5.: The partial-wave point production amplitude R_l for a three-neutron system with the third neutron in a relative S-wave, $l = 0$. The results are fitted by a function $R(E) = aE^b$ at small (E=0 MeV) as well as large energies (E=100 MeV). The error of the fits is on the last digit shown. The small energy fit (blue dotted line), which can be compared to the predictions for free particles (cyan dash-dotted line), shows a very good agreement between theory and calculation. The fit at large energies (red dashed line) can further be compared to the predictions by nonrelativistic conformal field theory (orange loosely dashed line). Again, there is a good agreement between the results and the predictions.

Figure 11.6.: The same calculation as in Fig. 11.5, but for a relative P-wave, $l = 1$.

Figure 11.7.: The same calculation as in Fig. 11.5 and Fig. 11.6, but for a relative D-wave, $l = 2$.

The partial-wave point production amplitudes for these three partial waves can also be compared with each other (cf. Fig. 11.8). Assuming the same strength of the source term $g_{3,l} = 1$ for all partial waves, the dominant contribution is due to the P-wave. Comparing only S- and D-wave the S-wave contribution is more dominant at small energies, while the D-wave contribution becomes more dominant at larger energies. By modifying the strength of the source term the relative order of the different partial waves can be shifted. However, the results are directly proportional to the value of $g_{3,l}$ such that for a natural choice of $g_{3,l}$ due to the large difference in the order of magnitudes no change will be happen.
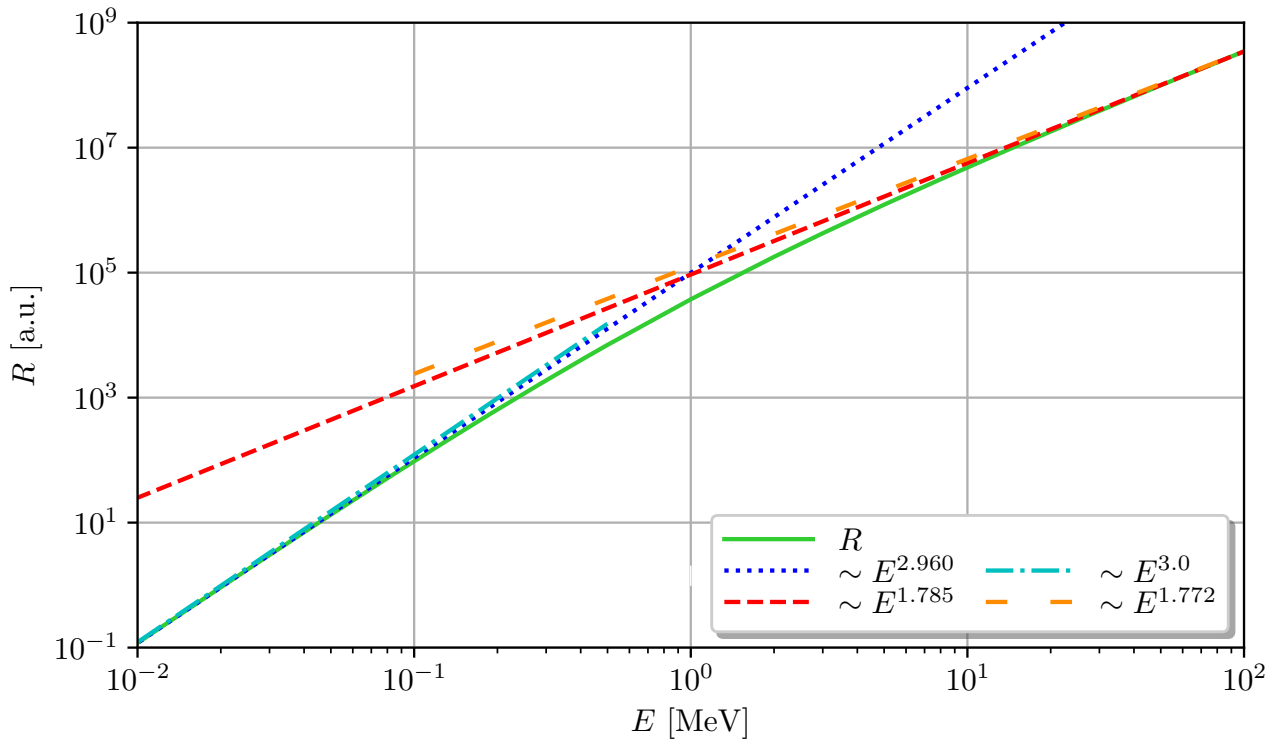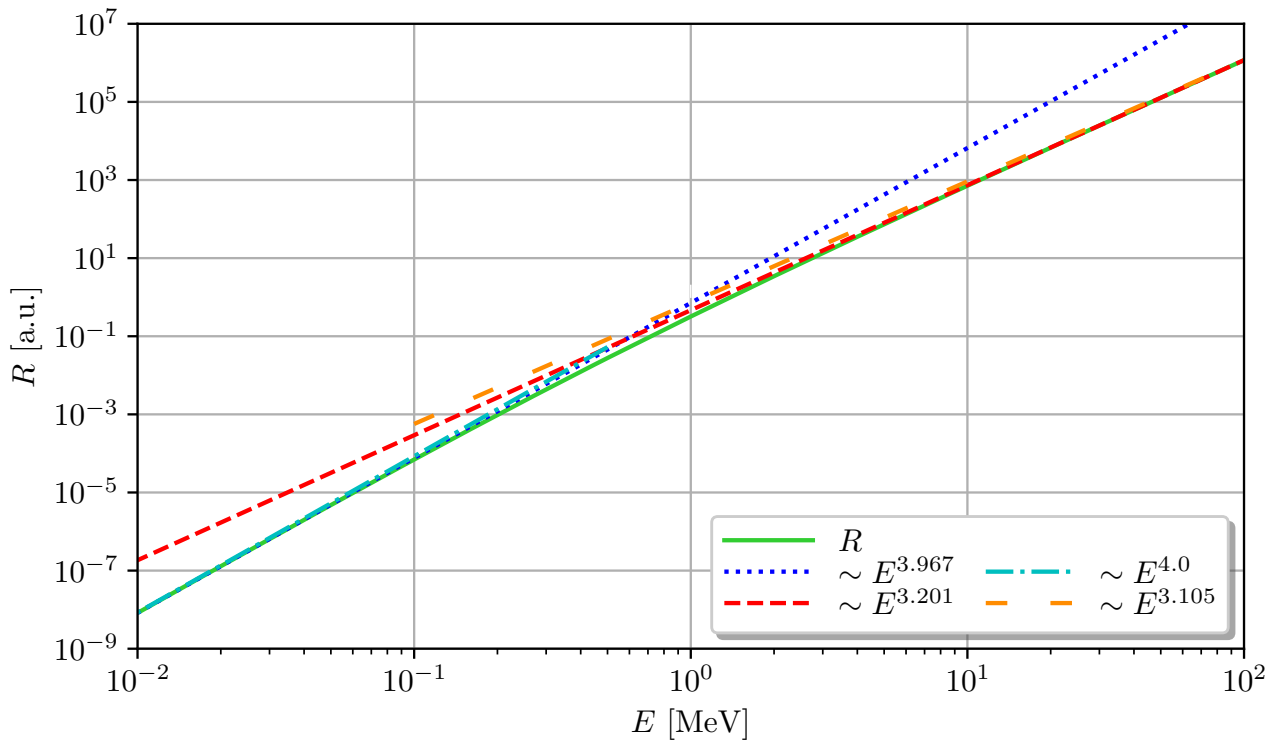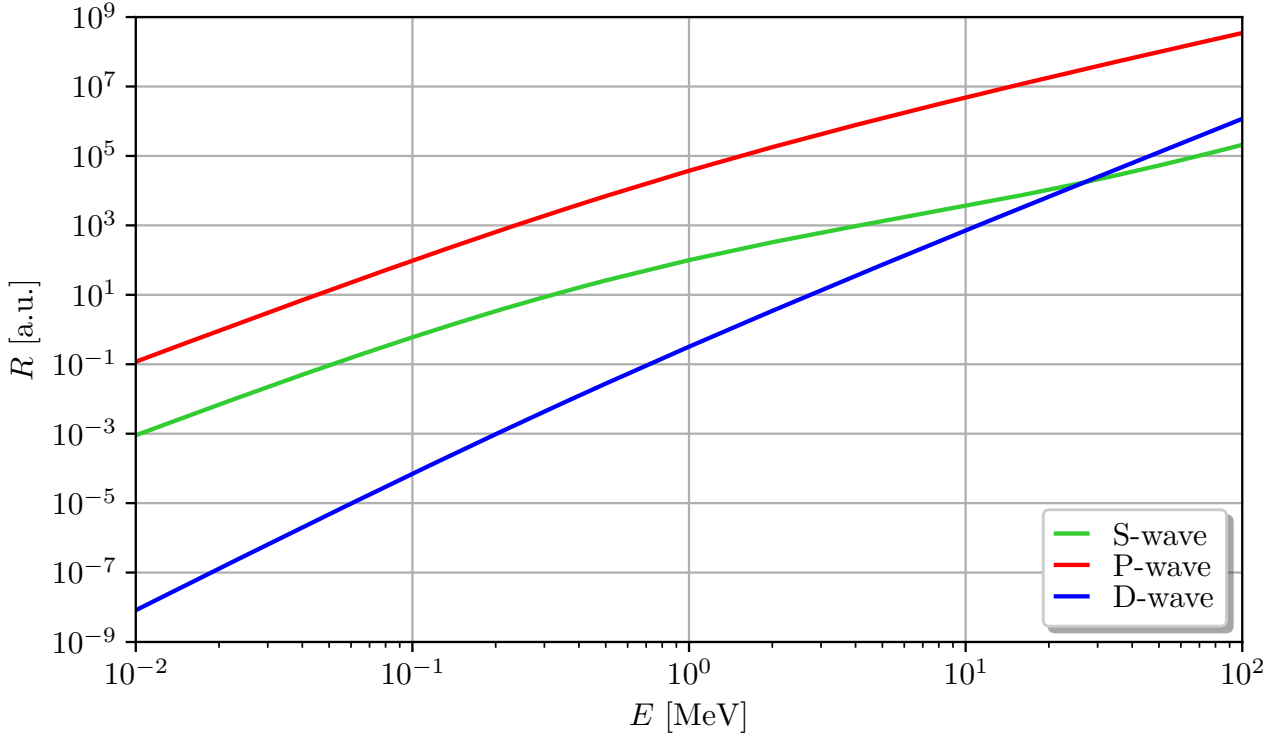

Figure 11.8.: The partial-wave point production amplitudes for the three partial waves considered. For all partial waves an equal strength of the source term, $g_{3,l} = 1$ is assumed.

Finally, the full amplitude containing the coupling of all three partial-wave contributions is investigated. The corresponding equation reads

$$R\left(E\right) = \frac{1}{4\pi^3} \int_0^\infty \mathrm{d}p\, p^2 \left(mE - \frac{3}{4}p^2 \right) \int_{-1}^{+1} \mathrm{d}\cos\theta_{\boldsymbol{p},\boldsymbol{k}} \frac{\left| \sum_{l=0}^2 (2l+1)\,\bar{\Gamma}_l\left(E; \boldsymbol{p}, -\frac{\boldsymbol{p}}{2} + \boldsymbol{k}\right) \right|^2}{\left| -\frac{2}{m}\sqrt{mE - \frac{3}{4}p^2} \right|} . \qquad (11.16)$$

Again, it is assumed that the source term within all partial waves is equivalent. The results for the full amplitude up to D- and P-wave are shown in Fig. 11.9 in comparison to the P-wave partial-wave amplitude. As shown before, the P-wave contribution is dominant, such that it can not be distinguished between these three curves. Further, the point production amplitude follows the predictions by theory over the whole energy range investigated. There is no structure visible, in comparison to the three-boson system, that can be connected to a resonance.
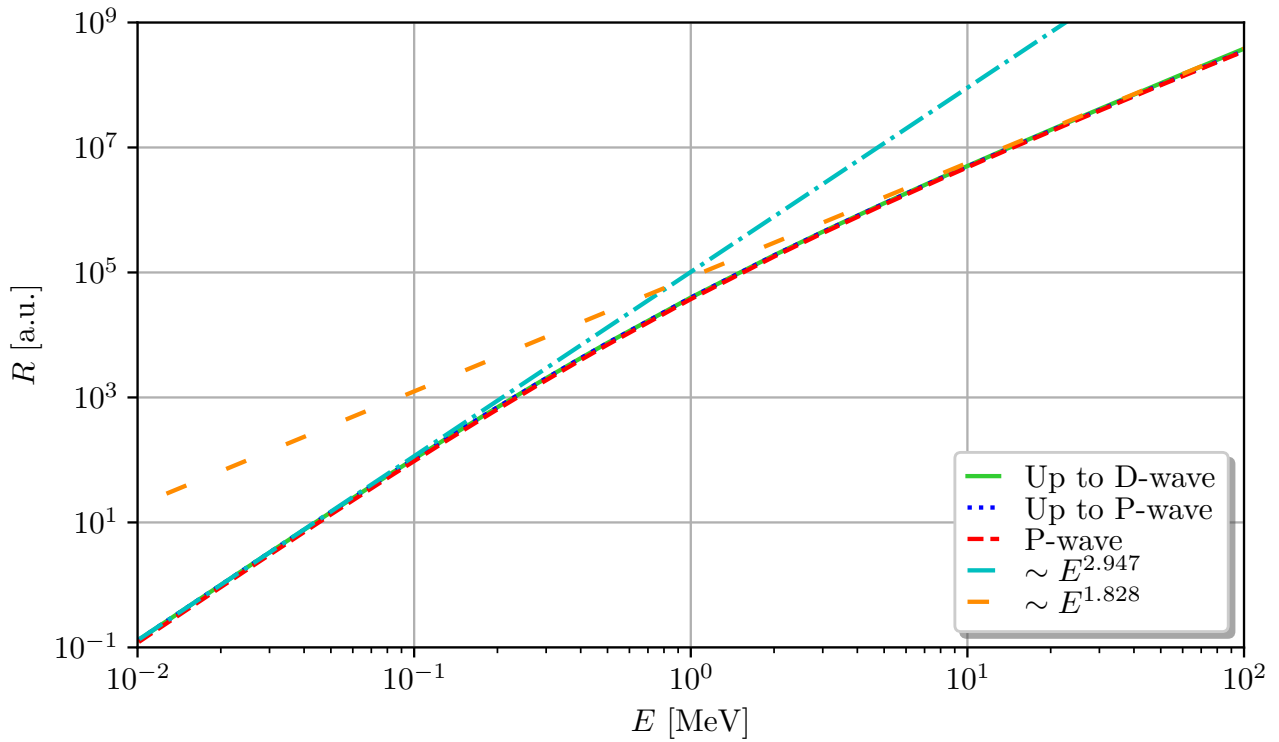
Figure 11.9.: The full three-neutron point production amplitude defined by Eq. (11.16) for partial waves up to D-wave and up to P-wave in comparison to the P-wave partial-wave point production amplitude shown in Fig. 11.6. Similar to the partial-wave amplitudes, the full amplitude up to D-wave is fitted by an exponential function at small (cyan dash-dotted line) and large energies (orange loosely dashed line). All curves shown are located almost on top of each other showing the dominant contribution of the P-wave amplitude. Further, the results fully follow the predictions from theory for free particles as well as the predictions by nonrelativistic conformal field theory. It is no structure visible that can be connected to a resonance.

11.4. Four neutrons

In the following, the point creation of four neutrons is investigated. Following the Faddeev-Yakubovsky theory [159–165] the equation splits up into two clusters. On the one hand, there is an amplitude describing the interaction of a three-neutron system and a single neutron (3+1). On the other hand, there exists an amplitude describing the interaction with two dimers in the final state (2+2). At the end, four free neutrons are observed. This is taken care off by including appropriate vertices and propagators. The final Faddeev-Yakubovsky equation describing the four neutron point creation is shown in Fig. 11.10.

Due to the fermionic nature of the system the equation has to be anti-symmetrized. The result of this antisymmetrization is shown in Fig. 11.11 and Fig. 11.12 for the 3+1 and 2+2 cluster, respectively.
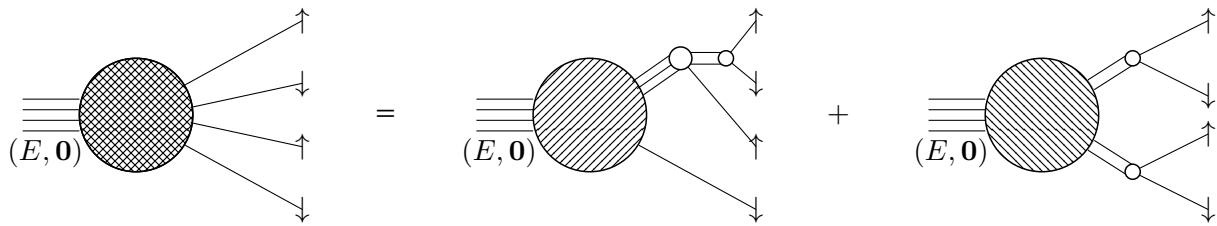
Figure 11.10.: Faddeev-Yakubovsky equation for the point creation of a 4n system.
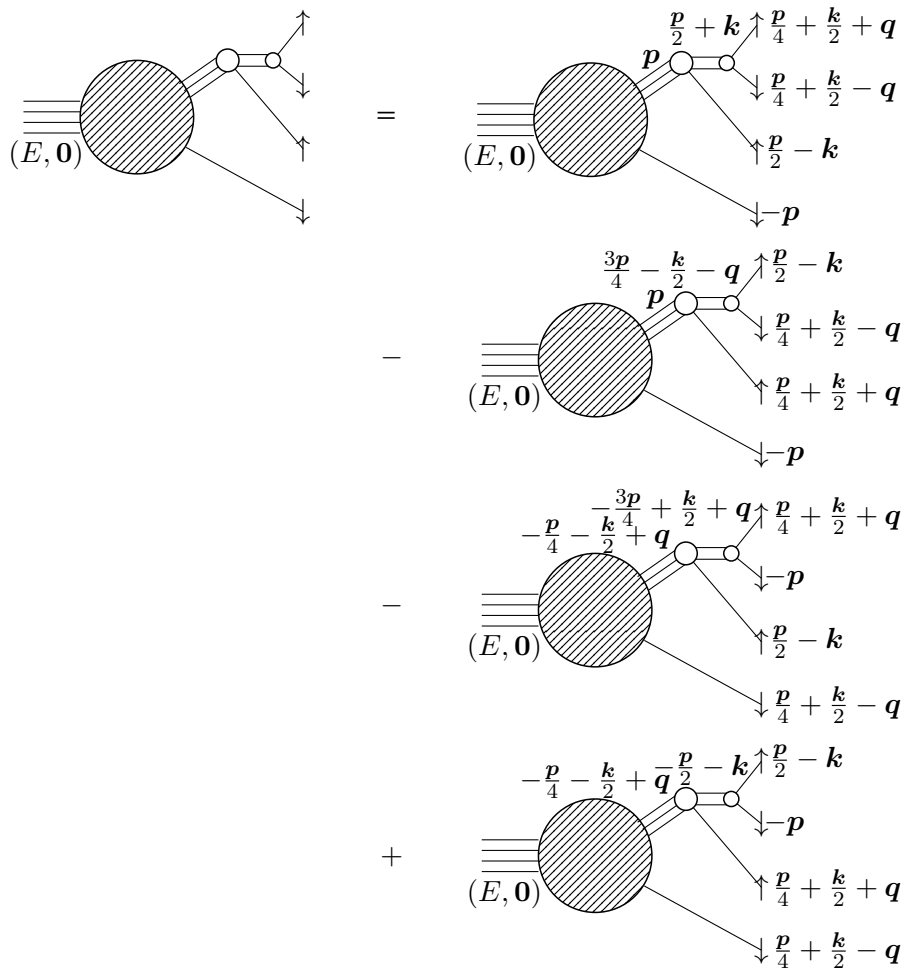
Figure 11.11.: Scattering equation for the point creation of a 4n system and a clustering into a trimer and a neutron.

These equations can be used to derive the production amplitudes. First, consider the $2+2$ channel. The
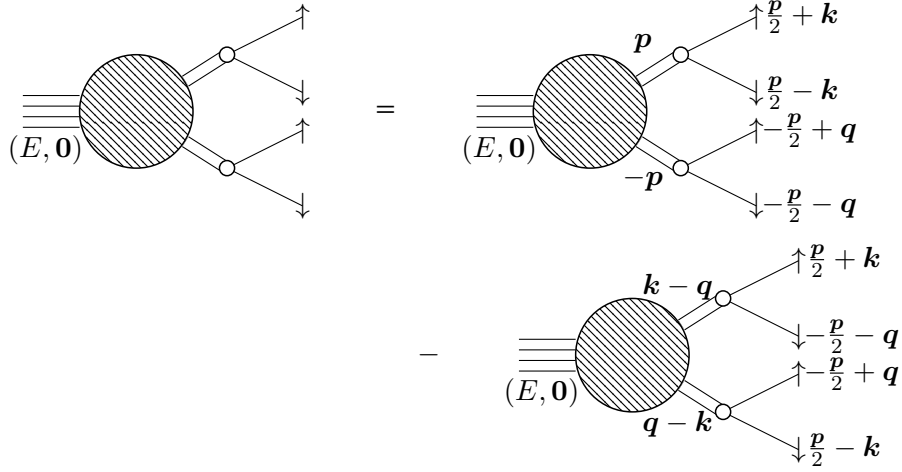
Figure 11.12.: Scattering equation for the point creation of a 4n system and a clustering into two dimer.

corresponding amplitude is defined by

$$
R_{2+2}(E) = \int \frac{\mathrm{d}^3 p}{(2\pi)^3} \int \frac{\mathrm{d}^3 k}{(2\pi)^3} \int \frac{\mathrm{d}^3 q}{(2\pi)^3} 2\pi\delta \left(E - E_{\frac{p}{2}+k} - E_{\frac{p}{2}-k} - E_{-\frac{p}{2}+q} - E_{-\frac{p}{2}-q} \right)
$$
$$
\times \left| Z^{-1} \frac{g^4}{\#} \left[\Gamma_{2+2}(E, \boldsymbol{p}) D(\boldsymbol{p}) D(-\boldsymbol{p}) - \Gamma_{2+2}(E, \boldsymbol{k}-\boldsymbol{q}) D(\boldsymbol{k}-\boldsymbol{q}) D(\boldsymbol{q}-\boldsymbol{k}) \right] \right|^2 . \tag{11.17}
$$

Similar to the three-body system, the vertices are partial-wave expanded,

$$
\Gamma_{2+2}(E, \boldsymbol{p}) = \sum_l (2l+1) \Gamma_{2+2,l}(E, p) P_l(\cos\theta) ,
$$
$$
\Gamma_{2+2}(E, \boldsymbol{k}-\boldsymbol{q}) = \sum_l (2l+1) \Gamma_{2+2,l}(E, |\boldsymbol{k}-\boldsymbol{q}|) P_l(\cos\theta') , \tag{11.18}
$$

where $\theta(\theta')$ is the angle between $\boldsymbol{p}(\boldsymbol{k}-\boldsymbol{q})$ and the z-axis of the coordinate system. The coordinate system is chosen such that the z-axis is parallel to $\boldsymbol{k}$. This results in the definitions

$$
\cos\theta = \frac{\boldsymbol{k}\cdot\boldsymbol{p}}{kp} ,
$$
$$
\cos\theta' = \frac{(\boldsymbol{k}-\boldsymbol{q})\cdot\boldsymbol{k}}{|\boldsymbol{k}-\boldsymbol{q}|\, k} = \frac{k - q\cos\theta''}{\sqrt{k^2 + q^2 - 2kq\cos\theta''}} . \tag{11.19}
$$

The energy conservation can be transformed to

$$
\begin{aligned}
\delta\left(E - E_{\frac{p}{2}+k} - E_{\frac{p}{2}-k} - E_{-\frac{p}{2}+q} - E_{-\frac{p}{2}-q}\right) \\
= \delta\left[E - \frac{1}{2m}\left\{\left(\frac{p}{2}+k\right)^2 + \left(\frac{p}{2}-k\right)^2 + \left(-\frac{p}{2}+q\right)^2 + \left(-\frac{p}{2}-q\right)^2\right\}\right] \\
= \delta\left[E - \frac{1}{2m}\left(p^2 + 2k^2 + 2q^2\right)\right] \\
= \frac{\delta\left(k - \sqrt{mE - \frac{p^2}{2} - q^2}\right)}{\left|-\frac{2}{m}\sqrt{mE - \frac{p^2}{2} - q^2}\right|} \,.
\end{aligned}
\tag{11.20}
$$

Altogether the amplitude reads

$$
\begin{aligned}
R_{2+2}(E) = {} & \left|Z^{-1}\frac{g^4}{\#}\right|^2 \int \frac{\mathrm{d}p}{(2\pi)^2}p^2 \int_{-1}^{+1}\mathrm{d}\cos\theta \int \frac{\mathrm{d}k}{2\pi^2}k^2 \int \frac{\mathrm{d}q}{(2\pi)^2}q^2 \int_{-1}^{+1}\mathrm{d}\cos\theta'' \\
& \times 2\pi \frac{\delta\left(k - \sqrt{mE - \frac{p^2}{2} - q^2}\right)}{\left|-\frac{2}{m}\sqrt{mE - \frac{p^2}{2} - q^2}\right|} \\
& \times \left|\sum_l (2l+1)\,\Gamma_{2+2,l}(E,p)\,P_l(\cos\theta)\,D(\boldsymbol{p})\,D(-\boldsymbol{p})\right. \\
& \left. - \sum_{l'} (2l'+1)\,\Gamma_{2+2,l'}(E,|\boldsymbol{k}-\boldsymbol{q}|)\,P_{l'}(\cos\theta')\,D(\boldsymbol{k}-\boldsymbol{q})\,D(\boldsymbol{q}-\boldsymbol{k})\right|^2 .
\end{aligned}
\tag{11.21}
$$

The energy conservation sets a limit on the momentum integration, $mE \geq \frac{p^2}{2} + q^2$.

Further consider the $3+1$ channel,

$$
\begin{aligned}
R_{3+1}(E) = {} & \int \frac{\mathrm{d}^3 p}{(2\pi)^3} \int \frac{\mathrm{d}^3 k}{(2\pi)^3} \int \frac{\mathrm{d}^3 q}{(2\pi)^3}\,2\pi\delta\left(E - E_{\frac{p}{4}+\frac{k}{2}+q} - E_{\frac{p}{4}+\frac{k}{2}-q} - E_{\frac{p}{2}-q} - E_{-p}\right) \\
& \times \left|\left(\sqrt{Z_3}\right)^{-1}\frac{g_{3\to 2+1}^2}{\#}g^2 \right. \\
& \times \left[\Gamma_{3+1}(E,\boldsymbol{p})\,G(\boldsymbol{p})\,D\left(\frac{\boldsymbol{p}}{2}+\boldsymbol{k}\right) - \Gamma_{3+1}(E,\boldsymbol{p})\,G(\boldsymbol{p})\,D\left(\frac{3\boldsymbol{p}}{4}-\frac{\boldsymbol{k}}{2}-\boldsymbol{q}\right)\right. \\
& - \Gamma_{3+1}\left(E, -\frac{\boldsymbol{p}}{4} - \frac{\boldsymbol{k}}{2} + \boldsymbol{q}\right)G\left(-\frac{\boldsymbol{p}}{4} - \frac{\boldsymbol{k}}{2} + \boldsymbol{q}\right)D\left(-\frac{3\boldsymbol{p}}{4} + \frac{\boldsymbol{k}}{2} + \boldsymbol{q}\right) \\
& \left.\left. + \Gamma_{3+1}\left(E, -\frac{\boldsymbol{p}}{4} - \frac{\boldsymbol{k}}{2} + \boldsymbol{q}\right)G\left(-\frac{\boldsymbol{p}}{4} - \frac{\boldsymbol{k}}{2} + \boldsymbol{q}\right)D\left(-\frac{\boldsymbol{p}}{2} - \boldsymbol{k}\right)\right]\right|^2 .
\end{aligned}
\tag{11.22}
$$

G represents the dressed three-particle Green's function. It is connected to the dimer-particle T-matrix by

$$
G(\boldsymbol{p}) = \frac{g^4}{Z}T(\boldsymbol{p}) \,.
\tag{11.23}
$$

The partial-wave expansion of the amplitude is given by

$$\Gamma_{3+1}(E, \boldsymbol{p}) = \sum_l (2l+1)\,\Gamma_{3+1,l}(E, p)\, P_l(\cos\theta)\,,$$

$$\Gamma_{3+1}\left(E, -\frac{\boldsymbol{p}}{4} - \frac{\boldsymbol{k}}{2} + \boldsymbol{q}\right) = \sum_l (2l+1)\,\Gamma_{3+1,l}\left(E, \left|-\frac{\boldsymbol{p}}{4} - \frac{\boldsymbol{k}}{2} + \boldsymbol{q}\right|\right) P_l(\cos\theta')\,.$$

(11.24)

Again, the coordinate system is chosen such that the z-axis is parallel to $\boldsymbol{k}$. This results in a definition of the angles as

$$\cos\theta = \frac{\boldsymbol{k} \cdot \boldsymbol{p}}{kp}\,,$$

$$\cos\theta' = \frac{\boldsymbol{k} \cdot \left(-\frac{\boldsymbol{p}}{4} - \frac{\boldsymbol{k}}{2} + \boldsymbol{q}\right)}{k\left|-\frac{\boldsymbol{p}}{4} - \frac{\boldsymbol{k}}{2} + \boldsymbol{q}\right|} = \frac{-\frac{kp\cos\theta}{4} - \frac{k^2}{2} + kq\cos\theta''}{k\sqrt{\frac{p^2}{16} + \frac{k^2}{4} + q^2 + \frac{kp\cos\theta}{4} - kq\cos\theta'' - \frac{pq\cos(\theta - \theta'')}{2}}}\,.$$

(11.25)

Beside the amplitudes, the (on-shell) dimer-particle T-matrix is to be partial-wave expanded, too,

$$T(\boldsymbol{p}) = \sum_l (2l+1)\,T_l(p) P_l(\cos\theta)\,,$$

$$T\left(-\frac{\boldsymbol{p}}{4} - \frac{\boldsymbol{k}}{2} + \boldsymbol{q}\right) = \sum_l (2l+1)\,T_l\left(\left|-\frac{\boldsymbol{p}}{4} - \frac{\boldsymbol{k}}{2} + \boldsymbol{q}\right|\right) P_l(\cos\theta')\,.$$

(11.26)

Further, the energy conserving δ-function can be simplified to

$$\delta\left(E - E_{\frac{\boldsymbol{p}}{4} + \frac{\boldsymbol{k}}{2} + \boldsymbol{q}} - E_{\frac{\boldsymbol{p}}{4} + \frac{\boldsymbol{k}}{2} - \boldsymbol{q}} - E_{\frac{\boldsymbol{p}}{2} - \boldsymbol{q}} - E_{-\boldsymbol{p}}\right)$$

$$= \delta\left[E - \frac{1}{2m}\left\{\left(\frac{\boldsymbol{p}}{4} + \frac{\boldsymbol{k}}{2} + \boldsymbol{q}\right)^2 + \left(\frac{\boldsymbol{p}}{4} + \frac{\boldsymbol{k}}{2} - \boldsymbol{q}\right)^2 + \left(\frac{\boldsymbol{p}}{2} - \boldsymbol{q}\right)^2 + p^2\right\}\right]$$

$$= \delta\left[E - \frac{1}{2m}\left(\frac{11}{8}p^2 + \frac{k^2}{2} + 3q^2 + \frac{\boldsymbol{k} \cdot \boldsymbol{p}}{2} - \boldsymbol{p} \cdot \boldsymbol{q}\right)\right]$$

$$= \frac{\delta(k - k_1)}{\left|-\frac{1}{2m}\left(k_1 + \frac{p\cos\theta}{2}\right)\right|} + \frac{\delta(k - k_2)}{\left|-\frac{1}{2m}\left(k_2 + \frac{p\cos\theta}{2}\right)\right|}\,,$$

(11.27)

where $k_{1/2} = -\frac{p\cos\theta}{2} \pm \sqrt{2}\sqrt{2mE - \frac{11}{8}p^2 - 3q^2 + \frac{p^2\cos^2\theta}{8} + pq\cos(\theta - \theta'')}$.

Altogether, the equation reads

$$R_{3+1}(E) = \int \frac{\mathrm{d}p}{(2\pi)^2} p^2 \int_{-1}^{+1} \mathrm{d}\cos\theta \int \frac{\mathrm{d}k}{2\pi^2} k^2 \int \frac{\mathrm{d}q}{(2\pi)^2} q^2 \int_{-1}^{+1} \mathrm{d}\cos\theta''$$

$$\times 2\pi \left(\frac{\delta(k-k_1)}{\left| -\frac{1}{2m}\left(k_1 + \frac{p\cos\theta}{2}\right) \right|} + \frac{\delta(k-k_2)}{\left| -\frac{1}{2m}\left(k_2 + \frac{p\cos\theta}{2}\right) \right|} \right)$$

$$\times \left| \left(\sqrt{Z_3}\right)^{-1} \frac{g_{3\to2+1}^2}{\#} \frac{g^6}{Z} \right|^2$$

$$\times \left| \sum_{l,\tilde{l}} (2l+1)\left(2\tilde{l}+1\right) \Gamma_{3+1,l}(E,p) P_l(\cos\theta) T_{\tilde{l}}(p) P_{\tilde{l}}(\cos\theta) D\left(\frac{\boldsymbol{p}}{2} + \boldsymbol{k}\right) \right.$$

$$- \sum_{l',\tilde{l}'} (2l'+1)\left(2\tilde{l}'+1\right) \Gamma_{3+1,l'}(E,p) P_{l'}(\cos\theta) T_{\tilde{l}'}(p) P_{\tilde{l}'}(\cos\theta) D\left(\frac{3\boldsymbol{p}}{4} - \frac{\boldsymbol{k}}{2} - \boldsymbol{q}\right)$$

$$- \sum_{l'',\tilde{l}''} (2l''+1)\left(2\tilde{l}''+1\right) \Gamma_{3+1,l''}\left(E, \left|-\frac{\boldsymbol{p}}{4} - \frac{\boldsymbol{k}}{2} + \boldsymbol{q}\right|\right) P_{l''}(\cos\theta')$$

$$T_{\tilde{l}''}\left(\left|-\frac{\boldsymbol{p}}{4} - \frac{\boldsymbol{k}}{2} + \boldsymbol{q}\right|\right) P_{\tilde{l}''}(\cos\theta') D\left(-\frac{3\boldsymbol{p}}{4} + \frac{\boldsymbol{k}}{2} + \boldsymbol{q}\right)$$

$$+ \sum_{l''',\tilde{l}'''} (2l'''+1)\left(2\tilde{l}'''+1\right) \Gamma_{3+1,l'''}\left(E, \left|-\frac{\boldsymbol{p}}{4} - \frac{\boldsymbol{k}}{2} + \boldsymbol{q}\right|\right) P_{l'''}(\cos\theta')$$

$$\left. T_{\tilde{l}'''}\left(\left|-\frac{\boldsymbol{p}}{4} - \frac{\boldsymbol{k}}{2} + \boldsymbol{q}\right|\right) P_{\tilde{l}'''}(\cos\theta') D\left(-\frac{\boldsymbol{p}}{2} - \boldsymbol{k}\right) \right|^2.$$

$$(11.28)$$

While the derivation of these equations is rather straightforward, the solution requires are large numerical effort. This was within the time frame of this work not possible to be done. Nevertheless, following the predictions by nonrelativistic conformal field theory it is possible to make a statement on the existence of a resonance in the four-neutron system [92, 166]. Figure 11.13 shows the predictions for the four-neutron point production amplitude by the theory of free particles as well as by conformal field theory. At the transition point between both theories the slope evolves rather little. It presents no indication of a possible peak structure as in the three-boson system that could be connected to a resonance. If there is four-neutron resonance, as indicated by recent experimental works [69, 70], it would be beyond the scope of this theory.
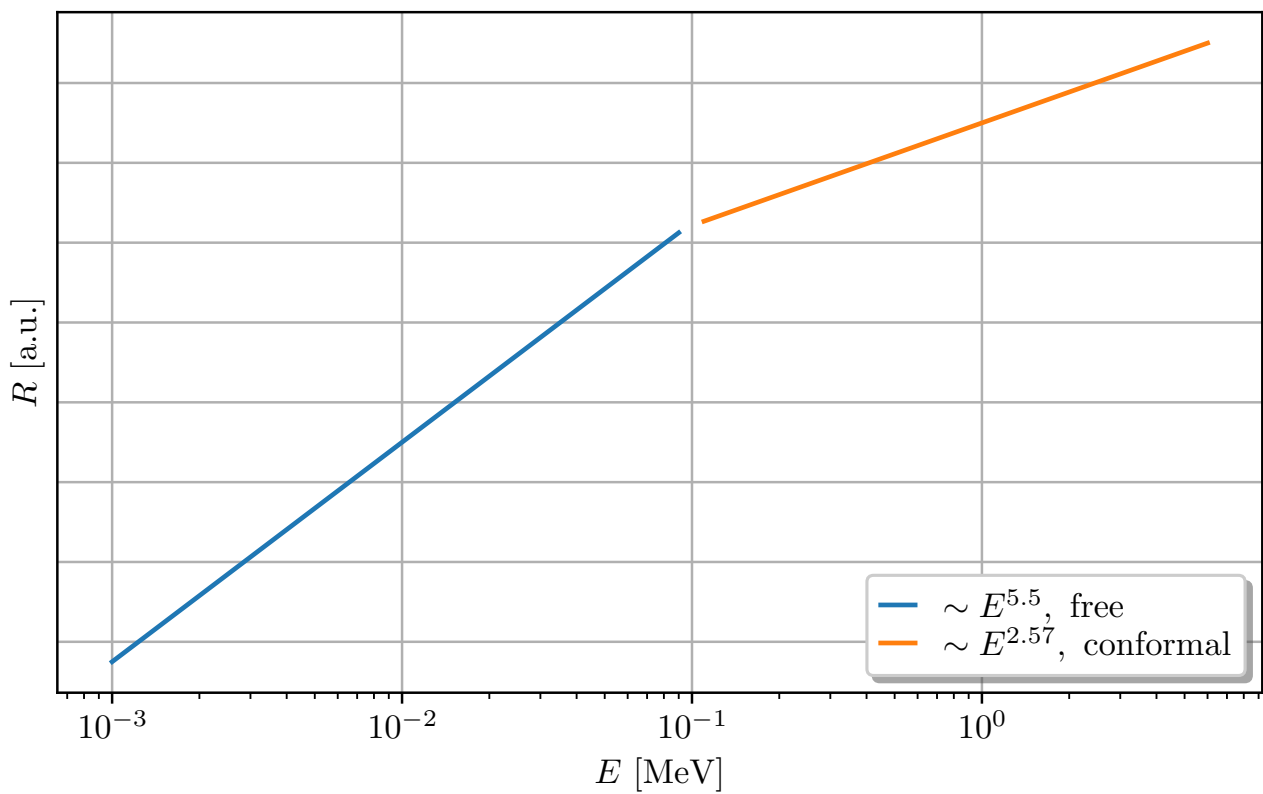
Figure 11.13.: The predictions for the 4n point production amplitude by the theory of free particles and by nonrelativistic conformal field theory. At the transition point between both theories no peak that could be connected to a resonance is visible.

12 Dimer-neutron and dimer-dimer scattering in a finite volume

Beside calculations on the physical or on the unphysical sheets a third group of methods can be applied to search for resonances, the finite volume formalism [68, 72–76]. So, our system is located in a finite cubic volume L^3 with periodic boundary conditions. This type of formalism is well known in the context of lattice calculations [13, 14]. A resonance in finite volume manifests itself by a so-called avoided level crossing [76]. However, already the finite volume spectrum of smaller systems includes a high density of levels with different quantum numbers that do not allow it to project easily to the right states. Due to this structure it is difficult or almost impossible to identify avoided level crossings. Within this Chapter, the energy spectrum for dineutron-neutron and dineutron-dineutron scattering in finite volume is determined using the approach by Lüscher [77–79]. The dineutron states are unphysically bound by considering the neutron-neutron scattering length with a positive sign, $a_0 = 18.9$ fm. These spectra have to be corrected due to the binding of the dineutron, the so-called topological effect [167, 168]. On the basis of these spectra, one can identify the levels which do not correspond to the reaction of interest in a finite volume calculation. In this way, these levels can be traced back, while the scattering length is reduced to the physical value, $a_0 = -18.9$ fm.

12.1. Lüscher Z and S function

Following the work by Lüscher [78, 79] the S-matrix, or equivalently the phase shifts, are determined as a solution of the equation

$$\det\left[e^{2i\delta_l} - U(\Gamma)\right] = 0\,,\tag{12.1}$$

where

$$U(\Gamma) = \frac{M(\Gamma) + i}{M(\Gamma) - i}\,.\tag{12.2}$$

The operator M is defined in Ref. [79] together with an overview of its matrix elements for different irreducible representations of the cubic group Γ. In finite volume one can not apply the usual rotational group, but must apply the cubic group due to the reduced symmetry of the system. In general, M can be expressed as a linear combination of the so-called Lüscher Z-functions. These are defined by

$$Z_{lm}(s; q^2) = \frac{1}{\sqrt{4\pi}} \sum_{\boldsymbol{n} \in \mathbb{Z}^3}{}' Q_{lm}(\boldsymbol{n})\left(\boldsymbol{n}^2 - q^2\right)^{-s}\,,\tag{12.3}$$

where

$$Q_{lm}(\boldsymbol{n}) := \sqrt{\frac{4\pi}{2l+1}}\, n^l Y_{lm}(\theta, \phi)\,.\tag{12.4}$$

Y_{lm} are the spherical harmonics. Further, the notation $\sum'$ is introduced, which excludes states with $\boldsymbol{n}^2 = q^2$. The definition is restricted to complex s with $\mathrm{Re}\, s > \frac{1}{2}(l+3)$. To calculate the phase shifts a representation for $s = 1$ can be derived by analytical continuation. Following the work by Yamazaki *et al.* [169] it reads

$$
\begin{aligned}
Z_{00}(1; q^2) = \frac{1}{2\sqrt{\pi}} \Bigg[&\sum_{\boldsymbol{n} \in \mathbb{Z}^3} \frac{e^{-(\boldsymbol{n}^2 - q^2)}}{\boldsymbol{n}^2 - q^2} \\
&+ \int_0^1 \mathrm{d}t \left(\frac{\pi}{t}\right)^{3/2} e^{tq^2} \left(\sum_{\boldsymbol{n} \in \mathbb{Z}^3} e^{-\frac{\pi^2}{t} \boldsymbol{n}^2} - 1\right) + \sum_{j=0}^\infty \frac{\pi^{3/2}}{j - \frac{1}{2}} \frac{(q^2)^j}{j!} \Bigg].
\end{aligned}
\tag{12.5}
$$

Here, only a single channel is considered. So, the determinant in Eq. (12.1) simplifies to

$$
\begin{aligned}
e^{2i\delta_l} &= \mathcal{U}_{l,l'}(\Gamma)\,, \\
&= \frac{\mathcal{M}_{l,l'}(\Gamma) + i}{\mathcal{M}_{l,l'}(\Gamma) - i}\,.
\end{aligned}
\tag{12.6}
$$

Within this work, we are interested in the cases $l = 0$, which is included in the representation $\Gamma = A_1^+$, and $l = 1$, which corresponds to the representation $\Gamma = T_1^-$. In both cases the operator M takes the value $\mathcal{Z}_{00}$, where $\mathcal{Z}$ is a modified Lüscher Z-function. It is defined by

$$
\mathcal{Z}_{js} = \frac{Z_{js}\left(1; q^2\right)}{\pi^{3/2}\sqrt{2j+1}\, q^{j+1}}\,.
\tag{12.7}
$$

Altogether, the S-matrix for $l = 0, 1$ reads

$$
S_l = e^{2i\delta_l} = \frac{Z_{00}\left(1; q^2\right) + i\pi^{3/2}q}{Z_{00}\left(1; q^2\right) - i\pi^{3/2}q}\,, \qquad q = \frac{kL}{2\pi}\,,
\tag{12.8}
$$

where L is the edge length of the cubic volume. Applying the definition of the S-matrix together with Eq. (12.8) a connection to observables can be made

$$
k \cot \delta_l(k) = \frac{2}{\sqrt{\pi}L} Z_{00}\left(1; q^2\right) := \frac{1}{\pi L} S\left(q^2\right)\,, \qquad l = 0, 1\,,
\tag{12.9}
$$

where $S\left(q^2\right)$ is the so-called Lüscher S-function. It is shown in Fig. 12.1. The momentum spectrum $p\left(L\right)$ in finite volume can be determined by solving Eq. (12.9) together with the ERE for different box sizes L.

12.1.1. Topological corrections

To derive the finite volume energy spectrum different effects have to be considered. In infinite volume the energy is connected to the momenta by

$$
E\left(L = \infty\right) = \frac{k^2}{2\mu} - \#_{nn} B_{nn}\,,
\tag{12.10}
$$

where μ is the reduced mass of the two scattering objects and $\#_{nn}$ and B_{nn} are the number of dineutron states in the process and their infinite-volume binding energies, respectively. The dineutron binding energies B_{nn} are affected by the finite volume. These are the so-called topological corrections [167,
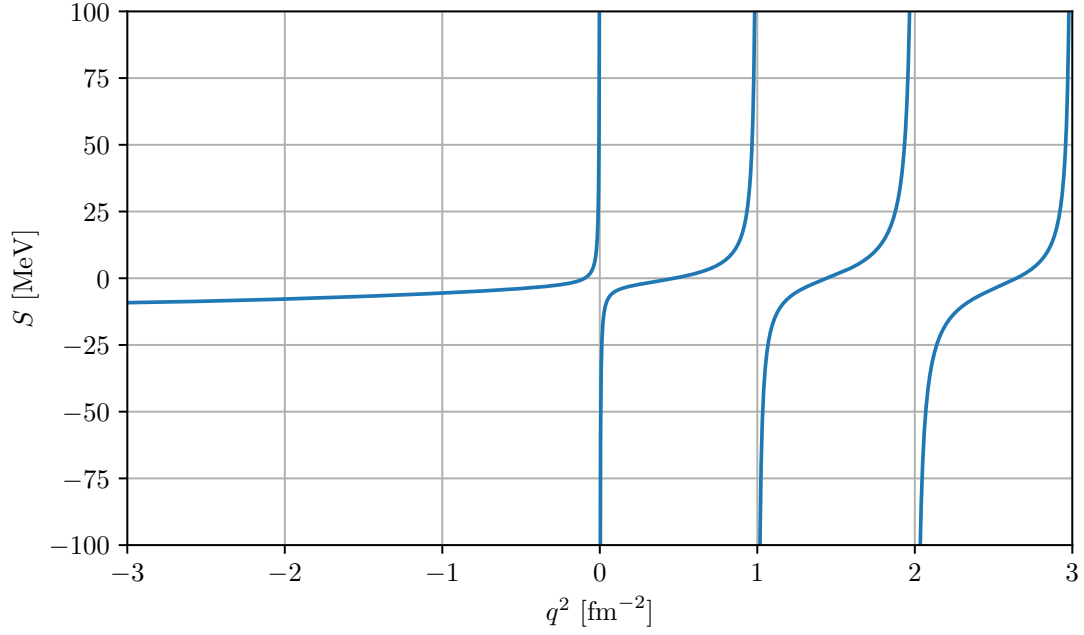
Figure 12.1.: The Lüscher S-function defined by Eq. (12.9).

168], which vanish in the limit $L \to \infty$. They are taken into account by the application of the topological factors $\tau_{nn}(q^2)$,

$$\tau_{nn}\left(q^2\right) = \left[\sum_{\boldsymbol{n}} \frac{1}{\left(\boldsymbol{n}^2 - q^2\right)^2}\right]^{-1} \sum_{\boldsymbol{n}} \frac{\sum_{j=1}^{3} \cos\left(2\pi\alpha n_j\right)}{3\left(\boldsymbol{n}^2 - q^2\right)^2} . \tag{12.11}$$

For a dineutron bound state the parameter α takes the value 0.5. The topological factor is shown in Fig. 12.2.
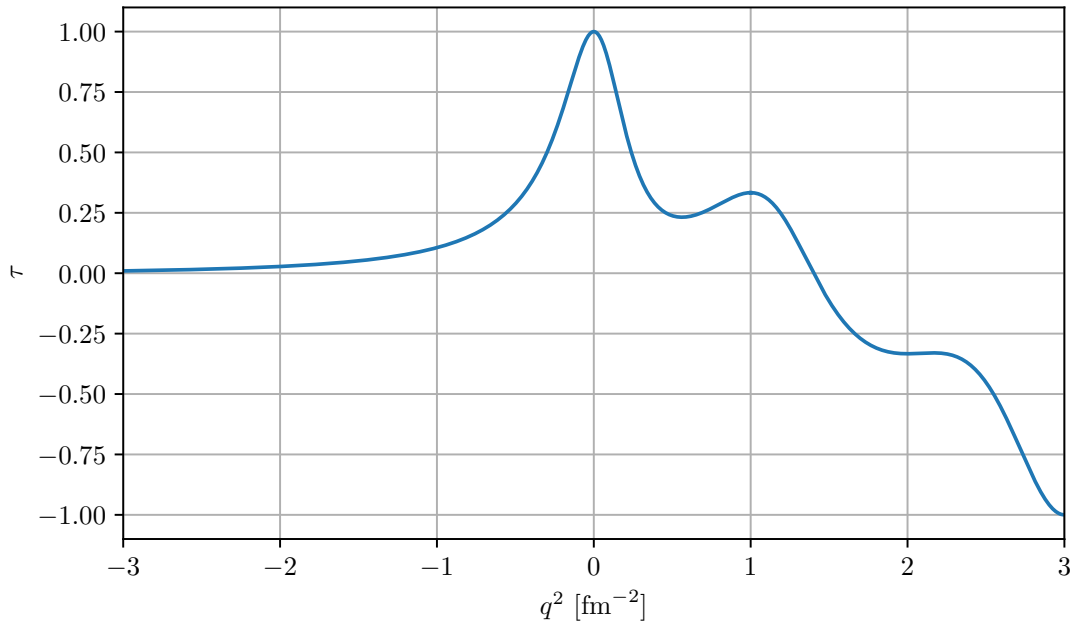
Figure 12.2.: The topological factor for a bound dimer state defined by Eq. (12.11) with $\alpha = 0.5$.

Including the corrections due to the topological factor, the finite volume energy reads

$$E\left(L\right) = \frac{k^2}{2\mu} - \#_{nn}B_{nn} - \#_{nn}\tau_{nn}\left(q^2\right)\Delta B_{nn}(L)\,, \tag{12.12}$$

where $\Delta B_{nn}(L) = B_{nn}(L) - B_{nn}$ is the finite volume correction due to the dineutron binding energy. It can be determined from the finite-volume dineutron spectrum shown in Fig. 12.3. This spectrum as well as the further spectra used for comparison within this Chapter are calculated by solving the Hamilonian in finite volume on the basis of a discrete variable representation (DVR) [68, 76, 170, 171] and the finite volume eigenvector continuation (FVEC) [172, 173]. These calculations were performed by König [156].

The dineutron energy in infinite volume is affected by the rather small cutoff $\Lambda = 150\,\text{MeV}$. So, it will not be determined by LO pionless EFT, but by extrapolation of the groundstate of the dineutron spectrum using the famous equation by Lüscher [78]:

$$E_{nn}\left(L\right) = E_{nn}\left(L = \infty\right) + \frac{c}{L} \cdot \exp\left(-\sqrt{2\mu_{nn}E_{nn}\left(L = \infty\right)}L\right)\,. \tag{12.13}$$

The fit is shown together with the spectrum in Fig. 12.3. It results in the binding energy $B_{nn}(L = \infty) = 0.161\,\text{MeV}$. This value is in contrast to the LO pionless EFT binding energy, $B_{nn}(L = \infty) = 0.116\,\text{MeV}$.

Figure 12.3.: The dineutron finite volume energy spectrum for $a_0 = 18.9\,\text{fm}$, a Gaussian regulator, $N = 48$ mesh points to construct the two-neutron DVR basis, $S_z = 0$ and the irreducible representation A_1^+ calculated by König [156]. The dineutron ground state is extrapolated to infinite volume using Eq. (12.13) (dashed line). The ground state energy is indicated by a horizontal dotted line at $B_{nn}(L = \infty) = 0.161\,\text{MeV}$.

Dimer-neutron and dimer-dimer scattering in a finite volume

12.2. Dineutron-neutron scattering

First, we consider the scattering of a dineutron and a neutron in a relative P-wave. The corresponding ERE reads

$$k^3 \cot \delta_1(k) = -\frac{1}{a_{nn-n}} + \frac{r_{nn-n}}{2}k^2 - P_{nn-n}r_{nn-n}^3 k^4 + \mathcal{O}\left(k^6\right) . \tag{12.14}$$

The ERE parameters a_{nn-n}, r_{nn-n} and P_{nn-n} are given by the universal relation Eq. (9.6) derived in Section 9.1.1,

$$k^3 \cot \delta_1 = -\frac{-1.0499(1)}{a_0^3} + \frac{4.3859(11)}{2a_0}k^2 + 1.3338(6)a_0 k^4 + \mathcal{O}\left(k^6\right) . \tag{12.15}$$

The solution of Eq. (12.9) together with the ERE given by Eq. (9.6) results in the spectrum shown in Fig. 12.4, where the energy is derived not including the topological corrections:

$$E\left(L\right) = \frac{3k^2}{8\mu_{nn}} - B_{nn} . \tag{12.16}$$

Further, the plot shows the finite volume spectrum obtained applying the DVR together with the FVEC by König [156]. Here, the 9 lowest energy levels are shown. Note that this spectrum is only restricted to levels with $S_z = 1/2$ and a negative parity. So, it includes further states beyond the scope of this Section. Comparing the energy levels of the DVR/ FVEC and the Lüscher formalism, one sees that the two lowest levels derived applying the Lüscher formalism present a larger disagreement to the DVR results. The third lowest energy level, in opposite, agrees very well with the finite volume spectrum obtained using the DVR/ FVEC formalism. However, due to performance reasons the DVR/ FVEC calculation could only be performed for a rather low cutoff $\Lambda = 150$ MeV. Including the EFT uncertainty $\pm E\sqrt{2\mu_{nn-n}E}/\Lambda$ in the order of 40% induced by this cutoff the results applying the Lüscher and the DVR/ FVEC formalism are in agreement with each other.
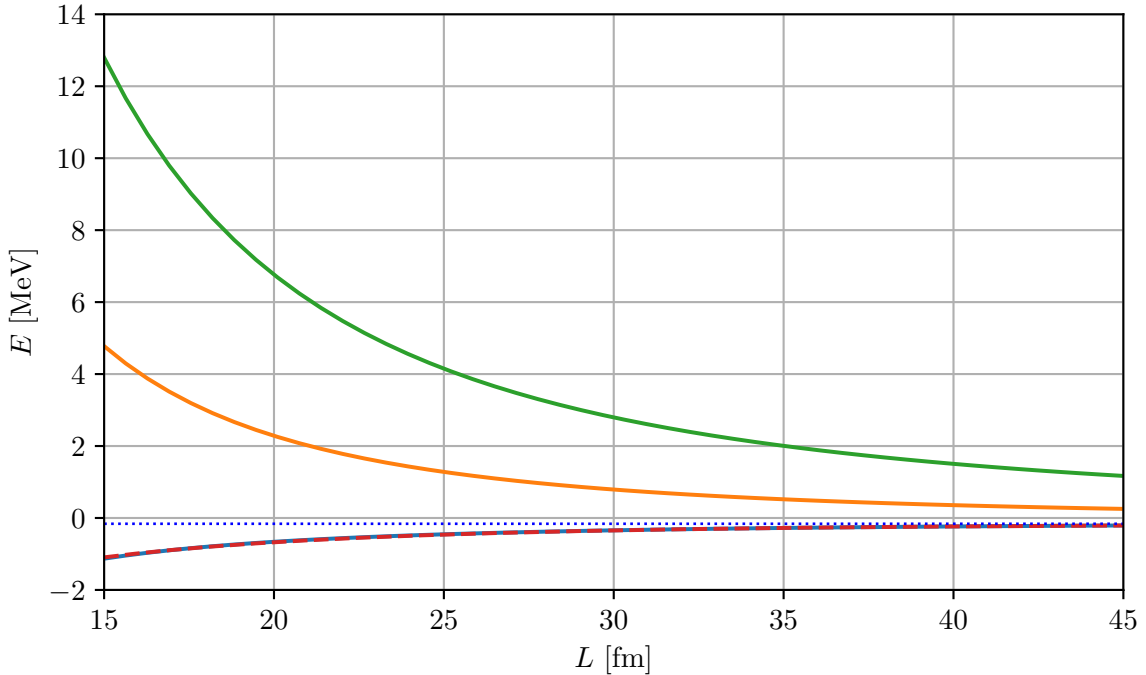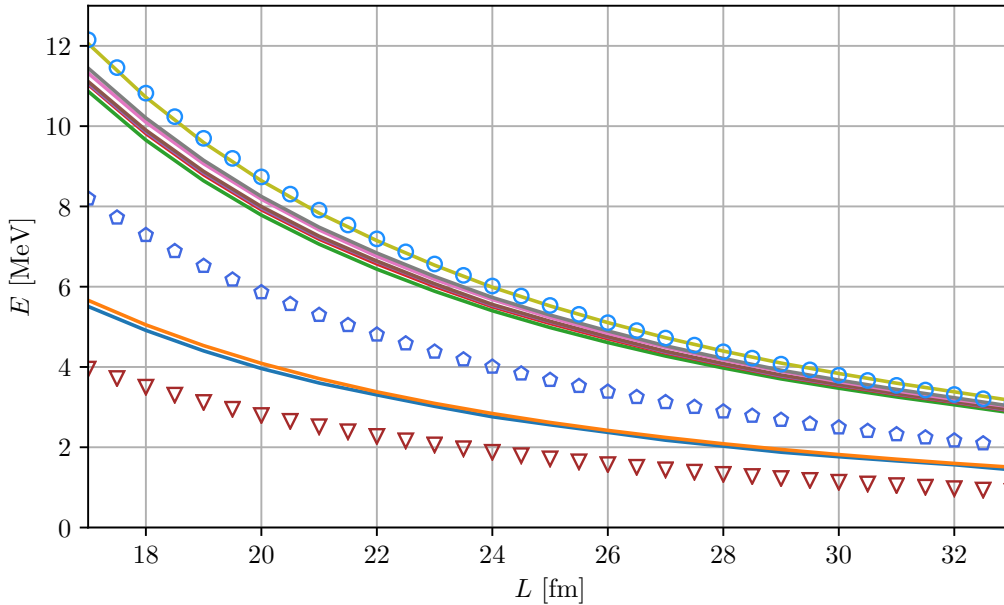

Figure 12.4.: The 3n finite volume energy spectrum for $a_0 = 18.9$ fm, a Gaussian regulator, $N = 30$ mesh points to construct the three-neutron DVR basis, $S_z = 1/2$ and negative parity (courtesy by König [156]). Further, the lowest three energy levels derived by solving Eq. (12.16) are shown by open symbols.

12.2.1. Topological corrections

Now, the spectrum has to be corrected due to the bound dineutron. The finite volume spectrum including the topological corrections following Eq. (12.12) reads

$$E(L) = \frac{3k^2}{8\mu_{nn}} - B_{nn} - \tau_{nn}\left(q^2\right)\Delta B_{nn}(L). \tag{12.17}$$

It is shown in Fig. 12.5 together with the spectrum not including the topological corrections. Due to the large box sizes, the difference between the finite and infinite volume dineutron binding energies vanishes. So, also the topological corrections are very small and the agreement within the uncertainty of the Lüscher and DVR/ FVEC results persists.

Already for this enhanced interaction strength, the spectrum does not present any avoided level crossing or equivalently no resonance. Therefore, it is very unlikely that a resonance will occur for the physical interaction strength.
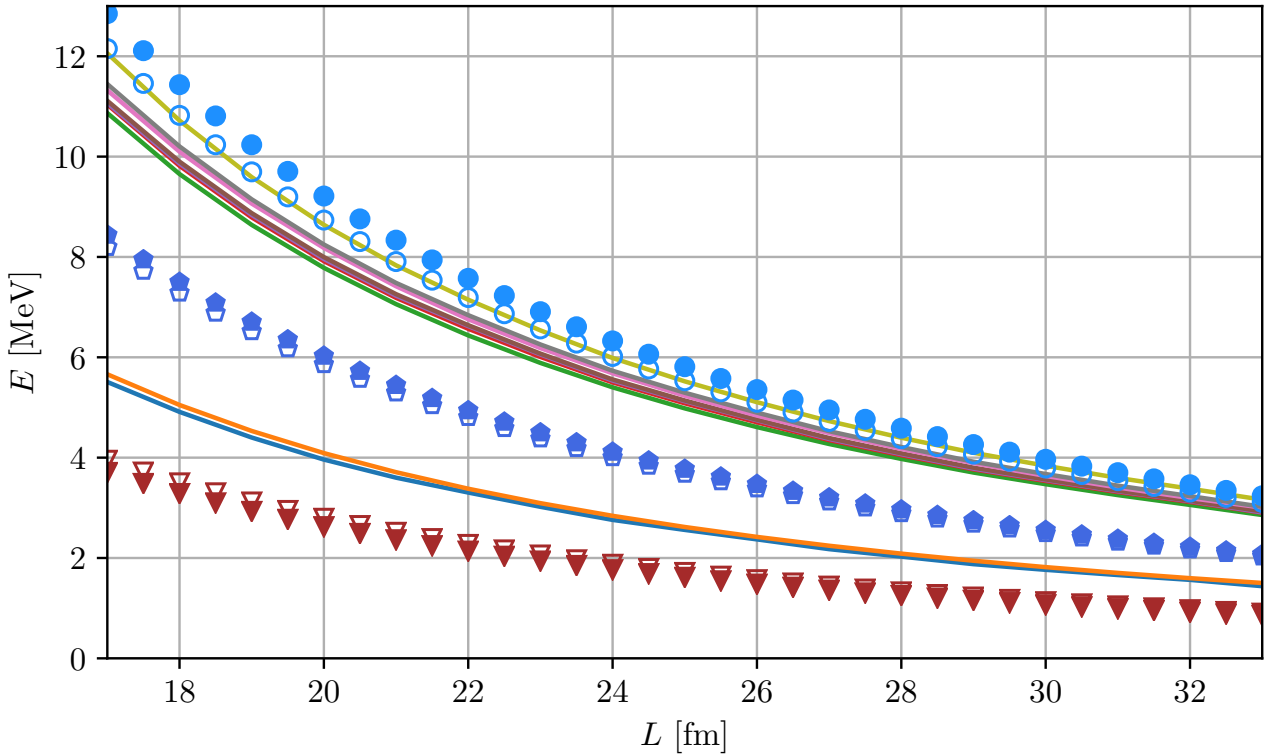
Figure 12.5.: The same plot as in Fig. 12.4. Further, the spectrum including the topological corrections given by Eq. (12.17) is shown by closed symbols. The effect of the topological corrections is negligible for these large box sizes.

12.3. Dimer-dimer scattering

In the following, the scattering of two spinless dimers in a relative S-wave should be considered, e.g. the scattering of two dineutron systems. So, the ERE reads

$$k \cot \delta_0(k) = -\frac{1}{a_{\mathrm{dd}}} + \frac{r_{\mathrm{dd}}}{2} k^2 + \mathcal{O}\left(k^4\right) , \tag{12.18}$$

where a_{dd} and r_{dd} are the dimer-dimer scattering length and effective range, respectively. In the unitary limit these can be connected to the scattering length a_0 of the particles forming the dimer, as in the previous case, too. Different calculations to determine this connection have been performed. In the following, two of them will be considered. On the one hand, there is a calculation by von Stecher *et al.* [174] using the hyperspherical formalism together with a correlated Gaussian basis. On the other hand, Elhatisari *et al.* [168] calculated these factors using lattice effective field theory. The results of both calculations are presented in Table 12.1. Besides these two calculations a third case will be considered, where the effective range is explicitly set to zero, while $a_{\mathrm{dd}}/a_0 = 0.61$ is chosen.

	a_{dd}/a_0	r_{dd}/a_0
von Stecher *et al.* [174]	0.608(2)	0.13(2)
Elhatisari *et al.* [168]	0.618(30)	$-0.431(48)$

Table 12.1.: The dimer-dimer scattering length and effective range as functions of the dimer scattering length for calculations by von Stecher *et al.* [174] and Elhatisari *et al.* [168].

As in the case of the dineutron-neutron scattering, first the spectrum without topological corrections is considered. Here, the energy is given by

$$E(L) = \frac{k^2}{2\mu_{dd}} - 2B_d = \frac{k^2}{4\mu_{nn}} - 2B_{nn} . \tag{12.19}$$

The spectra for the three cases considered are shown in Fig. 12.6. In general, the results of the three different models are located rather close to each other. While for smaller box sizes the difference is bigger, it decreases in the infinite volume limit.

These curves can now be compared to the finite volume spectrum of the four-neutron system derived using the DVR/ FVEC formalism. Figure 12.7 shows the lowest three energy levels derived from the Lüscher formalism together with the six lowest level of the DVR/ FVEC spectrum. The results of both formalism show a good agreement with each other. Within the EFT uncertainty bands in the order of 40% all three different models used for the Lüscher formalism match to the DVR/ FVEC levels. So, it is not possible to make a clear statement on which describes the DVR/ FVEC results the best. Nevertheless, the aim of this calculation was to show which levels of the DVR/ FVEC spectrum are due to the dineutron-dineutron scattering. At least for the lower-lying levels this task is possible for all three models considered for the Lüscher formalism.
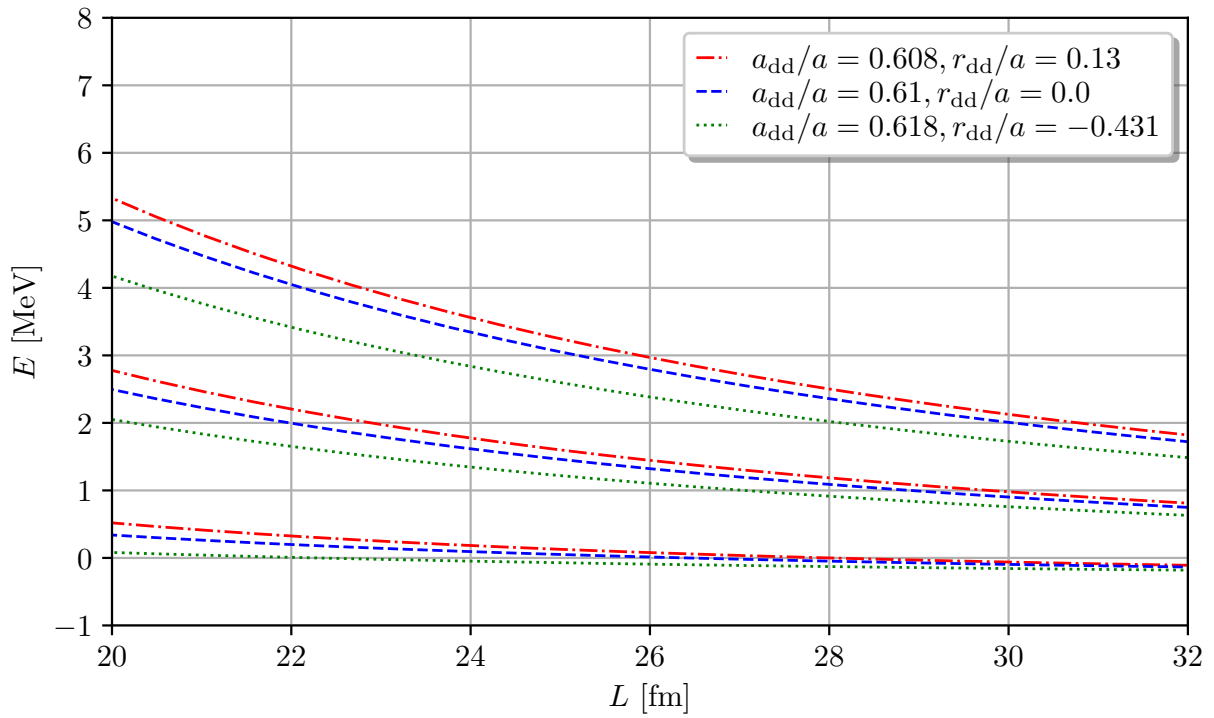
Figure 12.6.: The dimer-dimer finite volume energy spectrum derived solving Eq. (12.18) together with Eq. (12.9) for the three different cases described in the text.
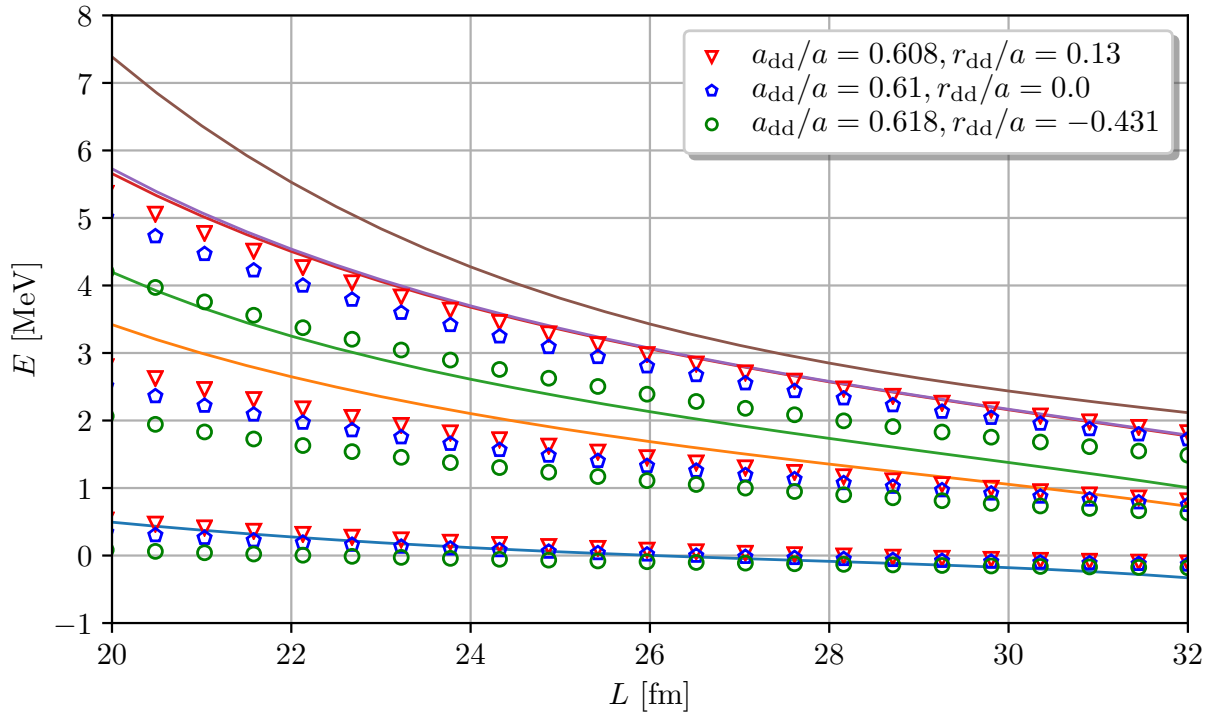
Figure 12.7.: The six lowest level of the four-neutron finite volume energy spectrum using the DVR/FVEC formalism for $a = 18.9$ fm, $N = 12$, $S_z = 0$ and the irreducible representation A_1^+ (courtesy by König [156]). Further, the three lowest energy levels for the three different models also shown in Fig. 12.6 are represented by open symbols.

12.3.1. Topological corrections

Again, we have to consider topological corrections. Here, the effect is twice as large as for the dineutron-neutron system as our system consists of two dimers. Following Eq. (12.12), the energy spectrum is given by

$$
\begin{aligned}
E(L) &= \frac{k^2}{2\mu_{\mathrm{dd}}} - 2B_{\mathrm{d}} - 2\tau_{\mathrm{d}}\left(q^2\right)\Delta B_{\mathrm{d}}(L) \\
&= \frac{k^2}{4\mu_{\mathrm{nn}}} - 2B_{\mathrm{nn}} - 2\tau_{\mathrm{nn}}\left(q^2\right)\Delta B_{\mathrm{nn}}(L)\,.
\end{aligned}
\tag{12.20}
$$

The spectrum is shown in Fig. 12.8 together with the energies without topological corrections. Due to the topological corrections some levels are shifted closer to the DVR/ FVEC results, while other levels are shifted further away. Overall the best agreement can be found for larger r_{dd}/a, while the results of the model following the work by Elhatisari *et al.* [168] present the least agreement. Nevertheless, using the Lüscher formalism it is possible to make a statement on which levels are connected to the scattering of two dineutrons. Furthermore, this energy spectrum does not show an avoided level crossing. So, reducing the neutron-neutron interaction strength from the enhanced to the physical value the existence of a four-neutron resonance is even more unlikely.
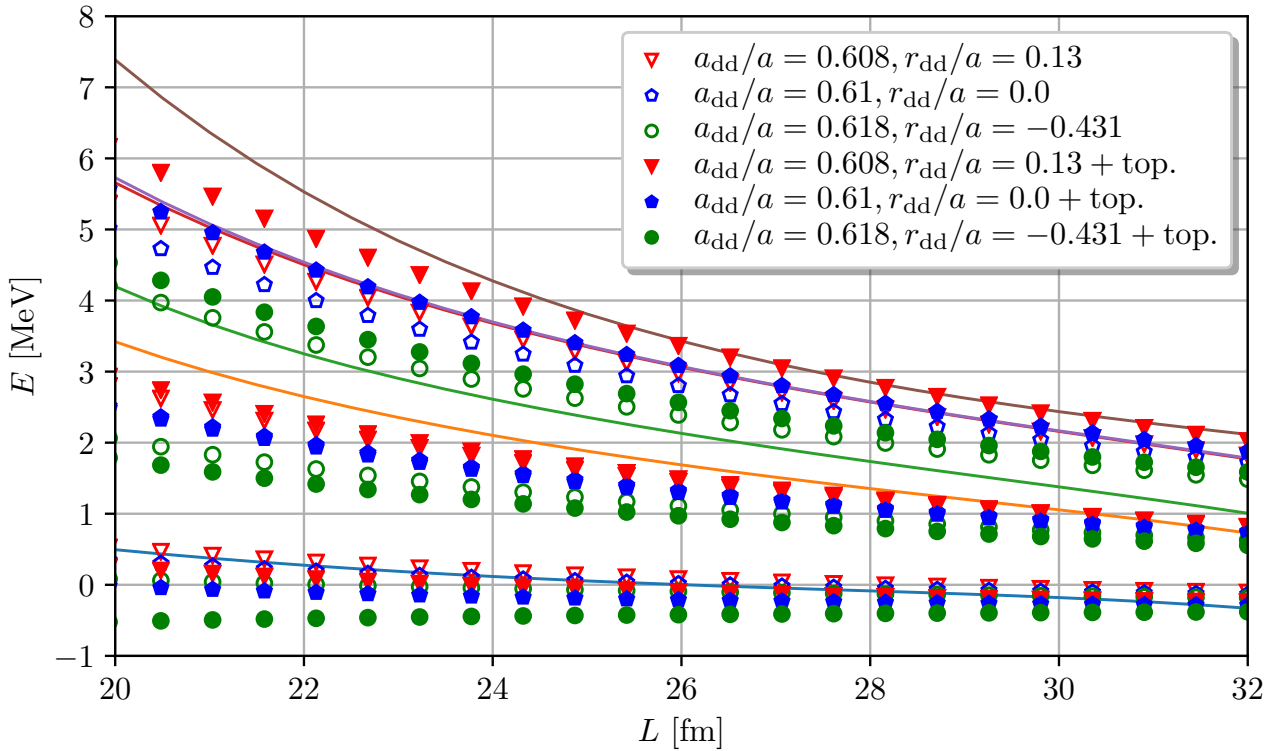
Figure 12.8.: The plot shown in Fig. 12.7 together with the results derived from the Lüscher formalism including the topological corrections (closed symbols).

13 **Summary & Outlook**

In this thesis, the continuum structure of few-body systems applying potentials derived from pionless effective field theory at leading order was addressed. In particular, the focus of these investigations was on the continuum-structure of pure neutron systems, e.g., the possible existence of three- and four-neutron resonances. For this purpose, different complementary methods were derived and their applications and results were compared.

The starting point of all these investigations were the momentum-space scattering equations for two, three and four particles, the Lippmann-Schwinger, Faddeev and Faddeev-Yakubovsky equations, respectively. A significant part of this work was devoted to the application of the method of analytical continuation. It provides an unambiguous definition of the continuum structure by relating it to the poles of the T-matrix on the unphysical sheets of the complex energy plane. This high expressiveness has the disadvantage of a laborious derivation of the corresponding scattering equations. These were carried out in Chapter 5 for general two- and three-body systems. The analytical continuation is based on a transformation of the cuts between the physical and unphysical sheets of the complex energy plane. Explicit as well as implicit transformations of the cuts, following the works by Afnan [87–91] and Glöckle [44], were investigated. In particular, the difficulty of correctly defining the momentum as a function of the energy was discussed. Furthermore, systems consisting of several particles show effects of the subsystems, e.g., the presence of the two-body T-matrix within the kernel of the Faddeev equation. Thereby, the correct choice of the functional dependencies on the momentum was analyzed for different regulators.

The results of the analytical continuation were compared in Chapter 6 for two two-particle toy potentials with calculations on the physical sheet. Here, on the one hand, the effects of the continuum states on the physical sheet were considered using the phase shifts and time delays. On the other hand, the analytical continuation in the coupling constant (ACCC) was applied to perform a simplified "continuation" onto the unphysical sheets. It could be shown that, as far as possible, the results of an explicit as well as implicit transformation of the cut for the analytical continuation are indistinguishable. Further, it became clear that the ACCC results are far from being able to keep up with the proper analytical continuation and are more comparable to the calculation of the phase shifts. It was shown for both methods, the phase shifts and the ACCC, that their accuracy decreases with increasing distance to the physical sheet. In particular, it was shown that as soon as the pole structure on the unphysical sheet becomes more complicated, e.g., multiple poles exist, no statement can be made or false statements are made. The reason for this is that the methods extrapolate an overall picture of the continuum structure, which does not allow clean distinctions between individual contributions. In summary, it was shown that only the analytical continuation can compute the correct pole structure on the unphysical sheets with high accuracy, while calculations on the physical sheets are limited to cases with a simple pole structure close to the physical sheet. In the latter case, it is equally possible to make statements with relatively high accuracy.

On the basis of these findings, a system of three spinless bosons with a large scattering length was investigated in Chapter 7. It presents a very rich continuum structure for both, a bound and an unbound

two-boson subsystem. Furthermore, it includes a three-body force already at leading order. The structure of this three-body force for representations derived from the Lagrangian as well as from the Faddeev theory were compared and the relevant structures for performing an analytical continuation were identified. For positive scattering lengths the tower of bound Efimov states evolves into virtual states going through the two-body branch cut. We followed this pole trajectory up to the end of the range of applicability performing an implicit transformation of the integration contour. The obtained results are compared to a previous calculation by Yamashita *et al.* [134] presenting a qualitative agreement. The more significant continuum structure is present in the case of an unbound two-boson subsystem. Here, the sheet structure is equal to that of the three-neutron system. Furthermore, the Efimov states turn into resonances as they cross the three-particle threshold. Applying an explicit contour transformation, the previous calculations by Bringas *et al.* [95] and Deltuva [135] were confirmed, both qualitatively and quantitatively. Moreover, our results are qualitatively consistent with the pole trajectories of Jonsell [136] and Hyodo *et al.* [137]. The trajectories of these Efimov resonances not only serve as benchmark calculations for the three-neutron system, but can also be used to explain the behavior of the three-body recombination rate of three spinless bosons at low temperatures [136, 175].

Within Chapter 8 the neutron-deuteron system was investigated. Due to the large difference in the order of magnitude of the scattering lengths, the doublet channel presents a phase shift anomaly at the deuteron breakup threshold. This anomaly was investigated as a function of the triplet scattering length and the three-body force. It was shown that, due to the dominant contribution of the quartet channel, it does not effect the cross section.

In the following, the focus shifted to the main system of this work, the three-neutron system. As shown previously for the two-body toy potentials, phase shifts are a meaningful tool for states on the unphysical sheets close to the physical one. By the work of Glöckle [44], it is known that the three-neutron system in the limiting case of a vanishing dineutron binding energy has a state at the origin of the complex energy plane. Therefore, it can be assumed that a small shift of the dineutron binding momentum from $\gamma_0 = 0 \, \text{fm}^{-1}$ to the physical value $\gamma_0 = -18.9^{-1} \, \text{fm}^{-1}$ also results in only a small shift of the three-neutron state. So, if there is a three-neutron state on the unphysical sheet next to the lower rim of the physical sheet it should be accessible by calculating the phase shifts. However, phase shifts are in general a quantity which is defined only for (effective) two-particle systems. Therefore, in Chapter 9, we calculate the phase shifts for a three-neutron system with a bound dineutron and extrapolate to the physical, unbound dineutron. Here, a third neutron in a relative S-, P- and D-wave was investigated. These phase shifts are further used to determine universal relations for the effective range expansion, valid for energies up to the breakup of the dineutron. Together with other models, these universal relations are used to extrapolate the phase shifts. The obtained results are compared to the work by Higgins *et al.* applying an adiabatic hyperspherical formalism [64, 65] and the similarities and differences were discussed. It was possible to show, that applying the phase shifts no three-neutron resonance is present.

This result was supported in Chapter 10 by applying the analytical continuation formalism using an explicit contour transformation. Here, the third neutron in a relative S- and P-wave was considered. This results in the channels $J^\pi = \frac{1}{2}^+$ and $\frac{1}{2}^-, \frac{3}{2}^-$, respectively. In comparison to the two-body toy potentials and the three-boson system, the three neutrons have a further complicating feature. To validate the results derived by analytical continuation one usually tries to trace the pole trajectory from the physical to the unphysical sheets. However, we have shown that it is not possible to bind three neutrons in pionless effective field theory at leading order. Therefore, the results for large positive scattering lengths were compared with the results of a model calculation using the Yamaguchi model, which was originally performed by Glöckle [44]. These results could be reproduced within the range of applicability of our effective field theory. Tracing the pole trajectory further to the physical neutron-neutron scattering

length, we could show that the three-neutron system neither presents a resonance nor a virtual state, which is in perfect agreement with the phase shift calculation.

Nevertheless, multi-neutron energy spectra contain much interesting physics, even if multi-neutron resonances are not present. In Ref. [92], e.g., it was pointed out that the multi-neutron spectra for center-of-mass energies E in the range $1/(ma_0^2) \approx 0.1\,\text{MeV} \ll E \ll 1/(mr_0^2) \approx 5\,\text{MeV}$ are determined by conformal symmetry up to an overall normalization. Conformal symmetry implies that the multi-neutron correlation functions have only cuts but no poles, which is consistent with our results for the three-neutron system. The neutron spectra show power-law behavior with, in general, fractional exponents determined by the scaling dimension of the corresponding conformal field operators. The agreement of these predictions with the spectrum of the three-neutron system was investigated in Chapter 11 considering the point production approach. Again, the system of three spinless bosons was considered first. Because of the additional scale due to the three-body force it does not follow the predictions by nonrelativistic conformal field theory. The point production amplitude R, a quantity similar to the cross section, was calculated and the effect of a resonance on it was examined. Based on this benchmark calculation, the three-neutron system was considered. Similar to the three-boson system, the point production amplitude for a third neutron in a relative S-, P- and D-wave was calculated. Assuming the same coupling for all three partial waves, it was shown that the P-wave dominates. Further, the spectrum was compared to the scaling predicted for free particles and by conformal symmetry. It was shown to follow these predictions perfectly. Additionally, the four-neutron system was considered. Here, the point production amplitude on the basis of the Faddeev-Yakubovsky equations was derived, but due to the large numerical effort not calculated. Based on the predictions by nonrelativistic conformal field theory, it was argued that it is unlikely that the four-neutron system presents a resonance either.

Finally, the last type of formalism searching for resonances was applied in Chapter 12, a finite volume approach. Using the Lüscher formalism [78, 79] together with universal relations of the effective range expansion, the finite volume energy spectra for a dineutron-neutron and a dineutron-dineutron system were calculated. For this purpose, it was assumed that the dineutron is bound with the positive value of the physical scattering length, $a_0 = 18.9\,\text{fm}$. On the one hand, these spectra show that already for an enhanced interaction strength neither the three-neutron nor the four-neutron system present an avoided level crossing what conditions the existence of a resonance. These results agree with a recent investigation of the three-neutron system in finite volume determining the finite volume energy spectrum using a discrete variable representation approach [68]. On the other hand, finite volume calculations complicate the identification of individual channels in the spectrum. However, this is necessary for the identification of an avoided level crossing. The results presented here support this approach for calculations of the four-neutron spectrum currently performed using the discrete variable representation together with a finite volume eigenvector continuation approach [172]. Preliminary results of these calculations further show that a four-neutron resonance seems to be unlikely.

All in all, we have applied different approaches to search for resonances and virtual states in few-body systems applying a leading order pionless EFT interaction. Here, we could show, in agreement of all methods, that the three-neutron system has neither resonances nor virtual states. Our model-independent result agrees with several other recent theoretical studies [60, 64–66]. Although we use pionless EFT at leading order, we expect our result to hold also in the presence of higher-order interactions. In pionless EFT the higher-order terms, including the effective range r_0 and P-wave interactions, are purely perturbative and cannot produce any new poles. Thus the existence of a low-energy three-neutron resonance or virtual state would also imply the breakdown of pionless EFT in the three-neutron system. Furthermore, we could motivate that a resonance in the four-neutron system is unlikely by applying the point production and finite volume approaches.

On the basis of this work, further studies of the continuum structure of few-body systems with four and more particles can be performed. While in this thesis, for the four-neutron system, the non-existence of a resonance was motivated, the question can be discussed in the future using more sophisticated methods. Similar to the three-neutron system, the status of the four-neutron system is rather inconclusive. Within the recent years, several experiments and theoretical calculations have been performed. From the experimental side, experiments at GANIL [176] and RIKEN [69, 70] presented a possible evidence of a four-neutron resonance, while a work at the Technical University Munic even suggested a bound four-neutron state [71]. From a theoretical point of view, the situation is more complicated. It is generally accepted that a bound four-neutron state can be excluded. However, there are different results regarding the existence of a resonance. Within the recent years, there have been calculations applying a Quantum Monte Carlo approach [58], the no-core shell model [177] and the no-core Gamow shell model [63, 178], which resulted in possible four-neutron resonance candidates. In contrast, further theoretical calculations rule out the possible existence of a four-neutron resonance [53, 61, 64, 65, 179–183]. These results are in agreement with the predictions by non-relativistic conformal field theory presented in Chapter 11. Additionally, these results are supported by preliminary calculations on the basis of the finite volume approach presented in Ref. [68] together with a finite volume eigenvector continuation formalism [172], which will be published in near future. Furthermore, theoretical works attempt to resolve the contradiction between experimental results and the majority of theoretical work. In this regard, the work of Lazauskas *et al.* [184] may be cited as an example. They try to explain the results of the experiment of Duer *et al.* [69] by the existence of dineutron-dineutron correlations. Altogether, the situation of the four-neutron system is comparable to the one of the three-neutron system. From the experimental side new experiments proposed will try to solve this puzzle [185, 186].

Building on the work done in this thesis, we can also contribute from the theoretical side to make a clear statement on the status of the four-neutron system. In general, all methods applied within this work can be extended to the four-neutron system. In part, as in the case of the point production, this has already been done. Nevertheless, the most meaningful method applied within this work is the analytical continuation. While the derivation of the scattering equations is rather complicated, the application results in clear statements on the continuum structure. In comparison to three-body systems, the complexity for four-body systems is increased due to the extended sheet and cut structure. Nevertheless, as shown in Chapter 5, a challenging part of the derivation is the correct inclusion of the structure of the subsystems. However, it is possible to express the Faddeev-Yakubovsky equations as functions of the two-body T-matrix [159–165], for which the hard work on the analytical continuation has already been performed within this work. Furthermore, the correct choice of the momentum as a function of the energy presents a complicating feature. The basics for this were also discussed in this thesis, which should make it relatively easy to extend this to more particles. Thus, overall, it should be possible to extend the method of analytical continuation to the four-neutron system with limited effort.

A Conventions

Within this thesis two different basis conventions are used. The first convention is the one commonly applied when using the EFT's to derive Feynman rules from the Lagrangian. It is denoted by $\mathfrak{N}_L$. If we apply a formalism connected to this type it takes the value $\mathfrak{N}_L = (2\pi)^3$, otherwise $\mathfrak{N}_L = 1$. The second convention is typically applied within scattering theory calculations, e.g. the Faddeev formalism. It is used everywhere else, denoted by $\mathfrak{N}_S$ and takes the values $\mathfrak{N}_S = (2\pi)^3$ $(= 1)$ within (without) a calculation connected to this field.

The first basis we consider is a coordinate-space vector basis of the relative coordinates between particles 1 and 2, $\boldsymbol{r} := \boldsymbol{r}_1 - \boldsymbol{r}_2$. It fulfills the completeness and orthogonality relations

$$\int \frac{\mathrm{d}^3 r}{\mathfrak{N}_S} \left| \boldsymbol{r} \right\rangle \left\langle \boldsymbol{r} \right| = \mathbb{1} \,,$$

$$\left\langle \boldsymbol{r} | \boldsymbol{r}' \right\rangle = \mathfrak{N}_S \delta^{(3)} \left(\boldsymbol{r} - \boldsymbol{r}' \right) \,. \tag{A.1}$$

The complementary momentum-space vector basis for relative momenta, $\boldsymbol{k} := \boldsymbol{k}_1 - \boldsymbol{k}_2$, analogously fulfills

$$\int \frac{\mathrm{d}^3 k}{\mathfrak{N}_L} \left| \boldsymbol{k} \right\rangle \left\langle \boldsymbol{k} \right| = \mathbb{1}$$

$$\left\langle \boldsymbol{k} | \boldsymbol{k}' \right\rangle = \mathfrak{N}_L \delta^{(3)} \left(\boldsymbol{k} - \boldsymbol{k}' \right) \,. \tag{A.2}$$

The overlap between both bases is given by

$$\left\langle \boldsymbol{r} | \boldsymbol{k} \right\rangle = e^{i \boldsymbol{k} \cdot \boldsymbol{r}} \,. \tag{A.3}$$

Beside the cartesian bases we can consider bases in spherical coordinates, $\left| \boldsymbol{r} \right\rangle = \left| r\phi\theta \right\rangle$ and $\left| \boldsymbol{k} \right\rangle = \left| k\phi\theta \right\rangle$. Commonly the angular part of the coordinate is summarized in the solid angle $\left| \Omega \right\rangle := \left| \phi\theta \right\rangle$. The corresponding completeness and orthogonality relations are

$$\int_0^\infty \frac{\mathrm{d}r}{\mathfrak{N}_S} r^2 \int \mathrm{d}\Omega \left| r\Omega \right\rangle \left\langle r\Omega \right| = \mathbb{1} \,,$$

$$\left\langle r\Omega | r'\Omega' \right\rangle = \mathfrak{N}_S \frac{\delta \left(r - r' \right)}{r^2} \delta^{(2)} \left(\Omega - \Omega' \right) \,,$$

$$\int_0^\infty \frac{\mathrm{d}k}{\mathfrak{N}_L} k^2 \int \mathrm{d}\Omega \left| k\Omega \right\rangle \left\langle k\Omega \right| = \mathbb{1} \,,$$

$$\left\langle k\Omega | k'\Omega' \right\rangle = \mathfrak{N}_L \frac{\delta \left(k - k' \right)}{k^2} \delta^{(2)} \left(\Omega - \Omega' \right) \,. \tag{A.4}$$

Finally, we introduce the coordinate- and momentum-space partial-wave bases. These bases are connected to the spherical bases by the spherical harmonics,

$$\langle r\Omega | r'l'm' \rangle = \mathfrak{N}_S \frac{\delta (r - r')}{r^2} Y_{l'm'} (\Omega) \ ,$$

$$\langle k\Omega | k'l'm' \rangle = \mathfrak{N}_L \frac{\delta (k - k')}{k^2} Y_{l'm'} (\Omega) \ . \tag{A.5}$$

The completeness and orthogonality relations for the partial-wave bases are given by

$$\sum_{lm} \int_0^\infty \frac{\mathrm{d}r}{\mathfrak{N}_S} r^2 \, |rlm\rangle \langle rlm| = \mathbb{1} \ ,$$

$$\langle rlm | r'l'm' \rangle = \mathfrak{N}_S \frac{\delta (r - r')}{r^2} \delta_{ll'} \delta_{mm'} \ ,$$

$$\sum_{lm} \int_0^\infty \frac{\mathrm{d}k}{\mathfrak{N}_L} k^2 \, |klm\rangle \langle klm| = \mathbb{1} \ , \tag{A.6}$$

$$\langle klm | k'l'm' \rangle = \mathfrak{N}_L \frac{\delta (k - k')}{k^2} \delta_{ll'} \delta_{mm'} \ .$$

Note that matrix elements of partial-wave basis states are diagonal in l and m.

B Partial-wave projection

B.1. Two-body systems

This Sectiondiscusses the partial-wave projection of the Lippmann-Schwinger equation Eq. (2.7). Here, we follow the convention $\mathfrak{N}_S = (2\pi)^3$ and $\mathfrak{N}_L = 1$.

Within the introduction into scattering theory the Lippmann-Schwinger equation in a plane-wave momentum space basis was derived by combining Eq. (2.11) and Eq. (2.12),

$$\langle \boldsymbol{k}|T(z)|\boldsymbol{p}\rangle = \langle \boldsymbol{k}|V|\boldsymbol{p}\rangle + \int \mathrm{d}^3 q \, \langle \boldsymbol{k}|V|\boldsymbol{q}\rangle \, G_0(z;q) \, \langle \boldsymbol{q}|T(z)|\boldsymbol{p}\rangle \, . \tag{B.1}$$

An analogue of this equation in the partial-wave momentum basis can be derived by using the partial-wave projection of the potential,

$$\begin{aligned}
\langle \boldsymbol{k}|V|\boldsymbol{p}\rangle &= \sum_{\substack{l,m \\ l',m'}} \int_0^\infty \mathrm{d}\tilde{k} \, \tilde{k}^2 \int_0^\infty \mathrm{d}\tilde{p} \, \tilde{p}^2 \, \underbrace{\left\langle \boldsymbol{k}\middle|\tilde{k}lm\right\rangle}_{\frac{\delta(k-\tilde{k})}{\tilde{k}^2}Y_{lm}(\Omega_k)} \, \left\langle \tilde{k}lm\middle|V\middle|\tilde{p}l'm'\right\rangle \, \underbrace{\left\langle \tilde{p}l'm'\middle|\boldsymbol{p}\right\rangle}_{\frac{\delta(p-\tilde{p})}{\tilde{p}^2}Y^*_{l'm'}(\Omega_p)} \\
&= \sum_{\substack{l,m \\ l',m'}} \int_0^\infty \mathrm{d}\tilde{k} \int_0^\infty \mathrm{d}\tilde{p} \, \delta(k-\tilde{k})\delta(p-\tilde{p}) Y_{lm}(\Omega_k) Y^*_{l'm'}(\Omega_p) \left\langle \tilde{k}lm\middle|V\middle|\tilde{p}l'm'\right\rangle \\
&= \sum_{l,m} \langle klm|V|plm\rangle \, Y_{lm}(\Omega_k) Y^*_{lm}(\Omega_p) \, ,
\end{aligned} \tag{B.2}$$

where in the last line it was applied that the potential conserves the l and m quantum numbers. A similar expression can be derived for the T-matrix,

$$\langle \boldsymbol{k}|T(z)|\boldsymbol{p}\rangle = \sum_{l,m} \langle klm|T|plm\rangle \, Y_{lm}(\Omega_k) Y^*_{lm}(\Omega_p) \, . \tag{B.3}$$

Altogether, the partial-wave projected Lippmann-Schwinger equation reads

$$\langle klm|T|plm\rangle = \langle klm|V|plm\rangle + \int_0^\infty \mathrm{d}q \, q^2 \, \langle klm|V|qlm\rangle \, G_0(z;q) \, \langle qlm|T|plm\rangle \, , \tag{B.4}$$

where the orthogonality of the spherical harmonics was applied.

B.2. Three-body systems

The derivation of a Faddeev equation using the Lagrangian ansatz of an EFT requires the projection to a partial wave. The general way to project a T-matrix onto a given partial wave is by using the projection operator

$$\frac{1}{2} \int_{-1}^{+1} \mathrm{d}\cos\theta \, P_l\left(\cos\theta\right) ,\tag{B.5}$$

where θ is the angle between the in- and outgoing momentum.

The simpler term to consider is the inhomogeneous term. It represents a potential-like structure given by the integral over the free Green's function,

$$-\int_{-1}^{1} \mathrm{d}\cos\theta \frac{P_l(\cos\theta)}{k^2 + p^2 + kp\cos\theta - mE - i\varepsilon}$$
$$= \begin{cases} -\frac{1}{kp}\log\left(\frac{k^2+p^2-mE-i\varepsilon+kp}{k^2+p^2-mE-i\varepsilon-kp}\right) , & \text{for } l = 0 , \\ -\frac{1}{k^2p^2}\left[2kp - \left(k^2 + p^2 - mE - i\varepsilon\right)\log\left(\frac{k^2+p^2-mE-i\varepsilon+kp}{k^2+p^2-mE-i\varepsilon-kp}\right)\right] , & \text{for } l = 1 . \end{cases}\tag{B.6}$$

The calculation of the homogeneous integral term is more complicated. We have to apply the partial-wave expansion of the T-matrix Eq. (B.3), which can be rewritten to

$$\langle \boldsymbol{p}|T(E)|\boldsymbol{k}\rangle = \sum_l \left(2l + 1\right) P_l(\cos\theta) \langle plm|T(E)|klm\rangle \ , ,\tag{B.7}$$

using the addition theorem for the spherical harmonics (note the additional factor 4π by changed conventions)

$$P_l\left(\cos\gamma\right) = \frac{4\pi}{2l+1} \sum_{m=-l}^{l} Y_l^{m*}\left(\theta',\phi'\right) Y_l^m\left(\theta,\phi\right)$$
$$= P_l\left(\cos\theta\right) P_l\left(\cos\theta'\right) + 2 \sum_{m=1}^{l} \frac{(l-m)!}{(l-m)!} P_l^m\left(\cos\theta\right) P_l^m\left(\cos\theta'\right) \cos\left[m\left(\phi - \phi'\right)\right] .\tag{B.8}$$

Further, we have to introduce a coordinate system to define the angles. Choose $\boldsymbol{p}$ as the quantization axis and define

$$\boldsymbol{k} \cdot \boldsymbol{p} = kp \cdot \cos\theta ,$$
$$\boldsymbol{q} \cdot \boldsymbol{p} = qp \cdot \cos\theta' ,$$
$$\gamma = \theta - \theta' .$$

Using these definitions, we get for the homogeneous term

$$
\int_{-1}^{1} \mathrm{d}\cos\theta\, P_l\left(\cos\theta\right)\int\frac{\mathrm{d}^3 q}{(2\pi)^3} D\left(E-\frac{\boldsymbol{q}^2}{2m},\boldsymbol{q}\right) T(\boldsymbol{k},\boldsymbol{q};E)\frac{1}{\boldsymbol{q}^2+\boldsymbol{q}\cdot\boldsymbol{p}+\boldsymbol{p}^2-mE-i\varepsilon}
$$

$$
=\int_{-1}^{1}\mathrm{d}\cos\theta\,P_l\left(\cos\theta\right)\int\frac{\mathrm{d}q}{(2\pi)^3}q^2\int_0^{2\pi}\mathrm{d}\phi'\int_{-1}^{1}\mathrm{d}\cos\theta'\,D\left(E-\frac{\boldsymbol{q}^2}{2m},\boldsymbol{q}\right)
$$

$$
\times\sum_{l'}\left(2l'+1\right)P_{l'}(\cos\gamma)\,T_{l'}(k,q;E)\frac{1}{q^2+qp\cdot\cos\theta'+p^2-mE-i\varepsilon}
$$

$$
\overset{Eq.\ (B.8)}{=}2\pi\int_{-1}^{1}\mathrm{d}\cos\theta\,P_l\left(\cos\theta\right)\int\frac{\mathrm{d}q}{(2\pi)^3}q^2\int_{-1}^{1}\mathrm{d}\cos\theta'\,D\left(E-\frac{\boldsymbol{q}^2}{2m},\boldsymbol{q}\right)
$$

$$
\times\sum_{l'}\left(2l'+1\right)P_{l'}(\cos\theta)P_{l'}(\cos\theta')\,T_{l'}(k,q;E)\frac{1}{q^2+qp\cdot\cos\theta'+p^2-mE-i\varepsilon}
$$

$$
=4\pi\int\frac{\mathrm{d}q}{(2\pi)^3}q^2\,D\left(E-\frac{\boldsymbol{q}^2}{2m},\boldsymbol{q}\right)T_l(k,q;E)\int_{-1}^{1}\mathrm{d}\cos\theta'P_l\left(\cos\theta'\right)\frac{1}{q^2+qp\cdot\cos\theta'+p^2-mE-i\varepsilon}\,.
$$

$$\tag{B.9}$$

The remaining integral over $\cos\theta'$ is the same as in the inhomogeneous term.
For the second equality we used that the second term of the addition theorem cancels due to

$$
\int_0^{2\pi}\mathrm{d}\phi'\cos\left[m\left(\phi-\phi'\right)\right]=0\,\forall m\,.
\tag{B.10}
$$

The sum of over l' cancels due to the orthogonality of the Legendre polynomials

$$
\int_{-1}^{1}\mathrm{d}\cos\theta\,P_l\left(\cos\theta\right)P_{l'}\left(\cos\theta'\right)=\frac{2}{2l+1}\delta_{ll'}\,.
\tag{B.11}
$$

C Projectors

This Chapter motivates the projectors onto the singlet $^1S_0$ and triplet $^3S_1$ channels for a pionless EFT interaction in the two-body system.

C.1. Lagrangian representation

The LO two-body Lagrangian presents two projectors, Eq. (3.3),

$$
\begin{aligned}
(\mathcal{P}_t)^i &= \frac{1}{\sqrt{8}} \sigma^2 \sigma^i \tau^2 \,, \\
(\mathcal{P}_s)^i &= \frac{1}{\sqrt{8}} \sigma^2 \tau^2 \tau^i \,.
\end{aligned}
\tag{C.1}
$$

Each projector is the product of two factors.

First, we the effect of σ^2 is investigated. We treat the nucleon as a simple spin-doublet $(\uparrow, \downarrow)^T$ and consider

$$
(\uparrow, \downarrow)^T \underbrace{\begin{pmatrix} 0 & -i \\ i & 0 \end{pmatrix}}_{\sigma^2} \begin{pmatrix} \uparrow \\ \downarrow \end{pmatrix} = \uparrow\downarrow - \downarrow\uparrow \,.
\tag{C.2}
$$

The second Pauli matrix σ^2 anti-symmetrizes the state, which is a requirement for a fermionic system.

Now the remaining factor can be considered. To motivate its structure, two spin-$1/2$ fermions are coupled to a triplet and a singlet,

$$
\frac{1}{2} \otimes \frac{1}{2} = 1 \oplus 0 \,.
\tag{C.3}
$$

These states are given by

$$
\begin{aligned}
|1, 1\rangle &= |\uparrow\rangle \otimes |\uparrow\rangle \,, \\
|1, 0\rangle &= \frac{1}{\sqrt{2}} \left(|\uparrow\rangle \otimes |\downarrow\rangle + |\downarrow\rangle \otimes |\uparrow\rangle \right) \,, \\
|1, -1\rangle &= |\downarrow\rangle \otimes |\downarrow\rangle \,, \\
|0, 0\rangle &= \frac{1}{\sqrt{2}} \left(|\uparrow\rangle \otimes |\downarrow\rangle - |\downarrow\rangle \otimes |\uparrow\rangle \right) \,,
\end{aligned}
$$

with the Clebsch Gordan coefficients as prefactors.

Now apply the spin part of the first projector $\sigma^2\sigma^i$ to the nucleon $N = (\uparrow, \downarrow)^T$,

$$N^T \sigma^2 \sigma^1 N = -i\left|1,1\right\rangle + i\left|1,-1\right\rangle,$$
$$N^T \sigma^2 \sigma^2 N = \left|1,1\right\rangle + \left|1,-1\right\rangle,$$
$$N^T \sigma^2 \sigma^3 N = i\sqrt{2}\left|1,0\right\rangle$$

we obtain linear combinations of the spin-triplet. We are left with the isospin part of the projector τ^2. It result in a linear combination analogous to Eq. (C.2), which is the isospin-singlet.

Exchanging spin and isospin $\sigma \leftrightarrow \tau$, we obtain the same result for the other projector.

To project onto the physical states, e.g. the spin-triplet isospin-singlet, we can solve the three equations connecting the spin part of the first projector with the spin-triplet to obtain

$$\left(\tilde{P}_t\right)_{m=-1} = -i\sqrt{2}\left[\left(\hat{P}_t\right)^1 + i\left(\hat{P}_t\right)^2\right],$$
$$\left(\tilde{P}_t\right)_{m=0} = -2i\left(\hat{P}_t\right)^3, \tag{C.4}$$
$$\left(\tilde{P}_t\right)_{m=+1} = i\sqrt{2}\left[\left(\hat{P}_t\right)^1 - i\left(\hat{P}_t\right)^2\right].$$

The normalization of the projectors is chosen such that

$$\mathrm{tr}\left[\left(\hat{P}_t\right)^{i\dagger}\left(\hat{P}_t\right)^j\right] = \frac{1}{2}\delta_{ij} = \mathrm{tr}\left[\left(\hat{P}_s\right)^{i\dagger}\left(\hat{P}_s\right)^j\right]. \tag{C.5}$$

Note that the whole formalism of writing the projectors as products of Pauli matrices in spin- and isospin-space introduced before is just a shorthand notation for the Clebsch-Gordan coefficients that occur in the coupling of the states. It can only be used for spin-$1/2$-fermions. In the example above, we obtain

$$C^{1i}_{\frac{1}{2}\alpha\frac{1}{2}\beta} = \frac{1}{\sqrt{8}}\left[\left(\tilde{P}_t\right)_{m=i}\right]^\alpha_\beta, \tag{C.6}$$

considering only the spin part of the projectors.

C.2. Potential representation

At LO there are four possible operator structures to consider,

$$1, \boldsymbol{\sigma}_1 \cdot \boldsymbol{\sigma}_2, \boldsymbol{\tau}_1 \cdot \boldsymbol{\tau}_2, \boldsymbol{\sigma}_1 \cdot \boldsymbol{\sigma}_2 \boldsymbol{\tau}_1 \cdot \boldsymbol{\tau}_2. \tag{C.7}$$

However, the theory only presents two possible S-wave states, the triplet and the singlet. So, only two of these four operator structures are linearly independent.

First, recall the effect of the operators on a two-nucleon state

$$\langle S|\boldsymbol{\sigma}_1 \cdot \boldsymbol{\sigma}_2|S\rangle = 2S(S+1) - 3,$$
$$\langle T|\boldsymbol{\tau}_1 \cdot \boldsymbol{\tau}_2|T\rangle = 2T(T+1) - 3, \tag{C.8}$$

where S and T are the spin and the isospin of the system, respectively. Using these operators, it is possible to derive projectors onto the spin $S = 0$ and $S = 1$ states

$$
\begin{aligned}
\mathcal{P}_{S=0} &:= \frac{1 - \boldsymbol{\sigma}_1 \cdot \boldsymbol{\sigma}_2}{4} \,, \\
\mathcal{P}_{S=1} &:= \frac{3 + \boldsymbol{\sigma}_1 \cdot \boldsymbol{\sigma}_2}{4} \,.
\end{aligned}
\tag{C.9}
$$

Similar representations can be derived for the isospin $T = 0$ and $T = 1$ states by replacing $\boldsymbol{\sigma}_1 \cdot \boldsymbol{\sigma}_2$ by $\boldsymbol{\tau}_1 \cdot \boldsymbol{\tau}_2$. Neglecting regulators, the LO pionless EFT two-body potential can be written as [187]

$$
\begin{aligned}
V_2^{\text{LO}} &= C_{0,s} \mathcal{P}_{S=0,T=1} + C_{0,t} \mathcal{P}_{S=1,T=0} \\
&= \frac{1}{16} \Big[3 \left(C_{0,s} + C_{0,t} \right) + \left(-3 C_{0,s} + C_{0,t} \right) \boldsymbol{\sigma}_1 \cdot \boldsymbol{\sigma}_2 + \left(C_{0,s} - 3 C_{0,t} \right) \boldsymbol{\tau}_1 \cdot \boldsymbol{\tau}_2 \\
&\quad - \left(C_{0,s} + C_{0,t} \right) \boldsymbol{\sigma}_1 \cdot \boldsymbol{\sigma}_2 \boldsymbol{\tau}_1 \cdot \boldsymbol{\tau}_2 \Big] \,,
\end{aligned}
\tag{C.10}
$$

where the projectors are defined by $\mathcal{P}_{S=i,T=j} := \mathcal{P}_{S=i} \mathcal{P}_{T=j}$.

D Faddeev equations

D.1. Geometrical factor

Deriving the Faddeev equation for a given system, the geometrical factor $g_{\mathrm{ii'}}^{k\ \lambda_1\lambda_2\lambda_1'\lambda_2'}$ (cf. Eq. (4.18)), encoding information of the quantum numbers, is introduced. It is defined as [159]

$$
\begin{aligned}
g_{\mathrm{ii'}}^{k\ \lambda_1\lambda_2\lambda_1'\lambda_2'} &= \sqrt{\hat{\lambda}\hat{s}\hat{j}\hat{t}\,\hat{l}\hat{I}\ \hat{\lambda'}\hat{s'}\hat{j'}\hat{t'}\,\hat{l'}\hat{I'}}(-1)\begin{Bmatrix}\frac{1}{2} & \frac{1}{2} & t \\ \frac{1}{2} & T & t'\end{Bmatrix} \\
&\times \sum_{L,S}\hat{L}\hat{S}\begin{Bmatrix}\frac{1}{2} & \frac{1}{2} & s \\ \frac{1}{2} & S & s'\end{Bmatrix}\begin{Bmatrix}\lambda & s & j \\ l & \frac{1}{2} & I \\ L & S & J\end{Bmatrix}\begin{Bmatrix}\lambda' & s' & j' \\ l' & \frac{1}{2} & I' \\ L & S & J\end{Bmatrix}\hat{k}\left(\frac{1}{2}\right)^{\lambda_2+\lambda_1'} \\
&\times \sqrt{\frac{(2\lambda+1)!}{(2\lambda_1)!(2\lambda_2)!}}\sqrt{\frac{(2\lambda'+1)!}{(2\lambda_1')!(2\lambda_2')!}}\sum_{f,f'}\begin{Bmatrix}\lambda_1 & \lambda_2 & l \\ l & L & f\end{Bmatrix}C\left(\lambda_2 lf,00\right) \\
&\times \begin{Bmatrix}\lambda_2' & \lambda_1' & \lambda' \\ l' & L & f'\end{Bmatrix}C\left(\lambda_1'l'f',00\right)\begin{Bmatrix}f & \lambda_1 & L \\ f' & \lambda_2' & k\end{Bmatrix}C\left(k\lambda_1 f',00\right)C\left(k\lambda_2'f,00\right),
\end{aligned}
\tag{D.1}
$$

where $\hat{x}=2x+1$. The quantities within the curved brackets represent 6j and 9j symbols, respectively. The C's are representing Clebsch-Gordan coefficients. Here, the notation $C\left(j_1 j_2 J, m_{j_1} m_{j_2}\right)$ is applied.

The representation of the geometrical factor can be simplified by connecting 9j symbols to 6j-symbols [188],

$$
\begin{Bmatrix}j_1 & j_2 & j_3 \\ j_4 & j_5 & j_6 \\ j_7 & j_8 & j_9\end{Bmatrix} := \sum_x (-1)^{2x}(2x+1)\begin{Bmatrix}j_1 & j_4 & j_7 \\ j_8 & j_9 & x\end{Bmatrix}\begin{Bmatrix}j_2 & j_5 & j_8 \\ j_4 & x & j_6\end{Bmatrix}\begin{Bmatrix}j_3 & j_6 & j_9 \\ x & j_1 & j_2\end{Bmatrix}.
\tag{D.2}
$$

Furthermore, a 6j symbol is solely a linear combination of 3j-symbols [188]

$$
\begin{aligned}
\begin{Bmatrix}j_1 & j_2 & j_3 \\ j_4 & j_5 & j_6\end{Bmatrix} &:= \sum_{m_1,\ldots,m_6}(-1)^{\sum_{k=1}^6(j_k-m_k)}\begin{pmatrix}j_1 & j_2 & j_3 \\ -m_1 & -m_2 & -m_3\end{pmatrix} \\
&\times \begin{pmatrix}j_1 & j_5 & j_6 \\ m_1 & -m_5 & m_6\end{pmatrix}\begin{pmatrix}j_4 & j_2 & j_6 \\ m_4 & m_2 & -m_6\end{pmatrix}\begin{pmatrix}j_4 & j_5 & j_3 \\ -m_4 & m_5 & m_3\end{pmatrix},
\end{aligned}
\tag{D.3}
$$

which itself is defined by a Clebsch-Gordan coefficient [188]

$$
\begin{pmatrix}j_1 & j_2 & j_3 \\ m_1 & m_2 & m_3\end{pmatrix} \equiv \frac{(-1)^{j_1-j_2-m_3}}{\sqrt{2j_3+1}}\langle j_1\,m_1\,j_2\,m_2|j_3\left(-m_3\right)\rangle.
\tag{D.4}
$$

Following the definition of the j-symbol's they are only not-vanishing if a given combination of angular momenta fulfills different conditions, e.g. the triangular inequality.

Considering the 3j symbol, we have to fulfill the conditions

- $|j_1 - j_2| \leq j_3 \leq j_1 + j_2$,

- $j_1 + j_2 + j_3 \in \mathbb{N}$,

- $m_i \in \{-j_i, \ldots, j_i\}$, $\quad i \in \{1, 2, 3\}$,

- $m_1 + m_2 + m_3 = 0$.

Using these conditions as well as the definition of the 6j-symbol with respect to the 3j-symbol we can derive some properties of the 6j symbols:

- Invariance under the exchange of columns

- Invariance under the exchange of the upper and lower numbers within one column

All in all, we have 6 possibilities for the upper left element of the 6j-symbol. This fixes the lower left element. Further, we have 4 possibilities for the upper middle element. So, the lower middle element as well as the two elements in the right column are fixed, too. Finally, the 6j symbol is invariant under the exchange of the two elements in the right column. So, all in all we have 24 possible representations of a 6j symbol. Following the definition via the Clebsch-Gordan coefficients, the 6j symbol is only not vanishing, if these four conditions are fulfilled

- $|j_2 - j_3| \leq j_1 \leq j_2 + j_3$,

- $|j_5 - j_6| \leq j_1 \leq j_5 + j_6$,

- $|j_2 - j_6| \leq j_4 \leq j_2 + j_6$,

- $|j_5 - j_3| \leq j_4 \leq j_5 + j_3$.

These information can be used to determine the range of the sums on f and f'. As f and f' appear together in a column with λ and λ' the conditions are independent of those. All in all, we get the following 6 conditions:

- $|\lambda_1 - \lambda_2| \leq f \leq \lambda_1 + \lambda_2$,

- $|L - l| \leq f \leq L + l$,

- $|\lambda_2' - k| \leq f \leq \lambda_2' + k$,

- $|\lambda_1' - \lambda_2'| \leq f' \leq \lambda_1' + \lambda_2'$,

- $|L - l'| \leq f' \leq L + l'$,

- $|\lambda_1 - k| \leq f' \leq \lambda_1 + k$.

These conditions are equivalent to $\min(|\lambda_1 - \lambda_2|, |L - l|, |\lambda_2' - k|) \leq f \leq \max(\lambda_1 + \lambda_2, L + l, \lambda_2' + k)$ and $\min(|\lambda_1' - \lambda_2'|, |L - l'|, |\lambda_1 - k|) \leq f' \leq \max(\lambda_1' + \lambda_2', L + l', \lambda_1 + k)$.

E Numerical implementation

E.1. Numerical solution of inhomogeneous integral equations

The two-body Lippmann Schwinger and the (single-channel) three-body Faddeev equations used within this work are both represented by a so-called Fredholm equation of the second kind. They present the general structure

$$T(p) = V(p) + \int_0^\Lambda \mathrm{d}q \, K(p,q)T(q). \tag{E.1}$$

The incoming momentum k is fixed, so that $T(p) \equiv T(k,p;E), V(p) \equiv V(k,p)$ and the kernel $K(p,q) \equiv K(k,p,q)$ are defined. Furthermore a sharp momentum cutoff Λ is applied. Evaluating an integral like this numerically always correspond to rewriting it into a sum with an infinite number of terms corresponding to the momenta going from zero to infinity. This integration interval can either be mapped to a finite one or a truncation for large momenta, as in this case Λ, has to be applied.

Assuming that the kernel has a pole at $q = q_0 + i\varepsilon$, we rewrite the equation to

$$T(p) = V(p) + \int_0^\Lambda \mathrm{d}q \frac{\tilde{K}(p,q)}{q - q_0 - i\varepsilon} T(q), \tag{E.2}$$

using the definition

$$\tilde{K}(p,q) = \begin{cases} (q - q_0) \, K(p,q), & \text{if } q \neq q_0, \\ \lim_{q \to q_0} (q - q_0) \, K(p,q), & \text{if } q = q_0. \end{cases} \tag{E.3}$$

Here and also in further calculations the limit $\varepsilon \to 0$ is carried out.

Using the principal value theorem and adding a zero $\left((-\tilde{K}(p,q_0)T(q_0) + \tilde{K}(p,q_0)T(q_0))/(q - q_0) \right)$ results in

$$T(p) = V(p) + \int_0^\Lambda \mathrm{d}q \frac{\tilde{K}(p,q)T(q) - \tilde{K}(p,q_0)T(q_0)}{q - q_0} + \tilde{K}(p,q_0)T(q_0) \left(i\pi + \underbrace{\mathcal{P} \int_0^\Lambda \mathrm{d}q \frac{1}{q - q_0}}_{\log\left(\frac{\Lambda - q_0}{q_0}\right)} \right). \tag{E.4}$$

This equation can be solved numerically by rewriting it as a system of linear equations

$$\begin{aligned} T_i &= V_i + \sum_{j=1}^N w_j \frac{\tilde{K}_{i,j}T_j - \tilde{K}_{i,N+1}T_{N+1}}{q_j - q_{N+1}} + \tilde{K}_{i,N+1}T_{N+1} \left(i\pi + \log\left(\frac{\Lambda - q_{N+1}}{q_{N+1}}\right) \right) \\ &= V_i + \sum_{j=1}^N w_j K_{i,j}T_j + \tilde{K}_{i,N+1}T_{N+1} \left(i\pi + \log\left(\frac{\Lambda - q_{N+1}}{q_{N+1}}\right) - \sum_{c=1}^N \frac{w_c}{p_c - p_{N+1}} \right), \end{aligned} \tag{E.5}$$

using discrete momenta $p \to p_i, q \to q_j, q_0 = q_{N+1}$ and the definitions $T\left(p_i\right) \equiv T_i, V\left(p_i\right) \equiv V_i, \tilde{K}\left(p_i, q_j\right) \equiv \tilde{K}_{i,j}$.

To solve this integral equation we need a further condition, which is given by an analogous equation for $i = N + 1$.

Combining these equations we get a system of $N + 1$ equations with $N + 1$ unknowns. It can be written in the short form

$$T_i = V_i + \sum_{j=1}^{N} M_{ij} T_j \tag{E.6}$$

with

$$M_{ij} = \begin{cases} K_{i,j} \cdot w_j, & j \leq N \\ \tilde{K}_{i,j} \cdot W, & j = N + 1 \end{cases} \quad \text{with } W = i\pi + \log\left(\frac{\Lambda - q_{N+1}}{q_{N+1}}\right) - \sum_{c=1}^{N} \frac{w_c}{p_c - p_{N+1}}. \tag{E.7}$$

This equation can now be solved numerically using standard linear algebra techniques.

A further equation structure we consider is the coupled doublet channel. It can be written as (cf. Eq. (3.42))

$$T_t(p) = V_t(p) + \int_0^\Lambda \mathrm{d}q \left[\frac{\tilde{K}_{11}(p,q)}{q - q_o^t - i\varepsilon} T_t(q) + \frac{\tilde{K}_{12}(p,q)}{q - q_o^s - i\varepsilon} T_s(q) \right], \tag{E.8}$$

$$T_s(p) = V_s(p) + \int_0^\Lambda \mathrm{d}q \left[\frac{\tilde{K}_{21}(p,q)}{q - q_o^t - i\varepsilon} T_t(q) + \frac{\tilde{K}_{22}(p,q)}{q - q_o^s - i\varepsilon} T_s(q) \right], \tag{E.9}$$

with $\tilde{K}_{ij}$ defined similar to Eq. (E.3). Adding a zero and applying the principal value theorem leads to

$$T_t(p) = V_t(p) + \int_0^\Lambda \mathrm{d}q \left[\frac{\tilde{K}_{11}(p,q) T_t(q) - \tilde{K}_{11}(p,q_0^t) T_t(q_0^t)}{q - q_o^t} + \frac{\tilde{K}_{12}(p,q) T_s(q) - \tilde{K}_{12}(p,q_0^s) T_s(q_0^s)}{q - q_o^s} \right]$$
$$+ \tilde{K}_{11}(p,q_0^t) T_t(q_0^t) \left(i\pi + \log\left(\frac{\Lambda - q_0^t}{q_0^t}\right) \right) + \tilde{K}_{12}(p,q_0^s) T_s(q_0^s) \left(i\pi + \log\left(\frac{\Lambda - q_0^s}{q_0^s}\right) \right), \tag{E.10}$$

$$T_s(p) = V_s(p) + \int_0^\Lambda \mathrm{d}q \left[\frac{\tilde{K}_{21}(p,q) T_t(q) - \tilde{K}_{21}(p,q_0^t) T_t(q_0^t)}{q - q_o^t} + \frac{\tilde{K}_{22}(p,q) T_s(q) - \tilde{K}_{22}(p,q_0^s) T_s(q_0^s)}{q - q_o^s} \right]$$
$$+ \tilde{K}_{21}(p,q_0^t) T_t(q_0^t) \left(i\pi + \log\left(\frac{\Lambda - q_0^t}{q_0^t}\right) \right) + \tilde{K}_{22}(p,q_0^s) T_s(q_0^s) \left(i\pi + \log\left(\frac{\Lambda - q_0^s}{q_0^s}\right) \right). \tag{E.11}$$

Now, the momenta are discretized and equations are rewritten into a coupled system of linear equations. Hereby similar definitions as in Eq. (E.5) as well as the definitions of the index $N + 1$ as corresponding

to q_0^t and the index $N+2$ as q_0^s are applied

$$
\begin{aligned}
T_i^t &= V_i^t + \sum_{j=1}^{N} w_j \left[\frac{\tilde{K}_{i,j}^{11} T_j^t - \tilde{K}_{i,N+1}^{11} T_{N+1}^t}{q_j - q_{N+1}} + \frac{\tilde{K}_{i,j}^{12} T_j^s - \tilde{K}_{i,N+2}^{12} T_{N+2}^s}{q_j - q_{N+2}} \right] \\
&\quad + \tilde{K}_{i,N+1}^{11} T_{N+1}^t \left(i\pi + \log\left(\frac{\Lambda - q_{N+1}}{q_{N+1}} \right) \right) + \tilde{K}_{i,N+2}^{12} T_{N+2}^s \left(i\pi + \log\left(\frac{\Lambda - q_{N+2}}{q_{N+2}} \right) \right) \\
&= V_i^t + \sum_{j=1}^{N} w_j \left[K_{i,j}^{11} T_j^t + K_{i,j}^{12} T_j^s \right] + \tilde{K}_{i,N+1}^{11} T_{N+1}^t \left(i\pi + \log\left(\frac{\Lambda - q_{N+1}}{q_{N+1}} \right) - \sum_{c=1}^{N} \frac{w_c}{p_c - p_{N+1}} \right) \\
&\quad + \tilde{K}_{i,N+2}^{12} T_{N+2}^s \left(i\pi + \log\left(\frac{\Lambda - q_{N+2}}{q_{N+2}} \right) - \sum_{c=1}^{N} \frac{w_c}{p_c - p_{N+2}} \right), \\
T_i^s &= V_i^s + \sum_{j=1}^{N} w_j \left[\frac{\tilde{K}_{i,j}^{21} T_j^t - \tilde{K}_{i,N+1}^{21} T_{N+1}^t}{q_j - q_{N+1}} + \frac{\tilde{K}_{i,j}^{22} T_j^s - \tilde{K}_{i,N+2}^{22} T_{N+2}^s}{q_j - q_{N+2}} \right] \\
&\quad + \tilde{K}_{i,N+1}^{21} T_{N+1}^t \left(i\pi + \log\left(\frac{\Lambda - q_{N+1}}{q_{N+1}} \right) \right) + \tilde{K}_{i,N+2}^{22} T_{N+2}^s \left(i\pi + \log\left(\frac{\Lambda - q_{N+2}}{q_{N+2}} \right) \right) \\
&= V_i^s + \sum_{j=1}^{N} w_j \left[K_{i,j}^{21} T_j^t + K_{i,j}^{22} T_j^s \right] + \tilde{K}_{i,N+1}^{21} T_{N+1}^t \left(i\pi + \log\left(\frac{\Lambda - q_{N+1}}{q_{N+1}} \right) - \sum_{c=1}^{N} \frac{w_c}{p_c - p_{N+1}} \right) \\
&\quad + \tilde{K}_{i,N+2}^{22} T_{N+2}^s \left(i\pi + \log\left(\frac{\Lambda - q_{N+2}}{q_{N+2}} \right) - \sum_{c=1}^{N} \frac{w_c}{p_c - p_{N+2}} \right).
\end{aligned}
\tag{E.12}
$$

We are only interested in the spin-triplet contribution. So we can neglect the last term in both equations, which corresponds to the spin-singlet. This is possible because this term is only non-zero (has a non-zero residue) for $q = q_0^s$. So it does not contribute to all other equations.

E.1.1. Modifications for implicit contour deformations

The Lippmann Schwinger and Faddeev equations performing implicit contour deformations to the unphysical sheets adjacent to the real energy axis are equivalent to those on the physical sheet plus a correction term,

$$
T(p) = V(p) + \int_0^\Lambda \mathrm{d}q \, K(p,q) T(q) + 2\pi i \tilde{K}(p, q_0) T(q_0) .
\tag{E.13}
$$

Performing an investigation similar to above, we only have to modify Eq. (E.7)

$$
M_{ij} = \begin{cases} K_{i,j} \cdot w_j, & j \le N \\ \tilde{K}_{i,j} \cdot W, & j = N+1 \end{cases} \qquad \text{with } W = 3i\pi + \log\left(\frac{\Lambda - q_{N+1}}{q_{N+1}} \right) - \sum_{c=1}^{N} \frac{w_c}{p_c - p_{N+1}} .
\tag{E.14}
$$

Note that to find poles on the unphysical sheets the kernel has to be evaluated on the unphysical sheet, too.

E.2. Method by Hetherington & Schick

The method of Hetherington and Schick [189, chapter 2.4] consists of three steps.

1. Continue the equation analytically for complex momenta.

2. Solve the equation for complex momenta.

3. Iterate the solution for complex momenta to obtain the result for real momenta.

Step 1
Fix the incoming momentum and energy to k and $E = \frac{3}{4m}k^2 - \frac{\gamma^2}{m}$.
Now we can define the integral equation for complex outgoing momenta $p \to pe^{-i\varphi}$ by also rotating the contour of integration by the same angle φ. This rotation is done by using Cauchy's integral formula, which shows that a line integral of a holomorphic function only depends on the end points of the integral

$$\int_0^\Lambda \mathrm{d}q = \int_0^{\tilde{\Lambda}} \mathrm{d}q + \int_{\tilde{\Lambda}}^\Lambda \mathrm{d}q \,, \tag{E.15}$$

with $\tilde{\Lambda} = \Lambda e^{-i\varphi}$.
The first path is parameterized by using $q \to qe^{-i\varphi}$ from $q = 0$ to $q = \Lambda$, the second one, by substituting $q \to \Lambda e^{-i\phi}$ from $\phi = \varphi$ to $\phi = 0$.
This results in

$$
\begin{aligned}
T(k, pe^{-i\varphi}; E) = V(k, pe^{-i\varphi}) + e^{-i\varphi} \int_0^\Lambda \mathrm{d}q K(qe^{-i\varphi}, pe^{-i\varphi})T(k, qe^{-i\varphi}; E) \\
+ \int_\varphi^0 \mathrm{d}\phi K(\Lambda e^{-i\varphi}, pe^{-i\varphi})T(k, \Lambda e^{-i\varphi}; E) \,,
\end{aligned}
\tag{E.16}
$$

with the restriction

$$\varphi < \arctan \frac{2\gamma}{k} \,. \tag{E.17}$$

Step 2
The next step is to solve this equation numerically. Therefore the method presented in Appendix E.1 is used.

Step 3
At last one has to connect the result in the complex plane with the result along the real axis.

Therefore consider the poles of the potential with finite ε (cf. Eq. (5.29))

$$p = \pm \left(\frac{1}{2}q \pm \sqrt{i\varepsilon + 2\mu E - \frac{3}{4}q^2} \right) \,. \tag{E.18}$$

Now we can separate between different cases. The relevant case is given by $0 \leq p < \sqrt{m_N E}$, with the corresponding solution for the real T-matrix

$$
T_q^0(k, p; E) = V(k, p) + \frac{1}{2\pi^2} e^{-i\varphi} \int_0^{\tilde{\Lambda}} \mathrm{d}q \; q^2 e^{-i2\varphi} V(qe^{-i\varphi}, p)
$$

$$
\times \frac{1}{-\gamma_t + \sqrt{\frac{3}{4}\boldsymbol{q}^2 e^{-i2\varphi} - M_N E - i\varepsilon}} T_q^0(k, qe^{-i\varphi}; E). \tag{E.19}
$$

14 Bibliography

[1] E. Rutherford. "Retardation of the α particle from radium in passing through matter". In: *The London, Edinburgh, and Dublin Philosophical Magazine and Journal of Science* 12.68 (1906), pp. 134–146. DOI: 10.1080/14786440609463525.

[2] H. Geiger and E. Rutherford. "On the scattering of the α-particles by matter". In: *Proceedings of the Royal Society of London. Series A, Containing Papers of a Mathematical and Physical Character* 81.546 (1908), pp. 174–177. DOI: 10.1098/rspa.1908.0067.

[3] H. Geiger, E. Marsden, and E. Rutherford. "On a diffuse reflection of the α-particles". In: *Proceedings of the Royal Society of London. Series A, Containing Papers of a Mathematical and Physical Character* 82.557 (1909), pp. 495–500. DOI: 10.1098/rspa.1909.0054.

[4] H. Geiger and E. Rutherford. "The scattering of α-particles by matter". In: *Proceedings of the Royal Society of London. Series A, Containing Papers of a Mathematical and Physical Character* 83.565 (1910), pp. 492–504. DOI: 10.1098/rspa.1910.0038.

[5] E. Rutherford. "The scattering of α and β particles by matter and the structure of the atom". In: *The London, Edinburgh, and Dublin Philosophical Magazine and Journal of Science* 21.125 (1911), pp. 669–688. DOI: 10.1080/14786440508637080.

[6] E. Rutherford and J. Nuttall. "Scattering of α particles by gases". In: *The London, Edinburgh, and Dublin Philosophical Magazine and Journal of Science* 26.154 (1913), pp. 702–712. DOI: 10.1080/14786441308635014.

[7] E. Rutherford. "Collision of α particles with light atoms. IV. An anomalous effect in nitrogen". In: *The London, Edinburgh, and Dublin Philosophical Magazine and Journal of Science* 37.222 (1919), pp. 581–587. DOI: 10.1080/14786440608635919.

[8] J. Chadwick. "The existence of a neutron". In: *Proceedings of the Royal Society of London. Series A, Containing Papers of a Mathematical and Physical Character* 136.830 (1932), pp. 692–708. DOI: 10.1098/rspa.1932.0112.

[9] H. Yukawa. "On the Interaction of Elementary Particles I". In: *Proc. Phys. Math. Soc. Jap.* 17 (1935), pp. 48–57. DOI: 10.1143/PTPS.1.1.

[10] C. M. G. Lattes et al. "Processes Involving Charged Mesons". In: *Nature* 159 (1947), pp. 694–697. DOI: 10.1038/159694a0.

[11] G. D. Rochester and C. C. Butler. "Evidence for the Existence of New Unstable Elementary Particles". In: *Nature* 160 (1947), pp. 855–857. DOI: 10.1038/160855a0.

[12] M. Gell-Mann. "A Schematic Model of Baryons and Mesons". In: *Phys. Lett.* 8 (1964), pp. 214–215. DOI: 10.1016/S0031-9163(64)92001-3.

[13] K. G. Wilson. "Confinement of Quarks". In: *Phys. Rev. D* 10 (1974). Ed. by J. C. Taylor, pp. 2445–2459. DOI: 10.1103/PhysRevD.10.2445.

[14] S. R. Beane et al. "Nuclear Physics from Lattice QCD". In: *Prog. Part. Nucl. Phys.* 66 (2011), pp. 1–40. DOI: 10.1016/j.ppnp.2010.08.002. arXiv: 1004.2935 [hep-lat].

[15] R. B. Wiringa, V. G. J. Stoks, and R. Schiavilla. "An Accurate nucleon-nucleon potential with charge independence breaking". In: *Phys. Rev. C* 51 (1995), pp. 38–51. DOI: 10.1103/PhysRevC.51.38. arXiv: nucl-th/9408016.

[16] S. Veerasamy and W. N. Polyzou. "A momentum-space Argonne V18 interaction". In: *Phys. Rev. C* 84 (2011), p. 034003. DOI: 10.1103/PhysRevC.84.034003. arXiv: 1106.1934 [nucl-th].

[17] S. Weinberg. "Phenomenological Lagrangians". In: *Physica A* 96.1-2 (1979). Ed. by S. Deser, pp. 327–340. DOI: 10.1016/0378-4371(79)90223-1.

[18] S. Weinberg. "Nuclear forces from chiral Lagrangians". In: *Phys. Lett. B* 251 (1990), pp. 288–292. DOI: 10.1016/0370-2693(90)90938-3.

[19] U. van Kolck. "Nucleon-nucleon interaction and isospin violation". In: *Lect. Notes Phys.* 513 (1998). Ed. by A. M. Bernstein, D. Drechsel, and T. Walcher, p. 62. DOI: 10.1007/BFb0104898. arXiv: hep-ph/9711222.

[20] U. van Kolck. "Effective field theory of short range forces". In: *Nucl. Phys. A* 645 (1999), pp. 273–302. DOI: 10.1016/S0375-9474(98)00612-5. arXiv: nucl-th/9808007.

[21] D. B. Kaplan, M. J. Savage, and M. B. Wise. "A New expansion for nucleon-nucleon interactions". In: *Phys. Lett. B* 424 (1998), pp. 390–396. DOI: 10.1016/S0370-2693(98)00210-X. arXiv: nucl-th/9801034 [nucl-th].

[22] D. B. Kaplan, M. J. Savage, and M. B. Wise. "Two nucleon systems from effective field theory". In: *Nucl. Phys. B* 534 (1998), pp. 329–355. DOI: 10.1016/S0550-3213(98)00440-4. arXiv: nucl-th/9802075 [nucl-th].

[23] A. Gardestig. "Extracting the neutron-neutron scattering length - recent developments". In: *J. Phys. G* 36 (2009), p. 053001. DOI: 10.1088/0954-3899/36/5/053001. arXiv: 0904.2787 [nucl-th].

[24] V. Ajdacic et al. "Reactions H-3 (n, p) 3n and H-3 (n, H-4) gamma at En=14.4 MeV". In: *Phys. Rev. Lett.* 14 (1965), pp. 444–446. DOI: 10.1103/PhysRevLett.14.444.

[25] S. T. Thornton et al. "Search for the Trineutron". In: *Phys. Rev. Lett.* 17 (13 Sept. 1966), pp. 701–702. DOI: 10.1103/PhysRevLett.17.701.

[26] E. Fuschini et al. "Experimental evidence against the existence of a bound state of three neutrons". In: *Il Nuovo Cimento B* 48 (1 Sept. 1967), pp. 190–193. DOI: 10.1007/BF02712457.

[27] G. G. Ohlsen, R. H. Stokes, and P. G. Young. "Search for States in the Three-Neutron and Triton Systems". In: *Phys. Rev.* 176 (4 Dec. 1968), pp. 1163–1165. DOI: 10.1103/PhysRev.176.1163. URL: https://link.aps.org/doi/10.1103/PhysRev.176.1163.

[28] K. Debertin and E. Rössle. "Search for a bound state of three neutrons". In: *Nucl. Phys. A* 107 (1968), pp. 693–694. DOI: 10.1016/0375-9474(68)90795-1.

[29] K. Fujikawa and H. Morinaga. "Search for tri-neutrons". In: *Nucl. Phys. A* 115 (1968), pp. 1–13. DOI: 10.1016/0375-9474(68)90637-4.

[30] H. Nakamura. "Cross section of t(n, p)^{3}n reaction". In: *Nucl. Phys. A* 118 (1968), pp. 17–24. DOI: 10.1016/0375-9474(68)90183-8.

[31] H. Jacob and V. K. Gupta. "Existence of the Trineutron". In: *Phys. Rev.* 174 (1968), pp. 1213–1220. DOI: 10.1103/PhysRev.174.1213.

[32] J. Sperinde et al. "Evidence for a low-energy resonance in the three-neutron system". In: *Phys. Lett. B* 32 (1970), pp. 185–186. DOI: 10.1016/0370-2693(70)90468-5.

[33] H. C. Benöhr. "Calculation of broad three-nucleon resonances for a soft-core two-nucleon potential". In: *Nucl. Phys. A* 149 (1970), pp. 426–440. DOI: 10.1016/0375-9474(70)90707-4.

[34] A. C. Phillips. "Non-resonance attraction between neutrons in the $\pi^- + {}^3\text{He} \to \pi^+ + 3\text{n}$ reaction". In: *Phys. Lett. B* 33 (1970), pp. 260–262. DOI: 10.1016/0370-2693(70)90263-7.

[35] K. F. Koral, E. A. Silverstein, and P. R. Bevington. "A search for the bound trineutron from ${}^7\text{Li}$ + n reactions". In: *Nucl. Phys. A* 175 (1971), pp. 156–166. DOI: 10.1016/0375-9474(71)90628-2.

[36] K. H. Bray et al. "Search for Excited States in ${}^3\text{He}$". In: *Phys. Rev. C* 3 (1971), pp. 1771–1785. DOI: 10.1103/PhysRevC.3.1771.

[37] H. C. Benöhr. "On the investigation of a possible broad three-neutron state by means of the reaction ${}^3\text{H(n,p)3n}$". In: *Phys. Lett. B* 34 (1971), pp. 448–450. DOI: 10.1016/0370-2693(71)90650-2.

[38] A. Reitan. "Three-neutron resonance in the reaction ${}^3\text{He}(\pi^-, \pi^+)3\text{n}$". In: *Phys. Lett. B* 35 (1971), pp. 368–370. DOI: 10.1016/0370-2693(71)90395-9.

[39] I. Slaus. *Few Particle Problems: Proceedings of the International Conference on Few Particle Problems in the Nuclear Interaction. (Los Angeles, August 28-September 1, 1972)*. Burlington: Elsevier Science, 1972, pp. 539–542. ISBN: 9780444104397.

[40] K. Möller. "Investigation of Resonances in the ${}^3\text{n}$-System". In: *ZfK - Proceedings of the 1977 European Symposium on Few Particle Problems in Nuclear Physics, Potsdam, Oct 11-14 1977* 347 (1977). Ed. by Kühn, B. and Möller, K., pp. 90–93.

[41] K. Möller. "On a Method for Calculating the Eigenvalues of the Faddeev Equation Kernel on the Nonphysical Sheet of Energy". In: *ZfK-Report* 327 (Mar. 1977).

[42] K. Möller. "On the calculation of the eigenvalues of the Faddeev equation kernel on the nonphysical sheet of energy". In: *ZfK-Report* 351 (Jan. 1978).

[43] K. Möller. "S Matrix Pole Trajectories of the Efimov States". In: *ZfK-Report* 357 (May 1978).

[44] W. Glöckle. "S-matrix pole trajectory in a three-neutron model". In: *Phys. Rev. C* 18 (1978), pp. 564–572. DOI: 10.1103/PhysRevC.18.564.

[45] K. Möller. "Untersuchung von Resonanzen in Dreinukleonensystemen". PhD thesis. Zentralinstitut für Kernforschung, Dresden, 1979.

[46] R. Offermann and W. Glöckle. "Is there a three-neutron resonance?" In: *Nucl. Phys. A* 318 (1979), pp. 138–144. DOI: 10.1016/0375-9474(79)90475-5.

[47] J. P. Miller et al. "Upper Limits for Bound States and Resonance Behavior in the Trineutron System". In: *Nucl. Phys. A* 343 (1980), pp. 347–355. DOI: 10.1016/0375-9474(80)90657-0.

[48] K. Möller. "Determination of the dominant resonance pole of the three-neutron system". In: *ZfK-Report* 437 (1981).

[49] A. Stetz et al. "Pion Double Charge Exchange on ${}^3\text{He}$ and ${}^4\text{He}$". In: *Nucl. Phys. A* 457 (1986), pp. 669–686. DOI: 10.1016/0375-9474(86)90474-4.

[50] D. R. Tilley, H. R. Weller, and H. H. Hasan. "Energy levels of light nuclei A = 3". In: *Nucl. Phys. A* 474 (1987), pp. 1–60. DOI: 10.1016/0375-9474(87)90193-X.

[51] A. Csoto, H. Oberhummer, and R. Pichler. "Searching for three nucleon resonances". In: *Phys. Rev. C* 53 (1996), pp. 1589–1592. DOI: 10.1103/PhysRevC.53.1589. arXiv: nucl-th/9510017.

[52] M. Yuly et al. "Pion double charge exchange and inelastic scattering on ³He". In: *Phys. Rev. C* 55 (1997), pp. 1848–1868. DOI: 10.1103/PhysRevC.55.1848.

[53] S. A. Sofianos, S. A. Rakityansky, and G. P. Vermaak. "Subthreshold resonances in few neutron systems". In: *J. Phys. G* 23 (1997), pp. 1619–1630. DOI: 10.1088/0954-3899/23/11/010. arXiv: nucl-th/9705016.

[54] H. Witala and W. Glöckle. "Resonances in the three neutron system". In: *Phys. Rev. C* 60 (1999), p. 024002. DOI: 10.1103/PhysRevC.60.024002. arXiv: nucl-th/9901074.

[55] A. Hemmdan, W. Glöckle, and H. Kamada. "Indications for the nonexistence of three neutron resonances near the physical region". In: *Phys. Rev. C* 66 (2002), p. 054001. DOI: 10.1103/PhysRevC.66.054001. arXiv: nucl-th/0208007.

[56] R. Lazauskas and J. Carbonell. "Three-neutron resonance trajectories for realistic interaction models". In: *Phys. Rev. C* 71 (2005), p. 044004. DOI: 10.1103/PhysRevC.71.044004. arXiv: nucl-th/0502037.

[57] R. Y. Kezerashvili. "Search of Trineutron and Tetraneutron". In: *6th International Conference on Fission and Properties of Neutron Rich Nuclei*. July 2016. DOI: 10.1142/9789813229426_0074. arXiv: 1608.00169 [nucl-th].

[58] S. Gandolfi et al. "Is a Trineutron Resonance Lower in Energy than a Tetraneutron Resonance?" In: *Phys. Rev. Lett.* 118.23 (2017), p. 232501. DOI: 10.1103/PhysRevLett.118.232501. arXiv: 1612.01502 [nucl-th].

[59] P. Truöl and J. Miller. *Comment on arXiv:1612.01502 'Is the Trineutron Resonance Lower in Energy than a Tetraneutron Resonance ?'* Aug. 2017. arXiv: 1708.04459 [nucl-ex].

[60] A. Deltuva. "Three-neutron resonance study using transition operators". In: *Phys. Rev. C* 97.3 (2018), p. 034001. DOI: 10.1103/PhysRevC.97.034001. arXiv: 1801.02919 [nucl-th].

[61] A. Deltuva and R. Lazauskas. "Comment on "Is a Trineutron Resonance Lower in Energy than a Tetraneutron Resonance?"" In: *Phys. Rev. Lett.* 123.6 (2019), p. 069201. DOI: 10.1103/PhysRevLett.123.069201. arXiv: 1904.00925 [nucl-th].

[62] S. Gandolfi et al. "Reply to Comment on "Is a Trineutron Resonance Lower in Energy than a Tetraneutron Resonance?"" In: *Phys. Rev. Lett.* 123 (2019), p. 069202. DOI: 10.1103/PhysRevLett.123.069202. arXiv: 1908.06610 [nucl-th].

[63] J. G. Li et al. "Ab initio no-core Gamow shell-model calculations of multineutron systems". In: *Phys. Rev. C* 100.5 (2019), p. 054313. DOI: 10.1103/PhysRevC.100.054313. arXiv: 1911.06485 [nucl-th].

[64] M. D. Higgins et al. "Non-resonant Density of States Enhancement at Low Energies for Three or Four Neutrons". In: *Phys. Rev. Lett.* 125.5 (2020), p. 052501. DOI: 10.1103/PhysRevLett.125.052501. arXiv: 2005.04714 [nucl-th].

[65] M. D. Higgins et al. "Comprehensive study of the three- and four-neutron systems at low energies". In: *Phys. Rev. C* 103.2 (2021), p. 024004. DOI: 10.1103/PhysRevC.103.024004. arXiv: 2011.11687 [nucl-th].

[66] S. Ishikawa. "Three-neutron bound and continuum states". In: *Phys. Rev. C* 102.3 (2020), p. 034002. DOI: 10.1103/PhysRevC.102.034002. arXiv: 2008.10980 [nucl-th].

[67] F. M. Marqués and J. Carbonell. "The quest for light multineutron systems". In: *Eur. Phys. J. A* 57.3 (2021), p. 105. DOI: 10.1140/epja/s10050-021-00417-8. arXiv: 2102.10879 [nucl-ex].

[68] S. Dietz et al. "Three-body resonances in pionless effective field theory". In: *Phys. Rev. C* 105.6 (2022), p. 064002. DOI: 10.1103/PhysRevC.105.064002. arXiv: 2109.11356 [nucl-th].

[69] M. Duer et al. "Observation of a correlated free four-neutron system". In: *Nature* 606.7915 (2022), pp. 678–682. DOI: 10.1038/s41586-022-04827-6.

[70] K. Kisamori et al. "Candidate Resonant Tetraneutron State Populated by the ^{4}He(^{8}He,^{8}Be) Reaction". In: *Phys. Rev. Lett.* 116.5 (2016), p. 052501. DOI: 10.1103/PhysRevLett.116.052501.

[71] T. Faestermann et al. "Indications for a bound tetraneutron". In: *Phys. Lett. B* 824 (2022), p. 136799. DOI: 10.1016/j.physletb.2021.136799.

[72] U. J. Wiese. "Identification of Resonance Parameters From the Finite Volume Energy Spectrum". In: *LATTICE 88. Proceedings, Symposium, Batavia, USA, September 22-25, 1988*. Vol. 9. 1989, pp. 609–613. DOI: 10.1016/0920-5632(89)90171-0.

[73] M. Lüscher. "Signatures of unstable particles in finite volume". In: *Nucl. Phys. B* 364 (1991), pp. 237–251. DOI: 10.1016/0550-3213(91)90584-K.

[74] K. Rummukainen and S. A. Gottlieb. "Resonance scattering phase shifts on a nonrest frame lattice". In: *Nucl. Phys. B* 450 (1995), pp. 397–436. DOI: 10.1016/0550-3213(95)00313-H. arXiv: hep-lat/9503028 [hep-lat].

[75] P. Klos et al. "Quantum Monte Carlo calculations of two neutrons in finite volume". In: *Phys. Rev. C* 94.5 (2016), p. 054005. DOI: 10.1103/PhysRevC.94.054005. arXiv: 1604.01387 [nucl-th].

[76] P. Klos et al. "Signatures of few-body resonances in finite volume". In: *Phys. Rev. C* 98.3 (2018), p. 034004. DOI: 10.1103/PhysRevC.98.034004. arXiv: 1805.02029 [nucl-th].

[77] M. Lüscher. "Volume Dependence of the Energy Spectrum in Massive Quantum Field Theories. 1. Stable Particle States". In: *Commun. Math. Phys.* 104 (1986), p. 177. DOI: 10.1007/BF01211589.

[78] M. Lüscher. "Volume Dependence of the Energy Spectrum in Massive Quantum Field Theories. 2. Scattering States". In: *Commun. Math. Phys.* 105 (1986), pp. 153–188. DOI: 10.1007/BF01211097.

[79] M. Lüscher. "Two particle states on a torus and their relation to the scattering matrix". In: *Nucl. Phys. B* 354 (1991), pp. 531–578. DOI: 10.1016/0550-3213(91)90366-6.

[80] V. I. Kukulin and V. M. Krasnopol'sky. "Description of few-body systems via analytical continuation in coupling constant". In: *Journal of Physics A: Mathematical and General* 10.2 (Feb. 1977), pp. L33–L37. DOI: 10.1088/0305-4470/10/2/002. URL: https://doi.org/10.1088/0305-4470/10/2/002.

[81] V. M. Krasnopolsky and V. I. Kukulin. "Theory of Resonance States Based on Analytical Continuation in the Coupling Constant". In: *Phys. Lett. A* 69 (1978), pp. 251–254. DOI: 10.1016/0375-9601(78)90177-9.

[82] V. I. Kukulin, V. M. Krasnopolsky, and M. Miselki. "Method of analytic continuation in the coupling constant in the theory of systems of several particles. Resonance state as analytic continuation of a bound state". In: *Sov. J. Nucl. Phys.* 29 (1979), p. 421.

[83] V. I. Kukulin et al. "Analytic continuation in the coupling constant in the theory of few-body systems. States in a complex and deformed potential and a potential with a repulsive core". In: *Sov. J. Nucl. Phys.* 30 (1979), p. 740.

[84] V. I. Kukulin, V. M. Krasnopol'sky, and J. Horáček. *Theory of Resonances*. 1st ed. Springer, Dordrecht, 1989. ISBN: 978-90-277-2364-2. DOI: https://doi.org/10.1007/978-94-015-7817-2.

[85] B. A. Lippmann and J. Schwinger. "Variational Principles for Scattering Processes. I". In: *Phys. Rev.* 79 (1950), pp. 469–480. DOI: 10.1103/PhysRev.79.469.

[86] L. D. Faddeev. "Scattering Theory for a Three-Particle System". In: *Sov. Phys. JETP* 12.5 (1961), pp. 1014–1019.

[87] B. Pearce and I. Afnan. "Resonance Poles in Three-body Systems". In: *Phys. Rev. C* 30 (1984), pp. 2022–2025. DOI: 10.1103/PhysRevC.30.2022.

[88] I. R. Afnan. "Resonances in few body systems". In: *Austral. J. Phys.* 44 (1991), pp. 201–216. DOI: 10.1071/PH910201.

[89] I. Afnan and B. Gibson. "Resonances in Lambda d scattering and the Sigma hypertriton". In: *Phys. Rev. C* 47 (1993), pp. 1000–1012. DOI: 10.1103/PhysRevC.47.1000.

[90] I. R. Afnan and B. F. Gibson. "Resonances in the Λnn system". In: *Phys. Rev. C* 92.5 (2015), p. 054608. DOI: 10.1103/PhysRevC.92.054608.

[91] B. Gibson and I. Afnan. "The Λn scattering length and the Λnn resonance". In: *AIP Conf. Proc.* 2130.1 (2019). Ed. by L. Tang and R. Schumacher, p. 020005. DOI: 10.1063/1.5118373.

[92] H.-W. Hammer and D. T. Son. "Unnuclear physics". In: *Proc. Nat. Acad. Sci.* 118 (2021), e2108716118. DOI: 10.1073/pnas.2108716118. arXiv: 2103.12610 [nucl-th].

[93] Y. Nishida and D. T. Son. "Nonrelativistic conformal field theories". In: *Phys. Rev. D* 76 (2007), p. 086004. DOI: 10.1103/PhysRevD.76.086004. arXiv: 0706.3746 [hep-th].

[94] A. Schwenk and C. J. Pethick. "Resonant Fermi gases with a large effective range". In: *Phys. Rev. Lett.* 95 (2005), p. 160401. DOI: 10.1103/PhysRevLett.95.160401. arXiv: nucl-th/0506042.

[95] F. Bringas, M. T. Yamashita, and T. Frederico. "Triatomic continuum resonances for large negative scattering lengths". In: *Phys. Rev. A* 69 (2004), p. 040702. DOI: 10.1103/PhysRevA.69.040702. arXiv: cond-mat/0312291.

[96] J. R. Taylor. *Scattering Theory: The Quantum Theory of Nonrelativistic Collisions*. 1972.

[97] J. Schwinger. *Lecture notes on nuclear physics at Harvard University*. unpublished. 1947.

[98] J. M. Blatt and J. D. Jackson. "On the Interpretation of Neutron-Proton Scattering Data by the Schwinger Variational Method". In: *Phys. Rev.* 76 (1949), pp. 18–37. DOI: 10.1103/PhysRev.76.18.

[99] H. A. Bethe. "Theory of the Effective Range in Nuclear Scattering". In: *Phys. Rev.* 76 (1949), pp. 38–50. DOI: 10.1103/PhysRev.76.38.

[100] E. P. Wigner. "Lower Limit for the Energy Derivative of the Scattering Phase Shift". In: *Phys. Rev.* 98 (1955), pp. 145–147. DOI: 10.1103/PhysRev.98.145.

[101] F. T. Smith. "Lifetime Matrix in Collision Theory". In: *Phys. Rev.* 118 (1960), pp. 349–356. DOI: 10.1103/PhysRev.118.349.

[102] S. R. Beane et al. "At the frontier of particle physics—handbook of QCD". In: World Scientific, Aug. 2000. Chap. From hadrons to nuclei: Crossing the border, pp. 133–271. DOI: 10.1142/9789812810458_0011. arXiv: nucl-th/0008064.

[103] P. F. Bedaque and U. van Kolck. "Effective field theory for few-nucleon systems". In: *Ann. Rev. Nucl. Part. Sci.* 52 (2002), pp. 339–396. DOI: 10.1146/annurev.nucl.52.050102.090637.

[104] E. Epelbaum, H.-W. Hammer, and U.-G. Meißner. "Modern Theory of Nuclear Forces". In: *Rev. Mod. Phys.* 81 (2009), pp. 1773–1825. DOI: 10.1103/RevModPhys.81.1773.

[105] H.-W. Hammer and S. König. "General aspects of effective field theories and few-body applications". In: *Lect. Notes Phys.* 936 (2017), pp. 93–153. DOI: 10.1007/978-3-319-53336-0_4. arXiv: 1610.02961 [nucl-th].

[106] H.-W. Hammer, S. König, and U. van Kolck. "Nuclear effective field theory: status and perspectives". In: *Rev. Mod. Phys.* 92.2 (2020), p. 025004. DOI: 10.1103/RevModPhys.92.025004. arXiv: 1906.12122 [nucl-th].

[107] P. F. Bedaque, H.-W. Hammer, and U. van Kolck. "The Three boson system with short range interactions". In: *Nucl. Phys. A* 646 (1999), pp. 444–466. DOI: 10.1016/S0375-9474(98)00650-2. arXiv: nucl-th/9811046.

[108] E. Braaten and H. .-. Hammer. "Universality in few-body systems with large scattering length". In: *Phys. Rept.* 428 (2006), pp. 259–390. DOI: 10.1016/j.physrep.2006.03.001. arXiv: cond-mat/0410417.

[109] D. B. Kaplan. "More effective field theory for nonrelativistic scattering". In: *Nucl. Phys. B* 494 (1997), pp. 471–484. DOI: 10.1016/S0550-3213(97)00178-8. arXiv: nucl-th/9610052.

[110] P. F. Bedaque, H. W. Hammer, and U. van Kolck. "Renormalization of the three-body system with short range interactions". In: *Phys. Rev. Lett.* 82 (1999), pp. 463–467. DOI: 10.1103/PhysRevLett.82.463. arXiv: nucl-th/9809025.

[111] G. V. Skorniakov and K. A. Ter-Martirosian. "Three body problem for short range forces. I. Scattering of low energy neutrons by deuterons". In: *Sov. Phys. JETP* 4 (1957), p. 648.

[112] G. S. Danilov. "On the three-body problem with short-range forces". In: *Sov. Phys. JETP* 13 (1961), p. 349.

[113] G. S. Danilov and V. I. Lebedev. "Calculation of the Doublet Neutron-deuteron Scattering Length in the Theory of Zero-range Forces". In: *Sov. Phys. JETP* 17 (1963), p. 1015.

[114] V. F. Kharchenko. "Solution of the Skornyakov-Ter-Martirosyan Equations for Three Nucleons with Cutoff at Large Momenta". In: *Sov. J. Nucl. Phys.* 16 (1973), p. 173.

[115] P. F. Bedaque and U. van Kolck. "Nucleon deuteron scattering from an effective field theory". In: *Phys. Lett. B* 428 (1998), pp. 221–226. DOI: 10.1016/S0370-2693(98)00430-4. arXiv: nucl-th/9710073.

[116] P. F. Bedaque, H.-W. Hammer, and U. van Kolck. "Effective theory for neutron deuteron scattering: Energy dependence". In: *Phys. Rev. C* 58 (1998), R641–R644. DOI: 10.1103/PhysRevC.58.R641. arXiv: nucl-th/9802057.

[117] P. F. Bedaque, H. W. Hammer, and U. van Kolck. "Effective theory of the triton". In: *Nucl. Phys. A* 676 (2000), pp. 357–370. DOI: 10.1016/S0375-9474(00)00205-0. arXiv: nucl-th/9906032.

[118] L. Platter, H.-W. Hammer, and U.-G. Meißner. "The Four boson system with short range interactions". In: *Phys. Rev. A* 70 (2004), p. 052101. DOI: 10.1103/PhysRevA.70.052101. arXiv: cond-mat/0404313.

[119] L. Platter, H.-W. Hammer, and U.-G. Meißner. "On the correlation between the binding energies of the triton and the alpha-particle". In: *Phys. Lett. B* 607 (2005), pp. 254–258. DOI: 10.1016/j.physletb.2004.12.068. arXiv: nucl-th/0409040.

[120] A. Stadler, W. Glöckle, and P. U. Sauer. "Faddeev equations with three-nucleon force in momentum space". In: *Phys. Rev. C* 44 (1991), pp. 2319–2327. DOI: 10.1103/PhysRevC.44.2319.

[121] V. N. Ostrovskii and E. A. Solov'ev. "Perturbation Theory for Weakly Bound States". In: *Sov. Phys. JETP.* 35 (1972), p. 89.

[122] I. M. Gel'fand and N. Y. Vilenkin. *Generalized Functions, Volume 4: Applications of Harmonic Analysis*. Academic Press, New York, 1964.

[123] C. Lovelace. *Strong Interactions and High Energy Physics*. Ed. by R. G. Moorhouse. London: Oliver and Boyd, 1964.

[124] J. Aguilar and J. M. Combes. "A class of analytic perturbations for one-body Schrödinger Hamiltonians". In: *Communications in Mathematical Physics* 22.4 (1971), pp. 269–279. ISSN: 1432-0916. DOI: 10.1007/BF01877510.

[125] E. Balslev and J. M. Combes. "Spectral properties of many-body Schrödinger operators with dilatation-analytic interactions". In: *Communications in Mathematical Physics* 22.4 (1971), pp. 280–294. ISSN: 1432-0916. DOI: 10.1007/BF01877511.

[126] T. Myo et al. "Recent development of complex scaling method for many-body resonances and continua in light nuclei". In: *Prog. Part. Nucl. Phys.* 79 (2014), pp. 1–56. DOI: 10.1016/j.ppnp.2014.08.001. arXiv: 1410.4356 [nucl-th].

[127] T. Myo and K. Kato. "Complex scaling: Physics of unbound light nuclei and perspective". In: *PTEP* 2020.12 (2020), 12A101. DOI: 10.1093/ptep/ptaa101. arXiv: 2007.12172 [nucl-th].

[128] R. Lazauskas. "Application of the complex scaling method in quantum scattering theory". Habilitation thesis. Apr. 2019. arXiv: 1904.04675 [nucl-th].

[129] Y. V. Orlov. "Analytic continuation of the integral equations of the theory of scattering by an unphysical energy sheet". In: *JETP Lett.* 33 (1981), pp. 363–367.

[130] V. G. Emelyanov, V. I. Klimov, and V. N. Pomerantsev. "The calculation of the three-body resonance energy and width above the threshold for the three-body break-up". In: *Phys. Lett. B* 157 (1985), pp. 105–107. DOI: 10.1016/0370-2693(85)91526-6.

[131] V. Efimov. "Energy levels arising form the resonant two-body forces in a three-body system". In: *Phys. Lett. B* 33 (1970), pp. 563–564. DOI: 10.1016/0370-2693(70)90349-7.

[132] V. N. Efimov. "Weakly-bound states of 3 resonantly-interacting particles". In: *Sov. J. Nucl. Phys.* 12 (1971), p. 589.

[133] P. Naidon and S. Endo. "Efimov Physics: a review". In: *Rept. Prog. Phys.* 80.5 (2017), p. 056001. DOI: 10.1088/1361-6633/aa50e8. arXiv: 1610.09805 [quant-ph].

[134] M. T. Yamashita et al. "Scaling limit of virtual states of triatomic systems". In: *Phys. Rev. A* 66 (2002), p. 052702. DOI: 10.1103/PhysRevA.66.052702. arXiv: physics/0209025.

[135] A. Deltuva. "Energies and widths of Efimov states in the three-boson continuum". In: *Phys. Rev. C* 102.3 (2020), p. 034003. DOI: 10.1103/PhysRevC.102.034003. arXiv: 2101.12654.

[136] S. Jonsell. "Efimov states for systems with negative scattering lengths". In: *Europhys. Lett.* 76 (2006), pp. 8–14. DOI: 10.1209/epl/i2006-10235-1.

[137] T. Hyodo, T. Hatsuda, and Y. Nishida. "Universal physics of three bosons with isospin". In: *Phys. Rev. C* 89.3 (2014), p. 032201. DOI: 10.1103/PhysRevC.89.032201. arXiv: 1311.6289 [hep-ph].

[138] H. W. Griesshammer. "Improved convergence in the three-nucleon system at very low energies". In: *Nucl. Phys. A* 744 (2004), pp. 192–226. DOI: 10.1016/j.nuclphysa.2004.08.012. arXiv: nucl-th/0404073.

[139] V. Efimov. "Qualitative treatment of three-nucleon properties". In: *Nucl. Phys. A* 362 (1981), pp. 45–70. DOI: 10.1016/0375-9474(81)90669-2.

[140] V. Efimov. "Is a Qualitative Approach to the Three-Body Problem Useful?" In: *Comments Nucl. Part. Phys.* 19.6 (1990), pp. 271–293.

[141] G. Ellerkmann. "Research on anomalous threshold breakup in elastic neutron - deuteron scattering with the help of the W matrix method". Diploma thesis. Dec. 1990.

[142] A. Kievsky et al. "Critical comparison of experimental data and theoretical predictions for nucleon deuteron scattering below the breakup threshold". In: *Nucl. Phys. A* 607 (1996), pp. 402–424. DOI: 10.1016/0375-9474(96)00240-0.

[143] E. G. Tkachenko. "On the irregularity in doublet neutron-deuteron elastic scattering near the deuteron breakup threshold". In: *Phys. Lett. B* 98 (1981), pp. 328–330. DOI: 10.1016/0370-2693(81)90917-5.

[144] G. Rupak et al. "Fate of the neutron–deuteron virtual state as an Efimov level". In: *Phys. Lett. B* 791 (2019), pp. 414–419. DOI: 10.1016/j.physletb.2018.08.051. arXiv: 1806.01999 [nucl-th].

[145] D. S. Petrov. "Three-body problem in Fermi gases with short-range interparticle interaction". In: *Phys. Rev. A* 67 (1 Jan. 2003), p. 010703. DOI: 10.1103/PhysRevA.67.010703. arXiv: cond-mat/0209246.

[146] D. S. Petrov, C. Salomon, and G. V. Shlyapnikov. "Scattering properties of weakly bound dimers of fermionic atoms". In: *Phys. Rev. A* 71 (1 Jan. 2005), p. 012708. DOI: 10.1103/PhysRevA.71.012708. arXiv: cond-mat/0407579.

[147] G. Rupak. "Dimer scattering in the epsilon expansion". In: (May 2006). arXiv: nucl-th/0605074.

[148] J. von Stecher, C. H. Greene, and D. Blume. "Energetics and structural properties of trapped two-component Fermi gases". In: *Phys. Rev. A* 77 (4 Apr. 2008), p. 043619. DOI: 10.1103/PhysRevA.77.043619. arXiv: 0801.2747.

[149] J. Levinsen. *Paired fermionic superfluids with s- and p-wave interactions*. 2008. DOI: 10.48550/ARXIV.0807.2840. arXiv: 0807.2840.

[150] J. Levinsen and D. S. Petrov. "Atom-dimer and dimer-dimer scattering in fermionic mixtures near a narrow Feshbach resonance". In: *Eur. Phys. J. D* 65 (2011), pp. 67–82. DOI: 10.1140/epjd/e2011-20071-x. arXiv: 1101.5979.

[151] S. Tan. "Energetics of a strongly correlated Fermi gas". In: *Annals of Physics* 323.12 (2008), pp. 2952–2970. ISSN: 0003-4916. DOI: https://doi.org/10.1016/j.aop.2008.03.004. arXiv: cond-mat/0505200.

[152] S. Bour et al. "Benchmark calculations for elastic fermion-dimer scattering". In: *Phys. Rev. C* 86 (2012), p. 034003. DOI: 10.1103/PhysRevC.86.034003. arXiv: 1206.1765 [nucl-th].

[153] P. F. Bedaque and H. W. Griesshammer. "Quartet S wave neutron deuteron scattering in effective field theory". In: *Nucl. Phys. A* 671 (2000), pp. 357–379. DOI: 10.1016/S0375-9474(99)00691-0. arXiv: nucl-th/9907077.

[154] Y. Yamaguchi. "Two nucleon problem when the potential is nonlocal but separable. 1." In: *Phys. Rev.* 95 (1954), pp. 1628–1634. DOI: 10.1103/PhysRev.95.1628.

[155] Y. Yamaguchi and Y. Yamaguchi. "Two Nucleon Problem When the Potential Is Nonlocal but Separable. 2". In: *Phys. Rev.* 95 (1954), pp. 1635–1643. DOI: 10.1103/PhysRev.95.1635.

[156] S. König. *private communication*. 2022.

[157] H. Georgi. "Unparticle physics". In: *Phys. Rev. Lett.* 98 (2007), p. 221601. DOI: 10.1103/PhysRevLett.98.221601. arXiv: hep-ph/0703260.

[158] H. W. Griesshammer. "Naive dimensional analysis for three-body forces without pions". In: *Nucl. Phys. A* 760 (2005), pp. 110–138. DOI: 10.1016/j.nuclphysa.2005.05.202. arXiv: nucl-th/0502039.

[159] W. Glöckle. *The quantum mechanical few-body problem*. Texts and monographs in physics. Berlin: Springer, 1983. DOI: 10.1007/978-3-642-82081-6.

[160] H. Kamada and W. Glöckle. "Solutions of the four-body Yakubovsky equations for the α -particle using realistic 2N interactions". In: *Phys. Lett. B* 292 (1992), pp. 1–4. DOI: 10.1016/0370-2693(92)90598-X.

[161] H. Kamada and W. Glöckle. "Solutions of the Yakubovsky equations for four-body model systems". In: *Nucl. Phys. A* 548 (1992), pp. 205–226. DOI: 10.1016/0375-9474(92)90009-9.

[162] W. Glöckle and H. Kamada. "On the inclusion of 3N-forces into the 4N-Yakubovsky equations". In: *Nucl. Phys. A* 560 (1993), pp. 541–547. DOI: 10.1016/0375-9474(93)90113-C.

[163] A. Nogga et al. "The Alpha particle based on modern nuclear forces". In: *Phys. Rev. C* 65 (2002), p. 054003. DOI: 10.1103/PhysRevC.65.054003. arXiv: nucl-th/0112026.

[164] W. Glöckle et al. "Selected topics in few-nucleon physics". In: *Nucl. Phys. A* 684 (2001), pp. 184–192. DOI: 10.1016/S0375-9474(01)00413-4.

[165] H. Kamada. "Four-Body Scattering Equations Including Three-Body Force". In: *Few Body Syst.* 60.2 (2019), p. 33. DOI: 10.1007/s00601-019-1501-4.

[166] H.-W. Hammer. "Unparticle physics and universality". KITP Program: Living Near Unitarity. 2022. URL: https://doi.org/10.26081/K6K64Q.

[167] S. Bour et al. "Topological phases for bound states moving in a finite volume". In: *Phys. Rev. D* 84 (2011), p. 091503. DOI: 10.1103/PhysRevD.84.091503. arXiv: 1107.1272 [nucl-th].

[168] S. Elhatisari et al. "Universal dimer–dimer scattering in lattice effective field theory". In: *Phys. Lett. B* 768 (2017), pp. 337–344. DOI: 10.1016/j.physletb.2017.03.011. arXiv: 1610.09095 [nucl-th].

[169] T. Yamazaki et al. "I = 2 pi pi scattering phase shift with two flavors of O(a) improved dynamical quarks". In: *Phys. Rev. D* 70 (2004), p. 074513. DOI: 10.1103/PhysRevD.70.074513. arXiv: hep-lat/0402025.

[170] S. König. "Few-body bound states and resonances in finite volume". In: *Few Body Syst.* 61.3 (2020), p. 20. DOI: 10.1007/s00601-020-01550-8. arXiv: 2005.01478 [hep-lat].

[171] A. Bulgac and M. M. Forbes. "Use of the discrete variable representation basis in nuclear physics". In: *Phys. Rev. C* 87.5 (2013), p. 051301. DOI: 10.1103/PhysRevC.87.051301. arXiv: 1301.7354 [nucl-th].

[172] N. Yapa and S. König. "Volume extrapolation via eigenvector continuation". In: *Phys. Rev. C* 106 (2022), p. 014309. DOI: 10.1103/PhysRevC.106.014309. arXiv: 2201.08313 [nucl-th].

[173] S. König. "Efficient few-body calculations in finite volume". In: Nov. 2022. arXiv: 2211.00395 [nucl-th].

[174] J. von Stecher, C. H. Greene, and D. Blume. "Energetics and structural properties of trapped two-component Fermi gases". In: *Phys. Rev. A* 77 (4 Apr. 2008), p. 043619. DOI: 10.1103/PhysRevA.77.043619. arXiv: 0801.2747.

[175] M. Yamashita, T. Frederico, and L. Tomio. "Three-boson recombination at ultralow temperatures". In: *Phys. Lett. A* 363 (2007), p. 468. DOI: 10.1016/j.physleta.2006.11.040. arXiv: cond-mat/0608542.

[176] F. M. Marques et al. "The Detection of neutron clusters". In: *Phys. Rev. C* 65 (2002), p. 044006. DOI: 10.1103/PhysRevC.65.044006. arXiv: nucl-ex/0111001.

[177] A. M. Shirokov et al. "Prediction for a four-neutron resonance". In: *Phys. Rev. Lett.* 117 (2016). [Erratum: Phys.Rev.Lett. 121, 099901 (2018)], p. 182502. DOI: 10.1103/PhysRevLett.117.182502. arXiv: 1607.05631 [nucl-th].

[178] K. Fossez et al. "Can tetraneutron be a narrow resonance?" In: *Phys. Rev. Lett.* 119.3 (2017), p. 032501. DOI: 10.1103/PhysRevLett.119.032501. arXiv: 1612.01483 [nucl-th].

[179] R. Lazauskas and J. Carbonell. "Is a physically observable tetraneutron resonance compatible with realistic nuclear interactions?" In: *Phys. Rev. C* 72 (2005), p. 034003. DOI: 10.1103/PhysRevC.72.034003. arXiv: nucl-th/0507022.

[180] E. Hiyama et al. "Possibility of generating a 4-neutron resonance with a $T = 3/2$ isospin 3-neutron force". In: *Phys. Rev. C* 93.4 (2016), p. 044004. DOI: 10.1103/PhysRevC.93.044004. arXiv: 1604.04363 [nucl-th].

[181] R. Lazauskas, E. Hiyama, and J. Carbonell. "Modeling the double charge exchange response function for a tetraneutron system". In: *PTEP* 2017.7 (2017), p. 073D03. DOI: 10.1093/ptep/ptx078. arXiv: 1705.07927 [nucl-th].

[182] A. Deltuva. "Tetraneutron: Rigorous continuum calculation". In: *Phys. Lett. B* 782 (2018), pp. 238–241. DOI: 10.1016/j.physletb.2018.05.041. arXiv: 1805.04349 [nucl-th].

[183] A. Deltuva and R. Lazauskas. "Tetraneutron resonance in the presence of a dineutron". In: *Phys. Rev. C* 100.4 (2019), p. 044002. DOI: 10.1103/PhysRevC.100.044002. arXiv: 1910.12333 [nucl-th].

[184] R. Lazauskas, E. Hiyama, and J. Carbonell. "Low energy structures in nuclear reactions with 4n in the final state". In: (July 2022). arXiv: 2207.07575 [nucl-th].

[185] K. Miki et al. *Correlations in multi-neutron systems*. Proposal at RIKEN. 2022.

[186] T. Nakamura and other. *SAMURAI47: Multi-neutron ^4n and ^6n states in extremely neutron-rich nuclei beyond the neutron drip line*. Proposal at RIKEN. 2022.

[187] J. Kirscher and D. Gazit. "The Coulomb interaction in Helium-3: Interplay of strong short-range and weak long-range potentials". In: *Phys. Lett. B* 755 (2016), pp. 253–260. DOI: 10.1016/j.physletb.2016.02.011. arXiv: 1510.00118 [nucl-th].

[188] A. Messiah. *Quantenmechanik Band 2*. De Gruyter, 1985. ISBN: 9783112327029. DOI: doi:10.1515/9783112327029.

[189] E. W. Schmid, H. Ziegelmann, and H. Stumpf. *The Quantum Mechanical Three-Body Problem: Vieweg Tracts in Pure and Applied Physics*. Burlington: Elsevier Science, 1974. ISBN: 9780080182407. URL: http://gbv.eblib.com/patron/FullRecord.aspx?p=1834260.